UNIVERSITY OF CALIFORNIA
RIVERSIDE

PROBING THE SPIN STRUCTURE OF THE PROTON USING POLARIZED PROTON-PROTON COLLISIONS AND THE PRODUCTION OF W-BOSONS

A Dissertation submitted in partial satisfaction
of the requirements for the degree of

Doctor of Philosophy

in

Physics

by

Michael J. Beaumier

August 2016

Dissertation Committee:

Professor Kenneth Barish , Chairperson
Professor Rich Seto
Professor John Ellison

The Dissertation of Michael J. Beaumier is approved:

Committee Chairperson

University of California, Riverside

Acknowledgments

I am indebted to my advisor, Ken Barish, whose calm, stoic and unabated support helped guide me through my research. Ken's advising style allowed me the freedom to pursue my own interests while keeping centered on scientific goals.

During my time at Brookhaven National Lab, I was mentored by many inspirational scientists and graduate students. Josh Perry taught me everything I know about PHENIX data acquisition. Martin Leitgab taught me the value of patience and tenacity when solving an intractable problem. Martin Purschke showed me the value of a sense of humor, even in stressful situations. Chris Pinkenburg demonstrated the advantage of doing things the right way, the first time.

Without Joe Seele, I would have never compiled a single line of code - his introduction to Makefiles and the wider world of computer science has been invaluable.

Richard Hollis has been a role model of persisance, patience, and good humor–he helped me edit this thesis, and always seemed to carve out time from his busy schedule to give me personalized attention.

Oleg Eyser pushed me to be the best graduate student possible. Even when I wanted to give up or just 'get the right answer', he did not lower his standards.

The team of researchers who carried out the 'W Analysis' with me comprise some of the most helpful and talented people I've ever worked with. Daniel Jumper has been my comrade in analysis since the beginning. Ralf Seidl has provided a constant cross check and push to improve. Francesca Giordano made time to explain even the simple things patiently to me, and guided me in my first foray into hardware assembly, with the RPCs. Along with Sangwha Park, Abraham Meles, Ciprean Gal, Chong Kim, and Hideyuki Oide, the W Analysis team has supported all aspects of this analysis with cross-checks, expert advice, and clearly written analysis notes and theses.

Angelika Drees and Amaresh Datta were both instrumental in directing and discussing my progress with the 'Vernier Analysis'.

I must also acknowlege my dear friends who have supported me emotionally throughout graduate school. Chris Heidt, Behnam Sarvestani, Pat Odenthal, Oleg Martynov, Corey Kownacki, Jackie Hubbard, Alex Natale-Anderson, and the DeGroots–I couldn't have done this without you guys.

Thank you to my mother and father, Bob and Marian, who always made time to support my various interests, and encouraged me to find my own way. They never once tried to force me onto one path, over another, and instead, gave me unconditional love, and the tools to become successful. Thank you to my two brothers, Joe and David, who have always had my back–I don't think anyone can ask for a better family than mine. Thank you to Emily, who put up with me when I was the worst, and helped me be at my best.

Some say that it takes a village to raise a child. The same can be said of raising a graduate student up to earning a PhD. This thesis is dedicated to the multitude who have helped me become the man I am today, and to students who struggle, and their mentors who do not give up on them.

ABSTRACT OF THE DISSERTATION

PROBING THE SPIN STRUCTURE OF THE PROTON USING POLARIZED PROTON-PROTON COLLISIONS AND THE PRODUCTION OF W-BOSONS

by

Michael J. Beaumier

Doctor of Philosophy, Graduate Program in Physics
University of California, Riverside, August 2016
Professor Kenneth Barish , Chairperson

This thesis discusses the process of extracting information about the spin structure of protons, specifically, spin contributions from the sea of quarks and anti-quarks, which are kinematically distinct from the 'valence quarks'. We have known since the 'proton-spin crisis' [1] of the late 1980s that proton spin does not entirely reside in the valence quarks, so the thrust of experimental efforts since then have been designed to determine both how to probe the proton spin structure, and how to validate models for proton spin structure. Here, I discuss one particular approach to understanding the sea-quark spin contribution, which utilizes the production of real W-bosons, and the W coupling with polarized spin structure in the proton sea, as produced from polarized proton-proton collisions. Only one of the colliding protons is longitudinally spin polarized, in this analysis, and they are collided at an energy of $500 GeV$. The experimental observable used is referred to as "A_L" which is expressed mathematically as a ratio of sums and differences of various helicity combinations of singly polarized interactions between two protons, i.e. $p + p^{\Rightarrow} :\rightarrow W \rightarrow \mu + \nu$. Once A_L has been experimentally measured, it can then be used to determine appropriate polarizations of proton sea-quarks, within a given uncertainty, if we write the cross-sections used in the calculation of A_L in terms of polarized parton distribution functions. Finally, this thesis will also include a discussion of my work experimentally determining the absolute luminosity of collisions at RHIC, which is needed as a normalization on any cross section used in the analysis. In particular, studying the cross section of the W interaction can help to validate our models for assigning a signal-to-background ratio to the $W \rightarrow \mu$ events.

Contents

List of Figures

List of Tables

Chapter 1

Introduction

THIS THESIS IS CURRENTLY AN UNPUBLISHED DRAFT. IT HAS NOT BEEN SUBMITTED AND MAY HAVE MISSING CITATIONS AND CONTENT

Although nuclear structure has been studied since at least late 19th century, a complete understanding of the proton's spin has eluded scientists. Early models of the proton structure such as the three valence quark model could accurately predict the charge and spin of the proton, yet when measured in the late 1980's this simplistic model was found to be wrong, in an event known as the'proton spin crisis' (Figure 1.1). One of the challenges of particle physics is to create a framework which can accurately describe matter, as well as predict the behavior of matter at all energy scales. Protons and neutrons are baryons which make up the majority of the mass in the visible universe, yet fully understanding the origins of their properties–such as spin, still eludes us. However, through the application of the scientific method over many generations of physicists, we have magnificently described this important particle, and understood many of its properties. However, one property which still defies our descriptions is its fundamental angular momentum, spin.

Our understanding of the proton has evolved and sharpened since the first experiments in deep inelastic scattering showed that the proton is not a fundamental particle [32]. Gell-Mann later planted the seeds of a theoretical framework which could in part describe some of the structure of baryons, a class of hadrons which we may näively describe as composed of three 'valence quarks' [33]. We can apply well known sum rules to the individual spins of the valence quarks which compose the proton in our naive valence-model to produce a correct prediction for the proton's spin $\frac{1}{2}$. When experimenters set out to measure the

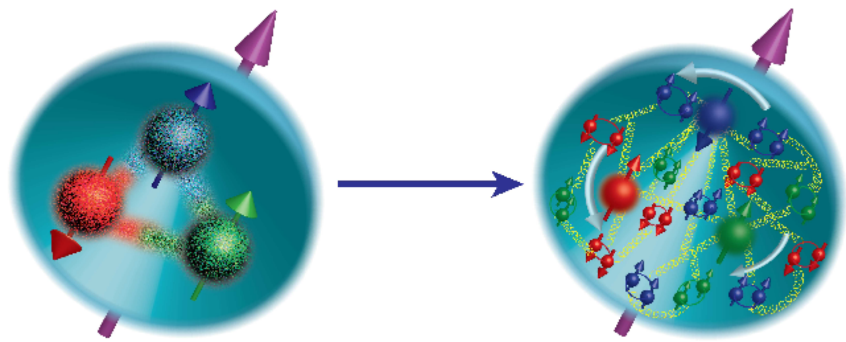

Figure 1.1: Left: the näive quark model, while predicting the correct spin of the proton, does not bear fruit when the quark spin contribution is measured. Right: a more realistic cartoon of the proton as a composite of gluons, valence quarks and sea-quarks [2].

contribution of these valence quarks in 1988 at the EMC experiment [1], they were surprised to find that the valence quarks carry only a small fraction of the proton's spin, especially in light of the fact that in the three-quark model, one can easily build a spin 1/2 particle from three spin 1/2 quarks.

Although recent papers [34] suggest that this 'spin crisis' (Figure 1.1) is simple due to mis-attribution of spin, most literature to date has focused on understanding how to model the proton with parton distribution functions. These parton distribution functions come in many varieties, and probe different degrees of freedom within the proton, in both the case of unpolarized parton distribution functions, and polarized parton distribution functions.

1.1 Scope and Objectives of This Work

In the first part of this thesis, I will describe the research I carried out between May of 2010 through August of 2016. This analysis comprises the body of work devoted to calculating A_L for the $W \to \mu$ decay. The results of this analysis are used in global fits to constrain the total contribution of quarks and anti-quarks in the so-called 'proton-sea' to the proton's total spin.

In the second portion of this work, I will discuss the 'Vernier Analysis', which is instrumental for every single-cross-section calculation taken with RHIC data. The thrust of the Vernier Analysis is to determine the beam luminosity at PHENIX's interaction point. This enables one to normalize the results to the p+p cross-section. This is done with a series of specialized Vernier-Scans, where beams are scanned across one-another in order to measure beam geometry. The luminosity can then be calculated from first principals, and compared to the estimated machine luminosity published by RHIC's collider-accelerator department. I produced an entire software framework for handling data cleaning, analysis, visualization and simulation.

Chapter 2

History

2.1 The Phenomenon of Spin

Spin is a fundamental quantity possessed by all elementary particles. We use the word ‘spin’ to describe the property, because particles which possess spin, behave as though they have some kind of intrinsic, hidden rotation, as if they were ‘spinning’. The dimension of spin, therefore is angular momentum. What is somewhat bizarre about spin, is that we do not observe anything physically spinning–although there are some phenomena (such as orbital angular momenta) which can be naively thought of as a ‘spinning system’ (but this description escapes classical analogy, due to its quantum, probabilistic nature). The role of spin in physics is of foundational importance, we should therefore strive to understand origin of spin in the building blocks of the visible universe - protons and neutrons.

The presence of spin in relativistic particles creates the phenomena of chirality, which has huge implications for how elementary particles can generate structure in matter itself [35]. In the case of the weak interaction, the presence of spin, which creates Chiral spinors breaks the left-right symmetry of weak coupling in matter (a fact which will be exploited in this thesis to probe the spin of the proton sea).

The phenomena of spin also changes the rules for how ensembles of particles may exist in a potential. Particles with spin are fermions, and because these particles must obey Fermi-statistics, we can observe structure in matter in the universe. Without spin, the world as we know it would collapse in on itself, making any kind of extended non-exotic structures which currently exist by virtue of the Pauli exclusion principal, impossible.

2.2 A Brief History of Relevant Physics

The study of Spin is really just an outgrowth of the general study of matter. Our models for matter, and the underlying structure of matter (in the modern sense), represents over a hundred years of experimental and theoretical efforts, and thousands of years of contemplating what makes up the universe.

Although indulgent on my part, I find it interesting, and humbling, to try and map out the path that humanity and science has trodden on its way to understanding the building blocks of the universe. To find the first time that humanity had murmurings that suggested our visible world is built from invisible, fundamental building blocks, we must travel back, nearly 2,500 years into the past.

Rather than provide a complete mathematical background to my measurement from a historic perspective, I will instead focus on the experimental historic narrative surrounding our quest to understand the structure of matter. After, I will present mathematical formalism relevant to this measurement directly–if the reader desires an exhaustive mathematical context, I invite them to read the classic tomes on Field Theory by Weinberg and reference the numerous theses written by my colleagues in theoretical physics and phenomenology.

2.3 Ancient Foundations

Sometime around 490 - 370 BCE lived two philosophers, Empedocles (Figure 2.1a), and Democritus (Figure 2.1b). Both men lived approximately at the same time, and made huge philosophical leaps in attempting to understand the nature of the visible world.

Democritus was part of a movement of thought which was first to make the intellectual jump that perhaps matter was not a continuum, but instead, composed of 'atomon', small, indivisible particles which when configured together, created all that is observable [38]. Empedocles was making equally important philosophical strides–in a manner complimentary to Democritus' opinion that matter must be made of atomon, Empedocles argued that matter is composed of elemental primitives [3].

Although Empedocles' 'periodic table' was only composed of Earth, Water, Fire, and Air, the idea that some unseen transmutation of elemental forces might generate ob-

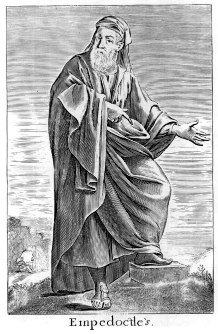

(a) Empedocles [36]

(b) Democritus [37]

Figure 2.1: Two Greek philosophers, who made important philosophical contributions our understanding of matter. Empedocles (left), postulated the precursor to the elemental theory of matter[3] and Democritus (right), postulated the precursor to the atomic theory of matter.

servables in nature with quite different (but perhaps reminiscent) properties then the 'pure substances' was an important step forward. Proto-scientists were beginning to generate models which derived our complicated observations, from simpler forms.

It took centuries of cultivation, leading up to the Scientific Revolution, for the next great steps to occur, for science. Thankfully, the luminaries of the Islamic Golden Age kept the fires of inquiry burning [39].

2.4 The Scientific Revolution

Thanks to the mathematical foundations laid out, built, and maintained by the minds of the Islamic Golden Age, Europe was well poised to reignite the flames of scientific inquiry, during the post Renaissance Scientific Revolution [39].

This period of growth in science was unprecedented during the Scientific Revolution, thanks to the seeds of empiricism germinated during the Islamic Golden Age, fertilized by the Italian Renaissance, and helped to flourish through British Empiricism [40].

(a) Galileo [41]

(b) Newton

Figure 2.2: Giants in the age of Empiricism, Newton (left) and Galileo (right) both made foundational contributions to Physics. Galileo lived in Italy, born in 1564 and dying in 1642. Newton lived in England from 1642 until his death in 1727

2.4.1 Galileo Galilei

While Galileo is best known for his work in Observational Astronomy, his importance to science extends beyond this. During his years in exile for his controversial views of the heliocentric universe, he produced some of his most important scientific work in kinematics [42]. What made this work remarkable is the care that Galileo took in merging careful mathematical modeling with well designed experimentation. This methodical approach to inquiry laid the foundation for others to slowly begin to pull back the curtains obscuring physical law.

Galileo's formalization of the scientific method inexorably set science on a course to delving deep into the nature of matter, and the laws of nature.

2.4.2 Isaac Newton

Fittingly born in the same year as Galileo's death, Isaac Newton would carry on Galileo's legacy of rigorous mathematical modeling mixed with experimentation. Perhaps no other scientist has touched so many different aspects of physics, from theories of propagation of light, to celestial mechanics, to mathematics, and kinematics.

Newton's Principia is perhaps the most important scientific work ever published. It opened the doors of the universe in a way that nobody has since duplicated. Newtons' laws of motion are still taught in school today, and although they have since been shown to be inaccurate at the smallest and largest scales, they still provide startlingly accurate predictions for the regular motion of matter.

One particularly tantalizing theory of Newton's was the corpuscular theory of light. Although not his most influential theory by far, the idea that an apparently continuous medium such as a beam of light might be made of small packets of energy (corpuscles) turned out to be partially right [43].

Newton's theories, and contributions to science are enormous, and have moved us deeper still into the underpinnings of matter. It would not be until roughly 200 years after his death, in the 19th century, that we finally can take the first steps into the world of the atomic, and sub-atomic: the world of the proton.

2.5 Atomic Theory

On the shoulders of giants such as Newton and Galileo, science finally came to know the tool which has been indispensable to modern particle physics: scattering. Rutherford and Thompson both carried out the most important scattering experiments in modern science, and provided us with the first hints of a hidden, quantum world, though it would not be until the 20th century that these important experiments would be fully contextualized with a theory of quantum scattering.

Scattering experiments offer a very powerful method where we one uses a well known initial state of matter (typically in the form of a beam), allows this beam to interact with an unknown configuration of matter, and measures the scattered beam. By carefully studying the kinematics of the scattered beam, we can create models which allow us to understand the structure of the target matter or describe the nature of the interaction between the beam and target.

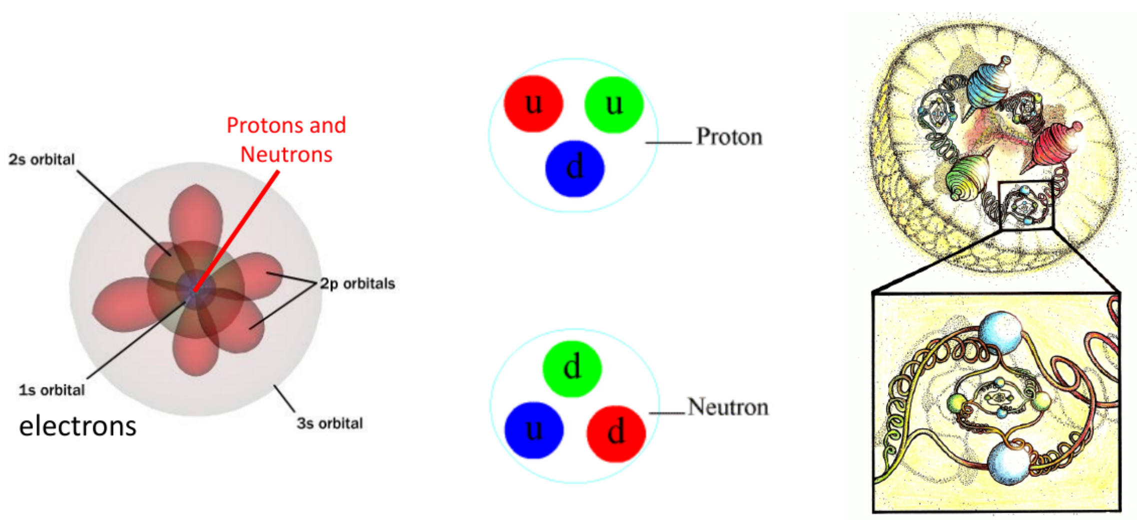

Figure 2.3: As we journey down further in scale, matter begins to look quite different. In fact, the models we use are scale dependent. Thomson 2.8, and Rutherford 2.5 began to see matter as collections of atoms (left) [4] (though not in terms of the orbital structure pictured), though it would not be until 20th century quantum mechanics that electron orbitals were discovered. Soon, nuclei were discovered to be divisible into protons an neutrons [5] (center), which in turn were discovered to be composed of a sea of quarks and gluons (right [6])

2.5.1 John Dalton

While many had postulated the existence of atoms, the first evidence based theory which suggested the existence of atoms was produced by John Dalton in the early 19th century. Dalton made an important conceptual leap to relate the existence of stoichiometric ratios in chemistry to the presence of small, individual functional units in his experiments with chemical reactions. Dalton's realization was only made possible due to his careful accounting of reactants in his experiments.

It was not until Einstein's 1905 theory on Brownian Motion was experimentally verified by Jean Perrin to place limits on the mass and size of atoms that Dalton's atomic theory was ultimately vindicated [44].

2.5.2 J.J. Thompson

(a) J.J. Thomson [45]

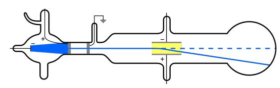

(b) Cathode Ray Tube [46]

Figure 2.4: Left: J.J. Thomson, who showed that cathode ray tubes were in fact producing the first observed subatomic particle: the electron. Right: A cartoon of Thomson's cathode ray tube setup. Electrons would be deflected by a magnetic field, sent from cathode to anode.

Thomson (Figure 2.4) would discover that atoms are not the smallest, indivisible piece of matter. In his landmark experiment, he used cathode ray scattering experiments to show that cathode rays were in fact subatomic particles. He showed these cathode rays were identical to particles given off by the photoelectric effect, and that these same particles were responsible for electric current. He had discovered the electron. And, if atoms were not the smallest piece of matter, then perhaps, atoms themselves might not be 'indivisible' as previously thought [47].

2.5.3 Ernest Rutherford

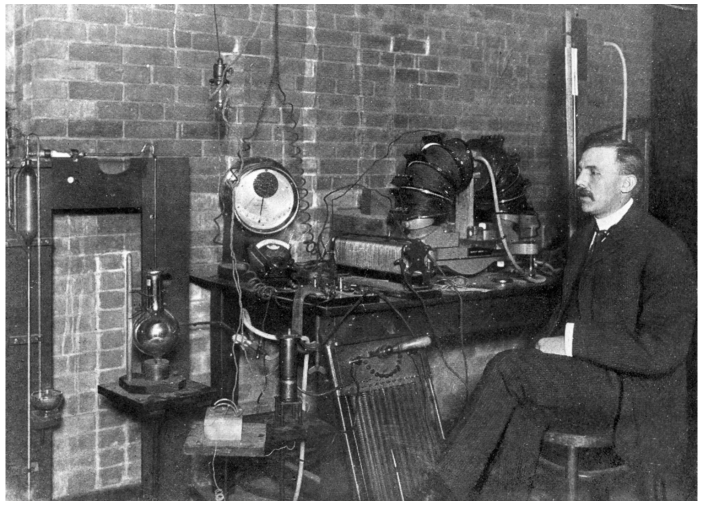

Figure 2.5: Ernest Rutherford, in his lab. [7]

Ernest Rutherford (Fig 2.5) was the first to show that atoms themselves were highly structured–and consisted of a small dense center, later called the nucleus.

Rutherford's work with radioactivity was of fundamental importance, he discovered and classified both alpha-particle radioactivity and beta-particle radioactivity. Further studies into these types of nuclear radiation would unlock the nucleus of atoms through the work of future scientists. Notably, Rutherford discovered the proton.

Rutherford's proposed planetary model for the nucleus, while technically wrong, shifted paradigms from the pudding model of atoms, to the more familiar nucleus + electron cloud model which has been spectacularly modeled and verified with the forthcoming scientists which defined the field of quantum mechanics.

Rutherford's work helped push us our of the cocoon of classical mechanics into the world of the quantum mechanics–scientists would soon find that the nucleus is not just a dense concentration of charge, but a probabilistic structure, with rich sub nuclear structure.

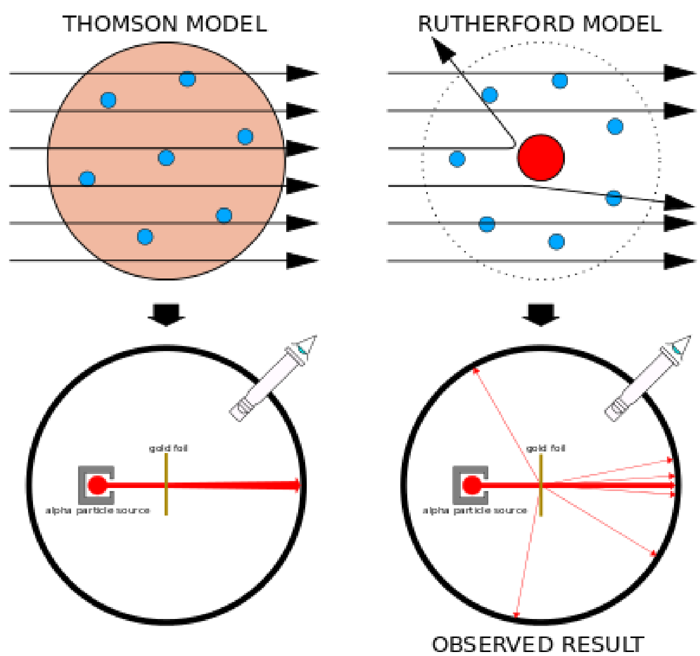

Figure 2.6: Ernest Rutherford's historic experiment, showing (top right) that atoms were composed of a small dense nucleus, in contrast to Thomson's 'pudding model' of homogeneous charge (top left). The experiment, (bottom left and right) contrast the expected results (bottom left) against the observed results (bottom right) [8].

Figure 2.7: The attendees of the Solvay Conference in Brussels, 1927 [9].

2.6 Early Quantum Theory

During Rutherford's time, experiments were already underway which were investigating modeling light as a wave phenomena. This was in contrast to Newton's (unverified) corpuscular theory of light. The argument whether light was wave-like or particle-like eventually lead to a classical field theory describing light, and the electromagnetic interaction, yet scientists such as Max Planck were proposing theories which required the quantization of light [48]. Einstein would show that in his analysis of the photoelectric effect, that light indeed was quantized into 'corpuscles'. The nascent atomic theory of matter was also hinting at a hidden, quantized world.

At the Solvay Conference in Brussels, Figure 2.7 in 1927, an unprecedented gathering of some of the most important figures in modern physics, built the foundations of what would become quantum mechanics. These scientists defined the nature and rules of quantum mechanics–the weird model which accommodates a duality of matter. Matter was modeled as having both wave-like, and particle-like behavior, depending on the observation and experiment. The notion that probing the structure of matter did not yield a simple, deterministic hierarchy of structure was revolutionary, confusing, and bizarre, and still is to this day.

It was found that not only light possesses this wave-particle duality, but also the very particles that make up atoms as well. These models were formalized by Dirac, Hilbert and Von-Neumann.

Though experiment tended to lead theory, regarding understanding the composition and rules of interactions in matter, in the mid 20th century, further refinements and additions to quantum mechanics gave birth to quantum field theory. While early quantum models were very successful at describing static particles trapped in static potentials–such as refining atomic theory to include predictions of observed atomic spectra, more work was needed to understand the relationship between electrical currents, light and magnetism. These concepts were all related by Maxwell [49] in the latter half of the 19th century, but did not make good predictions for systems in motion.

Dirac was first to create a model for describing the electron, its behavior in electromagnetic fields, and photon emission and absorption, under fully relativistic and quantum conditions [50]. Dirac's model was so successful, that it would become the basis for what we now call quantum electrodynamics. Much of the mathematical formalism has been reused to describe other field theories, which are the ultimate language which model and describe the structure of matter–including the insides of a proton.

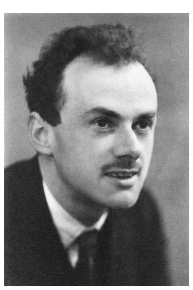

(a) Paul Dirac, 1933 [51]

$$\left(\beta mc^2 + c\left(\sum_{n=1}^{3} \alpha_n p_n\right)\right)\psi(x,t) = i\hbar\frac{\partial\psi(x,t)}{\partial t} \quad (2.1)$$

(b) The 'Original Form' of the Dirac Equation

Figure 2.8: Paul Dirac, next to his original formulation of the Dirac Equation, describing the wave function for an electron with rest-mass m, in terms of its space-time coordinates. Dirac's equation has been expressed free of any defined basis.

Dirac's work also began to incorporate relativistic effects in his wave equations modeling the electron, as well as crucially incorporating the spin (i.e. Dirac Spinors) of these particles, which were important for making precise predictions for atomic spectra [50].

By this time, the proton was already known to reside in the enigmatic nucleus of atoms, however, attempts to use Quantum Electrodynamics to describe the state of the nucleus failed–it was clear that there was a very strong force, holding together the protons of a nucleus tightly–far in excess of the electromagnetic repulsion felt by the positively charged particles. There was a completely different coupling strength between this apparent strong nuclear force, and the better known electromagnetic coupling. Further complicating an understanding of the nucleus is the fact that as the length scale of probing decreases, the energies probed increase, fundamentally making the nucleus a relativistic object. Experimental physics would once again, forge ahead, in attempting to understand the inner workings of the nucleus, in the time-honored tradition of performing scattering experiments.

2.7 Early Particle Physics and The Eightfold Way

The hydrogen atom, and its spectra was well modeled with quantum mechanics by the end of early 20th century, however attempts to study Helium were not as successful. However, in 1932, when Chadwick turned a beam of helium particles (at that time only known as α particles) on a sample of Beryllium, he observed that neutral, non-ionizing, penetrating radiation was produced [52]. Photons were ruled out as possible candidates, leading to the discovery of the neutron. Protons and neutrons were hypothesized by Heisenberg to both be the same state of a new conceptual particle, the nucleon, [53]. In the same year, Anderson discovered the positron.

By 1934, Hideki Yukawa (Fig. 2.9) had created an effective field theory for interactions of 'elementary particles' (at this time, thought to be protons and neutrons). He predicted the existence of mesons, and wrote down an effective field theory which described how protons and neutrons bind together in the nucleus [54].

Though non-relativistic quantum mechanics was mostly complete by 1934, scientists were already hard at work incorporating relativistic corrections to the theory. Experiments with cosmic rays soon revealed the existence of muons and the first observation of mesons.

Three separate paths eventually lead to the development of particle accelerators, which are to date, the best mechanism we possess in physics to probe nuclear structure. These accelerators are an outgrowth of ever more intense Rutherford-style experiments, Tandem Van-Der-Graaf generators, resonant acceleration techniques, RF linacs, and betatron accelerators [55].

By the 1950's, a cornucopia of strange new particles had been discovered, both matter and antimatter. But scientists drove forward, deeper, yearning to discover what was fundamental. By the 50's, neutrinos had been proposed, as well as Kaons, Pions, and Lambdas. Physicists were doing nuclear chemistry, in a sense, attempting to work out how quickly some particles decayed, and what decays were allowed or forbidden–science entered an age of nuclear alchemy.

"Strange" particles were discovered (K and Λ), so called because in bevatron experiments, they were produced in great quantities, but were slow to decay, unlike the faster π decay. Gell-Mann proposed that this strangeness in matter was due to a new

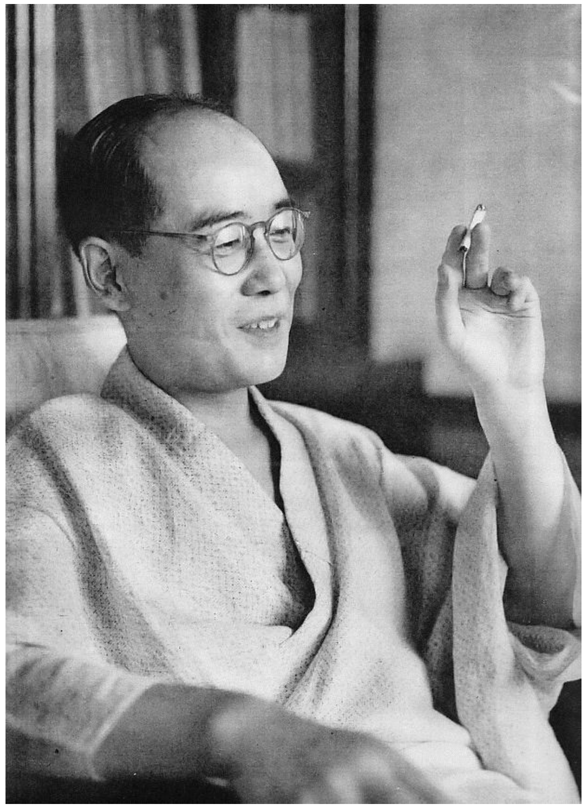

Figure 2.9: Hideki Yukawa, the first Japanese Nobel Laureate and publisher of influential research on the theory of mesons, and other elementary particles [10].

quantum number (he called it ‘strangeness’). The name stuck. [56], [57], [52]

The introduction of new conserved quantities, and the vast proliferation of particles was in full swing–the subatomic world by the 1950’s was confusing, and complex. In his book “The God Particle”, Leon Lederman recalled his adviser, Enrico Fermi frustratedly remarking ’Young Man, if I could remember the names of these particles, I would have been a botanist’. At this time, in the mid 1950’s, the number of mesons and baryons which had been discovered were at least in the dozens, if not more.

While the use of particle accelerators were speeding us along in our search for the structure of matter, one particular invention truly revolutionized the field–the bubble chamber (Figures 2.10 and 2.11.)

The bubble chamber was essentially a large vat of supercritical fluid which could easily be caused to boil with small perturbations. This feature was exploited, by positioning a bubble chamber in a magnetic field (to cause charged tracks to bend) near the interaction point between a particle beam and a fixed target. The bubble chamber itself was sometimes the target–since a popular liquid to use was hydrogen.

Figure 2.10: An old bubble chamber, once used at Fermilab, [11]

Invented by Donald Glaser in 1952, the bubble chamber was 'perfected' by Luis Alvarez when he helped to develop a version which could be used with liquid hydrogen. Hydrogen was desirable as a substance due to its extremely simple structure, which supplied much cleaner results than other fillings, unlike the original filler, Ether.

Soon after the advent of bubble chambers, physicists were able to macroscopically image these new, exotic particles interacting with normal matter as well as decaying–and develop novel computer techniques to analyze and catalog the massive influx of data.

The break-through came in 1961, when Gell-Mann and Nishijima leveraged recognized the underlying symmetry of the interactions taking place, and created what would be known as 'the eightfold way'. This theory created a scheme for organizing the observed

Figure 2.11: An example of the photographs taken with a Bubble Chamber, in 1973. In this picture, we see a 300 GeV proton producing particles as it travels through a hydrogen-filled bubble chamber at Fermilab [12].

baryons and mesons according to their properties in groupings called “octets”. These octets were in fact representations of the elements of members of the $SU(3)$ group. Another way of stating this, is that Gell-Mann had discovered the underlying structure of flavor-symmetry between the three lightest quarks–u, d, and s. This work directly led to the development of the quark model of matter, the foundation of what would become the foundation of the standard model of particles. To date, the standard model is the most successful theory describing particles, and their interactions.

Gell-Mann’s quark model soon made important predictions which were later verified, notably the Ω^-, which was the ground-state particle of the spin-3/2 decuplet–discovered at Brookhaven National Laboratory (the same lab from which my research has been derived!).

Gell-Mann formalized his quark theory of matter in 1964, however, due to the unforeseen phenomena of color confinement, it would be several years before evidence of quarks composing baryons and mesons was directly obtained from deep inelastic scattering experiments.

2.8 Quantum Chromodynamics and The Parton Model

Deep inelastic scattering experiments, Figure 2.12 were a natural outgrowth of Rutherford's experiment from the late 19th century. There are a few notable differences. Rutherford's scattering experiments can be modeled classically, by using a classical potential as a scattering source, and then solving as usual using an impact parameter and potential as in central force problems. Rutherford's experiments were considered generally 'elastic' because the target absorbed very little kinetic energy from the projectile, and no new particles were created from the kinetic energy of the projectile-target system.

However, in the late 20th century, scattering experiments became highly inelastic–targets would absorb a lot of kinetic energy–sometimes so much that targets would break apart and the kinetic energy of the system would create particles. When referring to scattering as 'deep inelastic', the 'deep' part refers to the process by which a scattering event occurs between a target particle and an internal, point-like element of some complex ensemble (such as a nucleus).

During the process of a high energy interaction between the projectile (often a beam) and the target, some kind of interaction occurs between the target and the projectile, in a way that changes the state of the projectile, and generates matter due to the high energies involved. One can observe the state of the projectile, and account for the matter which is created, and if there are laws which govern how the state of the projectile changes, or the kinds of matter that can be created, then we can run the clock backwards, reconstructing the kind of interactions that happened, to learn something about nuclear structure (or even partonic structure). In this way, one can also identify conserved quantities, which in turn suggest physical symmetries, which in turn help to build models.

One can think of interaction of a beam and target in terms of a probability of interaction–and this formalism will be discussed further in chapters related to the Vernier Analysis I worked on. Succinctly, however, one can mathematically 'separate' part of this interaction probability into a quantity called a 'cross-section', often denoted as σ for a total cross section, or $d\sigma$ for a differential cross section, or even $\frac{d\sigma}{d\Omega}$ to refer to a differential cross section scattered into a solid angle. The σ of any scattering experiment can be represented many different ways.

From a theoretical standpoint, we can represent protons (and other baryons) by selecting the relevant internal degrees of freedom we may want to study, and then devising some rules for the internal structure. We may be interested in the momentum fraction carried by some distribution of partons, or how the relative populations of partons within a certain kinematic regime changes with distance/energy scale. For all of these cases, we use parton distribution functions, or structure functions. Concretely, these functions depend on:

A subcategory of deep inelastic scattering is 'Semi-Inclusive Deep-Inelastic Scattering'. This refers to a case where a beam (say a lepton, such as an electron) interacts inelastically with a point-like internal structure of a target particle, and a hadron is produced (such as a π^+), which is then detected. Semi-Inclusive Deep-Inelastic scattering is then the process by which the scattered lepton and a specific hadron are measured in the final state of the interaction (but other particles that might be produced are neglected or ignored).

I said the word parton, which I have been carefully avoiding, but now the cat's out of the bag. Nuclei, as we will learn, are not elementary particles, but instead, are built up from what we assume are fundamental, elementary particles. Deep inelastic scattering experiments slowly revealed that nuclei (individual protons and neutrons) were not elementary particles, but instead, composite particles. It is natural to assume then, that the properties of protons and neutrons are not fundamental either. And in fact, the vast zoo of particles that were discovered in early inelastic scattering experiments, such as π or K or Λ (discussed briefly earlier) were not fundamental either.

In Michael Riordan's excellent 1992 summary of the discovery of quarks, Riordan lays out a very succinct and thorough history of the late 20th century experimental and theoretical works which built on Rutherford and Gell-Man's work. Riordan states that surprising 'results came from a series of electron scattering experiments...from 1967 through 1973' at MIT and SLAC, which comprised the first set of evidence produced in favor of the partonic model. As described earlier, Gell-Mann created a three-quark model to produce predictions consistent with these observations [58].

By the 1970's, collaborations between Bjorken, Feynman, and others had produced a coherent partonic model which contained quarks, and force mediating gluons. Additionally, the concept of Structure functions had been developed. Modified from Rutherford's original scattering formula, this new formula to describe the cross section of deep inelastic scattering incorporated structure functions, which separated out the momentum ex-

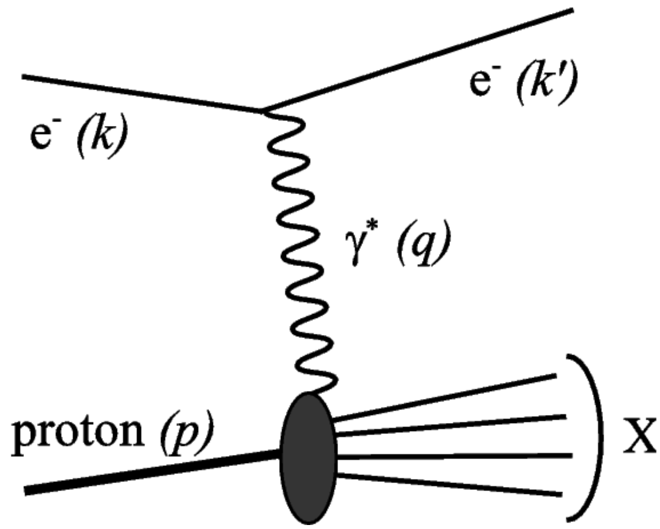

Figure 2.12: A schematic [13] of deep inelastic scattering, where the incoming electron inelastically scatters off the proton, producing results X, via virtual photon exchange, γ^*. The diagram is split into a perturbative portion (the electron) and a non-perturbative portion. Mathematically, we describe the interaction with kinematic variables summarized in Equations 3.1-3.3

change between target and projectile (via a virtual photon), and isolated this from W_1 and W_2, structure functions which were experimentally measured quantities representing the electron-proton interaction (the 'physics-y' part of the interaction).

This period of time, from 1970–1990 was truly the golden age of Deep Inelastic Scattering Experiments–the biggest laboratories running experiments were (and some are still running) The European Organization for Nuclear Research (CERN), The Stanford Linear Accelerator Center (SLAC), and The German Electron Synchrotron (DESY). Thousands of papers were published–some groundbreaking, such as the CERN's European Muon Collaboration experiment which showed a measurement of the spin asymmetry and determination of the proton structure function g_1 in muon-proton deep inelastic scattering [1].

The formalism of scattering theory continued to evolve during the booming period of particle physics from 1960 to present day. Though the mechanics of scattering experiments have remained essentially unchanged, vast improvements in technology in detectors, data collection and reconstruction, and beam production have evolved from Geiger and

Marsden's humble beginnings to create scientific measurements of particles and their properties with exquisite and unprecedented precision. The kind of precision I'm talking about is exemplified in Brookhaven National Laboratory's E821 Muon (g-2) experiment–which measured the anomalous magnetic moment, g-2, of the muon to a precision of 7 parts in ten million [59].

The advent of structure functions hailed an era of non-point-like baryonic matter. The mathematics of scattering formalism had to change to accommodate the underlying physical distribution of partonic matter in baryons. Deep Inelastic Scattering continued to probe various portions of these structure functions, and the structure of the standard model began to come into focus, distilled into the relatively simple mathematical structure of group theory. Concretely, the standard model is a gauge theory, which contains the internal symmetries of $SU_c(3) \times SU_L(2) \times U_Y(1)$, Figure 2.13. The Standard Model is said by some to be "complete" with the discovery of the Higgs Boson, yet with emergent phenomena such as proton spin, it does not provide a straightforward prediction. The model still has not included gravitation and relativistic effects fully–and probably isn't entirely correct.

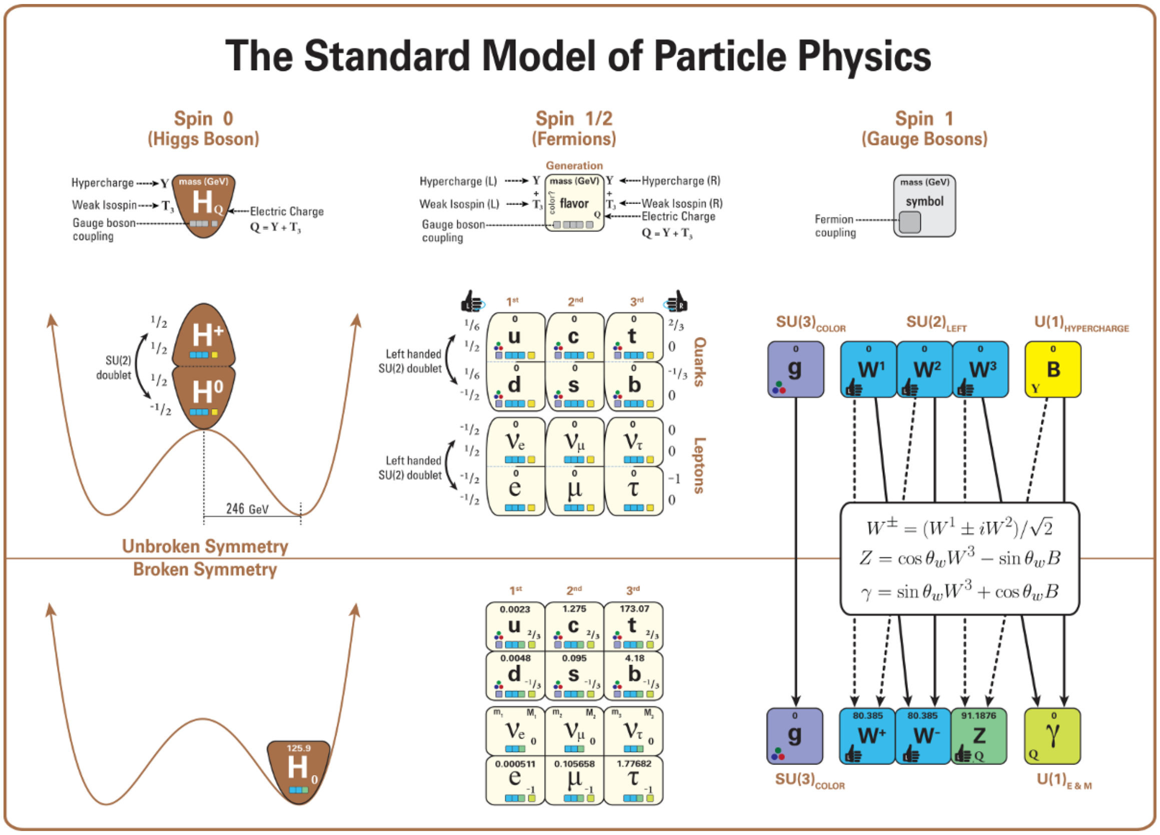

Figure 2.13: "This diagram displays the structure of the standard model (in a way that displays the key relationships and patterns more completely, and less misleadingly, than in the more familiar image based on a 4x4 square of particles). In particular, this diagram depicts all of the particles in the standard model (including their letter names, masses, spins, handedness, charges, and interactions with the gauge bosons – i.e. with the strong and electroweak forces). It also depicts the role of the Higgs boson, and the structure of electroweak symmetry breaking, indicating how the Higgs vacuum expectation value breaks electroweak symmetry, and how the properties of the remaining particles change as a consequence."[14].

2.9 The Era of Deep Inelastic Scattering

Here, I hope to highlight the last 40 years or so of physics produced by deep inelastic scattering experiments. We are now truly in an era of 'Big Science', where the boundaries of science are pushed by huge collaborations of men and women working together.

Since the era of deep-inelastic scattering brings us essentially up to speed with the physics needed to address the rest of this thesis, I will be rather broad in this final section of this chapter, sparing the explicit details for the next chapter.

This era of deep-inelastic scattering has unearthed some of the most surprising and monumental discoveries in physics–all the way from the recent discovery of the particle mediating the field that imbues all fundamental particles with mass, to the discovery that protons and neutrons are not fundamental particles at all, but are instead, highly relativistic balls of gluons.

The models trying to predict and describe the behavior of the proton and neutron, as well as the physics that creates a nuclear bound state have been in development since the late 1950's. By the late 1970's, we begin to approach a description of nuclear partons that closely resemble what we see in present day.

The early days of deep inelastic scattering led to the discovery of many of the fundamental particles we know and love today, in the standard model. The precise way these particles forms baryonic matter was not initially well understood, though with the introduction of structure functions and parton distribution functions, we began to make progress.

SLAC's E### (E80-E155) were some of the first experiments to probe the proton spin structure, operating from 1978-1999. SLAC pioneered the usage of spin asymmetries as a means of ruling out models for various parameterizations of quark structure functions, as well as provided important data constraining nuclear structure functions. SLAC's experiments focused on understanding the spin structure of the quarks (but not gluons) within protons.

The European Muon Collaboration at CERN was one of the first major international efforts to get underway studying the underlying structure of protons and neutrons with deep inelastic scattering. The collaboration produced scientific results from 1979 to 1997. The EMC's major contribution to our understanding of nuclear structure was to amass evidence which supported the parton model of protons and neutrons, as well as discovered the self-named 'EMC effect', which showed that the volume 'occupied' by quarks scales with heavier nuclei [60]. The EMC also elucidated the effects of quark fragmentation and hadron production, DIS in the nuclear medium, and produced some of the first measurements of the spin structure of the proton. Most famously, the EMC originally discovered the 'proton spin crisis' in its first measurement of the proton spin structure function, $g1$ where it found the spin carried by the proton's 'valence quarks' to be less than 1/2 [1].

CERN also produced another collaboration which contributed to our understanding of nuclear structure–the Spin Muon Collaboration. The SMC was active from 1993 to 1998, used polarized beams of muons shone onto a polarized target (ammonia and later p-butanol) to measure a virtual photon production asymmetry A_1 in order to measure information about the structure function, g_1 (discussed in detail in the following chapter). g_1 gives access to the quark polarization of protons. Spin structure physics has been explored at the COMPASS experiment since 2005. CERN's work to understand the spin structure of the proton probed the contributions of both the quark, and gluons.

In Germany, DESY is the premier accelerator science laboratory, and has been operating continuously since 1964. DESY's primary experiments in deep inelastic scattering with regards to nucleon structure have been underway since 1992. DESY operates several important deep inelastic scattering experiments including ZEUS, HERA (H1 and H2) and HERMES. The scientific goals of DESY are much broader, since it represents Germany's premier accelerator physics scientific effort, including fields such as condensed matter physics and astrophysics. However, the portion of DESY's research program devoted to spin structure seeks to understand both the quark and gluon contributions to proton spin.

Jefferson Laboratory (JLab) is an electron accelerator complex in Virginia specializing in the cutting edge of fixed target electron deep inelastic scattering experiments. Experiments in Hall A, B and C are all involved with studying both quark and gluon contributions to proton spin.

Of course, an important unmentioned player in the modern era is the Relativistic Heavy Ion Collider, and the experiment PHENIX. The cumulative results of these experiments and how they inform this thesis research with regards to our probing and modeling of the structure of protons are presented in the following chapter.

Chapter 3

Models and Associated Probes For Proton Spin Structure

With the advances made over the last half-century, we have come very close to obtaining a complete model describing the world around us. Rapid progress has been made in the last 40 years in the understanding of the structure of the nucleon. Protons and neutrons make up the majority of the mass in the visible universe–therefore understanding their nature completely is of fundamental importance to physics.

In the previous chapter, we discussed in the history behind studying the structure of matter, leading up to a brief discussion of the contemporary experiments in proton spin structure. Glaringly, I neglected to discuss the Relativistic Heavy Ion Collider (RHIC) and the Pioneering High Energy Nuclear Interaction eXperiment (PHENIX), since I wanted to put the program into a firm theoretical context in this chapter.

This thesis will discuss the experimental efforts of PHENIX to do something no other experiment has done–utilize the production of W-Bosons as a direct probe of proton spin. Before we discuss the specifics of this measurement, lets first put proton spin into a larger context.

3.1 Modeling the Proton Structure

One frequent theme in using particle accelerators to study any kind of nuclear structure is that we do not ever get to directly look at the innards of a proton, due to the phenomena of color confinement.

This means that often, we must deal with the process of how partons (quarks, gluons) fragment and decay after a proton proton collision. Additionally, we must deal with and account for the scale-variance of the fundamental forces.

The scale variance of the fundamental forces has large implications for the strong nuclear force, generally represented by the coupling constant, α_S. This constant scales with distance, and becomes highly non-perturbative at short distances. Writing models in high energy physics can be created to describe perturbative processes or non-perturbative models. In perturbative models, the general strategy is to write down a Hamiltonian or Lagrangian to describe a system, and then obtain predictions from the model by expanding in terms of a 'small' parameter. Then, predictions from the leading order, NLO, NNLO or NNNLO are made and verified with data. Non perturbative models often cannot write down the final solution to some differential equation which is thought to describe a solution–so instead, experiments are designed to constrain these models with data. The models can then make more predictions which can again be verified with experiments.

The internal degrees of freedom of the proton, and the small scales involved make models for the proton fall generally into non-perturbative regimes. We find that the very structure and distribution of partons and gluons in the nucleus is a scale-dependent phenomena, that is to say, if we take measurements at a lower energy, we get a different distribution of partons and gluons than if we measure at higher energy. This scale dependence requires many measurements to be taken which probe different scales in order to properly constrain models for proton structure.

In order to properly model the non-perturbative structure of the proton, we use a Factorization Theorem, which provides us a way to mathematically separate an probing interactions (such as electron-hadron scattering in DIS) into perturbative and non-perturbative parts (example, Figure 2.12). The non-perturbative aspect in the figure (the X) is often the portion which is experimentally constrained.

Because modern models for proton structure treat the particle as a largely non-perturbative object we create distribution functions which are experimentally measured (or constrained) to handle predictions of the proton's properties which arise from non-perturbative processes. One such property is the spin of the proton, which must arise in some way from the interactions of the quarks and gluons which swirl about inside of the proton.

As a note here, for this work on theoretical background of deep inelastic scattering in the first portion of this chapter, I reference Dr. Ciprean Gal's clear and coherent introduction to the subject, published in 2014 [61], in his thesis describing the complimentary analysis done at PHENIX at central rapidities. Later on, I will more heavily rely on Dr. Oide's work published in his respective thesis. Thanks guys!

3.1.1 Structure Functions

Given that the proton itself has so far been shown to be a non-perturbative object, we need a means to model the structure of the interaction when two protons collide, and generate particles. Generally, we can calculate a structure function associated with each hadronic process. The variables we define to describe the kinematics of deep inelastic scattering are (see Figure 2.12):

$$P \tag{3.1}$$

$$Q^2 \equiv -q^2 \tag{3.2}$$

$$x \equiv \frac{Q^2}{2P \cdot q} \tag{3.3}$$

P is the total hadron momentum (in our case, the proton's momentum), Q^2 is the energy exchange between the proton and probe lepton, and x is the fraction of the total proton's momentum carried by the quark scattering with the lepton. q, in Equation 3.3 is four-momentum transferred from the lepton to the quark.

We can then write down structure functions in terms of these variables. We have:

$$F_1(x, Q^2) = \frac{1}{2} \sum_f e_f^2 \left(q_f(x) + \bar{q}(x)\right) \tag{3.4}$$

$$F_2(x, Q^2) = 2xF_1(x, Q^2) \tag{3.5}$$

The subscript, f refers to the quark flavors represented in the structure functions, with e_f referring to the charge of each quark being summed over (i.e. $\pm\frac{1}{3}$ or $\pm\frac{2}{3}$). $q(x)$ refers to the parton distribution function associated with each quark flavor.

An integration over the momentum fraction, x of Equation 3.5 and the gluon structure function $g(x)$ yields the familiar 'valence quark' structure of the proton, i.e. two up-quarks and one down quark, with remaining quark flavors q_h summing to zero:

$$\int_0^1 F_2(x,Q^2) + g(x)dx = \int_0^1 \left(x \sum_f e_f^2 \left(q_f(x) + \bar{q}(x)\right) \right) + g(x)dx \tag{3.6}$$

$$\int_0^1 \left(u(x) + \bar{u}(x)dx\right) dx = 2 \tag{3.7}$$

$$\int_0^1 \left(d(x) + \bar{d}(x)dx\right) dx = 1 \tag{3.8}$$

$$\int_0^1 \left(q_h(x) + \bar{q}_h(x)dx\right) dx = 0 \tag{3.9}$$

The rest of the world data on $F_2(x, Q^2)$ is summarized in Figure 3.1

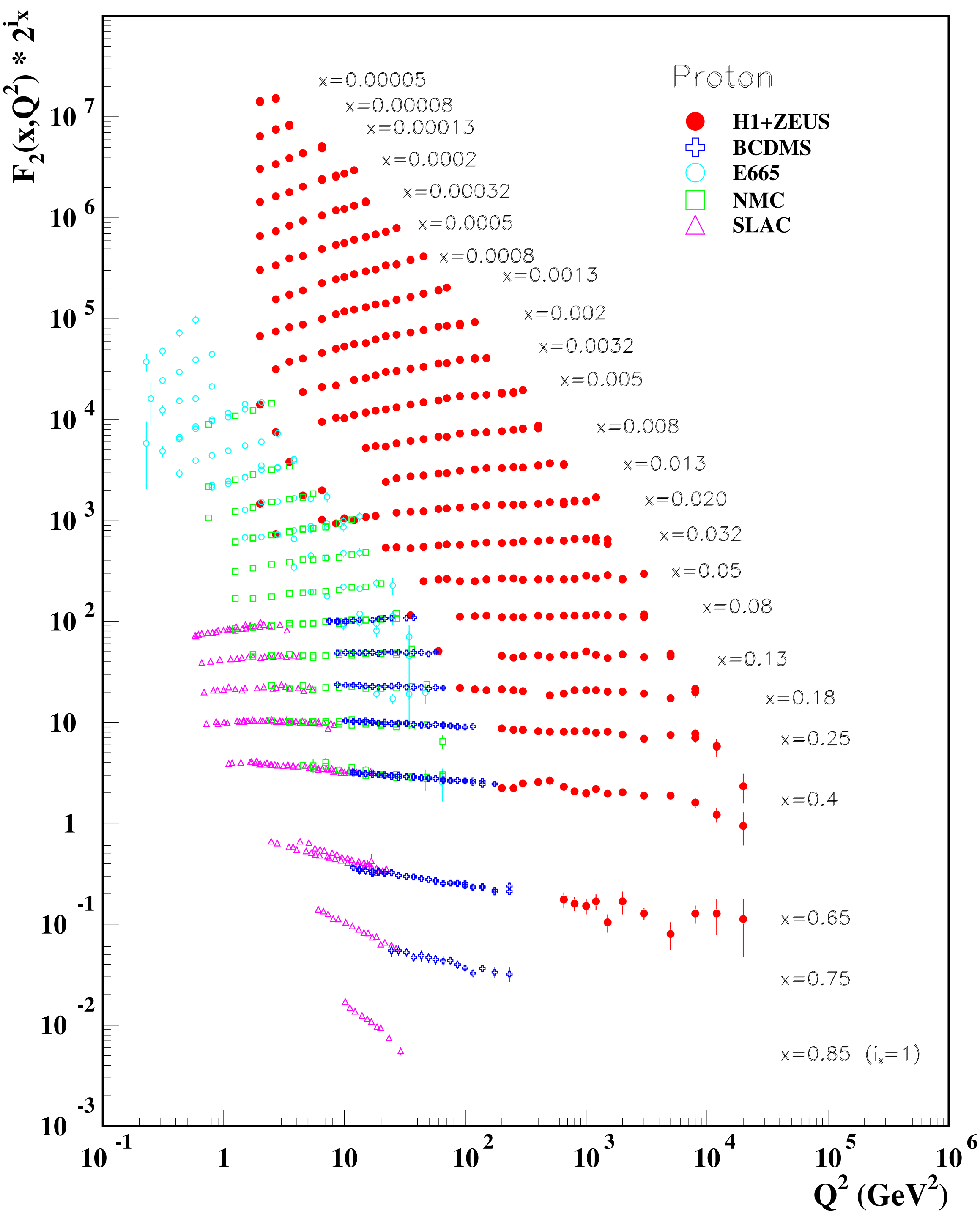

Figure 3.1: Here, we see "the proton structure function, F_2^p measured in electromagnetic scattering experiments of electrons and positrons on protons" from experiments including H1+Zeus, BCDMS, E665, NMC and SLAC [15]

3.2 Parton Distribution Functions

From this dataset, we can extract Parton Distribution Functions for any combination of x and Q^2. Under this particular framework, we can use the DGLAP evolution equations to evolve PDFs observed at one Q^2 to some other Q^2 [62].

With QCD evolution, one can additionally undertake a global analysis, which effectively puts a constraint on Parton Distribution functions using 'evolved projections' of x and Q^2 into the kinematic range of the experimental probes [61].

The world data on proton structure can by evolved with the DGLAP equations [63] to generate parton distribution functions representing the momentum fraction carried by various partons building up the proton, the summary of this is shown in Figure 3.2.

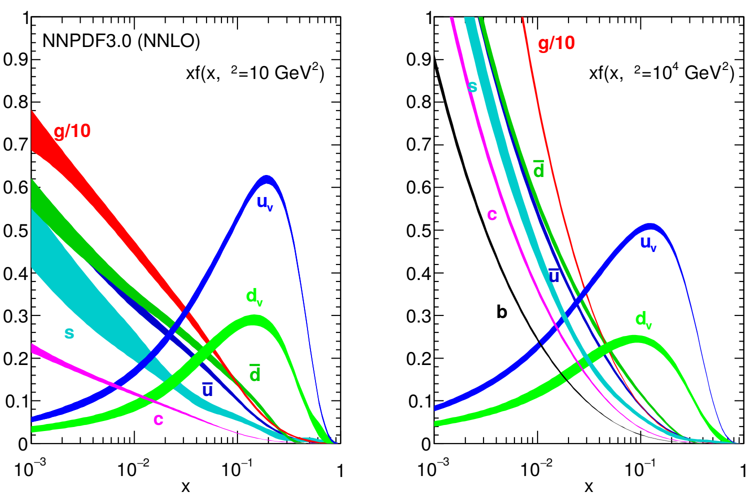

Figure 3.2: Here, we see as expected–the PDF for u is about twice as large as d indicating the valence structure of the proton at high-x (> 0.1). On the left is the NNPDF calculation of PDFs with world data (width is related to uncertainty) at 10 GeV, while 10 TeV is shown on the right. Note that at low x, the proton is dominated by gluons. [15].

While DIS, and Semi-Inclusive Deep Inelastic Scattering have provided a wealth of data on the proton's internal structure–we have the advantage at RHIC to undertake a complimentary analysis, using hadron-hadron collisions, instead of hadron-lepton collisions. A similar picture to DIS can be drawn of hadron-hadron interactions to the DIS schematic, as seen in Figure 3.3.

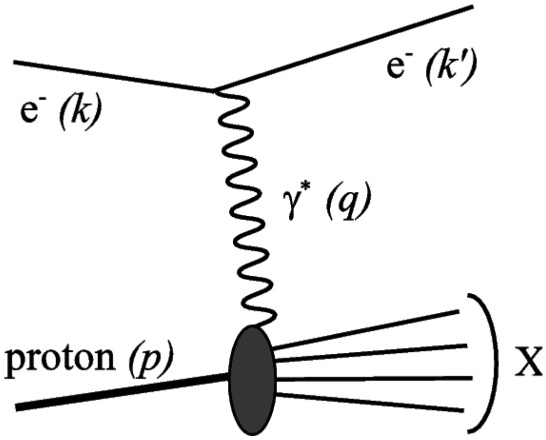

(a) Leptonic Deep Inelastic Scattering

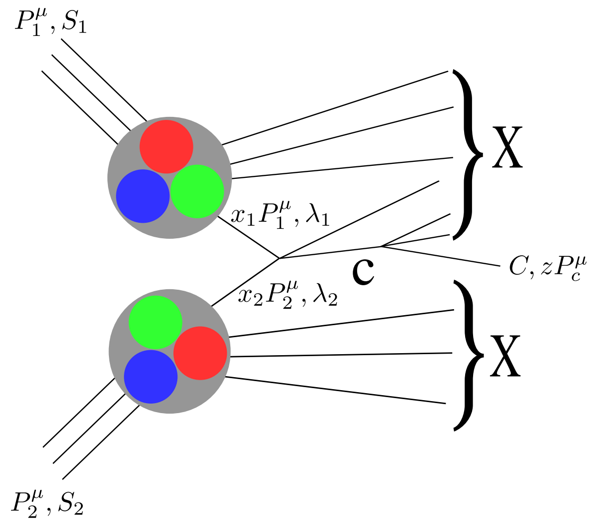

(b) Hadronic Inelastic Scattering

Figure 3.3: Deep Inelastic Scattering Process (left) alongside Hadron-Hadron inelastic scattering (right). In hadron inelastic scattering, one may try to select initial state with scattering between arbitrary partons in order to probe various proton structures.

Hadron-Hadron scattering can be a useful means to determine PDFs experimentally, but often intermediate states are not known and it is difficult to isolate a single PDF. Hadron-hadron scattering experiments are an excellent way to constrain gluon PDFs.

3.2.1 Polarized Parton Distribution Functions

Polarized parton distributions are measured with the same methods discussed above–except the beam and target in the scattering formalism are spin-polarized. We can similarly write down the structure functions for polarized protons, in the same manner as F_1 and F_2:

$$g_1 = \frac{1}{2}\sum_q e_q^2 (q^+(x) - q^-(x)) = \frac{1}{2}\sum_q e_q^2 \Delta q(x) \tag{3.10}$$

Here, e_q is the charge of the quark-flavor (i.e., $1/3e$, $2/3e$), with the sum taken over all quark/anti-quark flavors. The q terms refer to the number density of each particularly quark flavor associated with the "+" or "-" quark spin orientation (relative to the struck hadron), such that "+" refers to a parallel spin and "-" refers to an anti-parallel spin. g_1 describes the longitudinal spin polarization of the nucleus, while g_2 describes the transverse spin polarization of the nucleus. A knowledge of both longitudinal and transverse spin structure is necessary for a complete understanding of the three-dimensional structure of the proton. This thesis presents my analysis of the longitudinal spin structure, so I will leave a further discussion of g_2 in the capable hands of my colleagues.

The experimental tool for measurement of the spin structure of the proton is the 'spin asymmetry'. The spin asymmetry is defined in two ways–one, through cross-sections, which crucially, may be additionally defined in terms of the structure functions. For any value of x and Q^2, we may write down the asymmetry:

$$A(x, Q^2) = \frac{\sigma^+ - \sigma^-}{\sigma^+ + \sigma^-} \tag{3.11}$$

$$\equiv \frac{g_1(x, Q^2)}{F_1(x, Q^2)} \tag{3.12}$$

With our knowledge of F_1 from fits to the world's data, we can use the asymmetry to measure g_1 directly. With the discovery that the proton's spin is not entirely carried by the valence quarks, we can construct additional spin-dependent parton distribution functions, and design experiments to measure and constrain them. Thus far, the world's data to do so has been used to generate predictions of these PDFs summarized in Figures 3.4 and 3.5.

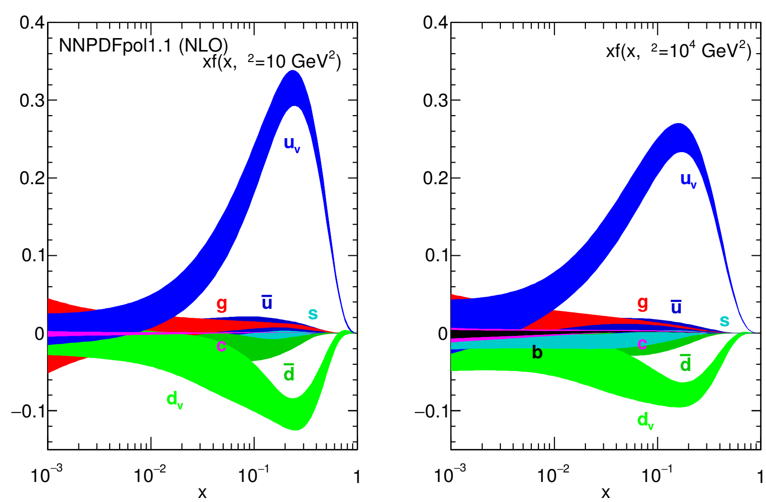

Figure 3.4: World data used to generate fits to predict the parton distribution functions of various quark flavors in the proton at 10 GeV (left) and 10 TeV (right) [15]

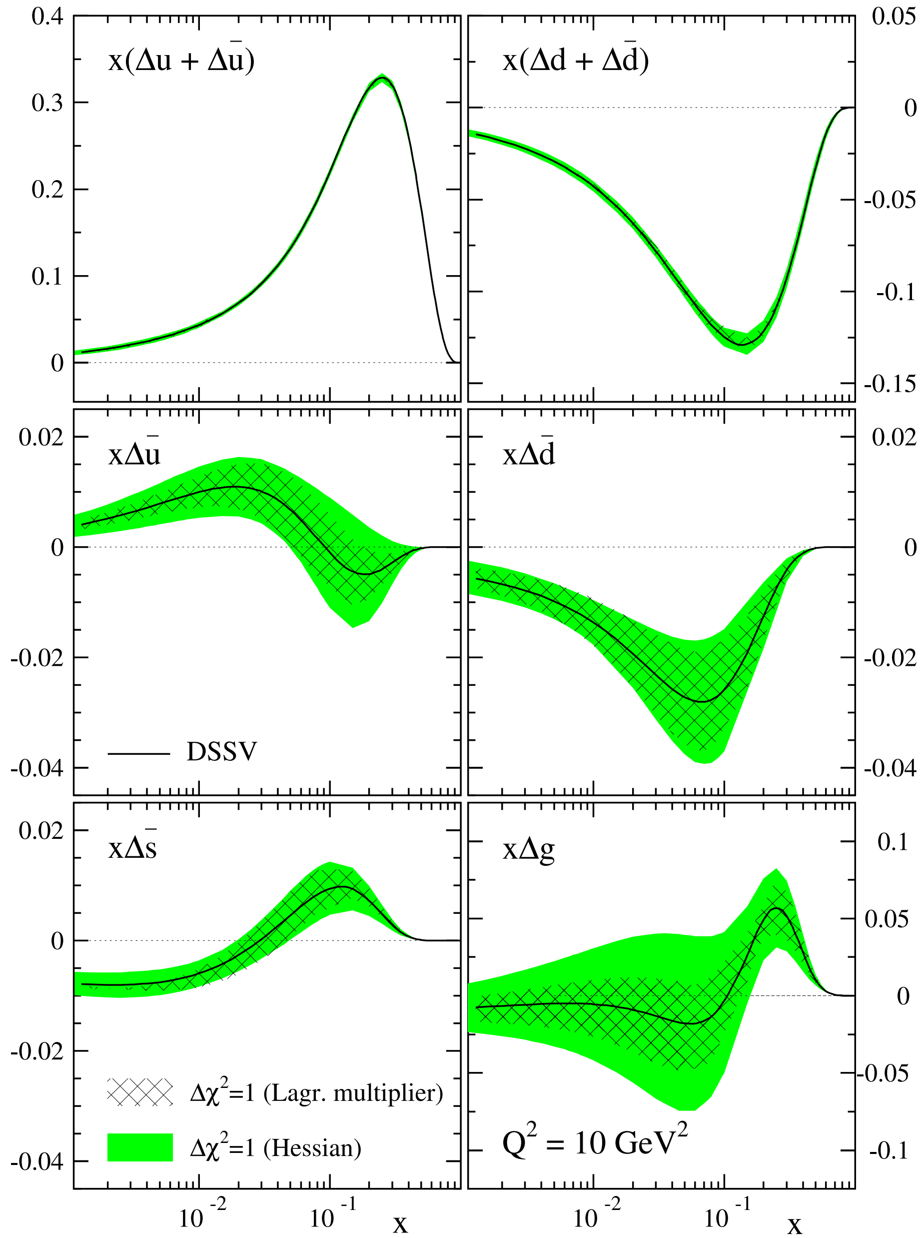

Figure 3.5: de Florian, Vogelsang, Sassot and Stratmann produced predictions at 10 GeV for the PDFs for quarks and anti-quarks and gluons in the proton. The uncertainties for the gluon and anti-quark PDFs are quite large, warranting experimental investigation [16].

3.3 Proton Spin Decomposition with the Ellis-Jeffe Sum Rule

We may write down the spin contribution of the proton as a sum of the various spin contributions via the polarized parton distribution functions of the partons inside the proton in various gauges:

Gauge invariant Ellis-Jeffe

$$\langle P,\frac{1}{2}|\hat{J}_z|P,\frac{1}{2}\rangle = \frac{1}{2} = \frac{1}{2}\Delta\Sigma + L_q + J_g \tag{3.13}$$

Infinite momentum decomposition:

$$\langle P,\frac{1}{2}|\hat{J}_z|P,\frac{1}{2}\rangle = \frac{1}{2} = \frac{1}{2}\Delta\Sigma + L_q + \Delta g + L_g \tag{3.14}$$

Quark decomposition:

$$\Delta\Sigma = (\Delta u + \Delta\bar{u}) + (\Delta d + \Delta\bar{d}) + (\Delta s + \Delta\bar{s}) \tag{3.15}$$

There is a large uncertainty in the contribution of the anti-quarks to the proton spin 3.15, which this thesis will seek to constrain.

3.4 The Spin Asymmetry: An Experimental Probe

As discussed in the previous sections, the spin asymmetry is an important experimental probe into the longitudinal spin structure function, g_1 from which we can derive polarized parton distribution functions. At RHIC, we can use hadron inelastic scattering to construct asymmetries for various final-states to measure and constrain the parton distribution function. These probes are summarized in Figure 3.6.

One potential pit-fall of using hadronic initial states in spin measurements is the issue of fragmentation. It can be difficult to construct a clean probe, since often, the final measured state can be something like a photon decay from a π^0–and these π^0's can be produced in a vast array of fragmentation processes. It can be hard to isolate the parent interaction which produced the particles of interest. However, the production of W-Bosons offers a clean probe free of fragmentation into the polarization of anti-quark parton distribution functions. While all weak processes are mediated by the W/Z boson, real W-Boson production from $q + \bar{q}$ interaction produces a clear Jacobean peak at central rapidities at the 510 GeV $\sqrt{s}$ collision energy of interest, and additionally can be identified at forward rapidities using statistical methods discussed later.

Reaction	Dom. partonic process	probes	LO Feynman diagram
$\vec{p}\vec{p} \to \pi + X$	$\vec{g}\vec{g} \to gg$ $\vec{q}\vec{g} \to qg$	Δg	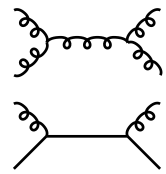
$\vec{p}\vec{p} \to \text{jet(s)} + X$	$\vec{g}\vec{g} \to gg$ $\vec{q}\vec{g} \to qg$	Δg	(as above)
$\vec{p}\vec{p} \to \gamma + X$ $\vec{p}\vec{p} \to \gamma + \text{jet} + X$ $\vec{p}\vec{p} \to \gamma\gamma + X$	$\vec{q}\vec{g} \to \gamma q$ $\vec{q}\vec{g} \to \gamma q$ $\vec{q}\vec{\bar{q}} \to \gamma\gamma$	Δg Δg $\Delta q, \Delta\bar{q}$	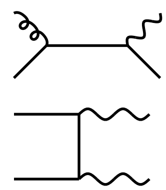
$\vec{p}\vec{p} \to DX, BX$	$\vec{g}\vec{g} \to c\bar{c}, b\bar{b}$	Δg	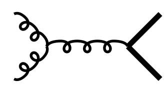
$\vec{p}\vec{p} \to \mu^+\mu^- X$ (Drell-Yan)	$\vec{q}\vec{\bar{q}} \to \gamma^* \to \mu^+\mu^-$	$\Delta q, \Delta\bar{q}$	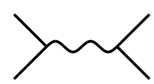
$\vec{p}\vec{p} \to (Z^0, W^\pm)X$ $p\vec{p} \to (Z^0, W^\pm)X$	$\vec{q}\vec{\bar{q}} \to Z^0,\ \vec{q}'\vec{\bar{q}} \to W^\pm$ $\vec{q}'\bar{q} \to W^\pm, q'\vec{\bar{q}} \to W^\pm$	$\Delta q, \Delta\bar{q}$	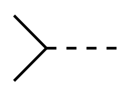

Figure 3.6: A summary of the various probes for longitudinally polarized protons. The **"Reaction"** column summarizes the reaction observed experimentally. The **"Dom. partonic process"** column describes the dominant process at the partonic level. The **"probes"** column shows which proton spin structure can be measured with the reaction. Finally, the leading order Feynman diagram for the partonic process is drawn. Figure is reproduced from: [17].

3.5 W Production

Though W-Bosons obviously can be created in collisions with the right ingredients and correct energy, the W-Bosons that we're interested in at RHIC are very special. The collision conditions around the protons at colliding at PHENIX provides just enough energy to create real W-Bosons from interaction of quarks and anti-quarks between two colliding protons. The energy is not sufficiently high enough to produce real W-Bosons from other processes in amounts which would significantly dilute the primary source.

The standard model tells us that W production occurs through a pure vector-axial interaction, this implies that the helicity of the parents particles–in particular $u + \bar{d} \rightarrow W^+$ and $\bar{u} + d \rightarrow W^-$ have fixed helicities, due to the relativistic final state neutrino (which is not measured, of course). To visualize the leading order of W production, with regards to the quark-sea element being probed, the leading order diagrams for the interaction are shown in Figure 3.7 [17]

Since Δq, the polarized parton distribution function can be split into contributions from valence quarks, and also sea quarks, understanding $\Delta\bar{q}$ is an important step towards understanding Δq better to better understand the total proton spin.

Though both protons in the collision are polarized, the polarization of one participant proton can be effectively ignored by summing over all polarization states for one of the two protons. With this assumption, we may construct a single spin asymmetry for colliding protons by counting difference in the number of positively and negatively polarized W's produced in collisions, scaled by the total production:

$$A_L{}^W = \frac{1}{P} \times \frac{N_-(W) - N_+(W)}{N_-(W) + N_+(W)} \tag{3.16}$$

This is a relatively easy experimental probe to measure (assuming that we can accurately count events which produced a W, which naturally, is nearly impossible, as we will see in Section 7.4).

As we saw earlier, in Section 3.2.1, we can write an asymmetry in terms of the scattering cross section for the process responsible for particle yields. These cross-sections were shown to be written in terms of polarized parton distribution functions, thus, we cut to the chase to write down the full expression of the theoretical asymmetries for this process in terms of those parton distribution functions.

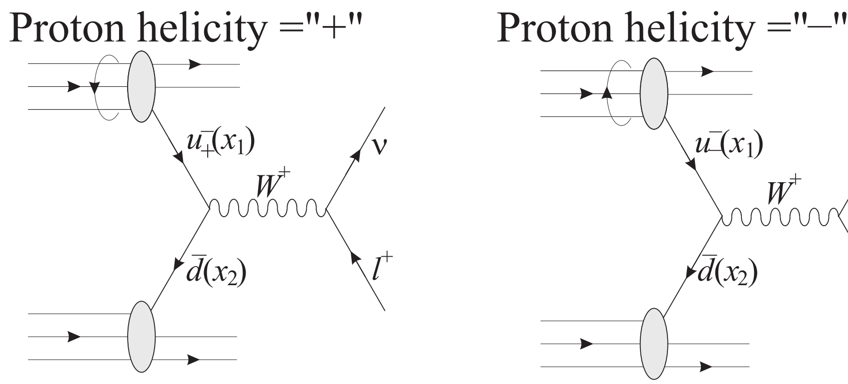

(a) Probe for Δu at lowest order.

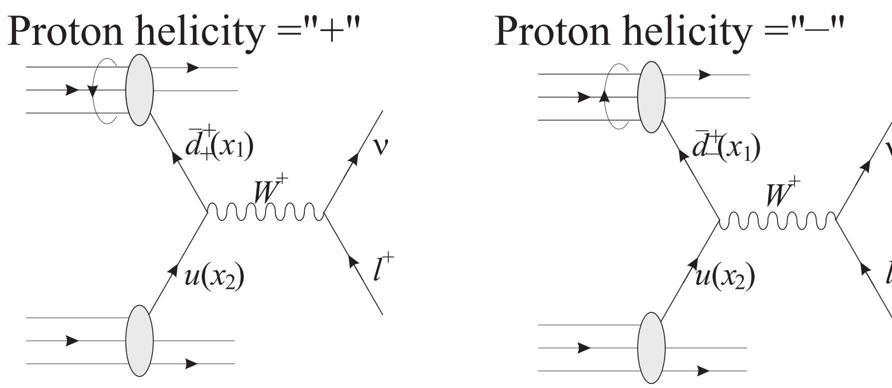

(b) Probe for $\Delta \bar{d}$ at lowest order

Figure 3.7: Real W^+ production as produced at PHENIX. The helicity of the initial state fixes the helicity of the partonic participants due to the relativistic final state of the neutrino + the handedness of the W boson. x_1 and x_2 are the momentum fractions of the quarks participating from the participant partons [17].

The following equations all contain an implied integration over x_1 and x_2.

For W^+ and u:

$$A_L^{W^+} = \frac{u_-^-(x_1)\bar{d}(x_2) - u_+^-(x_1)\bar{d}(x_2)}{u_-^-(x_1)\bar{d}(x_2) - u_+^-(x_1)\bar{d}(x_2)} \tag{3.17}$$

For W^+ and $\bar{d}$

$$A_L^{W^+} = \frac{\bar{d}_-^+(x_1)u(x_2) - \bar{d}_+^+(x_1)u(x_2)}{\bar{d}_-^+(x_1)u(x_2) + \bar{d}_+^+(x_1)u(x_2)} \tag{3.18}$$

Observationally, we see a superposition of 3.17 and 3.18, which is expressed in Equation 3.19:

$$A_L^{W^+} = \frac{\Delta u(x_1)\bar{d}(x_2) - \Delta\bar{d}(x_1)u(x_2)}{u(x_1)\bar{d}(x_2) + \bar{(d)}(x_1)u(x_2)} \tag{3.19}$$

For the case of W^-, we observe $\bar{d}$ and u: For W^- and d:

$$A_L^{W^+} = \frac{d_-^-(x_1)\bar{u}(x_2) - d_+^-(x_1)\bar{u}(x_2)}{d_-^-(x_1)\bar{u}(x_2) - d_+^-(x_1)\bar{u}(x_2)} \tag{3.20}$$

For W^- and $\bar{u}$

$$A_L^{W^+} = \frac{\bar{u}_-^+(x_1)d(x_2) - \bar{u}_+^+(x_1)d(x_2)}{\bar{u}_-^+(x_1)d(x_2) + \bar{u}_+^+(x_1)d(x_2)} \tag{3.21}$$

Observationally, we see a superposition of 3.20 and 3.21, which is expressed in Equation 3.22:

$$A_L^{W^-} = \frac{\Delta d(x_1)\bar{u}(x_2) - \Delta\bar{u}(x_1)d(x_2)}{d(x_1)\bar{u}(x_2) + \bar{(u)}(x_1)d(x_2)} \tag{3.22}$$

Kinematics of the collision can simplify the equations even further, when at very forward or very backward rapidities [17]. Concretely, this is shown via integration over the momentum fractions, x_1 and x_2, explicitly writing the W decay in terms of the scattering cross section for polarized proton collisions (a derivation reproduced from Hideyuki Oide's thesis [28]):

$$\begin{aligned} d\sigma\left(p^{\Rightarrow} + p \to W^+ \to \ell + \nu_\ell\right) = \\ \frac{K}{3}\int dx_1 dx_2 \sum_{i,j}\left(q_{i-}^{\Rightarrow}(x_1)\bar{q}_{j+}(x_2) + \bar{q}_{j+}^{\Rightarrow}(x_1)q_{i-}(x_2)\right) \\ \times\, d\hat{\sigma}(q_i + \bar{q}_j \to W^+ \to \ell^+ + \nu_\ell) \end{aligned} \tag{3.23}$$

Similarly, we may write the interaction cross-section for the opposite helicity in the initial state:

$$\begin{aligned} d\sigma\left(p^{\Leftarrow} + p \to W^+ \to \ell + \nu_\ell\right) = \\ \frac{K}{3}\int dx_1 dx_2 \sum_{i,j}\left(q_{i-}^{\Leftarrow}(x_1)\bar{q}_{j+}(x_2) + \bar{q}_{j+}^{\Leftarrow}(x_1)q_{i-}(x_2)\right) \\ \times\, d\hat{\sigma}(q_i + \bar{q}_j \to W^+ \to \ell^+ + \nu_\ell) \end{aligned} \tag{3.24}$$

Neglecting quark mass, we can assume that the helicity state of the quarks is identical to the chirality state. Then, we substitute in the definition for polarized parton distribution functions $\Delta q \equiv q_+^{\Rightarrow} - q_-^{\Rightarrow}$, and sum over quark flavors, neglecting strange contributions:

$$A_L\left(p^{\Rightarrow} + p \to W^+ \to \ell^+ + \nu_\ell\right) = \frac{\int dx_1 dx_2 \sum_{i,j}\left(-\Delta q_i(x_1)\bar{q}_j(x_2) + \Delta\bar{q}_j(x_1)q_i(x_2)\right)\cdot d\hat{\sigma}}{\int dx_1 dx_2 \sum_{i,j}(q_i(x_1)\bar{q}_j(x_2) + \bar{q}_j(x_1)q_i(x_2))\cdot d\hat{\sigma}} \tag{3.25}$$

$$\approx \frac{\int dx_1 dx_2 \left(-\Delta u(x_1)\bar{d}(x_2) + \Delta\bar{d}(x_1)u(x_2)\right)\cdot d\hat{\sigma}}{\int dx_1 dx_2 (u(x_1)\bar{d}(x_2) + \bar{d}_j(x_1)u(x_2))\cdot d\hat{\sigma}}$$

Since we have restricted ourselves to only the case for $u\bar{d}$, we are of course looking at the case of A_L^{W+}. We may rewrite Equation 3.25 to reflect its rapidity dependence:

$$A_L^{W+}(y_\ell) = \frac{\int dx_1 dx_2 \left(-\Delta u(x_1)\bar{d}(x_2)(1-cos\hat{\theta})^2 + \Delta\bar{d}(x_1)u(x_2)(1+cos\hat{\theta})^2\right)}{\int dx_1 dx_2 \left((u(x_1)\bar{d}(x_2)(1-cos\hat{\theta})^2 + \bar{d}_j(x_1)u(x_2))(1+cos\hat{\theta})^2\right)} \tag{3.26}$$

In this case, we follow Dr. Oide's convention of redefining $\hat{\theta}$ in terms of the angle between the direction of momentum of the polarized proton and the lepton in the center of mass frame. Therefore we see kinematic isolation of the polarized pdfs at forward or backward rapidity.

We may write $A_L^{W-}(y_\ell)$ similarly:

$$A_L^{W-}(y_\ell) = \frac{\int dx_1 dx_2 \left(-\Delta\bar{u}(x_1)d(x_2)(1-cos\hat{\theta})^2 + \Delta d(x_1)\bar{u}(x_2)(1+cos\hat{\theta})^2\right)}{\int dx_1 dx_2 \left((\bar{u}(x_1)d(x_2)(1-cos\hat{\theta})^2 + d_j(x_1)\bar{u}(x_2))(1+cos\hat{\theta})^2\right)} \tag{3.27}$$

With a clear understanding of the W-Boson production cross section, and the beam luminosity at RHIC, we may proceed!

Chapter 4

The Relativistic Heavy Ion Collider

4.1 Overview

While there have been many experiments which have performed deep inelastic scattering over the years, the experiments built around the Relativistic Heavy Ion Collider at Brookhaven National Laboratory are positioned to take advantage of this unique accelerator.

The Relativistic Heavy Ion Collider (RHIC) is the world's only intersecting ring particle accelerator which is capable of colliding polarized proton beams. The beams are differentiated with the mnemonic "Blue" and "Yellow" labels. The blue beam circulates clockwise when viewed from above the RHIC complex, the yellow beam circulates counter-clockwise. As is typical for intersecting ring experiments, the beams are bunched, with bunches of ions intersecting at designated intersection points, around which experiments are built. The filled bunches from the blue and yellow beams cross at a frequency of 106 nanoseconds. PHENIX's timing is set to correspond to the crossing rate of the blue and yellow beams. Because bunches always collide simultaneously, the blue beam timing clock is used as a matter of convention, though there are other timing clocks available for use. The bunches in the beams are numbered as a means of associating the bunch polarization configuration with the bunch crossing at each interaction region. This is necessary for any measurement which requires a knowledge of the initial polarization state of colliding hadrons (such as any spin physics measurement). This will be discussed more in the section of discussing the beam polarization at RHIC 4.3.

RHIC generally separates data taking into beam 'fills' which are uniquely numbered, and for which general data characterizing the machine state is logged in various databases and online logbooks. Logging is an important part of data quality assurance, but also plays a fundamental role in the physics. For example, the initial spin state of the colliding bunches is logged in databases, without which, spin analyses are impossible. The trigger configuration is recorded along with the rates associated with each trigger. Data logged into logbooks and databases characterizing a fill's performance also plays an important forensic role with regards to solving issues which occurred during data taking, but were not immediately caught. Furthermore, because PHENIX is an international collaboration, this logged data is fundamentally important to communicating the state of the machine and data collection to the collaboration, as well as establishing a record of operations.

RHIC fills are composed of a unique population of bunched ions, circulating around the rings. During polarized fills, every bunch is polarized according to a planned polarization pattern. At the end of each fill, (typically 8 hours of collisions), the beam is dumped, and a new fill is generated. Experiments built around RHIC generally subdivide fills into 'runs', where a run is a period of time where the experiment is taking data during which there were no obvious machine malfunctions. When major issues occur during a run, data taking is interrupted until the problem is remedied, and the data is discarded. At PHENIX, runs are always segregated within a fill–no run will ever contain data from multiple fills, due to the additional complexity of potentially changing machine conditions, significant downtime between fills, and the potential of beam-dumps into sensitive high voltage enabled electronics.

Scientists at RHIC have come up with many ingenious ways to create and maintain beam polarization (Section 4.3), once this is accomplished, various kinematically select probes are engineered, based on collisions observed which provide important cross-checks to DIS data as well as original discoveries and measurements of proton structure. RHIC is a unique collider in that it is quite flexible. Beams may be transversely or longitudinally polarized, a variety of ions may be used to fill the beams. To date, RHIC has collided many beam ions and species, summarized in Figure 4.2 and Figure 4.3.

RHIC is an facility which has been built on top of previous accelerator experiments–a Linear Accelerator, a booster ring, and an Alternating Gradient Synchrotron, all of which now have been re-purposed to create the necessary beam injection conditions appropriate for RHIC. Many experiments are still set up around various egress points along the acceleration chain, which are publicised on the Brookhaven National Laboratory website www.bnl.gov

At the time of writing of this Thesis (Spring of 2016), there are two experiments which are actively taking data from collisions produced by RHIC: The Pioneering High Energy Nuclear Interaction Experiment (PHENIX, Section 4.4, Figure 4.5), and the Solenoidal Tracker at RHIC (STAR, Figure 4.5). STAR and PHENIX are complimentary to each other–PHENIX has a very high precision centrally covering Electromagnetic Calorimeter, and other high precision detectors, but lacks full kinematic coverage, whereas STAR has lower precision (with some measurement dependent exceptions), but has the advantage of nearly full kinematic coverage around the beam intersection at its center.

RHIC's luminosity and beam polarization has been continuously improving (Figure 4.4) since RHIC was first turned on. As we will discuss later (Section 5.1), the increased luminosity observed in 2013, was maximally leveraged with upgrades to the PHENIX detector.

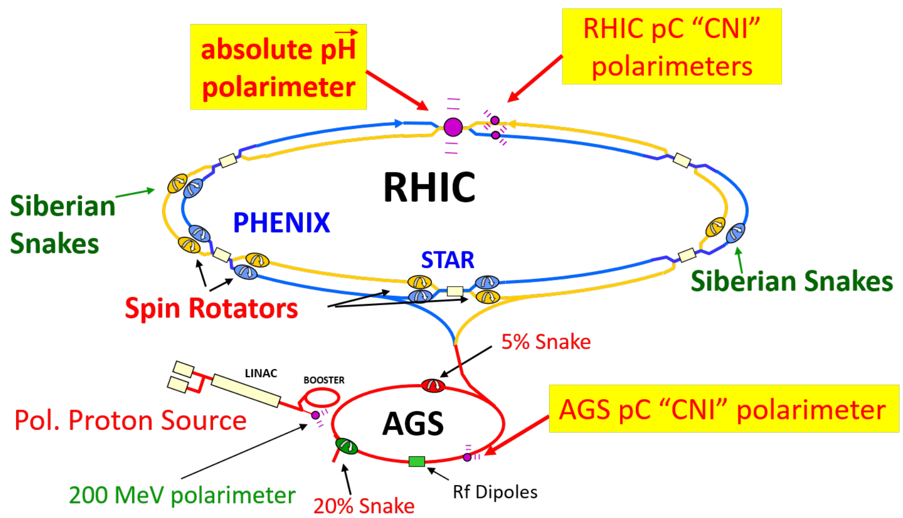

(a) Diagram of RHIC Accelerator Complex, (Figure from Kiyoshi Tanida)

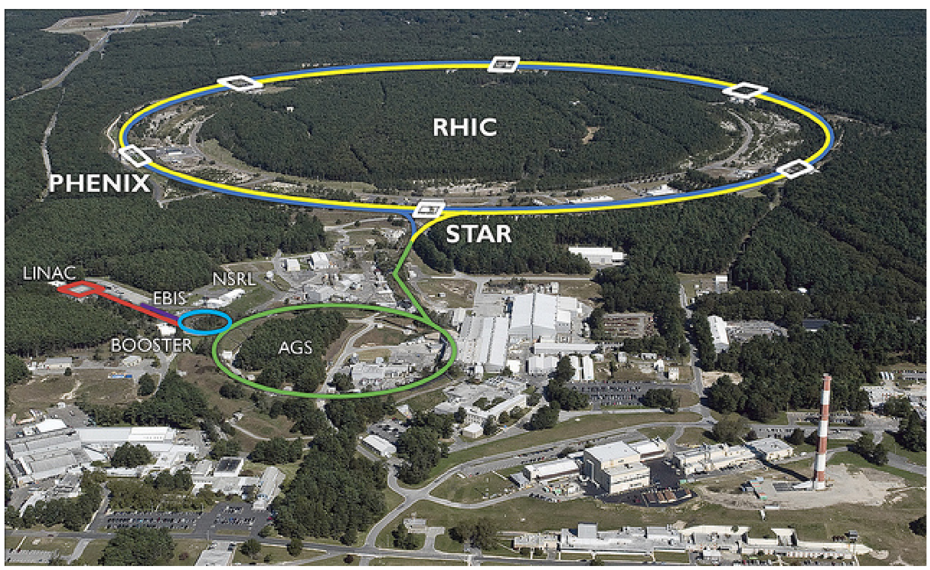

(b) Aerial photograph of RHIC Complex [64]

Figure 4.1: A diagram of the acceleration process of RHIC is shown in the top panel, and aerial view is shown in thin the bottom panel. RHIC is nearly four miles in circumference and collides a variety of ions at center-of-mass energies between 5 Gev $\sqrt{s}$ and 510 GeV $\sqrt{s}$.

RHIC operating modes and total integrated luminosity delivered to 6 experiments					
Run	**species**	**total particle energy [GeV/nucleon]**	**calendar time in physics**	**total delivered luminosity**	**average store polarization, (H-jet)***
Run-1 CY2000, FY2000 33.6 cryo-weeks	$^{197}Au^{79+}+^{197}Au^{79+}$	27.9	3 shifts	< 0.001μb^{-1}	—
	$^{197}Au^{79+}+^{197}Au^{79+}$	65.2	5.3 weeks	20 μb^{-1}	—
Run-2 CY2001/02, FY2001/02 40.7 cryo-weeks	$^{197}Au^{79+}+^{197}Au^{79+}$	100.0	15.9 weeks	258 μb^{-1}	—
	$^{197}Au^{79+}+^{197}Au^{79+}$	9.8	2 shifts	0.4 μb^{-1}	—
	polarized p + p	100.2	8.3 weeks total, no continous physics operation	1.4 pb^{-1}	14%
Run-3 CY2002/03, FY2003 30.4 cryo-weeks	d +$^{197}Au^{79+}$	100.7 + 100.0	10.2 weeks	73 nb^{-1}	—
	polarized p + p	100.2	9.0 weeks total, no continous physicsoperation	5.5 pb^{-1}	34%
Run-4 CY2003/04, FY2004 26.7 cryo-weeks	$^{197}Au^{79+}+^{197}Au^{79+}$	100.0	12.0 weeks	3.53 nb^{-1}	—
	$^{197}Au^{79+}+^{197}Au^{79+}$	31.2	9 days	67 μb^{-1}	—
	polarized p + p	100.2	6.1 weeks total, no continous physicsoperation	7.1 pb^{-1}	46%
Run-5 CY2004/05, FY2005 31.4 cryo-weeks	$^{63}Cu^{29+}+^{63}Cu^{29+}$	100.0	7.8 weeks	42.1 nb^{-1}	—
	$^{63}Cu^{29+}+^{63}Cu^{29+}$	31.2	12 days	1.5 nb^{-1}	—
	$^{63}Cu^{29+}+^{63}Cu^{29+}$	11.2	5 shifts	0.02 nb^{-1}	—
	polarized p + p	100.2	9.4 weeks	29.5 pb^{-1}	47%
	polarized p + p	204.9	2 stores	0.1 pb^{-1}	30%
Run-6 CY2006, FY2006 21.2 cryo-weeks	polarized p + p	100.2	13.1 weeks	88.6 pb^{-1}	55%
	polarized p + p	31.2	12 days	1.05 pb^{-1}	50%

Figure 4.2: Runs 1–3 at RHIC focused on commissioning work for experiments measuring collisions at RHIC. Work was mostly characterized by heavy-ion measurements related to understanding Quark-Gluon Plasma. The spin program began with Run 5. Table produced from data posted at the RHIC run page [18].

RHIC operating modes and total integrated luminosity delivered to 6 experiments					
Run	**species**	**total particle energy [GeV/nucleon]**	**calendar time in physics**	**total delivered luminosity**	**average store polarization, (H-jet)***
Run-7 CY2006/07, FY2006 18.4 cryo-weeks	$^{197}Au^{79+}+^{197}Au^{79+}$	100.0	12.8 weeks	7.25 nb^{-1}	—
	$^{197}Au^{79+}+^{197}Au^{79+}$	4.6	3 shifts total, no continous physicsoperation	small	—
Run-8 CY2007/08,FY2008 19.0 cryo-weeks	d +$^{197}Au^{79+}$	100.7 + 100.0	9.0 weeks	437 nb^{-1}	—
	polarized p + p	100.2	3.4 weeks	38.4 pb^{-1}	44%
	$^{197}Au^{79+}+^{197}Au^{79+}$	4.6	3 shifts	small	—
Run-9 CY2008/09, FY2009 22.0 cryo-weeks	polarized p + p	249.9	4.1 weeks	110 pb^{-1}	34%
	polarized p + p	100.2	9.9 weeks	114 pb^{-1}	56%
	polarized pp2pp	100.2	3.5 days	0.6 nb^{-1}	63%
Run-10 CY2009/10, FY2010 27.1 cryo-weeks	$^{197}Au^{79+}+^{197}Au^{79+}$	100.0	10.9 weeks	10.3 nb^{-1}	—
	$^{197}Au^{79+}+^{197}Au^{79+}$	31.2	2.9 weeks	544 μb^{-1}	—
	$^{197}Au^{79+}+^{197}Au^{79+}$	19.5	1.8 weeks	206 μb^{-1}	—
	$^{197}Au^{79+}+^{197}Au^{79+}$	3.85	4.6 weeks	4.23 μb^{-1}	—
	$^{197}Au^{79+}+^{197}Au^{79+}$	5.75	1.4 weeks	7.8 μb^{-1}	—
Run-11 CY2010/11, FY2011 24.4 cryo-weeks	polarized p + p	249.9	9.7 weeks	166 pb^{-1}	48%
	$^{197}Au^{79+}+^{197}Au^{79+}$	9.8	1.4 weeks	33.2 μb^{-1}	—
	$^{197}Au^{79+}+^{197}Au^{79+}$	100.0	6.4 weeks	9.79 nb^{-1}	—
	$^{197}Au^{79+}+^{197}Au^{79+}$	13.5	8 days	63.1 μb^{-1}	—
Run-12 CY2011/12, FY2012 22.9 cryo-weeks	polarized p + p	100.2	4.4 weeks	74.0 pb^{-1}	59%
	polarized p + p	254.9	4.9 weeks	283 pb^{-1}	52%
	$^{238}U^{92+}+^{238}U^{92+}$	96.4	3.1 weeks	736 μb^{-1}	—
	$^{63}Cu^{29+}+^{197}Au^{79+}$	99.9 + 100.0	5.4 weeks	27.0 nb^{-1}	—
Run-13 CY2012/13, FY2013 17.0 cryo-weeks	polarized p + p	254.9	13.3 weeks	1.04 fb^{-1}	53%

Figure 4.3: Though RHIC is currently still running (as of May 9, 2016), I include runs here up to and including the run producing my data set (Run 13). An unprecedented 13.3 cryo-weeks of running was awarded to the W-Physics group. Table produced from data posted at the RHIC run page [18].

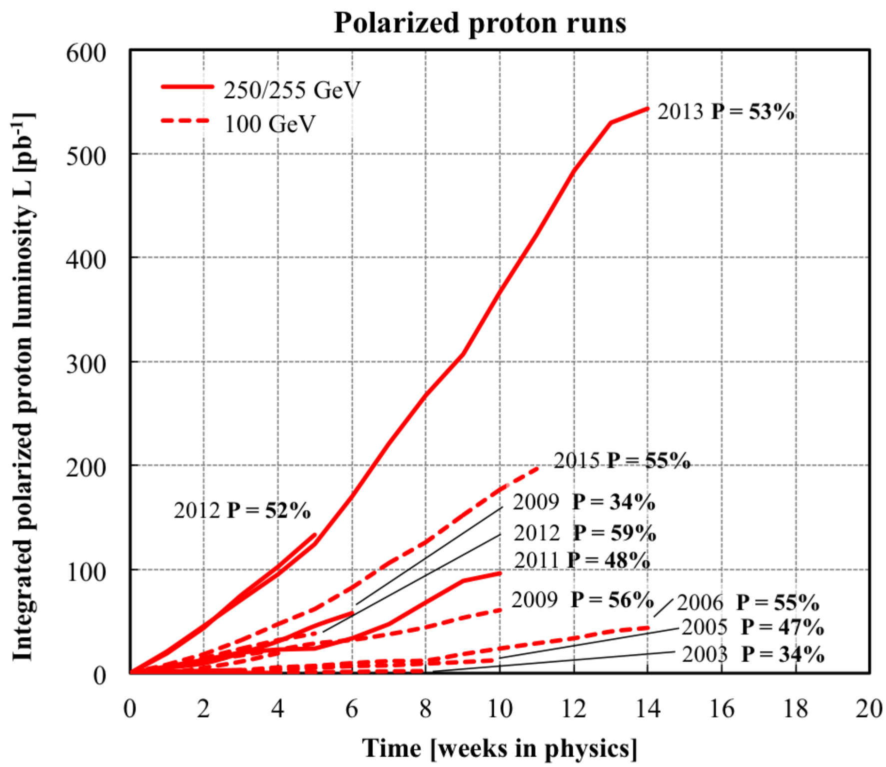

Figure 4.4: Upgrades to RHIC's electron lens have enabled massive improvements to luminosity–seen in the year 2013. The high luminosity was taken advantage of with an extra long proton+proton run. Figure obtained from [18]

4.1.1 Experimental Apparatus

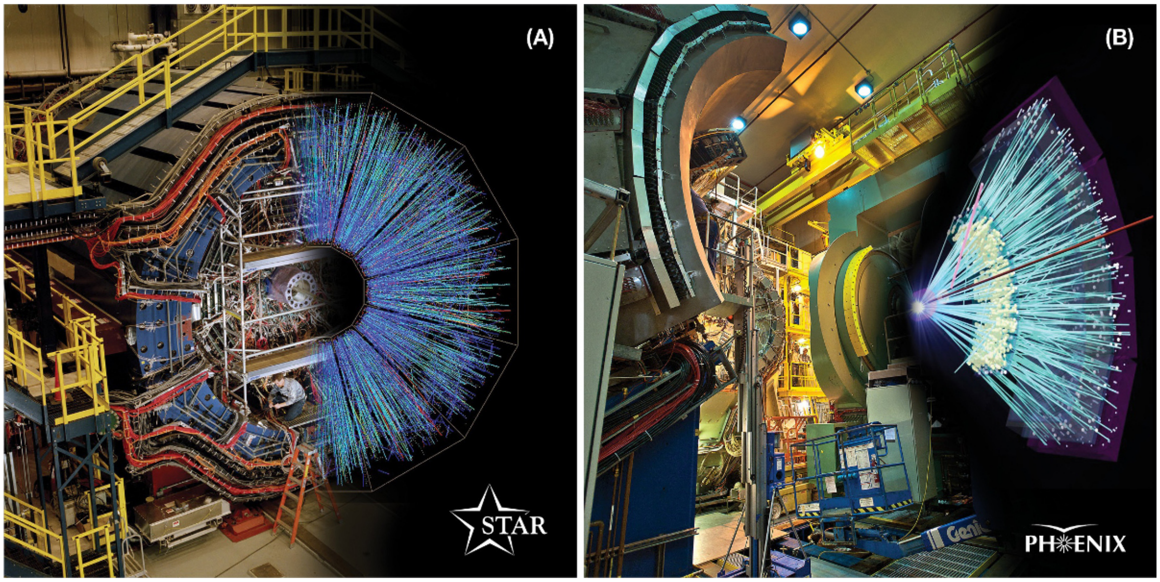

Figure 4.5: STAR (a) and PHENIX (b) with cutaways showing the event display for a heavy-ion collision as reconstructed by the detectors' electromagnetic calorimeters [19].

RHIC accelerates ions in a multi-stage process, summarized in Figure 4.1. The source of the beams is the **Electron Beam Ion Source**, built on top of a 200 MeV linear accelerator (Linac). Once ions are injected into the Linac, they travel to the **Booster Synchrotron**. At this stage, ions are accelerated with pulsed RF fields. After the beam of ions has been accelerated to nearly the speed of light, they are fed into the **Alternating Gradient Synchrotron** or AGS. At this time, ions are traveling at about 0.37 c. By the time the ions leave the AGS, they are moving at 0.997 c. When the ions have reached the appropriate injection energy (which is ion-species dependent), they are transferred to the **AGS-to-RHIC Line**, where a switching magnet pumps bunches of ions into either the counterclockwise circulating ring of RHIC, or the clockwise circulating ring of RHIC. The ions are accelerated here to maximum speed–each beam-ion travels a distance of 2.4 miles every 12.8 microseconds (0.99999 c at 510 GeV $\sqrt{s}$ beam energy), for the duration of a physics-fill [65].

When the RHIC rings are filled with ions, the ions are bunched into rotating electromagnetic potentials called 'buckets'. There are 360 beam-buckets in total, but typically

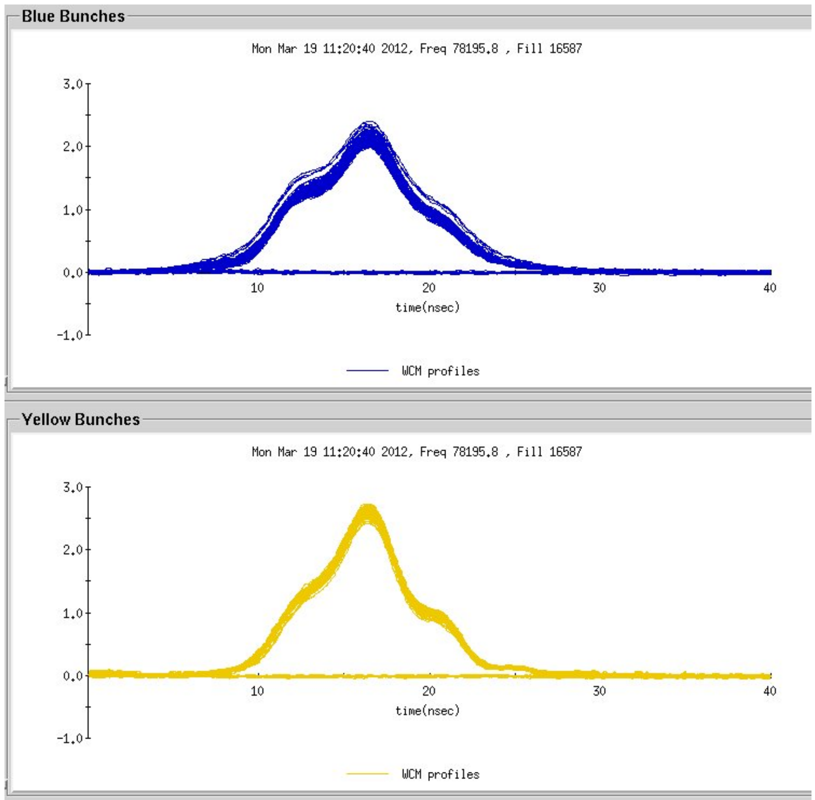

Figure 4.6: The longitudinal distribution of all bunches in a typical fill are overlaid. The bunches from the blue beam (top) and yellow beam (bottom) are shown for over a 40 nanosecond time period.

only a fraction are filled with ions. For this analysis, we took data with beams with 110 filled buckets. The sequence of beam buckets from one filled bunch to the next is referred to as a 'bunch'–and are rather long - Figure 4.6. The bunch length is 12 meters longitudinally. The bunch width is quite narrow–with Gaussian geometry, it is between 150 mm and 300 mm depending on the beam energy. Understanding the beam bunch geometry is a crucial component to understanding total the total luminosity delivered by RHIC to PHENIX. . A detailed presentation of beam dynamics with regards to luminosity will be presented in chapter 9.

4.2 Production of Polarized Proton Beams

The production of polarized beams is crucial to the physics of this measurement - without polarized beams, no spin structure analysis can be done at RHIC. This is due to the fact that the helicity state of the protons in the initial state of any proton proton collision can be connected to the final observed states in a way which provides information about the spin structure function, as was discussed in Section 3.

The production of polarized beams is a multistage process, and involves several experimental components. The importance of polarizing the beams is fully realized once polarized beams are collided at relatively high center of mass energies–where the beams behave less like polarized proton beams, but more like polarized beams of quarks and gluons [66]. The is produced from a special polarized ion source, (OPPIS, Figure 4.7). Polarization is at its maximum at production time, and over the course of the acceleration through the various apparatuses described below, we work to maintain polarization by limiting and mediating depolarizing resonances, Figure4.1. The exact details of beam injection and polarization management is presented in the RHIC Configuration Manual [21], with the relevant portions summarized here.

4.2.1 Polarized Injection

RHIC uses an optically pumped polarized ion source (OPPIS), Figure 4.7 to produce a polarized ion source greatly in excess of RHIC's design intensity. This is used to our advantage, as the emittance of the beam can be lowered to create a highly collimated beam for physics use.

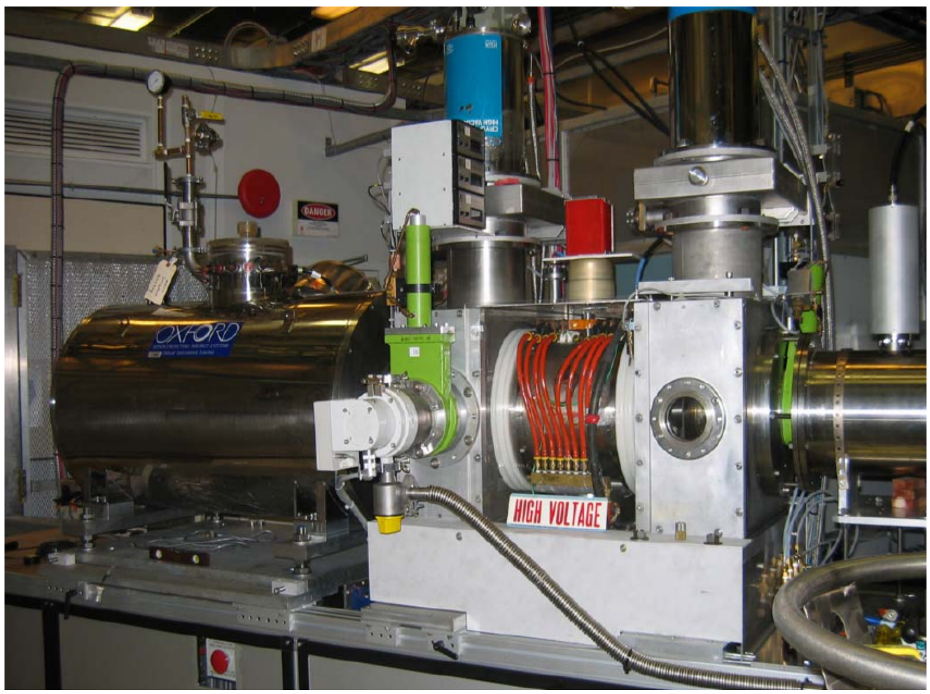

Figure 4.7: RHIC's optically pumped polarized ion source. Produces 0.5-1.0 mA current of polarized H^- ions. The optical pumping is pulsed at 400 μs, [20]

4.2.2 AGS to RHIC Transfer Line

Once ions have been optically pumped, we have a direct-current beam at approximately 80% polarization. This is accomplished using optically pumped Rubidium vapor. The polarized ions are then moved into the booster from the Linac, where some polarization is lost to spin precession, intrinsic to accelerating charged ions in a circular path. However, polarization is maintained, for the most part, by matching the precession resonance to the orbiting frequency of the booster ring. The Siberian snakes (Section 4.3.1) at this stage serve to incrementally flip the ion spin such that the natural depolarization works to re-polarize the orbiting ions, every full-turn. The full details of this procedure are well described in Reference [21].

After the ions are sufficiently polarized and filled in the AGS, they are moved into the AGS to RHIC Transfer line, Figure 4.9. The beam is focused and fed through a switching magnet–which must be timed with great precision in order to fill the blue and yellow beams with the appropriate polarization patters. In fact, the precision is so great, that the Earth's curvature must be taken into account over this relatively short injection line. The entry point and exit point are bent ever-so-slightly due to the curvature of the Earth, with the entry being 12.51 mrad and the egress being 12.46 mrad [21]. At the point of injection in the transfer line, the beam size and emittance are measured, as well as the beam polarization.

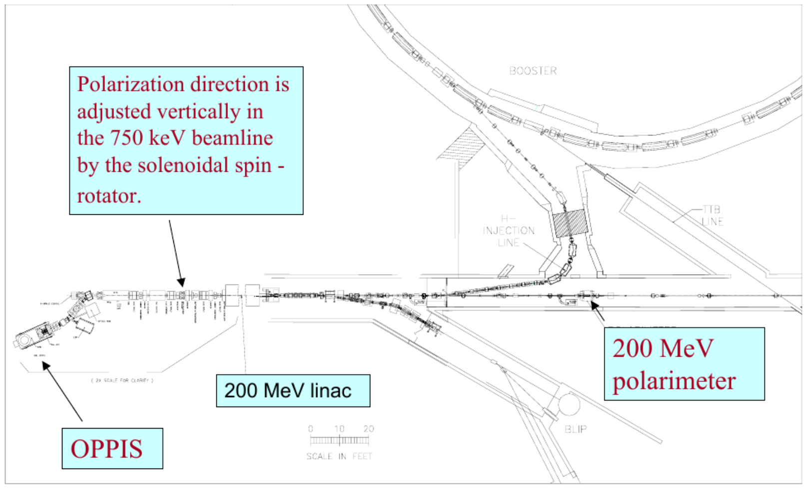

(a) Technical schematic of Polarized Injection Line [20]

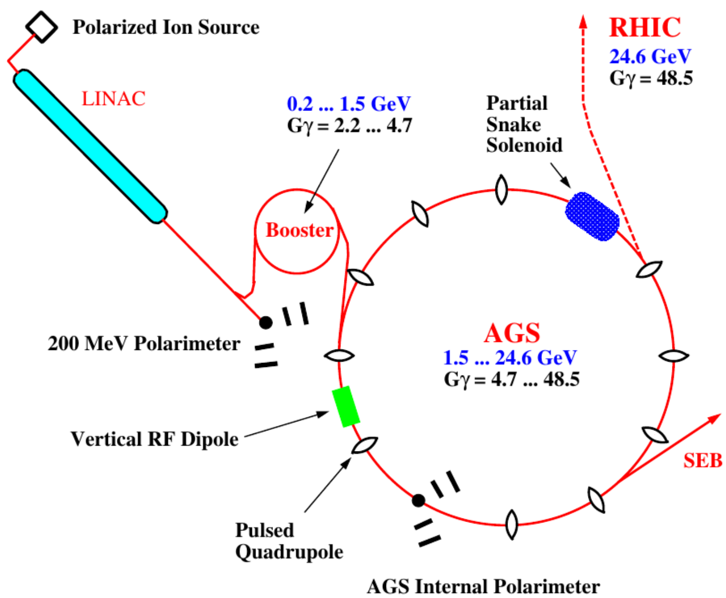

(b) Overhead view of Polarized Injection Line [21]

Figure 4.8: A view of the RHIC polarized injection system. Panel (a) shows a zoomed in technical view of the OPPIS to the booster. Panel (b) shows a zoomed out cartoon of the next step in the polarization injection system, including the AGS, and the feeder line to RHIC.

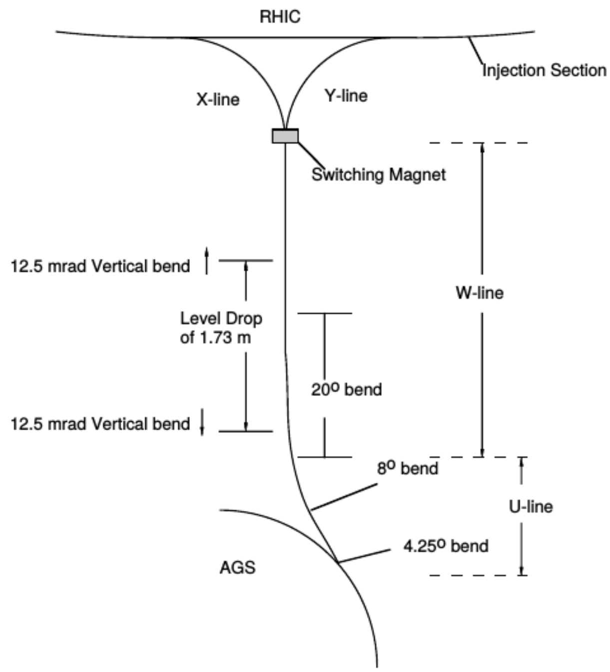

Figure 4.9: A schematic of the geometry of the AGS-to-RHIC transfer line [21].

4.3 Maintaining Beam Polarization

The creation of polarized beams is only half the battle. Depolarizing resonances in any particle beam are intrinsic in the design of any circulating beam particle accelerator–without intervention, after a few rotations, RHIC's polarized beams would be unpolarized. RHIC uses several strategies in concert to correct for the largest of these depolarizing resonances–including beam orbit corrections, the Siberian Snakes, Betatron Tune Spreading, and sextupole magnetic depolarizing resonances.

4.3.1 Siberian Snakes and Spin Rotators

The Siberian Snakes are positioned at two locations on the RHIC ring (as well as others along the injection sequence). The most stable configuration of spin injected in RHIC is such that the spin axis is perpendicular to the plane of the accelerator ring. The Siberian snake is a helical magnet which forces the spin to rotate 180 degrees every half rotation. This special configuration of snakes (see Figure 4.1) ingeniously takes advantage of the rotational precision of the spin (a depolarizing resonance) to re-polarize the beam, every half-orbit.

The spin rotators are located outside of experimental interaction regions around PHENIX and STAR. These special dipole magnets rotate the spin of the beams onto a longitudinal (parallel with beam) axis–these magnets are important for any measurement (such as this one) requiring longitudinal spin polarization. Transverse spin polarization has also been used in RHIC operations to probe the transverse spin structure of protons. It is a complementary and vital area of inquiry, but is not presented in this work.

4.3.2 Measuring Beam Polarization

The RHIC Collider-Accelerator Department provides several means of measuring the beam polarization over the course of the data taking period. PHENIX takes special data runs which are used to determine the real beam polarization delivered to the detector, in a yearly analysis. This analysis is referred to "Local Polarimetry", or "LPol".

CAD will additionally measure polarization in via inelastic proton-carbon scattering in the Coulomb-Nuclear Interference (CNI) region. Relative polarization can be determined with to within 10% in only a few seconds of measurement.

Figure 4.10: This cartoon illustrates one potential polarization pattern configuration of the beams as they collide at PHENIX's interaction region. As beams are longitudinally rotated into position for collision, it is crucial to keep careful track of the magnet currents rotating the beams, as well as the overall polarization pattern.

Vertical polarization is determined through the calculation of the left and right particle production, with a known analyzing power ([21], Ch 8):

$$P_B = \frac{1}{A_p}\frac{N_L - N_R}{N_L + N_R} \tag{4.1}$$

Where P_B is the beam polarization, N_L and N_R are the left-scattering produced particles, and right-scattering produced particles and A_p is the analyzing power, which can be calculated from first principals, and experimentally verified. Scattering takes place as a carbon filament is swept across the beam.

As many decisions are financially constrained, this one was too. Using a p-Carbon CNI polarimeter provides an economically viable way to measure beam polarization within the precision needed for the spin experiments.

4.3.2.1 The Spin Monitor

During a RHIC run, it is crucial to keep track of the polarization patterns being collided at the PHENIX IR 4.10.

One of my major contributions to the PHENIX experiment was in the upkeep and development of the spin monitoring systems for the online data taking portions of the experiment, show in Figure 4.11.

The spin monitor's purpose is to provide real-time feedback on the dipole magnets used to orient proton spin orientation prior to collision, as well as comparing the RHIC spin fill pattern against the measured spin pattern delivered to the PHENIX interaction region.

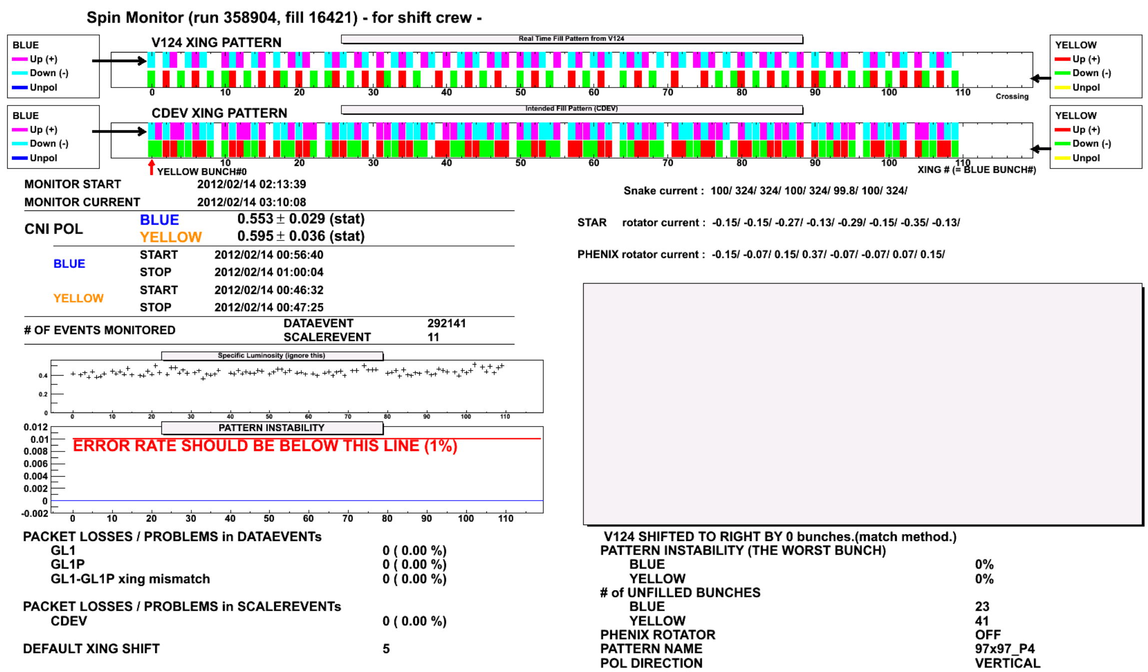

Figure 4.11: The shift-crew display output for the Spin Monitor. The upper panel shows the polarization of the blue and yellow beams, and other panels summarize information including magnet currents (needed to understand the spin orientation), issues with data packet loss, the recognized spin-pattern, as well as a large boxed area on the lower left where errors could be shown to the shift crew along with the proper response.

4.4 The Pioneering High Energy Nuclear Interaction Experiment

The Pioneering High Energy Nuclear Interaction Experiment (PHENIX) is a synthesis of many smaller detectors all of whom were commissioned for various physics goals, some of whom have been repurposed from their original application once its primary physics was completed. PHENIX has several major physics thrusts, which are discussed below.

Much of PHENIX collaboration's early published work focused on creating and studying quark gluon plasma in heavy ion collisions, but in following years spin papers came too. Major question in physics that PHENIX set out to answer with its heavy-ion program include studying confinement–i.e. why are quark color charges confined to exist in the nucleus, baryons and mesons? PHENIX sought to study this via examination of the J/Psi and measuring screening length in heavy ion collisions. Additional research topics included the study of chiral symmetry restoration, thermal radiation of hot gasses, QCD Phase transition, Strangeness and Charm Production, Jet Quenching, and Space-time evolution [67] .

The remaining physics goal of the PHENIX collaboration is to study the origins of proton spin. The PHENIX spin program 'officially' started with the RHIC upgrade to enable production of polarized proton beams.

The spin program came shortly after the 2001 commissioning run. The first polarized proton run was produced by RHIC for PHENIX in 2002, with 8.3 total weeks of data. Data was taken over several discrete periods, as RHIC was still being optimized for spin physics.

The purpose of the PHENIX spin program has been to understand the spin structure of the proton, and has historically used various particle production asymmetries (left-right and forward-backward) as an experimental probe for polarized parton distribution functions (as discussed in Chapter 3).

PHENIX studies the proton spin structure as modeled by the Ellis-Jeffe sum rule (Chapter 3). The PHENIX spectrometer is particularly well suited to studying gluon polarization, Δg and the anti-quark polarization, $\Delta \bar{q}$. Additionally, the 'nature of parity non-conservation itself can be directly studied' [68] using polarized beams, and spin asymmetries in collisions. This measurement requires a means of reconstructing jets, inclusive or leading particle production can be used as a proxy with some small asymmetry remaining.

The configuration of the PHENIX spectrometer changes from year to year, as part of planned upgrades. The configuration of the detector for the 2013 physics run is shown in Figure 4.12.

PHENIX makes use of many classic detectors, including Cherenkov light detectors, resistive plate chambers, electromagnetic calorimeters, silicon chip detectors, time of flight detectors, scintillation light detectors, cathode strip chambers, and proportional tube counters.

While all of these subsystems are interesting, and have produced excellent physics results, I will focus only on those pertinent to this analysis.

PHENIX is generally thought of as two 'halves' being comprised of two broadly defined 'arms'–the forward muon arms, and the central arms. As the names suggest, the central arms cover the central rapdity range (close to $y = 0$), whereas the muon arms cover larger rapidities and specialize in detecting muons. While both kinematic regions are used for heavy ion and spin physics analyses, this analysis exclusively uses the forward muon and the Beam Beam Counters. The majority of the central arms systems will not be discussed in detail in this thesis.

4.4.1 Units

The data taken by PHENIX as well as the geometry of the detector can be characterized by various measurements and units. The data taken by the detector is shown relative to the PHENIX Coordinate System (Figure 4.13). Some accelerator-specific units are summarized in Table 4.1. The full description of the data taken by PHENIX is saved for Chapter 6.

A closely related analysis measures $W \rightarrow e$ processes uses the central arms. As different arms are sensitive to different rapidity ranges, complimentary results are obtained from central and forward analyses. The central analysis is presented in References [61] and [69].

PHENIX also utilizes a complex data acquisition system (DAQ) which streams data from each detector, assembles this data into a labeled event, compresses and finally stores into a proprietary storage format. The work-flow of the DAQ is summarized in Figure 4.14.

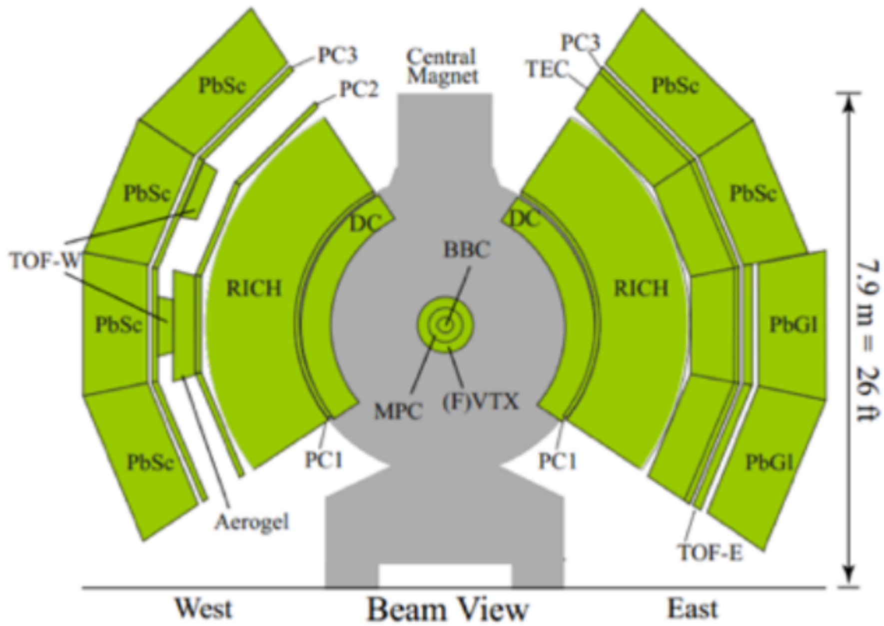

(a) Central Arms

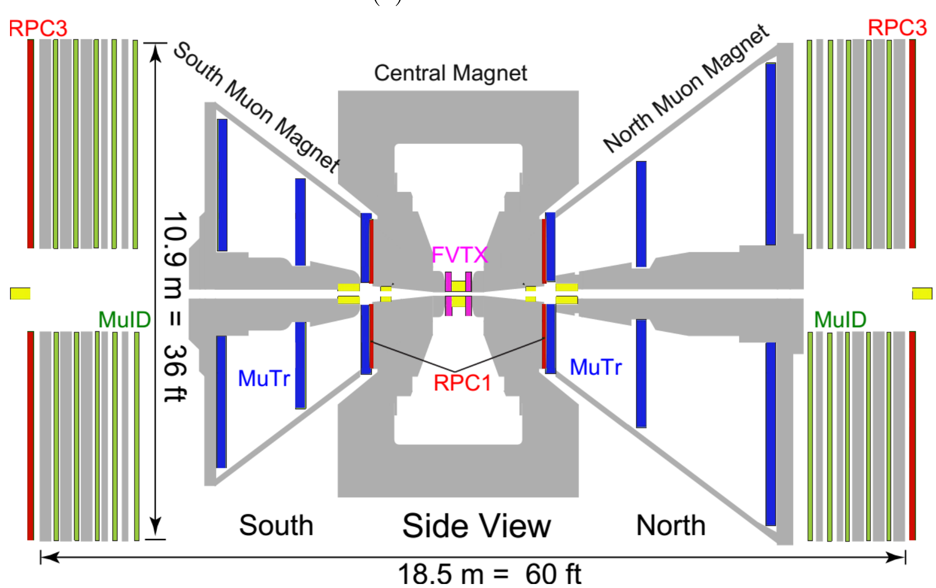

(b) Forward Muon Arms

Figure 4.12: Shown: The two main arms of the PHENIX Spectrometer. The central arms are shown via the beam-on view of PHENIX (a) and Forward Muon Arms are highlighted via the 90-degree rotated view (b). In both cases, the 2013 configuration is shown. The beams are brought into intersection at the geometric center of each figure (immediately between the BBCs)

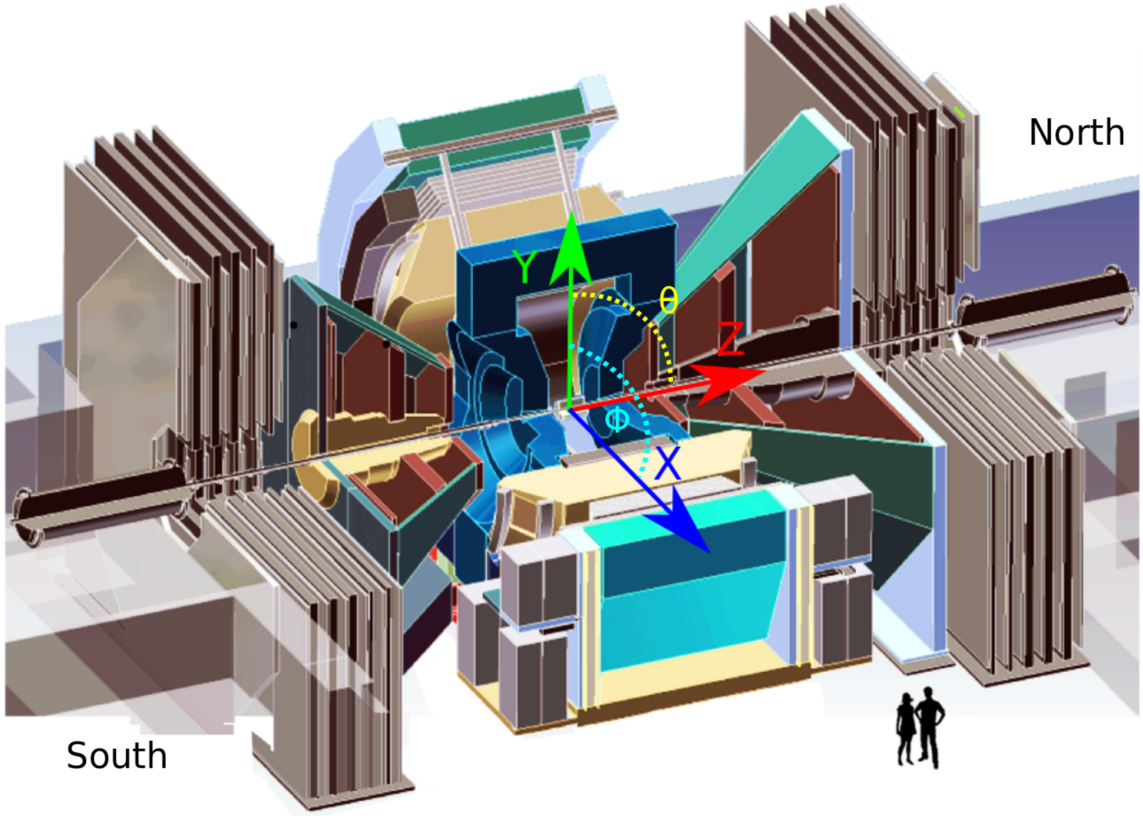

Figure 4.13: The PHENIX coordinate system is shown (RGB arrows) at the center of the nominal interaction point within PHENIX, the origin, in this quarter-cutaway drawing. The small black figures are actually miniaturized human beings, the PHENIX detector is very small–this is a full scale drawing of PHENIX. Shown: the x, y, and z coordinates, as well as the azimuthal coordinate, θ and polar coordinate ϕ [22]

For each event, any particles which interact with the detector material are transduced by. The transduced signals are serialized into a detector-specific data stream, such that the state of the detector's excitation can be recorded and reproduced later. This information is stored on the front-end-electronics modules (FEMs), and synchronized with timing information from the clock (ticks once every time there is a bunch crossing) and a Global Trigger decision, i.e. whether or not the right parts of the detector lit up to make this particular event worth keeping. If the detector triggering heuristics determine that an event is worthy of keeping, the uncompressed serialized information is sent to the DCMs (Data Collection Modules), where it is assembled into a packet, and then sent to the event

Quantity	Definition	Description
x, y, z		Cartesian coordinates whose origin is at the center of the PHENIX spectrometer.
θ		Polar coordinate relative to origin of PHENIX coordinate system describing angle between the positive z-axis and a reference point
ϕ		Polar coordinate relative to the origin of the PHENIX coordinate system describing the angle between a reference point and the x-axis
v		Speed of a particle
c		Speed of light
E		Relativistic energy of a particle
p	(p_x, p_y, p_z, E)	Total four-momentum of a particle
y	$tanh^{-1}(v/c)$, $\frac{1}{2}ln\frac{E+p_zc}{E-p_zc}$	Spatial coordinate, rapidity, describing the hyperbolic angle differentiating between two frames of reference in relative motion. When described in terms of E, p_z, y describes the relativistic boost along the z-axis of the beam
η	$-ln\left[tan\left(\frac{\theta}{2}\right)\right]$	Spatial coordinate describing the angle of a particle relative to the beam axis

Table 4.1: Some units describing the geometry of and data taken by PHENIX.

builder (EvB). At the EvB, all packets originating from a common collision are assembled into an event. The event is compressed into a proprietary PRDF (PHENIX Raw Data File Format) format, and sent to the Buffer Boxes, a cache of high density local storage. Finally, this cached data is sent off to high density, robotic magnetic tape storage on magnetic for ultra-stable archival. Later, this data is copied to a computing cluster, and reconstructed into ‘analysis-ready’ data structures, such as track reconstruction variables, event vertices and so-on. This is discussed in Chapter 6 and Chapter 7.

A complete summary of PHENIX detector subsystems (excluding the new Forward Vertex Detector, Silicon Vertex Detector, and Resistive Plate Chambers, which discussed separately) can by found in Table 4.2.

Element	η	ϕ	**Features**
Magnets			
Central Magnet	$\|\eta\| < 0.35$	360°	1.15 T
Muon Magnet North	$1.1 < \|\eta\| < 2.2$	360°	0.72 T
Muon Magnet South	$1.1 < \|\eta\| < 2.4$	360°	0.72 T
Minimum Bias			
Beam Beam Counter	$(3.1 < \|\eta\| < 3.9)$	360°	Vertex Reconstruction
Zero Degree Calorimeter	$\pm 2mrad$	360°	Minimum Bias Trigger
Central Detectors			
Drift Chambers	$\|\eta\| < 0.35$	$90° \times 2$	Central p and m resolution
Pad Chambers	$\|\eta\| < 0.35$	$90° \times 2$	Pattern Recognition, Tracking
Ring Imaging Cherenkov	$\|\eta\| < 0.35$	$90° \times 2$	Electron ID
Time of Flight	$\|\eta\| < 0.35$	45°	Hadron ID, $\sigma < 100pm$
PbSc EMCal	$\|\eta\| < 0.35$	90°, 45°	Calorimetry, photon, and electron energy
PbGl EMCal	$\|\eta\| < 0.35$	45°	$e^{\pm}$, $\mu^{\pm}$ separation at $p > 1GeV/c$ EM Shower and $p < 0.35GeV$, $K^{\pm}$ $\pi^{\pm}$ separation up to $1GeV/c$
Muon Arms			
Muon Tracker South	$1.15 < \|\eta\| < 2.25$	360°	North installed 2003
Muon Tracker North	$1.15 < \|\eta\| < 2.44$	360°	
Muon ID South	$1.15 < \|\eta\| < 2.25$	360°	Steel absorbers, larocci tubes
Muon ID North	$1.15 < \|\eta\| < 2.44$	360°	””

Table 4.2: A summary of PHENIX hardware [30]. $e^{\pm}/\pi^{\pm}$ separation and π/K separation requires the Time of Flight (ToF) working with PbGl and PbSc data. PbGl refers to “Lead Glass Scintillator” and PbSc refers to “Lead Scintillator”. The Muon Identifier (Muon ID, MuID) can help suppress hadrons by absorbing them in the iron layers.

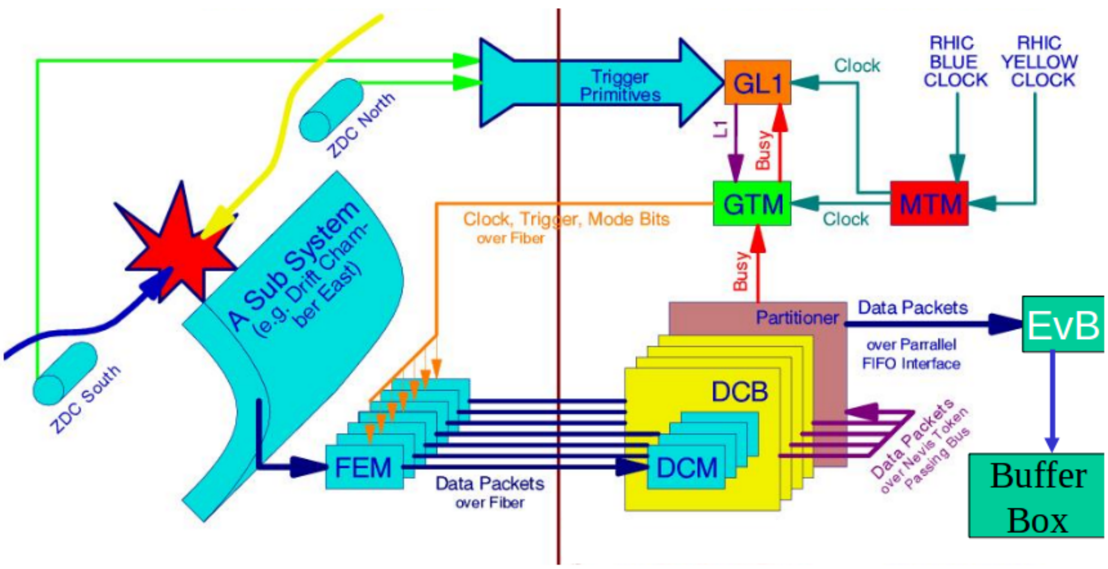

Figure 4.14: Shown: A flow chart summarizing the PHENIX DAQ [23].

4.4.2 Subsystems

The major subsystems contributing to this work include the Muon Arms, the Beam Beam Counters (BBCs), and the Forward Vertex Detector, since the analysis is characterized by calculating the asymmetry for $W \rightarrow \mu$ interactions, only muon reconstruction and identification is required. For the complimentary central arm analysis, the $W \rightarrow e$ decay mode is explored.

4.4.2.1 Beam Beam Counters

The Beam-Beam counters (BBCs, Figure 4.16) are photomultiplier tubes with scintillating lead-glass crystals. These detectors are situated 144 cm from either side of the nominal center of the PHENIX interaction region. The primary purpose of the BBCs is to provide the time of a beam-beam collision for triggering, and to measure the Z-Vertex of the collision (Figure 4.15).

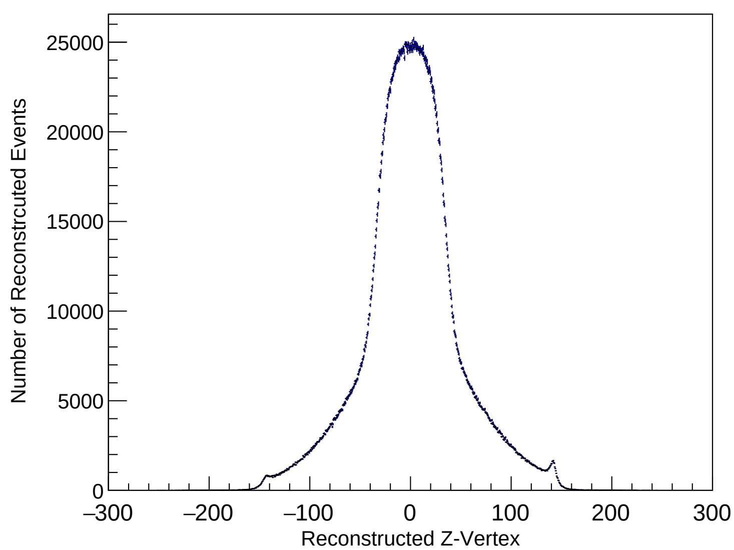

Figure 4.15: Here, we see a typical BBC z-vertex distribution for one run's worth of data, over a z-vertex range of -300 cm to 300 cm. The central peak is close to the nominal interaction point of z = 0 cm. The peaks to the left and right (at $\pm$144 cm) are from collisions outside of the BBC.

When a collision occurs, each BBC measures the arrival time of the leading charged particles, T_S for the south BBC, and T_N for the north BBC (Figure 4.17). These times are defined as the average of times within the established timing window - each element of the BBC is capable of 52±4 ps, which is a factor of $\tilde{2}500$ less than the bunch crossing rate (1 bunch every 106 ns) [70].

The Z-Vertex is determined from T_N and T_S as follows:

$$Z_{vertex} = c * (T_S - T_N)/2.0 \tag{4.2}$$

Note that a consequence of the way the z-vertex is calculated, when there are collisions occurring are outside of the BBCs (i.e. $-144cm > z_{vertex}, z_{vertex} > 144cm$), the reconstructed z-vertex will either be at 144 cm or -144 cm. These events are removed with a vertex cut on the data.

The BBCs are used to record data with minimal bias towards any events containing any particular physics characteristic. This is important as a means for reconstructing the absolute abundance of particle production, which is crucial for determination of any inelastic scattering cross section and normalization of any cross-section of interesting scattering events. The Beam-Beam counters provide a measurement of vertex reconstruction by way of analyzing the time delay between triggering of the North and South BBCs. The delay window is then used to reconstruct the event vertex by assuming the impinging particles were traveling at near the speed of light, Figure 4.17.

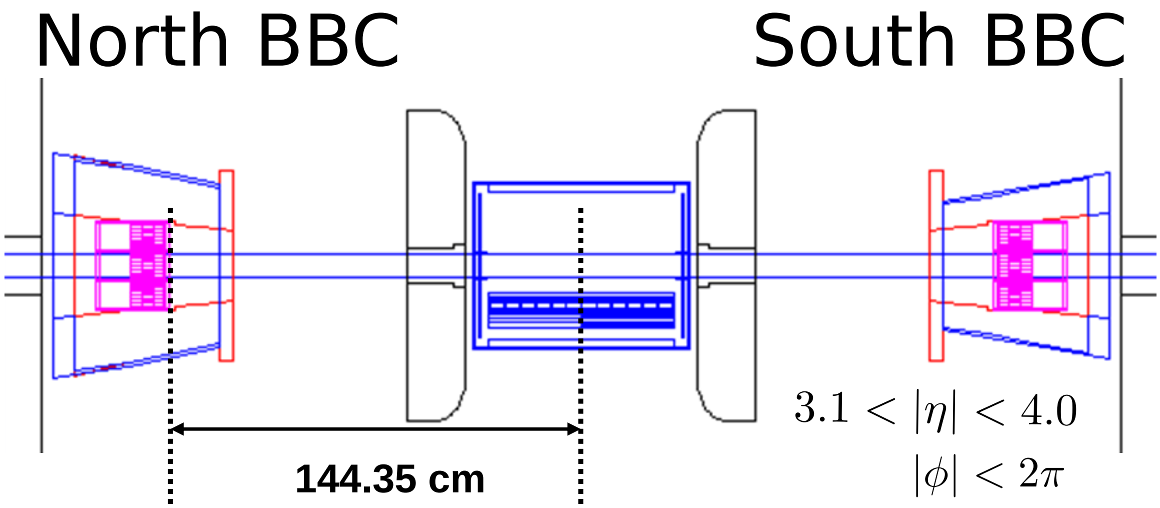

Figure 4.16: Shown: a schematic of the exact proportions of the detector as viewed alongside the beam pipe, along with the pseudorapidity and azimuthal coverage [24]

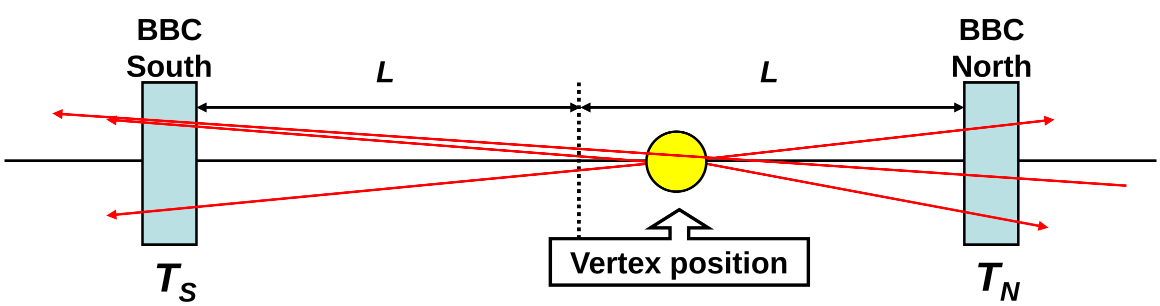

Figure 4.17: Showers from the primary event vertex impinge on the north and south BBC. The average timing of these particles are used to calculate T_N and T_S, allowing for the calculation of event z-vertex (Equation 4.2)

4.4.2.2 Forward Vertex Detector

The Forward Vertex Detector (FVTX), Figure 4.18 is a silicon detector, which enables detection of secondary event-vertices. This provides additional information to improve the precision to the Muon Tracking system. As a result of this improvement, secondary vertices can be measured allowing the distinction of particles decaying at the primary event vertex.

For this analysis, the FVTX can provide an important additional layer of precision, because it can help to identify background-events which do not originate from the primary event vertex of a collision [25].

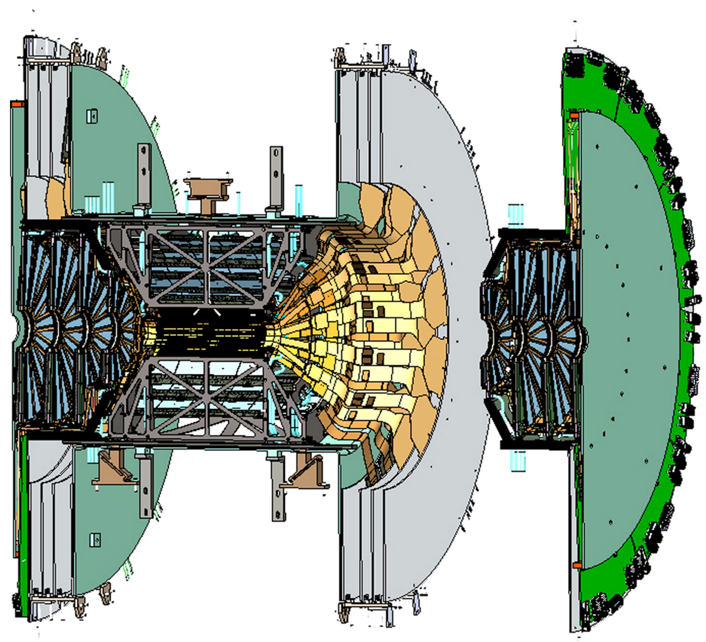

Figure 4.18: A schematic of the Forward Vertex Detector, showing the silicon chip layers (light blue wedges), and readout electronics (green). The FVTX was designed to mount directly onto the Silicon Vertex Detector (center) [25]. This configuration allows for a very high density of interleaved chips, in several layers, covering a maximum area around the beam pipe for detection of secondary vertex events. Secondary vertices are expected to occur rapidly after the primary vertex, making the region close to the primary vertex important real-estate to occupy.

Chapter 5

Resume Here!

5.0.2.3 The Muon Arms

The Muon Arms are composed of several subsystems, including the Muon Tracker (MuTR, cathode strip chambers), the Muon Identifier (MuID, shielding and scintillation layers), and the Resistive Plate Chambers (RPC(s), bakelite gas gaps and azimuthal oriented capacitively coupled copper readout strips). The job of the muon tracker is to identify muons with the penetration through the many layers of the MuID, and provide momentum and charge reconstruction for muon tracks. Tracks are matched to the event vertex with Kalman filter during reconstruction, and can even be matched with FVTX secondary vertices as a means of rejecting non W-Boson decays. Prior to the Forward Upgrade (Section 5.1), the muon arms consisted solely of the Muon Tracker and the MuID.

The Muon Tracker has a radial magnetic field, leading to charged particles traversing the tracker to have a helical bend. This was suitable for lower energy muon tracks, such as muons coming from the JΨ decay, which was one of the primary decays targeted in the original design of the muon tracker.

However, these J/Ψ muons have much lower energy then muons which decay from areal W-Boson production. To extend the muon tracker's usefulness into tracking these high energy muons, an upgrade to the triggering system was required to obtain adequate back-ground rejection for the Forward W analysis. The details of the muon arms will be discussed in the next section.

5.1 The Forward Upgrade

The muon arms were the subject of significant upgrades from 2011-2013. New front end electronics were added to improve triggering, and entire new detector subsystems (The RPCs) were added. The full details of these subsystems will be discussed in the forthcoming sections (Section 5.1).

One of the main stated physics goals of PHENIX is to constrain the sea-quark polarization of the proton spin. While this contribution is expected to be small, it is not because it is expected to be uniformly zero. Instead, the expectation is that the matter contribution to the quark sea is strongly positively polarized, while the antimatter contribution is strongly negatively polarized [17]. Measuring this polarization via A_L (Equation 3.16) is the means by which we will accomplish this. Prior to the Forward Upgrade, we only had results from the Central $W \to \mu$ analysis, but to better constrain our models, we require lower uncertainty in the forward kinematic regime–thus, the Forward Upgrade.

The first data for this measurement was taken in 2009, and published in 2010 under [71] and [72], but only for central rapidities, where a clear Jacobean peak could be found in the electron invariant mass spectrum at $40GeV$ mass-energy (half the rest mass of the W-Boson). This made evaluating yields and calculating asymmetries relatively straight-forward.

However, in forward kinematic regimes, it was very difficult to discriminate real $W \to \mu$ from other sources $X \to \mu$. As one can observe in Figure 5.1, only at high p_T does the W-boson signal become dominant. The old muon trigger electronics did not allow triggering sufficiently close to the W-Boson production threshold to allow for enough data to be taken. This is because of how the Muon Tracker identifies the charge and momentum of particles–which is via track bending. As tracks become very straight (i.e. high p_T), the muon tracker struggles to reconstruct the correct charge and momentum. The original Forward Upgrade called for a nose-cone calorimeter, which would have helped greatly for particle rejection, but was canned for budget reasons.

The Forward Upgrade to PHENIX increased the muon triggering threshold from about 2 GeV to 10 GeV, enough to insure that all muons produced from W-Boson decays can be recorded, with no loss of statistics. This of course is not to say, that these events were recorded without any background processes–the removal of the muon background was

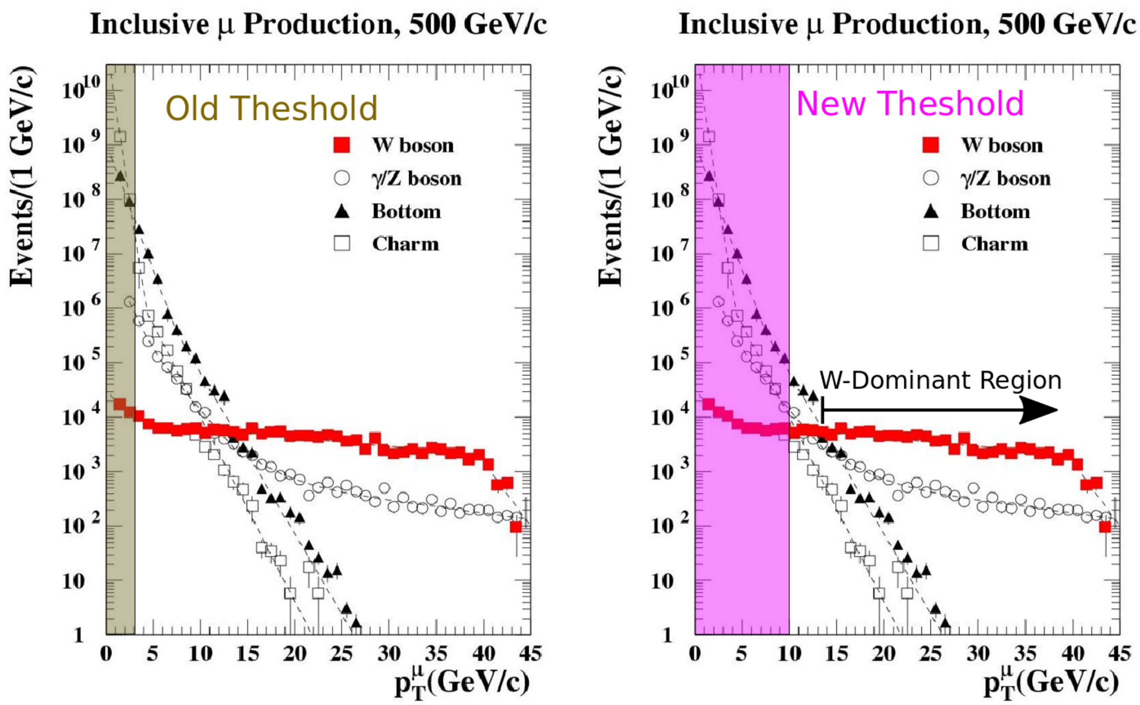

(a) The original Muon Trigger Threshold

(b) Muon Trigger Threshold, Forward Upgrade

Figure 5.1: Observing the simulated production of muon as a function of p_T, we can see that in the kinematic region of W production that the dominant sources of muons come from other processes. The new PHENIX muon trigger threshold is sensitive at 10 GeV/c and above. The threshold is still high enough that with other methods, we can record all events which come from the W boson, with triggering, whereas with the old threshold, this was impossible.

a substantial effort in this analysis, described in Section 7.4.

5.1.1 The Muon Tracker

The primary purpose of the Muon Tracker is to reconstruct the energy and momentum of muons in the forward kinematic regime. Because the MuID is composed of larocci tubes sandwiched between solid steel sheets, only particles which penetrate all the layers of the MuID are identified as muons. The Muon Tracker has three cathode strip tracking planes in a volume of gas, with an applied radial magnetic field. Each plane has two faces of tracking strips, for six total tracking readouts total. The arrangement of cathode strips makes the Muon Tracker very sensitive to the azimuthal dimension, but coarsely sensitive to the radial direction. The Muon Arms have three tracking stations for momentum and charge identification, sandwiched between two RPCS.

Since the MuID will fire on Muons with a 2.5 GeV momentum threshold, it will trigger very rapidly at high beam energies and luminosities–too fast to record all data–event rates were in excess of 10 MHz in 2013, with only 2 kHz of DAQ bandwidth allocated to the W analysis. Thus, before the Forward Upgrade, the Muon Arms were insufficient. However, additional absorber was installed at the nose-cone of the muon tracker to block lower momentum particles. The addition of the RPCs as well as new Front End Electronics Modules allowed for the real-time calculation of pseudo-momentum to be fed into the trigger decision in order to provide high rejection power on tracks. These upgrades allowed us to trigger exclusively on relatively straight tracks, which is consistent with high momentum particles [26].

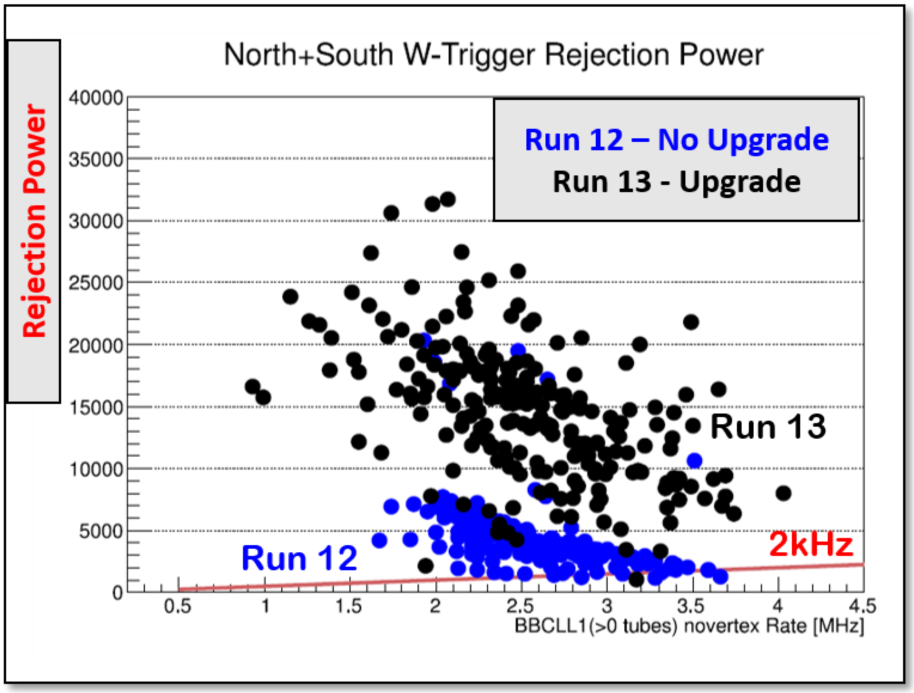

Figure 5.2: In 2013 with the final commissioning of the RPCs and the Forward Upgrade complete, we saw a drastic increase in rejection power, as planned.

5.1.2 The Resistive Plate Chambers

One of my major contributions to the PHENIX experiment was in the construction and testing of the RPCs at station 1, in 2012. An exploded view of the RPC is shown in Figure 5.4. The RPCs were a crucial part of the W-Physics muon trigger. One primary feature the presence of RPCs add to the PHENIX triggering system is timing resolution–2 nanoseconds (Table 5.1). This is crucial, because before the inclusion of RPCs, the only timing available was that of the BBCs. However - because the BBCs are minimally biased–they will fire nearly every time there is a collision–which at high luminosity is far greater than the assigned bandwidth to the W Physics trigger. The RPC provides local timing information, which allows the triggering system to record events which trigger the muon arm system, and not just the BBCs. This has the effect of significantly reducing backgrounds–by a factor of $>$ 6000 [26], Figure 5.2.

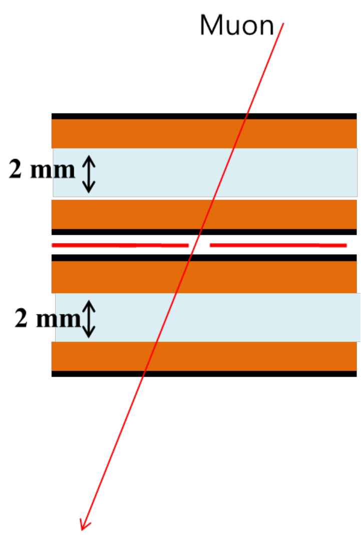

(a) A muon passing through the layers of the RPC

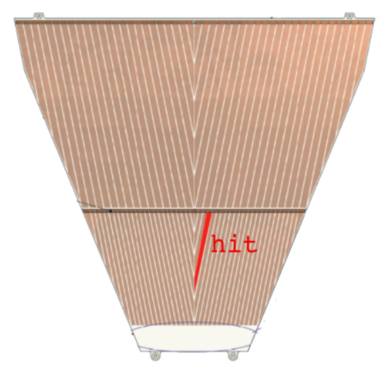

(b) Copper readout strip activated by passing muon

Figure 5.3: As a muon passes through the layers of the RPC (left), the gas in the bakelite gap is ionized. This charge migrates and collects near the highly resistive graphite coating. An image distribution is induced on the overlapping readout strip (right), which is passed along its own channel to the front-end electronics.

5.1.2.1 Design

As hinted at prior, the design goal of the Resistive Plate Chambers is to provide accurate timing information at high speed in order to build a Trigger which can record $W \to \mu$ events. RPCs were first implemented at the Large Hadron Collider at CERN, and their design has been adopted for use at PHENIX both because of its high speed, and low cost. In Figure 5.4 the basic design is shown–the means of signal transduction is via ionizing of gas inside a highly resistive chamber. The chamber is held at a large bias–at 8.5 kilovolts, such that any ionization will collect on the interior of the resistive chamber in a fixed, and relatively static distribution in time (relative to time scales of triggering system timing, in millionths of a second). This charge distribution is read out by capacitively coupled copper readout strips, into fast electronics (Figure 5.3). The design requirements of PHENIX is that when triggered, 2 or fewer clusters (strips) are activated, the efficiency of the detector must be at least 95%, the time resolution must be at least 2 nanoseconds, with a particle transduction rate of 500 Hz per square centimeter. These properties are summarized in Table 5.1 [26].

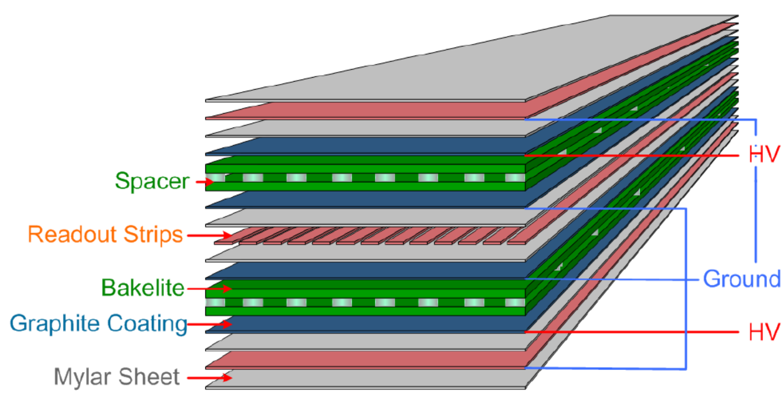

Figure 5.4: We can see the various layers that go into the construction of a typical RPC segment installed at PHENIX. A High Voltage bias is applied to the graphite coating on either side of bakelite gas-filled gaps. Readout strips are positioned between the two bakelite gaps. Finally, the entire double-gap structure is surrounded by a copper grounding cage, and wrapped in insulating mylar [26].

Cluster Size	<2 strips
Efficiency	>95% for MIP
Time Resolution	~2 nanoseconds
Rate Capability	0.5 kHz/cm^2

Table 5.1: The design characteristics of the RPCs [26]

5.1.2.2 Construction and Testing

Construction of the Resistive Plate Chambers took place in two stages over several years. Fabrication of the bakelite gas gaps was done overseas in Korea, and the aluminum chassis was manufactured in China. Pieces for the RPC 3 and RPC 1 were shipped to Brookhaven National Laboratory where they were assembled and tested, before being installed. The installation occurred over two years, with the first stage, the RPC 3, being installed in 2011, and the second stage, the RPC 1, being installed in 2012. After being fully commissioned, the capstone data set for W-Physics was taken in 2013, which is discussed in detail in Chapter 6.

The RPC 3 and RPC 1 construction efforts took place in a special clean-room built inside of the cavernous building 9-12 (Figure 5.5) at Brookhaven National Lab. Construction was overseen by Dr. Francesca Giordano, working as a post doctoral associate for Dr. Matthias Grosse Perdekamp for the University of Illinois at Urbana Champagne. The electronics of the RPCs were funded by professors Ken Barish and Rich Seto at the University of California, Riverside, via a grant from the Department of Energy. I am very grateful for Francesca for her guidance and trust, as she allowed me to construct and test many of these octants. I constructed the gaps with Arbin Timilsina, who was a very entertaining and helpful lab-mate. Ihnjei Choi and Young Jin Kim were instrumental in the design, construction, and QA of the RPCs as well.

The RPCs are modular in design–the larger RPC 3 North and South were separated into 16 half octants, whereas the smaller RPC 1 North and South were separated in to eight octants. Both North and South RPCs have the same full azimuthal coverage, but due to the differing size of the Muon Arms, they have different rapidity coverage.

The RPC 1 octants were installed directly on the nose-cone of the Muon Tracker, shown in Figure 5.6. Unlike to the RPC 3, the RPC 1 North and South are quite compact,

Figure 5.5: Two special tents inside building 912 at Brookhaven National Laboratory, built to house completed RPC octants and the laboratory used to construct and test the octants.

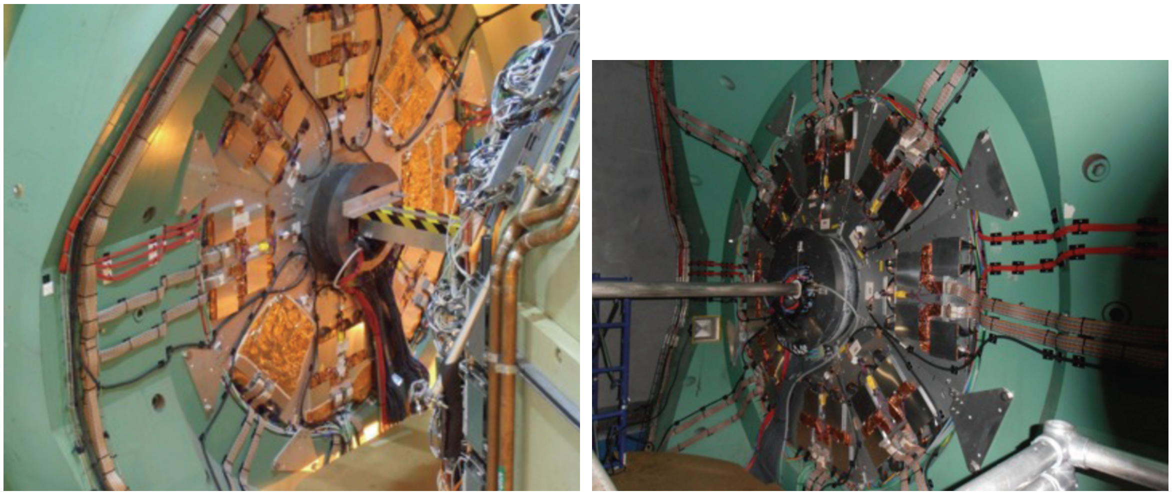

(a) RPC Station 1, North

(b) RPC Station 1, South

Figure 5.6: The North RPC Station 1 is installed on the muon tracker nosecone (left). Similarly we see the installation of the south RPC Station 1 (right). The metal tube in the center is the beryllium beam pipe.

and are the exact same size 5.7.

Each RPC1 octant was hand assembled, with components being tested at each stage of the construction, where relevant. The first stage of construction involved preparing the machined aluminum chassis. Mylar sheets were cut to fit the chassis baseplate, and secured to the aluminum with Kapton tape–chosen for robustness over high ranges of temperature, as well as good electrical insulating properties. The chassis itself is not one machined piece, but is bolted together with machine screws 5.8. The chassis is cleaned several times during the assembly process with methanol to remove any remaining machining debris.

Double-sided tape is then added to the mylar sheeting, and special foam is then placed down. Sections are removed from the foam to accommodate routing of the electrical hookup for setting the Bakelite gas-gaps to a high bias, Figure 5.9.

After the chassis has been prepared, the bakelite gas gaps are assembled. The gas gap itself (Figure 5.10, Figure 5.4), is composed of two layers of Bakelite, which are separated by small insulating spacers. On the outside, the Bakelite is coated with graphite

Figure 5.7: Here, we see one of the many hard-working physicists who tirelessly worked in building 911: a dusty, and irradiated construct built along the AGS beam-line. The physicist sits in the center of the RPC1 North chassis, for scale. More information can be found in [27].

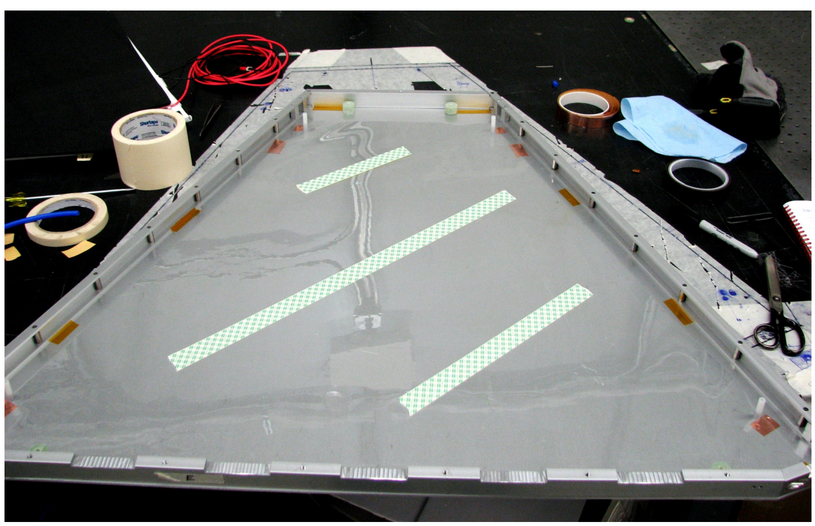

Figure 5.8: The chassis is prepared with insulating Kapton tape and mylar sheeting. The grooves along the bottom of the chassis are for routing cabling from the readout strips (shown later). The channels along the side of the chassis is for routing gas flow lines.

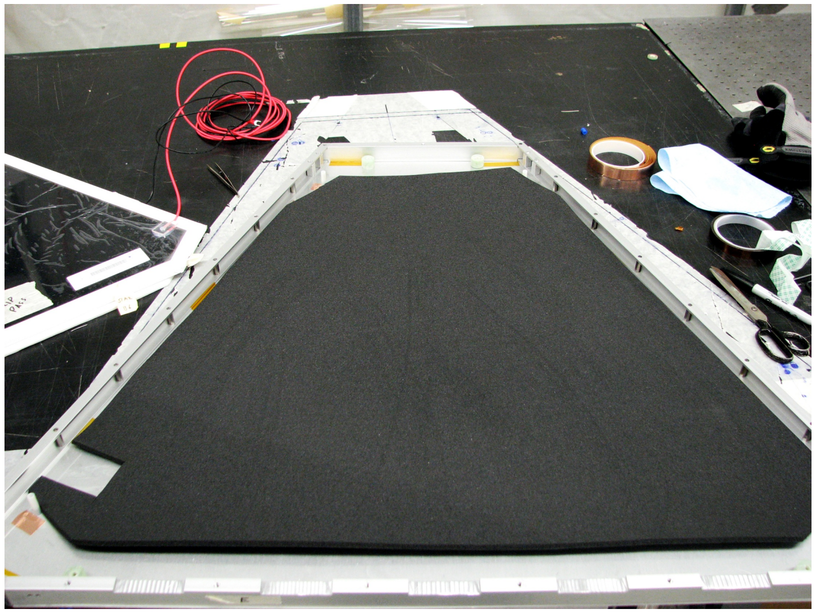

Figure 5.9: Foam shock insulation is added to the RPC 1 chassis.

suspended in linseed oil to produce outer surfaces that can be held at a fixed voltage bias. The separation of the plates forms a chamber, which is sealed from the outside. Electrodes are attached to the linseed oil to allow for bias, and plastic nipples are routed into the gap chamber allowing for gas flow. Tubes are cut to size and fixed to the gas chamber nipples, and then routed out down to the widest end. These gas feed tubes are color coded– a different color for each Bakelite section in the RPC. These gas gaps are leak/pop tested in the lab. This test involved pressurizing the gaps to 8.5 inches of water, and measuring pressure loss over a ten minute interval, using Argon. Pressure losses less than 1 inch was acceptable. During pressurization, I checked for an audible pop sound, which indicated one of the gap spacers popping lose. Popping noises, or bad pressure retention would both result in the gas gap being discarded. Finally, before installing the gap, the gap was 'burnt in', a process where the gaps were filled with the 'physics gas mixture' and then slowly voltage cycled to operating voltage over 24 hours.

After the bakelite gas gaps are tested and have passed, they are installed into the chassis, Figure 5.11. The chassis is prepared for installation with the addition of a layer of copper foil, to create a Faraday cage around the sensitive bakelite gaps. Tabs are left on the copper foil, such that they can be folded around the inner gaps, but not around the gas

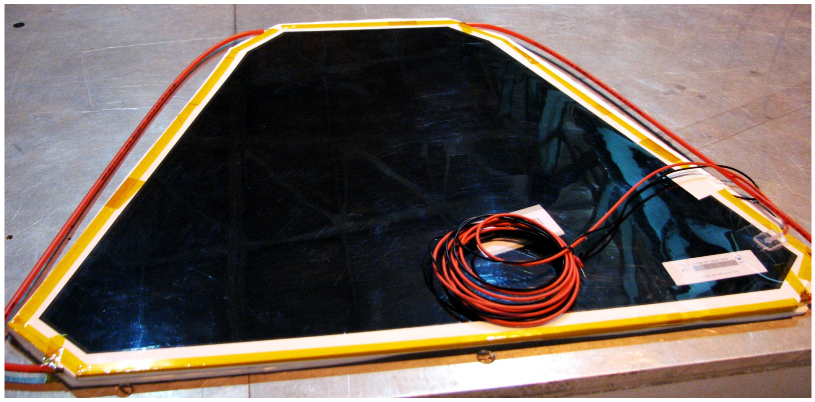

Figure 5.10: The assembled Bakelite gas gap, ready for leak/pop testing, followed by burn in.

lines. The bias cables and gas lines are routed through the chassis side channels.

Once the bottom gas gap has been installed and secured, the copper readout strips are added, Figure 5.12. The strips are oriented such that two annuli of readout strips are created (azimuthally) when the RPC 1 is installed onto the nose cone of the muon trackers. The readout strips are designed this way as to offer some rough radial tracking. The copper readout strips are laminated with mylar, and each is soldered to its own channel, which are gathered and soldered onto PCB chips. The readout strips are laminated such that mounting holes in the laminate attach in the same way to each octant, for consistency.

Following the installation of the readout strips, the final two gas gaps are installed, with their electronics and gas lines routed through the chassis similarly to the bottom gap, Figure 5.13.

Finally, the high voltage cables are grounded to the chassis and soldered to the relevant wires leading to the graphite electrodes on the outside of the Bakelite gas gaps. Wires, tubes, etc. are all fixed in place with Kaptan tape. The top of the chassis is screwed into place, and the front-end electronics are installed, with the copper readout chips plugging into the relevant FEM board. Ribbon cables are appropriately routed, and all electronics are encased in copper foil, and then additionally protected with aluminum shells, Figure 5.14.

After assembly, the RPCs were subjected to a barrage of tests, using a cosmic

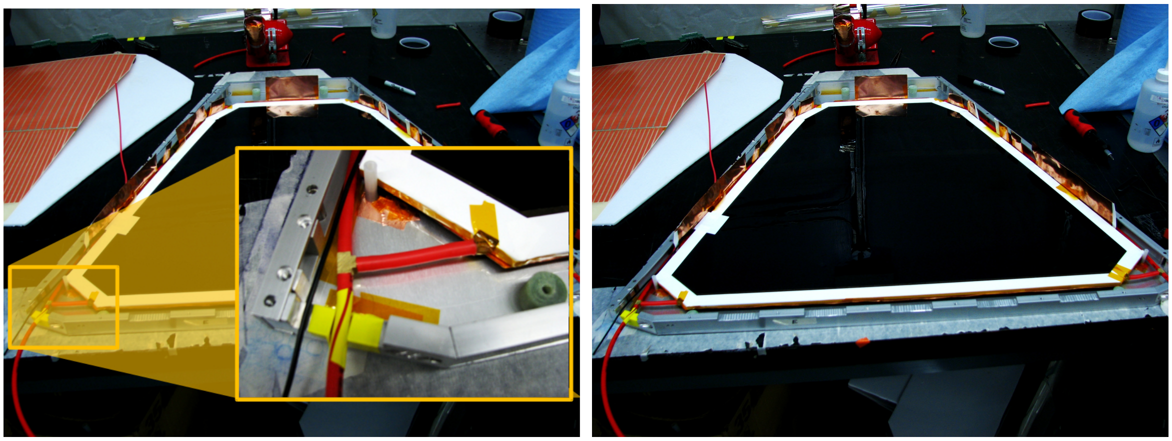

(a) Routing gas line (b) Gas gap installed

Figure 5.11: The egress port of the gas gap is carefully shielded with tape to prevent friction from causing tears, and routed out of the ports machined into the bottom of the chassis (right), with the final position of the first gap shown on the left.

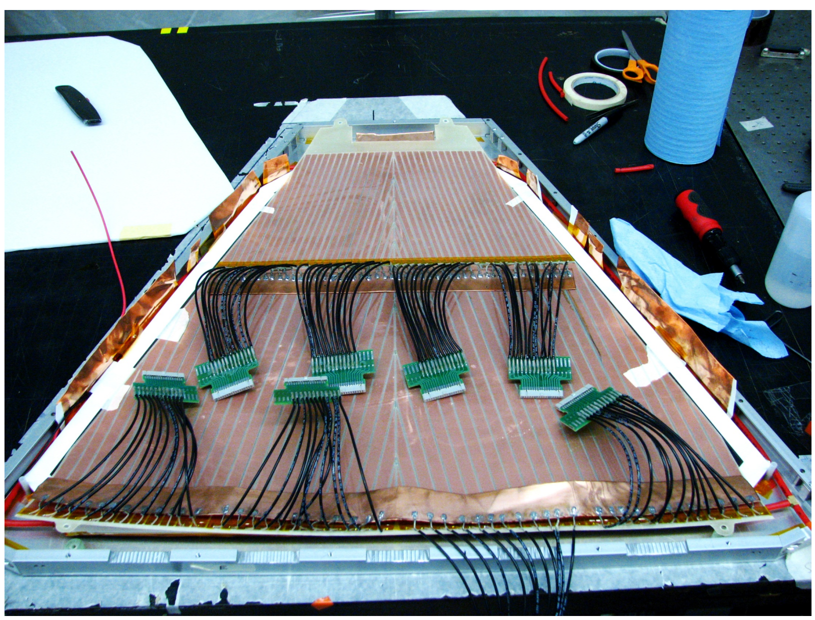

Figure 5.12: The copper readout strips are mounted to the chassis. Each readout strip is soldered to a copper wire, which in turn are gathered into readout chips.

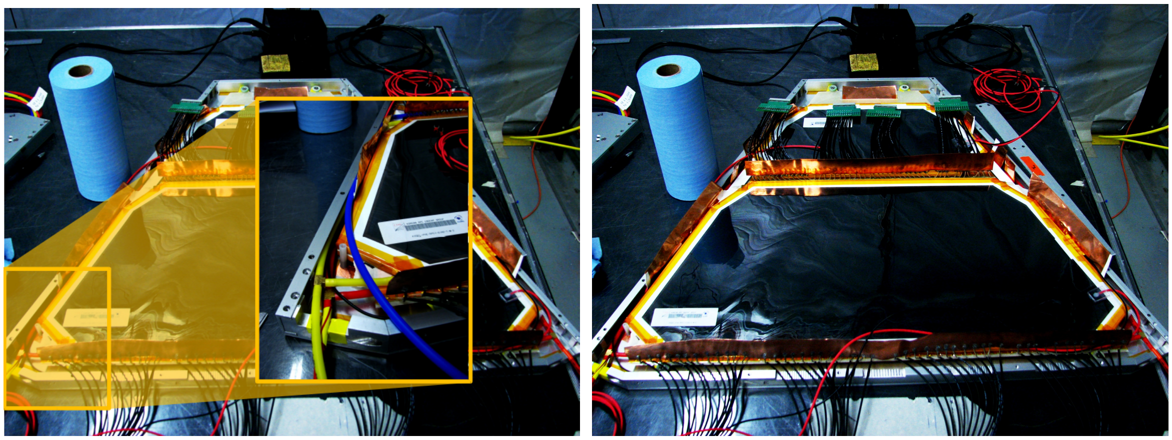

(a) Routing gas lines (b) Gas gaps installed

Figure 5.13: The final Bakelite gas gaps are installed on top of the copper readout strips. Gas lines are routed similarly to 5.11

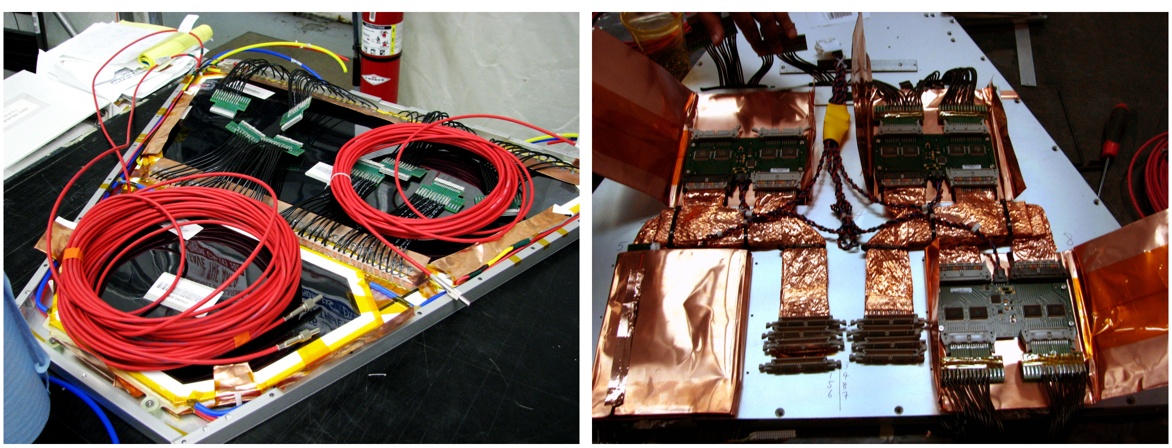

(a) Inside Assembly Complete (b) Front-End Electronics Installed

Figure 5.14: A completed RPC 1 octant, interior assembly complete, left, and the outer assembly completed on the right.

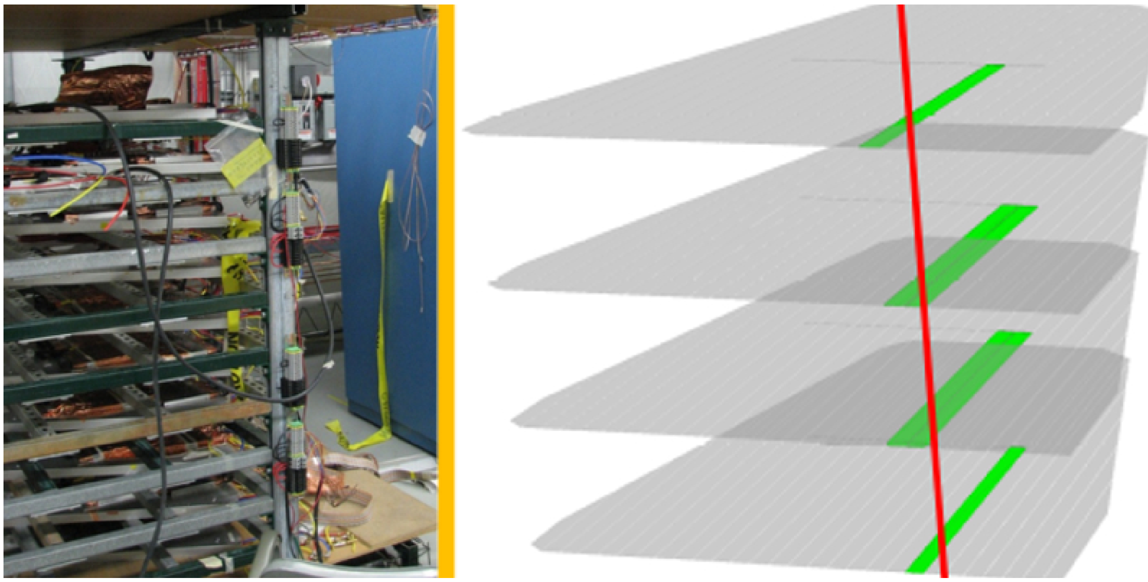

Figure 5.15: Left: the cosmic test stand setup. RPC octants were sandwiched between scintillators to run performance and efficiency tests. An example of the clustering due to a cosmic ray is shown on the right, with a particle (red) activating one or two strips per octant (activation shown in green).

ray test stand to measure clustering (Figure 5.15), designed to measure the activation threshold (combined with energy readings from scintillators above and below the test stand), determine the average cluster size, and measure overall detector efficiency. The overall ohmic 'dark-current' was also measured.

5.1.2.3 Performance

With the construction and installation of the RPCs and new Front End Electronics for the Muon Tracker, PHENIX was ready to take data for the W measurement by 2013. A dedicated run was taken, accumulating over $200pb^{-}1$ of data. All tolerances and design specifications for the upgrade were met.

5.1.3 Triggering and Data Acquisition

The new triggering scheme incorporating the RPCs and the new FEEs is summarized in Figure 5.16, while the final configuration of the PHENIX detector after the forward upgrade is show in Figure 5.17. As discussed, data was recorded at about 30% of the total PHENIX DAQ bandwidth of 8 kHz over the 2013 polarized proton+proton run, which was sufficient to record every single $W \rightarrow \mu$ event. This speaks to the relative rarity of this event, as compared to other events–the overall collision rate for protons at $510 GeV/c^2$ is as high as 10 MHz.

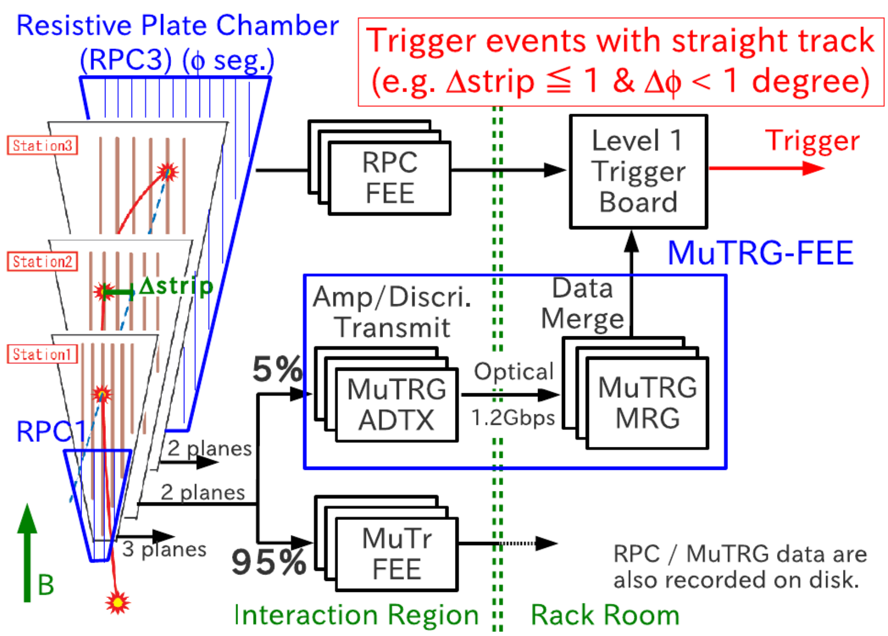

Figure 5.16: A schematic of the new muon trigger for recording W-Bosons [26]

5.1.3.1 2013 Data Set Triggers

In general, when two protons inelastically interact, we do not care about the particles that are produced because they simply tell us about physics which we already understand. To learn about new physics, or to test models, we must devise a way to preferentially record this 'interesting' data, since data recording bandwidth is limited. A decision must be made within the time scale of one beam crossing (nanoseconds) whether or not to archive the data which is produced. This process is called 'triggering'. The over all trigger rates must be recorded, so as to reconstruct the relative abundance of events after the fact. Once a trigger condition has been satisfied, the entire PHENIX spectrometer will

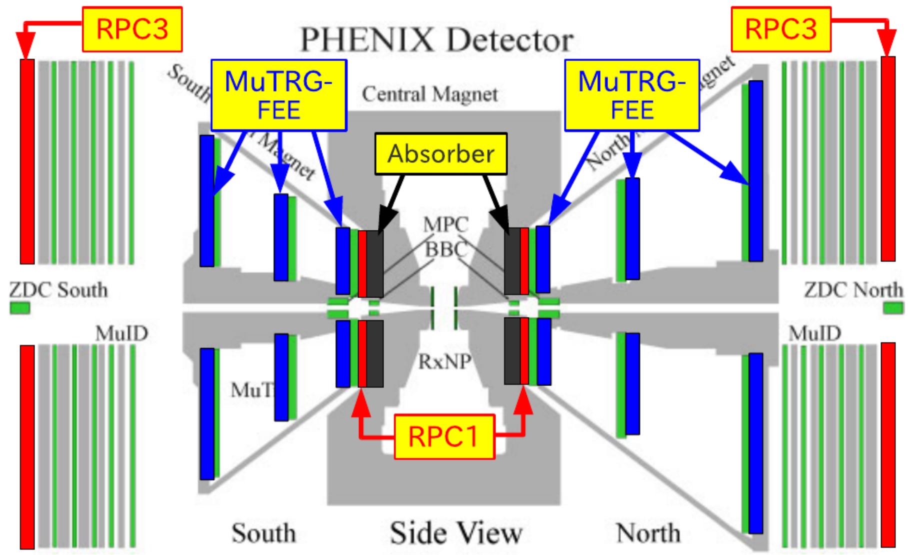

Figure 5.17: The position of the Front-End Electronics upgrades and new RPCs + Absorber are shown. Muon tracker stations are shown in blue (along with the front-end electronics). The RPCs sandwich the muon tracking stations and the MuID. The absorber material sits just inside of the muon arms, before the Forward Vertex Detectors and inner tracking stations of the muon tracker [26]

dump its data into the data stream.

The PHENIX DAQ can accommodate 32 different physics triggers. Any transduced signal by a part of the PHENIX spectrometer can be, provided the front end electronics are fast enough, be fed into a global triggering decision. Thus, PHENIX, like other triggered particle physics experiments can be arbitrarily configured to record a desired subset of data, from the total data set.

Of the 32 triggers available, one is always set to 'Noise' (but not recorded) and another is set to 'CLOCK' which is timed to trigger every beam crossing. No bandwidth is reserved for these triggers. No bandwidth is reserved for these triggers. There was one global physics trigger configuration used in the Run 13 data set, it was called 'PP510Run13'. An example configuration is shown in Table 5.2.

The each physics trigger is conveniently stored as a 32-bit integer. This is a very special integer, because it does not take on all possible values that a 32-bit integer can take on. A trigger with a bit-number of '2' means that the second binary digit of the trigger's

Name	Scale Down	Raw Trigger Rate	Livetime
BBCLL1(>0 tubes)	31141	1921013.65	0.89
BBCLL1(>0 tubes) novertex	6732	3196505.83	0.89
ZDCLL1wide	6227	370696.78	0.9
BBCLL1(noVtx)&(ZDCN||ZDCS)	6396	1498978.93	0.9
BBCLL1(>0 tubes) narrowvtx	4070	925279.35	0.89
ZDCNS	4411	233334.89	0.89
ERT_4x4b	0	93.22	0.88
ERTLL1_4x4a&BBCLL1(noVtx)	0	490.47	0.89
ERT_4x4c&BBCLL1(noVtx)	1	2191.87	0.9
SG3&MUID_1H_N||S	95	14830.21	0.88
ERTLL1_E&BBCLL1(narrow)	1	1039	0.9
CLOCK	46765	9388833.68	0.89
MPC_B	0	263.11	0.89
MPC_A	0	1511.4	0.89
MPC_C&ERT_2x2	0	189.37	0.9
(MPCS_C&MPCS_C)||(MPCN_C&MPCN_C)	0	10.19	0.63
((MUIDLL1_N2D||S2D)||(N1D&S1D))&BBCLL1(noVtx)	0	260.64	0.63
(MUIDLL1_N1D||S1D)&BBCLL1(noVtx)	55	20196.39	0.87
RPC1+RPC3_S	359	23841.89	0.9
RPC1+RPC3_N	539	72270.55	0.9
SG3&RPC3&MUID_1D_N||S	2	5526.47	0.86
SG1+RPC1(C)&MUIDLL1_N||S	0	146.32	0.86
MUON_S_SG1_RPC3A&MUID_S1D	0	31.27	0.89
MUON_N_SG1_RPC3A&MUID_N1D	0	74	0.84
MUON_S_SG1&BBCLL1(noVtx)	2697	323237.99	0.9
MUON_N_SG1&BBCLL1(noVtx)	11128	1095764.77	0.9
MUON_S_SG1_RPC3_1_B||C	0	66.32	0.89
MUON_N_SG1_RPC3_1_B||C	0	173.57	0.88

Table 5.2: A typical run from the 2013 data set, numbered with PHENIX's standard numbering scheme. Each trigger has a descriptive name hinting its composition (some triggers are actually constructed from trigger coincidences). Since PHENIX cannot record all data, we see the scale-down, the raw rate, and the live-time, which is basically a DAQ triggering efficiency.

binary representation is flipped to "1" and the rest of the digits are "0". In this way, one can easily store and check which triggers for a recorded event actually fired. Thus, an important variable called 'trigscaled' in this analysis can be created, to track which triggers which fired on a certain event by taking the bitwise-OR operation between all binary representations of triggers which fired for that event.

For example, consider a simplified version of this scheme with four assigned trigger bits. Lets say we have an event where the following triggers fired:

- Trigger 1 Fired: 0001
- Trigger 3 Fired: 0100
- Trigger 4 Fired: 1000

The boolean-OR bitwise comparison is then:

- Trigscaled: 1101

Note how we lost no information regarding which triggers fired for this event. We can recover later, in code, the trigger mix for every event by using bitwise-AND operations, so long as we know which triggers were assigned to which bit, and we have the trig-scaled number.

This bit-masked final number, ones and zeroes, is one of the crucial variables in all PHENIX data sets (discussed in the next chapter). It is crucial to know which triggers fired for which event so that the original collision conditions, and therefore the physics, can be reconstructed. Since each detector subsystem may not have the same geometric acceptance, trigger acceptance, signal traducing hardware, triggering, while necessary for taking data, introduces severe bias into the data set. Knowledge of which triggers fire for each recorded event gives us the ability to correct for these kinds of biases to recover the original conditions of the data sample.

Chapter 6

Data Analysis

The work discussed in this chapter was done in close collaboration with Dr. Ralf Seidl, Dr. Francesca Giordano, Daniel Jumper, and Abraham Meles. Eventually the analysis group merged with another year's analysis group, bringing in Dr. Sanghwa Park, and Dr. Chong Kim, who have made crucial contributions to this analysis, and have studied the complimentary 2012 data set, producing their own PhD theses on this analysis. Dr. Hideyuki Oide has also heavily influenced the techniques and work-flow of this analysis, pioneering many of the techniques used here (at PHENIX at least) for his analysis of the 2011 data set.

6.1 Overview

Although we have discussed in detail the theoretical motivations for the W physics program, as well as the machines producing the necessary collisions and recording data produced from these collisions, we have not yet addressed the form of the data set itself, and the substantial engineering it takes to extract the signal of interest out of that data set.

The relative abundance of the $p + p \rightarrow W^{\pm} \rightarrow \mu^{\pm} + \nu$ signal events is rather low, compared to the other interactions which may take place when two protons collide. We must allow several hundred million proton proton collisions to occur, before we have a high probability of observing just one W-Boson event.

We discussed in the previous chapter how careful triggering is employed in order to ensure that any time this event does occur, it is recorded. This does not guarantee that we *only* record these events. Background events are still recored much more frequently than signal events, even with the improved triggering. The number of $W \to \mu$ events produced over the 2013 data set number in the hundreds, while the total number of recorded events is approximately 15 billion.

This leads to the substantial problem of fishing out the appropriate physics events from the 15 billion event haystack. Why, I hear you ask, don't we just have a detector which can record only the W-Boson events of interest?

Because, as a multipurpose spectrometer, PHENIX must be ready to take all kinds of data, and satisfy many experimental requirements, in addition to fitting a lot of functionality into a relatively tight budget, as is common for federally funded research. Although this measurement would have been made much simpler with a forward calorimeter, we can't simply build and install a calorimeter the moment that an analysis would benefit from its presence.

So, instead, we must rely on our ingenuity and deep understanding of the data set, to tease out the results we want to measure.

6.2 Raw Data to Reconstructed Parameters

Any time a PHENIX trigger condition is satisfied, all of the information recorded by the PHENIX spectrometer are read out from temporary on-detector memory, and fed into a data stream that eventually is archived as a 'PHENIX Raw Data File Format' or PRDFF.

PRDFF data is hierarchical, first being organized by event-type, and then organized by packet-type. There are many event types–'DATAEVENTS' typically carry the information relevant to a physics analysis, whereas other event-types carry very important QA information for determining the status of the RHIC apparatus, the beam, polarization, and PHENIX performance.

Every packet has a header, which contains general information such as what the packet contains, and in what order that packet was received. Every packet recorded can be associated with a unique event-sequence number, which specifies roughly the order in which the event owning the packet was received by the DAQ. Within a given run number, an event-number is guaranteed to be unique. The complexity of the packet is limited by the bandwidth available to move data off PHENIX onto other storage, and the buffers/reconstruction ability of the front end electronics modules built onto PHENIX subsystems. PHENIX archives data from the DAQ at a rate of approximately 700 Megabytes per second–or one compact disk.

Generally, raw PHENIX data is too complex to use straight-away, because minimal to no reconstruction of physical properties for a certain event is done, due to hardware limitations and time limitations–some of this raw data is often directly used in triggering decisions, which must be made once every 106 nanoseconds or faster (the bunch crossing frequency).

The raw data collected from PHENIX undergoes a process called "Data Production", where physical parameters are reconstructed from the simpler raw data. Raw data could take any form–for example–which cathode strips were activated in an event in the muon tracker, or, the number of photons counted in a photomultiplier tube. This information is often combined with extensive survey information about the geometry of a given detector, the known magnetic field in a detector, to reconstruct quantities such as momentum, or deposited energy.

Once reconstruction has finished in a Data Production, the data are then repackaged into ROOT files, often times internally structured into custom output objects which are associated with a various detector. These output objects are simply custom written C++ classes which have a serialization scheme, which have libraries and dictionaries compiled that allow for them to be serialized into ROOT's file format.

For the purposes of this analysis, all data has been reconstructed and serialized into a specific type of output object called a 'picoDST' or even more concisely, 'pDST'. This name, like many others in PHENIX has historical context: DST stands for 'Data Summary Tape' hearkening back to the days when data was stored primarily on magnetic tape (it is still archived on magnetic tape!), and 'pico' because of its relatively small disk-space requirement, compared to 'nanoDST' files or simply 'DST' files. I'm not making this up, I swear!

6.3 Choosing Analysis Variables

Even data reduced to the point of a pDST still is much more complicated and comprehensive than what is needed for this analysis–there are thousands of variables relating to reconstruction parameters. We only need a handful of variables for this analysis, summarized on Tables 6.1,6.2, 6.3 and 6.4. When Cartesian coordinates are referenced, implicitly, the reference frame is the PHENIX Coordinate system (Figure 4.13).

As you can probably guess, the only variables which are truly relevant to this analysis need to be relevant to understanding two questions:

1. *Is this reconstructed muon track the result of a real W-Boson Decay?*

2. *What is the polarization of the two colliding protons for every recorded collision?*

To properly answer these questions, we need to comprehensively understand what processes are capable of producing muons, as well as whether or not our detector can be 'tricked' by signals which look like muons, but really aren't. Secondly, we need a means of recovering the proton spin polarization for each colliding bunch-pair.

Polarization recovery is straight-forward–we already have mechanisms in the data stream which number and track the colliding bunch pairs. We additionally have well defined spin patterns which are applied to the 120 bunches, the same way every time this pattern is applied to the fill. As discussed previously, we have good QA apparatuses in place to ensure the advertised spin pattern is the same as the delivered spin pattern. Since polarization patterns do not typically change in a standard physics beam fill (if they do, alarms are raised and the data is typically discarded), all that is needed is to associate a PHENIX run number, with a RHIC fill number, and then look up the spin pattern, which in effect, is a database-call. Of course, the overall beam polarization percentage is an important factor, which dilutes any spin asymmetry, but this is taken into account in the final spin database QA analysis [73].

This leaves us with the first question, and the difficulty in answering this question is essentially that it is challenging to differentiate signal $W \to \mu$ events from other $X \to \mu$ events, or even events which look like muons, but are really due to incorrect track reconstruction.

Therefore, the thrust of the Data Analysis portion of this work is really just to tease apart the real W-genic muons, from all other muon candidates. To this requires some substantial feature engineering, and creating some statistical models, as well as a means of evaluating the performance of these statistical models–which is difficult because validating any statistical differentiation technique (aka machine learning technique) requires a labeled

Name	Description
Run_Number	A unique number identifying a run in a RHIC fill for PHENIX
Evt_Number	A unique number within a single run identifying the approximate order an event was taken.
Evt_bbcZ	The event z-vertex calculated by the BBC
triggerbit	The result of a bit-wise 'OR' applied to all 32-bit trigger bits which fired
clockcross	The bunch number of the two colliding bunches $[0-119]$. Required to look up the spin polarization, along with Run_Number

Table 6.1: Variables characterizing events overall

Name	(Unit) Description
Evt_Nmu	The number of muon tracks reconstructed for a given event
charge	($\pm e$) The charge associated with a reconstructed muon track
p_z	(GeV) The z-momentum associated with the muon track
p	(GeV) The total momentum of a charged track
χ^2	The result of the Kalman fitter reconstructing the track
lastGap	The last gap in the Muon Tracker which was activated (there are 4)
η	The rapidity of the track
ϕ	(rad) The azimuthal position angle the track makes relative to the x-axis
DG0	(cm) A Track matching variable (matching between MuID and MuTR) associated with the MuID road, at MuID station 3.
DDG0	(degree) The opening angle between the MuID track road, and the MuTr projection onto the MuID
xSta$_i$	(cm) The x-coordinate of the track at Station i, $i \in 1,2,3$ of the MuTr
ySta$_i$	(cm) The y-coordinate of the track at Station i, $i \in 1,2,3$ of the MuTr
ϕ_i	(rad) The angle the track makes with Station i, $i \in 1,2,3$, i.e.: $\phi_i = tan^{-1}\left(\frac{x_1}{y_i}\right)$
θ	(rad) Azimuthal angle of track, $tan^{-1}\left(\frac{p_T}{p_z}\right)$
DCA$_z$	(cm) Distance of closest approach between the z-vertex positions extracted by projecting the MuTR track z-vertex back to the BBC z-vertex
DCA$_r$	(cm) Distance of closest approach between the track and beam axis

Table 6.2: Muon tracker variables. Generally, this data set is indexed on a subevent level, where one event will contain all reconstructed muon tracks seen for that event.

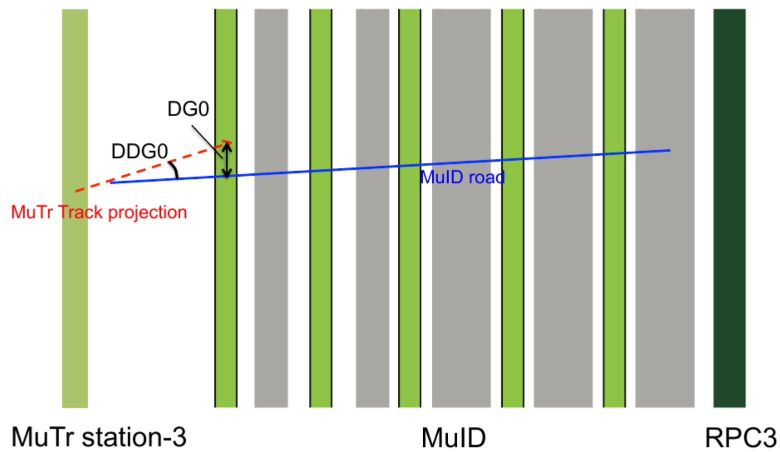

Figure 6.1: A schematic representation of the matching variables, DG0 and DDG0 at the intersection between the Muon Tracker and Muon Identifier [28]

Name	**Description**
$fvtx_{d\phi}$	The ϕ residual between MuTR track and FVTX track
$fvtx_{d\theta}$	The θ residual between the MuTR track and FVTX track
$fvtx_{dr}$	The radial residual between the MuTR track and the FVTX track
$fvtx_{conebits}$	The number of FVTX clusters inside a cone around the track defined by: $0.04rad < dR < 0.52rad$ where $dR = \sqrt{d\eta^2 + d\phi^2}$

Table 6.3: A summary of the variables reconstructed from FVTX raw data [31].

data set, and we intrinsically do not possess this, since otherwise, this analysis would not need to be done.

The engineered variables in this analysis are dw_{13}, dw_{23}, $d\phi_{13}$, and $d\phi23$. These variables are calculated from reconstructed physics data. They play an important role in our extraction of the signal to background ratio. The $d\phi_{ij}$ variables represent the difference in azimuthal angle observed at the MuTR station i and j respectively. dw_{ij} is constructed from $d\phi_{ij}$ as follows:

$$dw_{ij} = p_T \times sin(\theta) \times d\phi_{ij} \tag{6.1}$$

While ϕ_i is calculated from the x and y coordinates at Station i:

Name	Description
RpcMatchSt1	Distance of closest approach between projected MuTR track onto the RPC 1 and the closest hit cluster on RPC 1
RpcMatchSt3	Distance of closest approach between projected MuTR track onto the RPC 3 and the closest hit cluster on RPC 3

Table 6.4: RPC Track matching variables

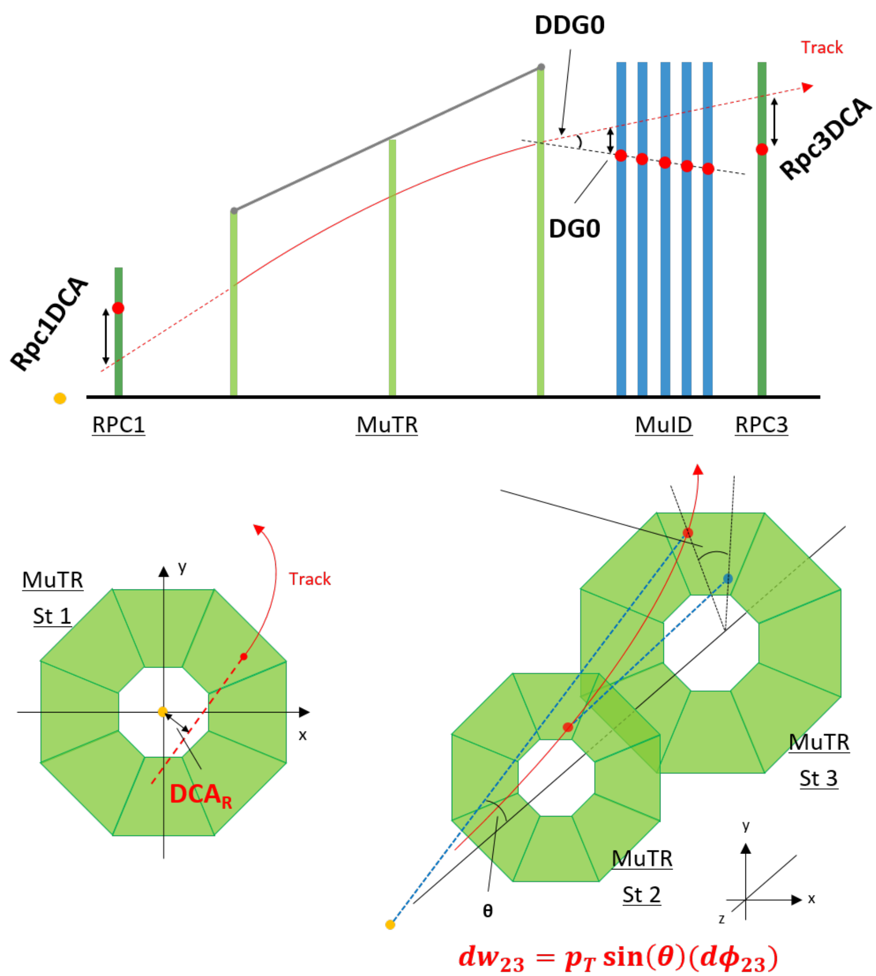

Figure 6.2: A nice summary of discriminating kinematic variables reproduced with permission from Dr. Chong Kim. We see the MuTR tracking planes in green, and a muon track penetrating the planes in red, and reference coordinates in the lower right-hand corner. The geometric relationship between the roads, reconstructed track are shown in the annotations.

$$\phi_i = tan^{-1}\left(\frac{ySta_i}{xSta_i}\right) \tag{6.2}$$

A common theme amongst these variables is that they should help us distinguish between high momentum muon tracks from W-Bosons, and other muon tracks. The hope is that the muon tracks from W-Bosons are kinematically restricted to have a relatively narrow momentum distribution in the forward kinematic regime, and so therefore, tracking variables can be used to partially differentiate between signal and background events.

In general, W-genic events will be mostly straight, geometrically, and so this constrains the values of variables such as DCA_r substantially, and other variables less so. Thus, dw_{23} should be a good discriminator, as it depends on p_T and the azimuthal bending of the charged tracks, due to the radial magnetic field in the MuTR.

Our secondary requirement of our variables is that they are relatively uncorrelated with each-other, to leave plenty of room for statistical modeling. Ultimately, we chose a subset of the available tracking variables to carry out the analysis, in two stages. The correlation of variables for both data and simulation are summarized in Figure 7.3.

In the first stage of the analysis, we use: DG0, DDG0, DCA_r, chi^2, Rpc1DCA, Rpc3DCA, $fvtx_{dr \times d\theta}$, $fvtx_{d\phi}$, and $fvtx_{cone}$. Of these variables, some were grouped to account for correlations: DG0 and DDG0, χ^2 and DCA_r. These variables are all related to track reconstruction. The Muon Tracker reconstructs tracks by essentially connecting the dots between x and y coordinate 'hits' that it records at each station. The lines connecting these hits are called 'roads'. Following this, the roads and hits are used to generate a curve fit to the data, given knowledge of the muon tracker's radial magnetic field. From this curve, we extrapolate the charge and momentum, and we construct variables which codify the difference between the reconstructed curve, and the 'connect the dots' roads. The smaller these differences are, the more straight the track is, and as discussed, straightness points to higher momentum, which ultimately leads to labeling as a W-genic particle, if the momentum is in the correct range.

In the second phase of the analysis, we use dw_{23} and η primarily. Both stages of the analysis are discussed in the following sections. dw_{23} is related to track straightness as well, and is referred to as "reduced azimuthal bending". Since we're interested in forward muons, η is used as our second variable.

Generally, we are interested in recovering forward $\mu+$, forward $\mu-$, backward

$\mu+$ and backward $\mu-$. As the muon arms do not have the same rapidity coverage, we separate the data into these four categories–forward positive charged tracks, forward negatively charged tracks, backwards positively charged tracks and backward negatively charged tracks. Due to the geometry of the muon arms, the North Arm will always correspond with forward positive rapdity, whereas the South Arm will always correspond with backward, negative rapidity. I will use 'forward and backward' interchangeably with 'North and Sout'. We perform all calculations with our data set in parallel between these four conditions.

The data is further subdivided based on the available track matching variables for a given event, but these subdivisions are not kept separate from the overall arm-charge separation. Some variables, such as the RPC track matching variables and the FVTX track matching variables exist for some events, but not others. We will discuss how this is managed in later sections, but this data is not generally partitioned in this way.

Chapter 7

Feature Engineering

The ultimate goal of Feature Engineering is to clean the data and transform the data with heuristic strategies that tag events coming from signal sources, as separate from events which come from our background, so that we can proceed with the calculation of the physics asymmetry.

Even with the Forward Upgrade (Section 5.1), our data set is still composed mostly of background events (Figure 7.1). The primary constituents of the data set are muons from the following sources:

- **Hadronic Background**
  - The hadronic background is composed of hadrons which are produced from the primary event vertex, and then travel into the muon arms. The hadrons then decay in the muon arms, and create hits at each station, which are mis-reconstructed as high-p_T muons.
- **Muon Background**
  - The muon background is composed of processes which produce real muons which fall into a similar kinematic regime of the W-genic muons
- **W Signal**
  - These are muons we are looking for. They come from the W boson decay, and carry information about the proton spin.

We will differentiate these types of data in two different step. In the first step, we will use likelihood event selection, where we lump hadronic background and muon background together, and merely distinguish it from W-genic events. In the second stage, we will further differentiate our model for the background, drawing heavily on the data to understand the hadronic background, and providing simulations of the W-genic events as well as simulation cocktail for other muon background events. Before we discuss this differentiation, it is important to discuss the simulations, as the rest of the analysis hinges on the simulation of both the W-genic events and the Muon Background events.

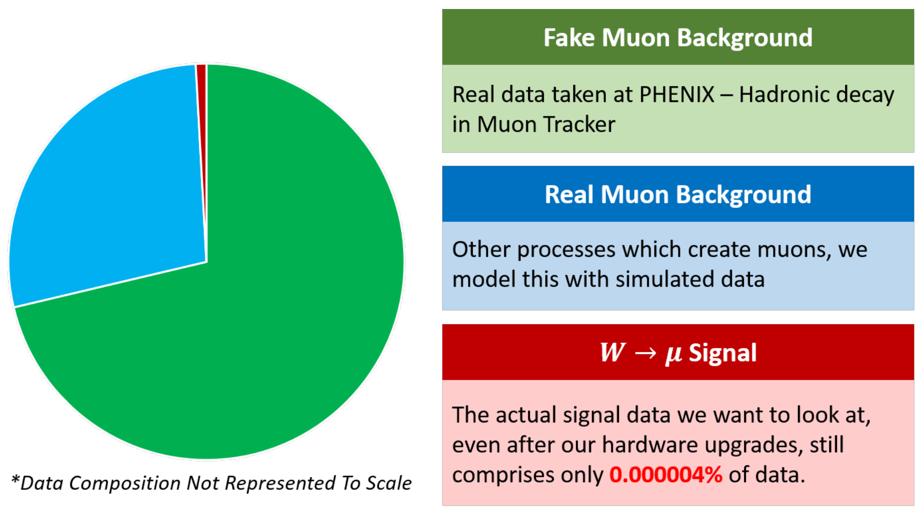

Figure 7.1: A cartoon of the dataset composition. The data, even after the Forward Upgrade, is mostly composed of hadronic background, which has tricked our Muon Tracker.

In subsequent sections, I will discuss what we do with the variables which we have chosen to use to identify W-genic events. Because our data set is so dominated by background sources, we must rely heavily on simulations to estimate what our signal events might look like. As of the time of this writing, the analysis has not yet incorporated the simulation of hadronic background, which is quite difficult, as there are a lot of effects at play–particles which interact with the material of PHENIX itself to produce secondary and tertiary vertices, for example. However, if we can simulate accurately the signal process (the W-Boson cross section and its scaling with energy is known to excruciating precision), and the muon background processes (known to similarly high precision), we can approach the problem from a standpoint of using our data set as a relatively good model for what ‘hadronic background’ looks like, and use simulations to fit the portions of the data which cannot come from this hadronic background.

7.1 The Basic Cut

The basic cut aims to remove all obviously bad events from our event mix. The cut approaches this from two premises. The first, is that if track reconstruction variables simply cannot have resulted from a W-genic event, then we remove the track. Secondly, if the track corresponds to a reconstructed energy which is larger than what is physically allowable for a W-genic track, we remove it.

The "Basic Cut" is defined:

Variable	**Lower Bound**	**Upper Bound**
MuID lastGap	*	Gap 4
χ^2	0	20
$DG0$	0	20
$DDG0$	0	9
μ candidate	*	1

Table 7.1: The Basic Cuts used in the Run 13 analysis. lastGap refers to the last gap in the MUID which saw a μ candidate event. The fourth gap is the furthest penetration possible, therefore suggesting a high energy muon. Other parameters are described in Tables 6.1, 6.2, 6.3, and 6.4

With this cut, we have removed quite a large fraction of background events from our dataset without worry of removing any events in that fall within the kinematic range of W-Boson production.

7.2 Simulations

I did not do any work to produce the simulations used in this analysis, all of that credit goes to Dr. Ralf Seidl. I will generally describe how the simulations were produced, and paraphrase from the analysis note which we co-wrote with contributions also from Dr. Giordano, Abraham Meles and Daniel Jumper: [29].

PHENIX has a rather well developed simulation framework, which uses the inhouse built "PHENIX Integrated Simulation Application" (PISA) [?] custom simulation framework. The simulation framework models in great detail the entire 12mx18mx18m volume of the PHENIX apparatus, as well as all the various material properties of the apparatus. The software package originated from the GEANT geometry and tracking packages. PISA encompasses more than this, though, it additionally encapsulates event-generators, a standalone geometry verification package, and the PHENIX offline analysis shell, to generate data that is completely compatible with PHENIX's data packaging framework. PISA has since been integrated into a simulation work-flow with the popular PYTHIA event generation system.

The simulations were created by selecting the biggest sources of muon background known to be produced at PHENIX as well as the W-Boson event and producing many events to generate good statistics. The primary purpose of simulating the muon background and W-Signal is to ultimately generate probability distribution functions for the variables which have the largest analyzing power–i.e. ability to differentiate between signal and background. The simulation and data both are ultimately described by the same variables.

The data are added together, when combined to generate a 'muon background pdf' or 'W-Signal pdf' according to the cross-section of the process and the number of generated events, so as to not add these ingredients into the cocktail in the wrong amounts. This process is described in the next section, but the simulations used in this analysis are summarized here, in Table 7.2. When adding the simulations together, one must be careful to scale the final-yields by a correction factor (called k-factor) such that events which produce boosted dimuons are properly accounted for.

PHENIX uses some somewhat exclusive jargon when describing the various quark bound states which contribute to the muon background, and signal events. Open charm or charmonium refer to the bound state of the $c\bar{c}$ quarks. Onium generally refers to any process where a particle is in a bound-state with its own antiparticle (without of course double-counting open charm/charmonoim). Direct photon, or alternatively $d\gamma$ (sometimes also written as DY) refers to photons that are produced as an immediate result of a inelastic scattering process, not from secondary decays. Open bottom refers to the bound state of $b\bar{b}$ quarks. Z/$d\gamma$ refers to the production and decay of the mixing between the Z-boson and virtual photons. ONLY Z refers to Z production and decay. W is naturally the signal event. W tau refers to the production of tau leptons, which can decay weakly, producing electrons or muons. W had refers to the production of W bosons from hadronic processes, rather than as the primary event vertex. All of these processes are summarized in Table 7.2. "

Reference Run 393888				
Process	**k factor**	σ (mb)	**# Events**	$\mathcal{L}$ (fb^{-1})
$c\bar{c}$	2.44	5.71e-01	5.85e+11	1.02
onium	0.415	1.35e-01	1.5e+11	1.11
$d\gamma$	0.0	5.32e-02	5.84e+10	1.10
$b\bar{b}$	1.83	7.30e-03	7.36e+09	1.01
ONLY Z	1.25	3.37e-07	1.73e+08	577.0
W	1.5	1.66e-06	3.38e+08	198.9
W tau	0.0	1.66e-06	3.43e+08	201.8
W had	0.0	1.66e-06	3.42e+08	201.2
Z	1.25	1.02e-06	2.93e+08	61.2

Table 7.2: Simulated sub processes in Run 13 including their generated event numbers as well as the corresponding luminosity and cross sections. Dr. Sanghwa Park has done an extensive analysis of the simulated data to determine an appropriate k-factor. Process which contribute very little to the muon background include W had, W tau, and $d\gamma$; they are scaled to zero.

The simulations must additionally be weighted for trigger efficiency. To accomplish this, we weight events for each arm and charge with the associated trigger efficiency when constructing probability density functions representing the muon background. The trigger efficiencies generally manifest as η dependent functions–thus we bin the data into 20 separate η bins and calculate the efficiency associated with each bin. The bin ranges, and efficiency corrections are summarized in Table 7.4 for the North arm, and Table 7.3 for the South

		South Arm	
η_{min}	η_{min}	$\mu^- \pm stat \pm sys$	$\mu^+ \pm stat \pm sys$
1.10	1.17	$0.27912 \pm 0.00297 \pm 0.10243$	$0.30607 \pm 0.00423 \pm 0.01108$
1.17	1.25	$0.40422 \pm 0.01642 \pm 0.04811$	$0.43125 \pm 0.01717 \pm 0.26702$
1.25	1.32	$0.27958 \pm 0.00056 \pm 0.05539$	$0.36619 \pm 0.00925 \pm 0.07316$
1.32	1.40	$0.26563 \pm 0.00542 \pm 0.02485$	$0.25312 \pm 0.00349 \pm 0.04927$
1.40	1.48	$0.39802 \pm 0.00497 \pm 0.07770$	$0.34295 \pm 0.00306 \pm 0.03127$
1.48	1.55	$0.43156 \pm 0.00633 \pm 0.17060$	$0.37567 \pm 0.00248 \pm 0.03644$
1.55	1.62	$0.34831 \pm 0.00309 \pm 0.03720$	$0.40246 \pm 0.00546 \pm 0.04605$
1.62	1.70	$0.33043 \pm 0.00280 \pm 0.09227$	$0.40219 \pm 0.00472 \pm 0.05637$
1.70	1.77	$0.33152 \pm 0.00318 \pm 0.11668$	$0.30805 \pm 0.00360 \pm 0.03644$
1.77	1.85	$0.34710 \pm 0.00633 \pm 0.00918$	$0.38565 \pm 0.00439 \pm 0.04295$
1.85	1.92	$0.32448 \pm 0.00404 \pm 0.14670$	$0.30118 \pm 0.00418 \pm 0.10071$
1.92	2.00	$0.31461 \pm 0.00714 \pm 0.01799$	$0.31263 \pm 0.00545 \pm 0.01643$
2.00	2.07	$0.64632 \pm 0.01161 \pm 0.23329$	$0.63252 \pm 0.01040 \pm 0.10507$
2.07	2.15	$0.60582 \pm 0.00565 \pm 0.05569$	$0.67335 \pm 0.01245 \pm 0.05630$
2.15	2.22	$0.45058 \pm 0.00697 \pm 0.45101$	$0.69619 \pm 0.01247 \pm 0.65623$
2.22	2.30	$0.45185 \pm 0.01358 \pm 0.36032$	$0.51436 \pm 0.01288 \pm 0.43781$
2.30	2.38	$0.43890 \pm 0.07336 \pm 0.34632$	$0.61623 \pm 0.06221 \pm 0.62209$
2.38	2.45	$0.00000 \pm 0.25000 \pm 0.00000$	$0.00000 \pm 0.25000 \pm 0.00000$
2.45	2.52	$0.00000 \pm 0.25000 \pm 0.00000$	$0.00000 \pm 0.25000 \pm 0.00000$
2.52	2.60	$0.00000 \pm 0.25000 \pm 0.00000$	$0.00000 \pm 0.25000 \pm 0.00000$

Table 7.3: η dependent trigger efficiencies are calculated for the South arm in 20 η bins. Each correction has both systematic and statistical error accounted for.

		North Arm	
η_{min}	η_{min}	$\mu^- \pm stat \pm sys$	$\mu^+ \pm stat \pm sys$
1.10	1.17	$0.56285 \pm 0.03834 \pm 0.32882$	$0.52850 \pm 0.01938 \pm 0.36163$
1.17	1.25	$0.67803 \pm 0.02249 \pm 0.13431$	$0.49546 \pm 0.00261 \pm 0.16304$
1.25	1.32	$0.69537 \pm 0.01551 \pm 0.03465$	$0.63287 \pm 0.01285 \pm 0.08350$
1.32	1.40	$0.39864 \pm 0.00724 \pm 0.02330$	$0.38435 \pm 0.00762 \pm 0.11954$
1.40	1.48	$0.52102 \pm 0.00750 \pm 0.05014$	$0.49573 \pm 0.00698 \pm 0.03733$
1.48	1.55	$0.48068 \pm 0.00498 \pm 0.11579$	$0.48874 \pm 0.00357 \pm 0.08063$
1.55	1.62	$0.54113 \pm 0.00860 \pm 0.04895$	$0.50041 \pm 0.00659 \pm 0.05165$
1.62	1.70	$0.45140 \pm 0.00822 \pm 0.05718$	$0.46948 \pm 0.00755 \pm 0.09718$
1.70	1.77	$0.43203 \pm 0.00547 \pm 0.04976$	$0.40722 \pm 0.00546 \pm 0.07957$
1.77	1.85	$0.42141 \pm 0.00815 \pm 0.04366$	$0.44450 \pm 0.00628 \pm 0.04575$
1.85	1.92	$0.37946 \pm 0.00620 \pm 0.01766$	$0.37183 \pm 0.00700 \pm 0.01848$
1.92	2.00	$0.37499 \pm 0.00782 \pm 0.05026$	$0.40156 \pm 0.00678 \pm 0.02291$
2.00	2.07	$0.51268 \pm 0.00547 \pm 0.10416$	$0.60041 \pm 0.00973 \pm 0.21212$
2.07	2.15	$0.56990 \pm 0.00614 \pm 0.14507$	$0.58276 \pm 0.01392 \pm 0.25179$
2.15	2.22	$0.60527 \pm 0.01524 \pm 0.10354$	$0.60766 \pm 0.00425 \pm 0.23618$
2.22	2.30	$0.70200 \pm 0.01678 \pm 0.25233$	$0.45067 \pm 0.01008 \pm 0.24192$
2.30	2.38	$0.48294 \pm 0.00294 \pm 0.12663$	$0.54157 \pm 0.02109 \pm 0.06230$
2.38	2.45	$0.47814 \pm 0.02338 \pm 0.42026$	$0.42606 \pm 0.03092 \pm 0.25031$
2.45	2.52	$0.61788 \pm 0.14438 \pm 0.61788$	$0.29673 \pm 0.06686 \pm 0.04941$
2.52	2.60	$0.00000 \pm 0.25000 \pm 0.00000$	$0.15630 \pm 0.15630 \pm 0.18223$

Table 7.4: η dependent trigger efficiencies are calculated for the North arm in 20 η bins. Each correction has both systematic and statistical error accounted for.

arm.

We can visualize the composition of the simulated data set by stacking the relative distributions of these variables. By looking the cross-sections of these variables as a function of p_T, for each arm and charge combination, we can get a feeling for how the data set composition varies with p_T (Figure 7.2).

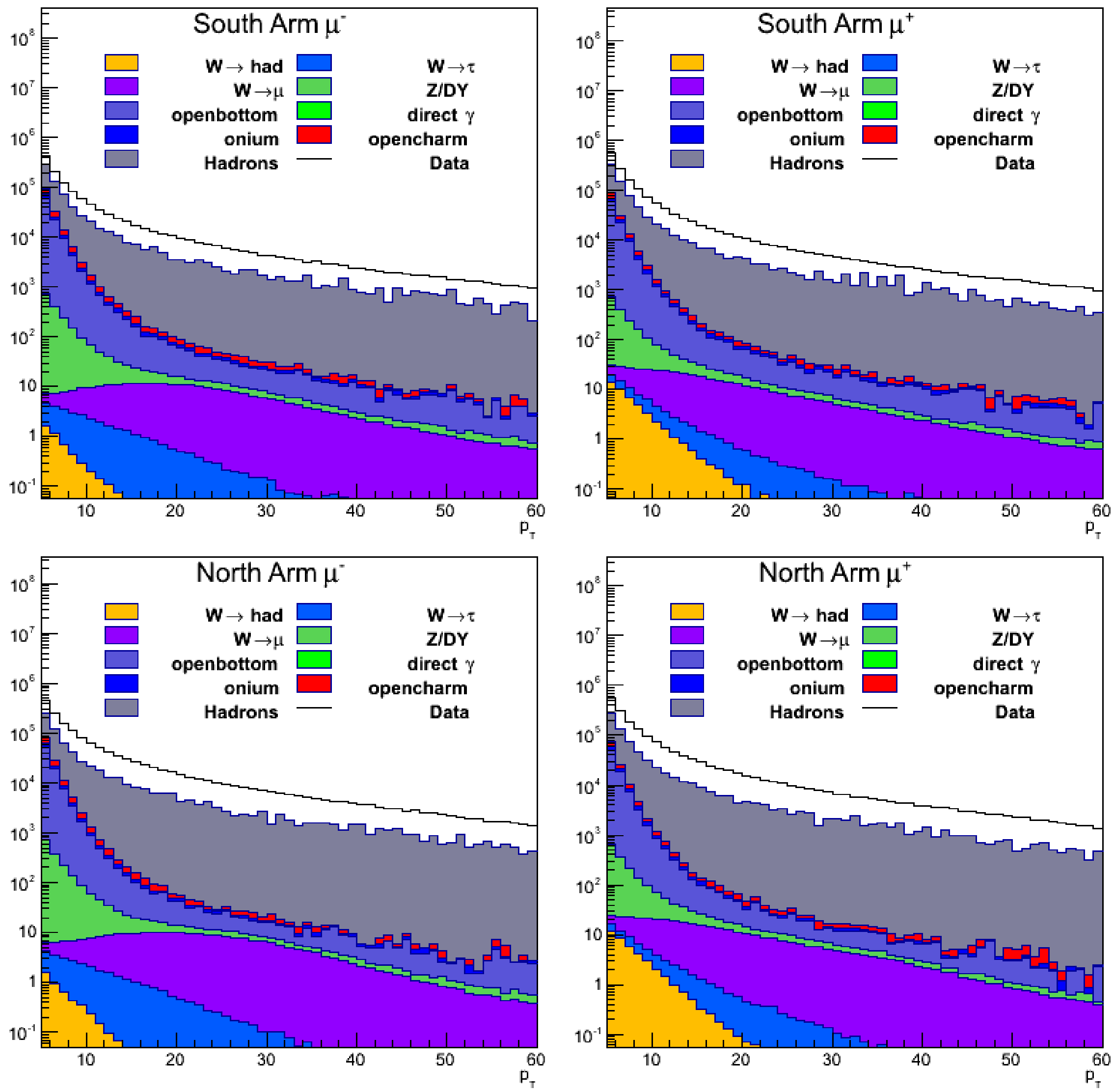

Figure 7.2: Here, we see the stacked cross-sections of all simulated processes as a function of p_T. All data shown has been created from the PISA+PYTHIA framework. Top Left: South $\mu-$, Top Right: South $\mu+$, Bottom Left: North $\mu+$, Bottom Right: North $\mu-$. Figure reproduced from my analysis note. Dr. Ralf Seidl produced the original [29]

7.3 W_{ness}: Likelihood Event Tagging

Recalling that we have already split the dataset into three main contributions: hadronic background, real muon background, and W-Signal, we are now tasked with formulating a means to separate signal from background, using the variables which can indicate the straight-ness of a muon track.

Previous analyses have attempted to separate the muon spectrum into p_T bins, to estimate the composition, however, because the $W \to \mu$ signal is so small in the forward kinematic regime, these methods are not sufficient, as there is no 'visible' cutoff in the spectrum.

However, we may use other methods to split up our spectrum, with the ultimate goal of calculating A_L, and correcting for background dilution using the signal to background ratio. We must use another method to effectively describe the difference between an event which comes from a signal, vs background event.

We expect that tracks which are straight are more likely to come from a W-Boson decay, because this indicates high momentum. One way of thinking of our data set can in terms of a classification problem. In a classification problem, one can use Bayes Theorem when one has a labeled testing data set to build predictive models which can classify data into two or more classes, provided that care is taken to not over-train the classifier, or attempt to classify data which has been used in the subset of data to train the classifier.

In our case, we have simulations which serve as the training data, guaranteeing that there will be no overlap between the physical data produced, and the data used to train the classifier. Thus, we implement a Naive Bayes Classifier (also known as Likelihood Selection) to label our data with two classes. Rather than labeling data with a binary classification, however, we opt to label the data with its likelihood, a posterior probability which tells us if a value is more or less likely to come from a W-Boson.

7.3.1 Naive Bayes Classification

There are many techniques available for classifying a collection of variables (a feature set) into categories. Naive Bayes classification is an excellent candidate for classification, in cases where we have two classifications with distributions of feature sets which are uncorrelated. Naive Bayes even works when feature sets are slightly correlated. It is a robust, fast, scalable machine learning technique. Traditionally used for classification of text documents, Naive Bayes is also able to handle numeric features whose distributions are known [74].

In our analysis, we begin with a Naive Bayes classifier which is trained to classify signal muons or background muons. We combine both Real Muon Background muons and Fake Muons (Hadronic Background Muons) in the label of “Background Muons” at this stage, though, later, we will separate out the muons further.

In order to obtain the best performance from our classifier, without over-training, we need to ensure that the variables (or feature set) used to determine a class are maximally uncorrelated. The variables which match this criteria are: DG0, DDG0, χ^2, $fvtx$ variables, Rpc1DCA, Rpc3DCA, DCA$_r$, and DCA$_z$. The Linear Correlations between these variables are shown for both the data, and the simulated W-Signal in Figure 7.3.

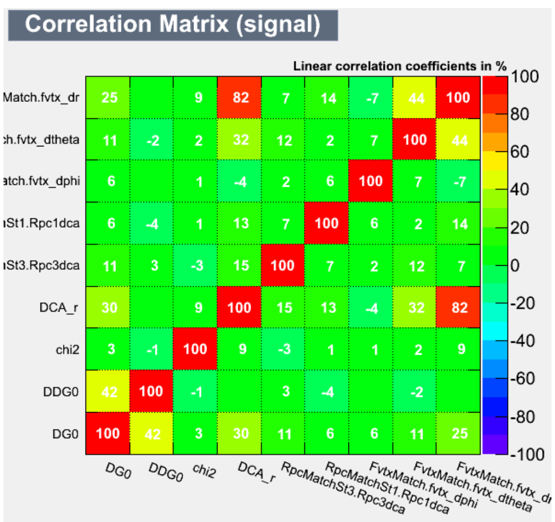

(a) Correlations between kinematic variables, produced from simulated data.

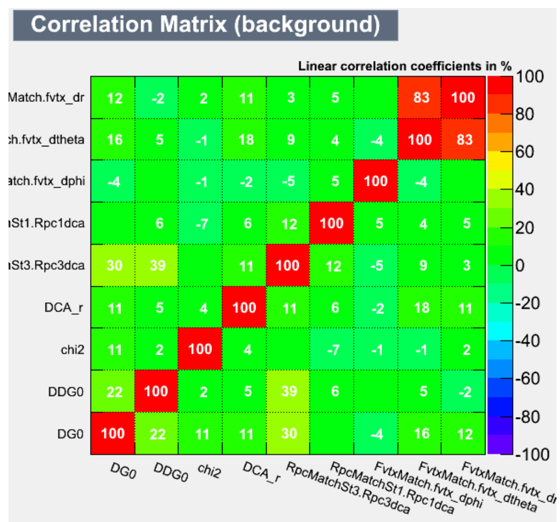

(b) Correlations between kinematic variables, produced from the data, which is composed mostly of hadronic background

Figure 7.3: Low correlations between the signal variable distributions (from simulation), and the background variable distributions make this data set a good candidate for classification using Naive Bayes

As one can see from Figure 7.3, DG0 and DDG0 are slightly correlated, as are chi^2 and DCA$_r$. A Naive Bayes classifier may be constructed from the core of the familiar Bayes Theorem from probability and statistics. In our case, we understand Naive Bayes as a conditional probability. Concretely, we consider a vector of features (i.e. our discriminating kinematic variables):

$$\mathbf{x} = (x_1, \ldots, x_n) \tag{7.1}$$

and assume independence between each feature x_n. We then define the probability of a given classification, C_k given a set of features x_n:

$$\mathcal{P}(C_k | x_1, \ldots, x_n) \tag{7.2}$$

This conditional probability is defined in terms of Bayes Theorem:

$$\mathcal{P}(C_k | \mathbf{x}) = \frac{\mathcal{P}(C_k)\ \mathcal{P}(\mathbf{x}|C_k)}{\mathcal{P}(\mathbf{x})} \tag{7.3}$$

The terms here are defined as:

- $\mathcal{P}(C_k) \rightarrow$ prior probability
- $\mathcal{P}(\mathbf{x}|C_k) \rightarrow$ likelihood
- $\mathcal{P}(\mathbf{x}) \rightarrow$ evidence

The probabilities described here are realized through constructing probability density functions from the data and simulations. The constraints of these probability distribution functions is that they are well behaved in the sense that they are finite and convergent in asymptotic limits, such that they can be meaningfully normalized.

In our case, we construct a likelihood ratio, using the posterior probability for each classification, which is defined as W_{ness}:

$$\lambda_{sig} = \prod_k \mathcal{P}(\mu_{sig}|C_k)$$
$$\lambda_{bak} = \prod_k \mathcal{P}(\mu_{bak}|C_k)$$

Where λ_{sig} and λ_{bak} represent the total likelihoods that a given track is either signal, or background, constructed from the product of likelihoods calculated from each probability density function. The λ's are combined to calculate the W_{ness}:

$$W_{ness} = \frac{\lambda_{sig}}{\lambda_{sig} + \lambda_{bak}} \tag{7.4}$$

Thus, we must construct probability density functions representing the likelihood of an event being W-genic or from the combined hadronic+muon background. Our data set after th basic cut has approximately 1 million events. Based on the cross-section of the $W \rightarrow \mu$ decay, we expect the final population of W-Bosons in the data set to be on the order of 1 thousand. Therefore, we can confidently use the data set as is, in order to generate PDFs representing the hadronic+muon background, as any effect from the signal would be only one part in a thousand. Thus, we loop over the data set, and the W-Simulation set, and filter the data into probability distribution functions. Because some events do not have archived data from all subsystems, we construct a variety of PDFs, selecting the appropriate PDF cocktail based on whether or not the requisite variables were archived for that given track, Figure 7.4.

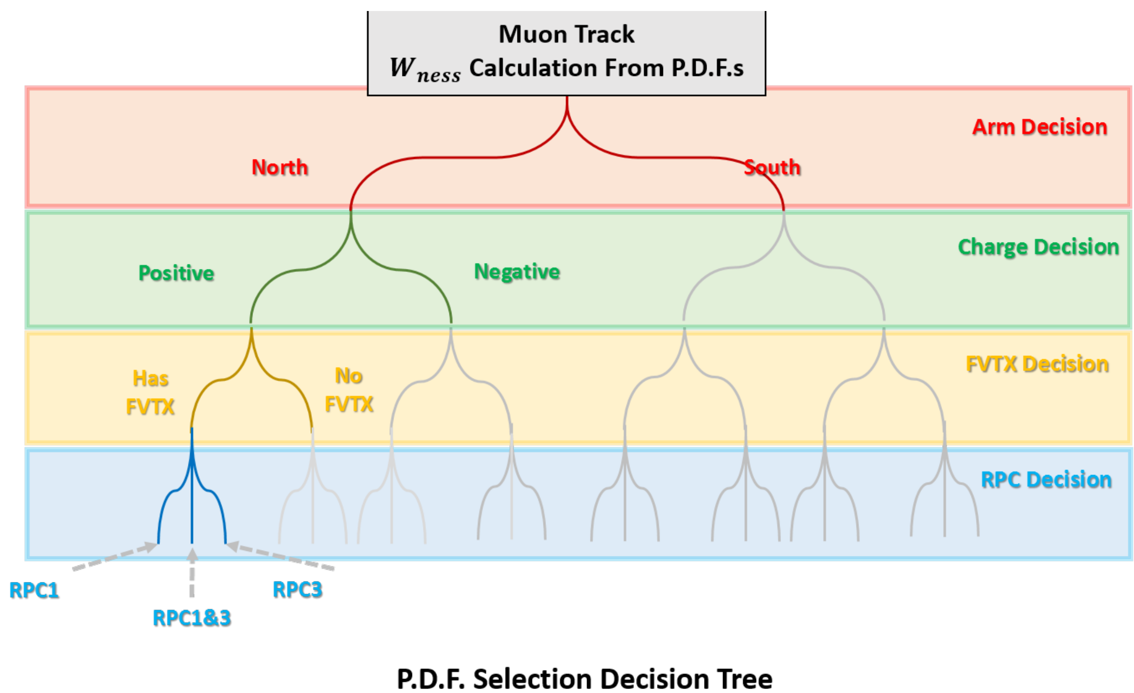

Figure 7.4: A cartoon of the decision tree to determine the PDF cocktail to use for quantifying the W_{ness} of a given track. The track's properties are used to traverse the tree, and select the cocktail contents.

In figures 7.5-7.10, we can see the various distributions which are used to create probability distribution functions. In the figures, we represent the product of all probability

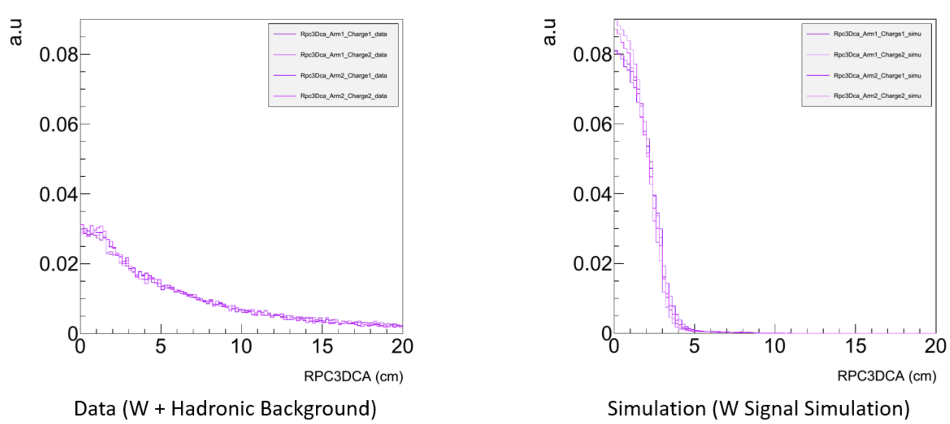

$$\lambda = p(DG0, DDG0)p(\chi^2)p(DCA_r)p(Rpc1/3dca)p(fvtx_{dr})p(fvtx_{d\theta})p(fvtx_{d\phi})$$

Figure 7.5: Left: the distribution of Rpc3dca for each arm and charge, produced from the PHENIX data set, after the basic cut. Right: the same distributions from a simulation of the W-Signal.

functions which are used to tag an event as λ such that $\lambda = \Pi_k \mathcal{P}(\mu|C_k)$.

Now that we have a complete set of probability density functions which predict the likelihood that a given track is a W-genic muon or not, we can loop over the real physics data set, and use our likelihood calculation strategy to label every muon track with a W_{ness}. We may also tag our simulated data set with W_{ness}. The distributions are shown in Figure 7.11.

As we can see from Figure 7.11, most of the simulated data falls in the high W_{ness} range while most of the physics data falls in the low W_{ness} range. The goal of the likelihood analysis is to tag the data with W_{ness} such that we can apply a cut on the data based on the parameter's value. We wish to apply the cut in a way that minimally removes any signal, and we may calculate the efficiency of this cut, summarized in Figure 7.12.

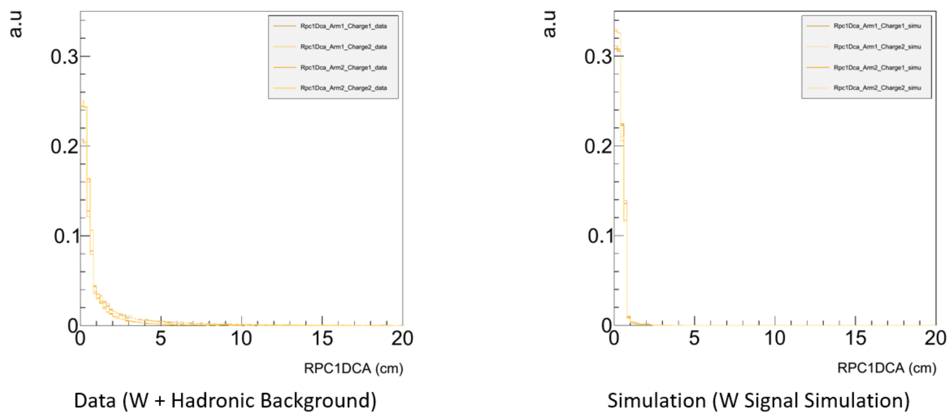

$$\lambda = p(DG0, DDG0)p(\chi^2)p(DCA_r)p(Rpc1/3dca)p(fvtx_{dr})p(fvtx_{d\theta})p(fvtx_{d\phi})$$

Figure 7.6: Left: the distribution of Rpc1dca for each arm and charge, produced from the PHENIX data set, after the basic cut. Right: the same distributions from a simulation of the W-Signal.

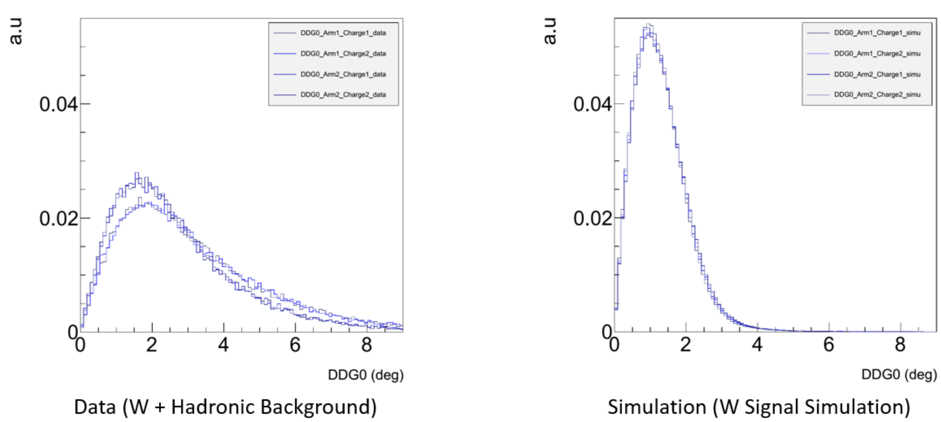

$$\lambda = p(DG0, DDG0)p(\chi^2)p(DCA_r)p(Rpc1/3dca)p(fvtx_{dr})p(fvtx_{d\theta})p(fvtx_{d\phi})$$

Figure 7.7: Left: the distribution of DDG0 for each arm and charge, produced from the PHENIX data set, after the basic cut. Right: the same distributions from a simulation of the W-Signal.

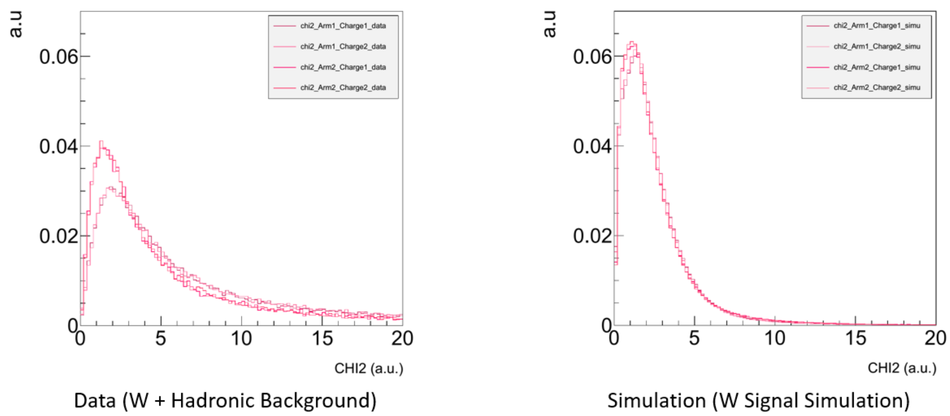

$$\lambda = p(DG0, DDG0)p(\chi^2)p(DCA_r)p(Rpc1/3dca)p(fvtx_{dr})p(fvtx_{d\theta})p\big(fvtx_{d\phi}\big)$$

Figure 7.8: Left: the distribution of χ^2 for each arm and charge, produced from the PHENIX data set, after the basic cut. Right: the same distributions from a simulation of the W-Signal.

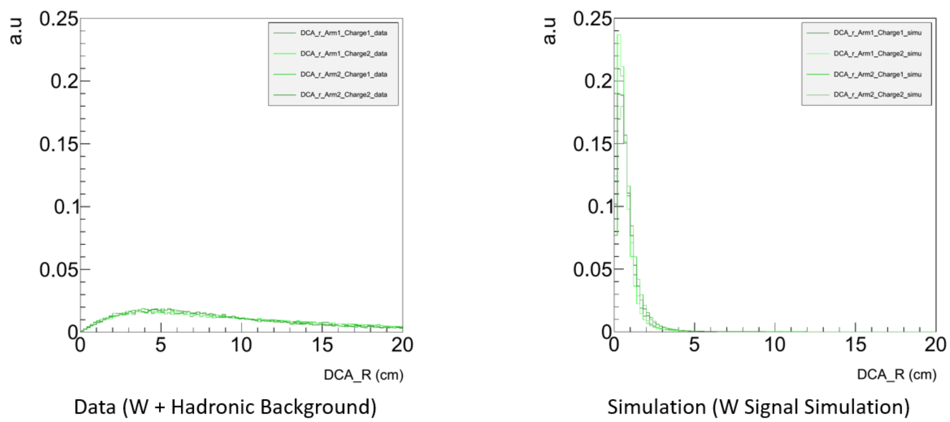

$$\lambda = p(DG0, DDG0)p(\chi^2)p(DCA_r)p(Rpc1/3dca)p(fvtx_{dr})p(fvtx_{d\theta})p\big(fvtx_{d\phi}\big)$$

Figure 7.9: Left: the distribution of DCA$_r$ for each arm and charge, produced from the PHENIX data set, after the basic cut. Right: the same distributions from a simulation of the W-Signal.

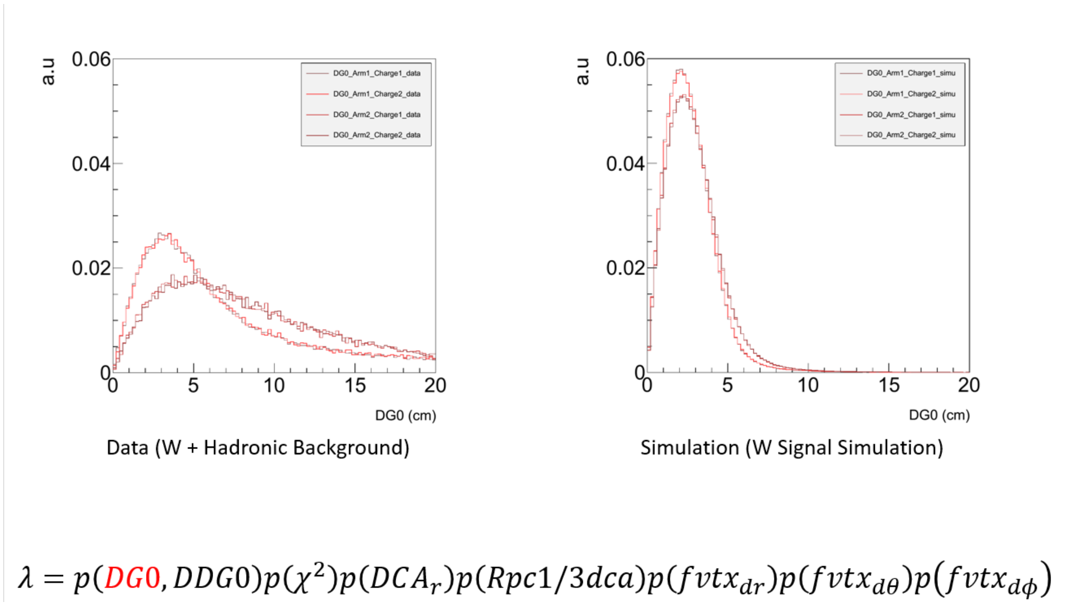

Figure 7.10: Left: the distribution of DG0 for each arm and charge, produced from the PHENIX data set, after the basic cut. Right: the same distributions from a simulation of the W-Signal.

As we make successive cuts in W_{ness}, we find that the optimum cutoff is at $W_{ness} < 0.95$. We can throw out all data below this threshold, and maintain a good portion of our signal data.

Note that now with this reduced data set, we could simply assume that all remaining data is signal, and calculate an asymmetry, however, there is clearly still a lot of background present. Any background that is still present will dilute our main observable, A_L. Therefore, we employ the unbinned maximum likelihood fit to a three dimensional data set, composed of W_{ness}, η, and dw_{23}.

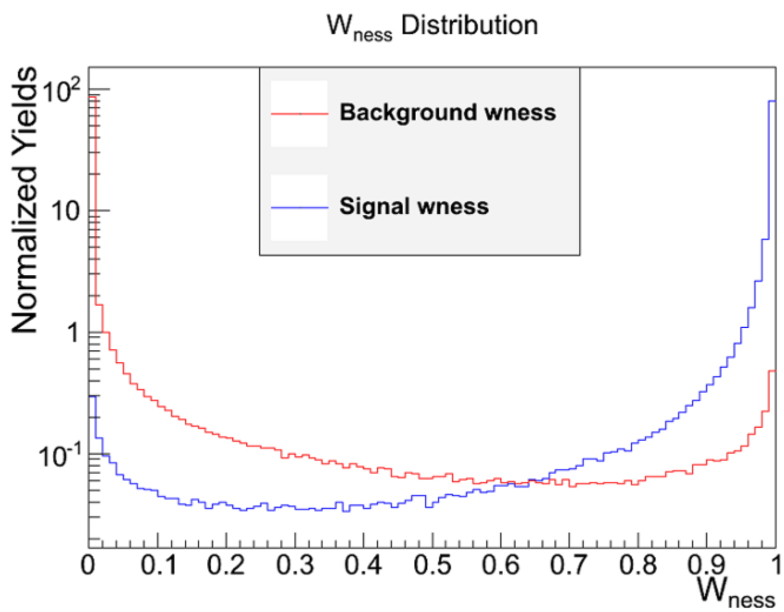

Figure 7.11: After W_{ness} tagging, we can visualize the classification of signal from background by comparing the distribution of W_{ness} in physics data, and the simulated data data. Note that the vertical is plotted on a log scale. The two distributions have been normalized prior to plotting.

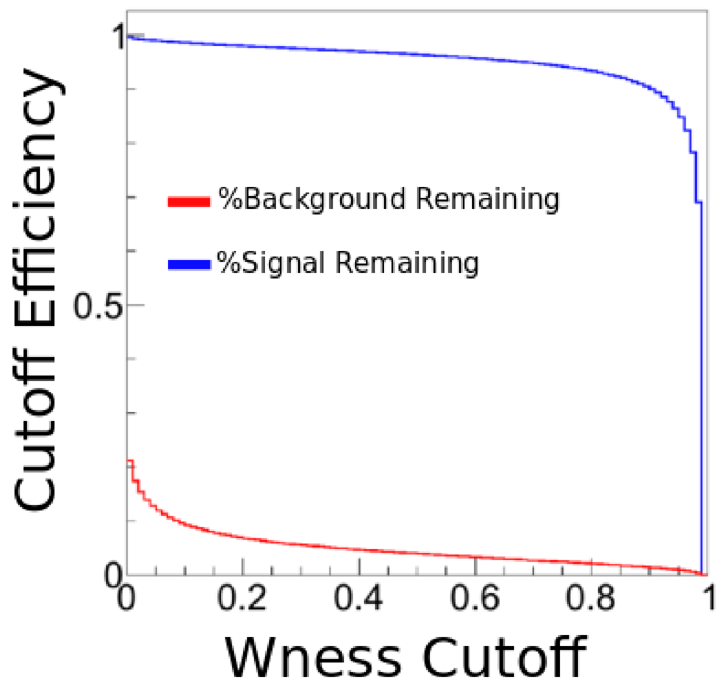

Figure 7.12: We look at the fraction of signal and background remaining in the total data set as we make successively higher cuts in W_{ness}. At the turning point of the blue distribution (the fraction of remaining signal) is where we choose to cut the data, corresponding to removing data with a W_{ness} value of less than 0.95.

7.4 Extended Unbinned Maximum Likelihood Selection: The Signal to Background Ratio

The goal of the Extended Unbinned Maximum Likelihood Fit (EULMF) is to calculate the signal to background ratio, so that we can calculate A_L and correct for the dilution from the background. The EULMF is another statistical method which relies on creating Probability Density Functions to represent the likelihood of given track to originate from a known source. However, at this stage in the analysis, we are interested in subdividing the background data set into contributions from the Hadronic Background and the Muon Background. We form our PDFs for the Muon Background by weighting the various individual muon processes and adding them together such that the relative frequencies of each process are comparable to the composition of the real physics data set. In broad strokes, we want to generate PDFs in the dimension of η and dw_{23} for Hadronic Background, Muon Background, and W-Signal distributions. However, since we will be applying this fit to a data set where we have applied a W_{ness} cut, we must be very careful to not over or under-fit the hadronic background.

In order to accomplish this, we parameterize the data set as a 2D function in dw_{23} and W_{ness}. We then fit this distribution, generated from the physics data, with a parameterization, over the nominal hadronic background dominated region from $0 < W_{ness} < 0.95$. We then extrapolate the shape of dw_{23} into the high $W_{ness} > 0.95$ region, hereafter referred to as the 'signal region', with $W_{ness} < 0.95$ referred to as the 'background region'.

Similarly to any analysis which uses probability density functions, the PDFs representing η and dw_{23} must be uncorrelated so as to not over-fit the data.

The purpose of the EULMF is to essentially scale the PDFs for each arm and charge for η and dw_{23} so as to obtain yields for W-genic muons, Muon Background muons, and hadronic background fake muons.

To use this method, we must construct the likelihood function (Equation 7.5) and maximize it. We write down the likelihood function in as a product of the individual likelihoods:

An unbinned maximum likelihood fit can then be performed to extract the number of events for each process: n_{sig}, n_{μ}, n_{had}. The likelihood function is defined accounting for a Poisson distribution of the events x_i:

$$\mathcal{L}(\theta|X) \equiv \frac{n^N e^{-n}}{N!} \prod_{x_i \in X}^{N} \sum_c \frac{n_c}{n} p_c(x_i), \ ;\text{with}\, n = \sum_c n_c \tag{7.5}$$

where X is the sample of N total events $x_i = (\eta_i, dw_{23i})$, and θ gives the parameters of the fit $\theta = (n_{sig}, n_\mu, n_{had})$. To reduce the number of parameters, we fixed the number of muon background events n_μ to the expected yield according to the cross section of muon background processes, and then we extracted the remaining parameters (n_{sig}, n_{had}) by minimizing the $-\log(\mathcal{L}(\theta|X))$. With Run 13 data we have enough statistics to divide the data sample in three η region: $1.10 < \eta < 1.40$, $1.40 < \eta < 1.80$ and $1.80 < \eta < 2.60$.

7.4.1 Hadronic Background PDFs

The main analysis challenge for the EULMF is obtaining an adequate description of the dw_{23} and η distributions for the hadronic background. They are shown, along with the W_{ness} distribution for the data, for the background region, in Figure 7.13, and the simulated W-genic data in Figure 7.14.

Two features to note from Figure 7.13 and Figure 7.14 is that the distribution for dw_{23} should be expected to be quite narrow for W-genic events, whereas η is more broad. We have good statistic for η over all orders of magnitude, so we can directly construct PDFs for this variable from a binned dataset. However, with dw_{23} we need to be more careful, as this variable will offer us the analyzing power.

We create a model for dw_{23}, to fully parameterize the event distribution when viewed as a function of dw_{23} vs W_{ness}. We model this by assuming that the dw_{23} vs W_{ness} distribution can be separated into two parts:

$$F(W_{ness}, dw_{23}) = f(W_{ness}) \times g(W_{ness}, dw_{23}) \tag{7.6}$$

$f(W_{ness})$ is modeled simply as a fourth-degree polynomial (the third column) of Figures 7.13 and 7.14. The polynomial fit is summarized in Equation 7.7 and Figure 7.15:

$$f(W_{ness}) = P_8 + P_9 W_{ness} + P_{10} {W_{ness}}^2 + P_{11} + {W_{ness}}^3 + P_{12} + {W_{ness}}^4 \tag{7.7}$$

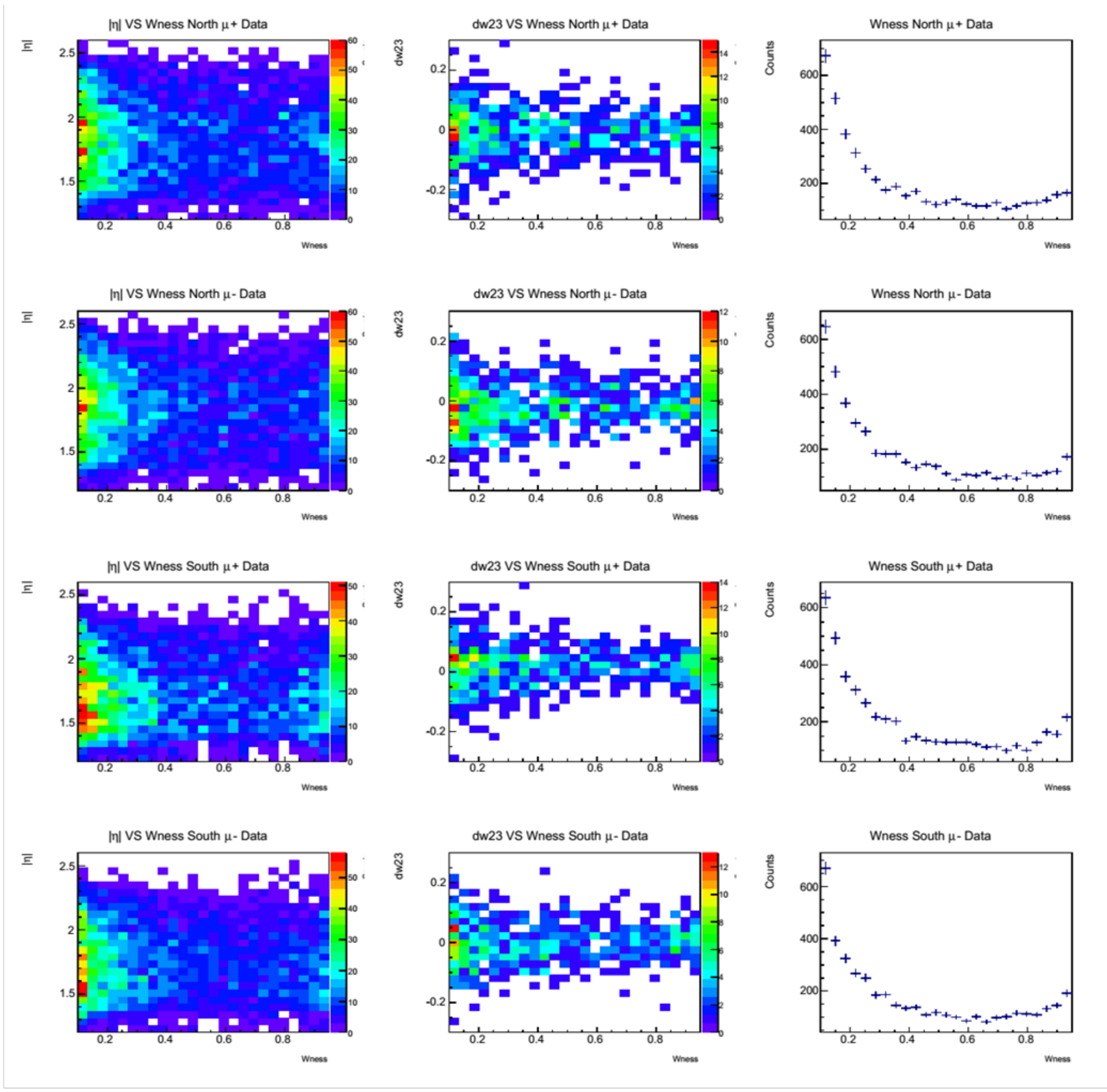

Figure 7.13: The first column of plots is η plotted as a function of W_{ness} where we see a 2D histogram of the even distribution. The middle column is dw_{23} as a function of W_{ness}, and the right column is a simple histogram of W_{ness}. The rows all correspond to the same arm and charge. From top to bottom: North, $\mu+$, North $\mu-$, South $\mu+$, North $\mu-$. Distributions shown here are all from the physics data set.

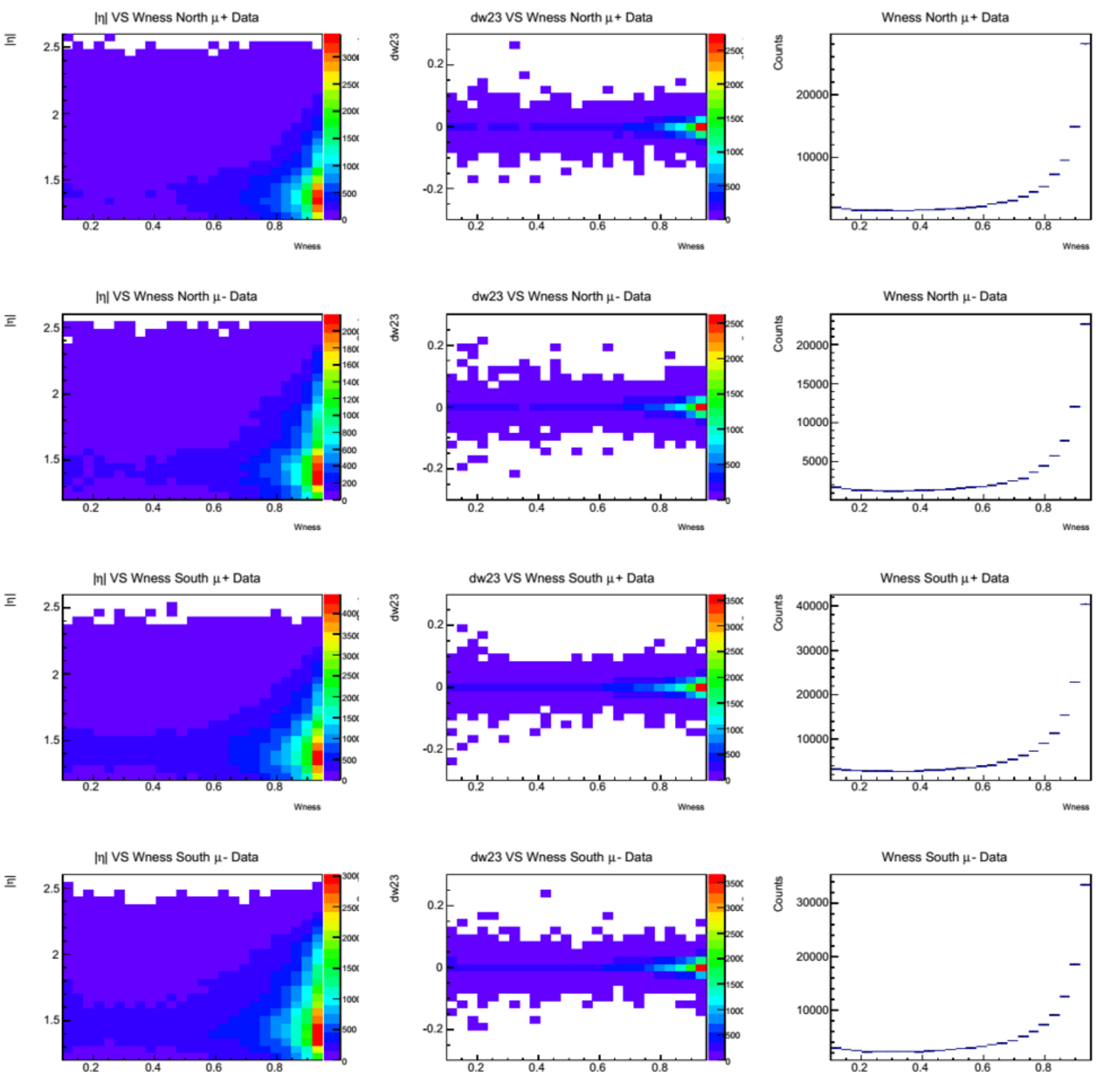

Figure 7.14: The first column of plots is η plotted as a function of W_{ness} where we see a 2D histogram of the even distribution. The middle column is dw_{23} as a function of W_{ness}, and the right column is a simple histogram of W_{ness}. The rows all correspond to the same arm and charge. From top to bottom: North, $\mu+$, North $\mu-$, South $\mu+$, North $\mu-$. Distributions shown here are all from simulated W-genic data set.

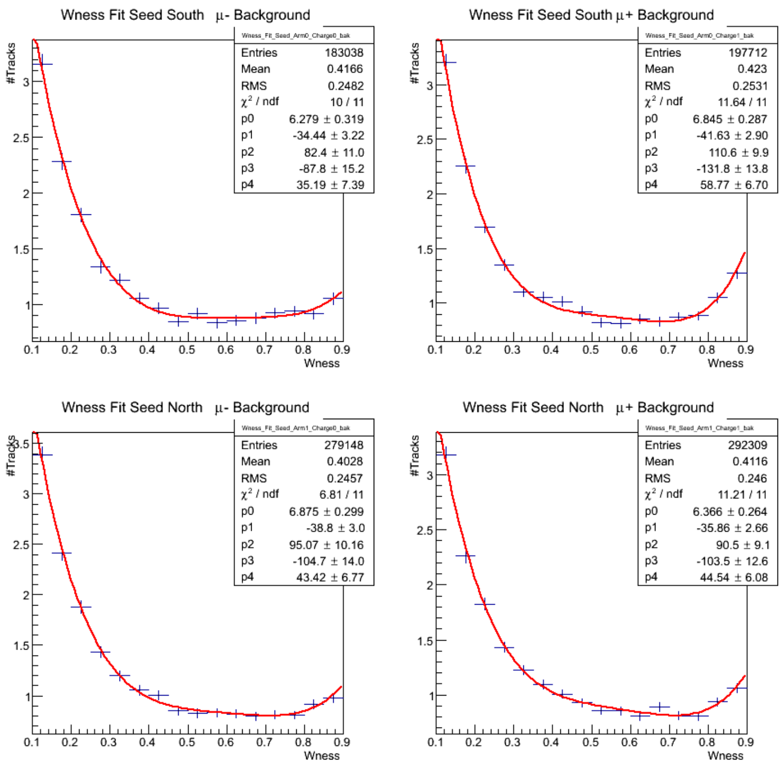

Figure 7.15: A summary of the fourth degree polynomial fit (Equation 7.7) to the W_{ness} distribution from the physics dataset in the background region.

We then model the other element of the distribution $g(W_{ness}, dw_{23}$ as a co-axial double Gaussian. We allow the Parameters of the co-axial double Gaussian to vary linearly with W_{ness}, as seen below:

$$\sigma_1 = P_1 + P_3 \times W_{ness} \qquad C_g = P_6 + P_7 \times W_{ness} \tag{7.8}$$

$$\sigma_2 = P_4 + P_5 \times W_{ness} \qquad \mu = P_0 + P_1 \times W_{ness} \tag{7.9}$$

$$g(W_{ness}, dw_{23}) = C_w \times \left(\left(\frac{1}{\sqrt{2\pi}\sigma_1 + C_g\sqrt{2\pi}\sigma_2} \right) \times \left(e^{\frac{1}{2}\left(\frac{dw_{23}-\mu}{\sigma_1}\right)^2} + C_g e^{\frac{1}{2}\left(\frac{dw_{23}-\mu}{\sigma_2}\right)^2} \right) \right) \tag{7.10}$$

We seed these linearized parameters by taking slices of dw_{23} in W_{ness} and then fitting this slice with a co-axial double Gaussian. The parameters of the results of these fits are then plotted against the value of the W_{ness} slice, and fit with a line. These parameters are then used to seed the fit of Equation 7.6 to the physics data set. Fits to the individual slices of dw_{23} are summarized in Figure 7.16. The results of the co-axial double Gaussian parameters as functions of W_{ness} slice are shown in Figure 7.17.

The results of this fitting procedure are summarized in Figure 7.18.

Finally, the extrapolation of dw_{23} was reproduced independently by four separate analyzers, Daniel, Abraham, Ralf and Myself, with distributions lining up very closely, Figure 7.20

The PDF for η was obtained by creating a histogram of the variable for events tagged with $W_{ness} < 0.9$.

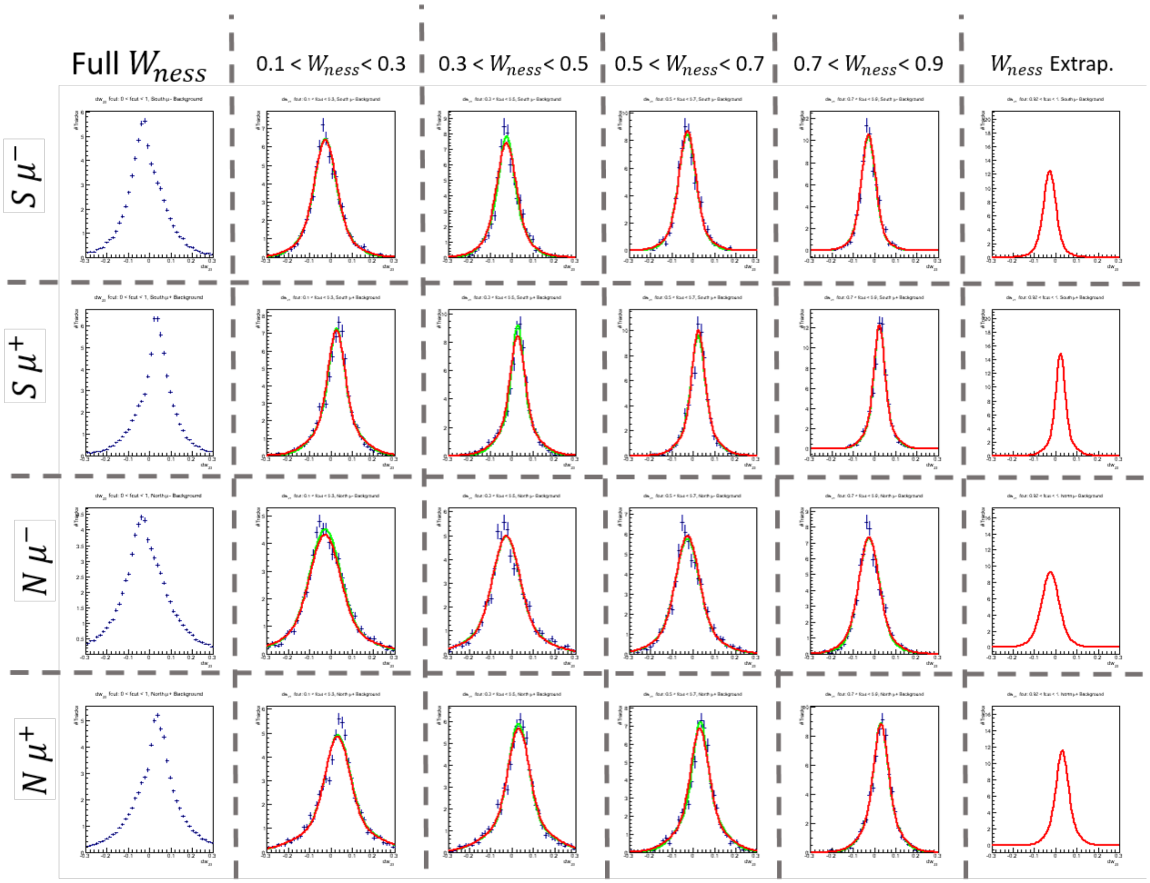

Figure 7.16: From left to right the columns are: dw_{23} for the full W_{ness} range, $0.1 < W_{ness} < 0.3$, $0.3 < W_{ness} < 0.7$, $0.3 < W_{ness} < 0.7$, $0.7 < W_{ness} < 0.9$, and finally the extrapolated shape for $W_{ness} > 0.95$. In red, we see the 1D projection of the 2D distribution to the slice. This overlays a green curve, which is a fit done independently to a slice. The rows are labeled with the Arm and charge corresponding to the subdivided dataset. As you can see, the matching is often exact, between green and red curves. As the final column is the extrapolation, there is no slice-fit.

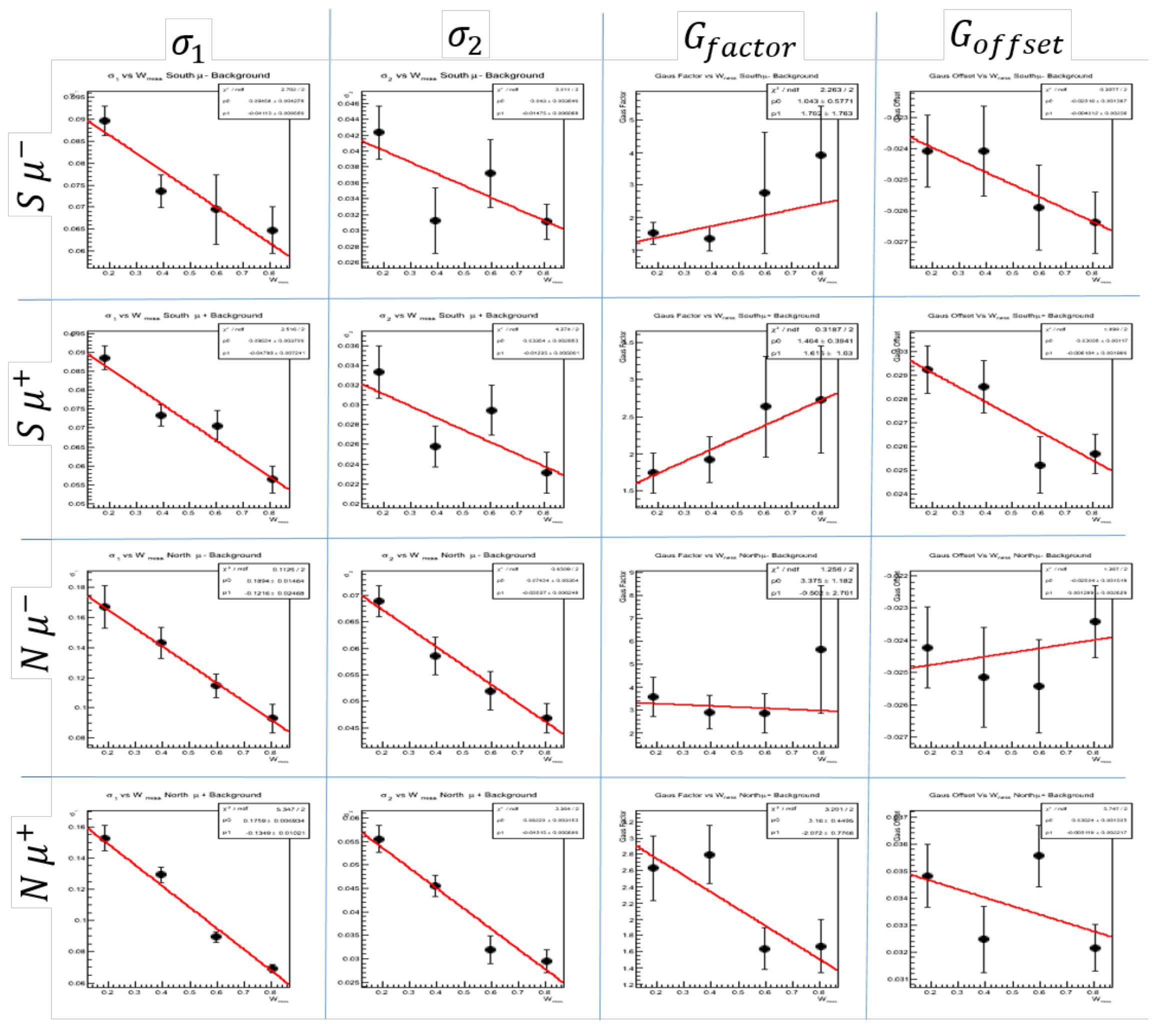

Figure 7.17: The four parameters from the co-axial Gaussian parameterization of dw_{23} as a function of W_{ness}. Though some parameters (G_{factor}, $N\mu-$) may appear to be non-linear, note that the uncertainty on some bins is quite large. Rows are arm/charge, labeled on the left, while columns are co-axial Gaussian parameters, summarized in Equation 7.10

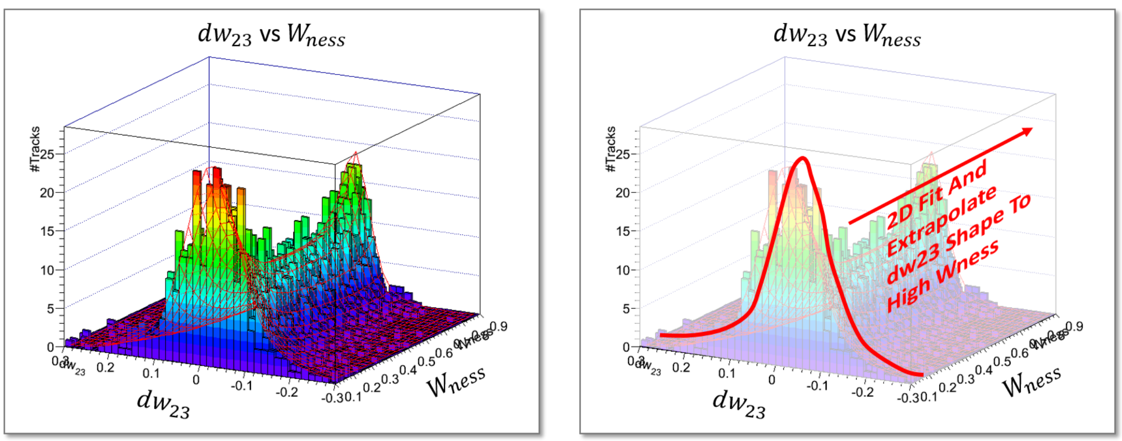

(a) The final fit to dw_{23} vs W_{ness}

(b) Cartoon of the extrapolation

Figure 7.18: The red wire-frame is the resultant fit of to the dw_{23} vs W_{ness} distribution. We extrapolate the shape of dw_{23} to the signal region to obtain the hadronic background PDF for dw_{23}.

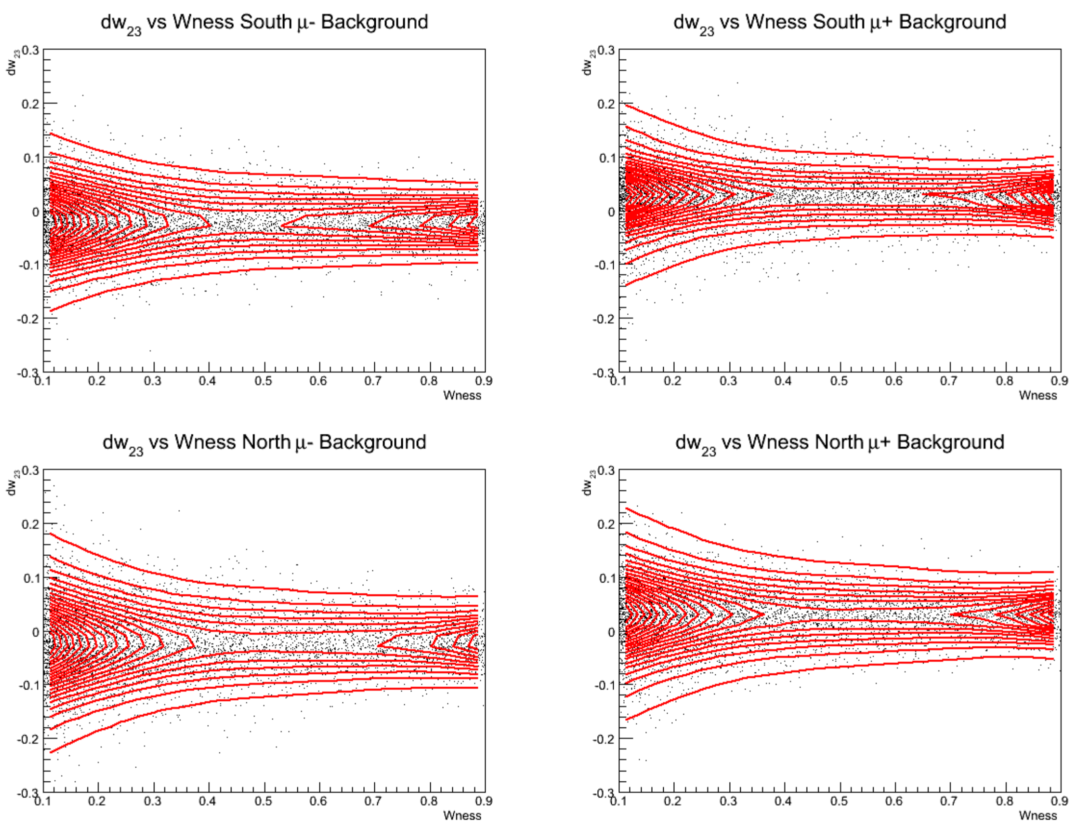

Figure 7.19: An overhead view of the various results of the dw_{23} vs W_{ness} fit for each arm and charge combination.

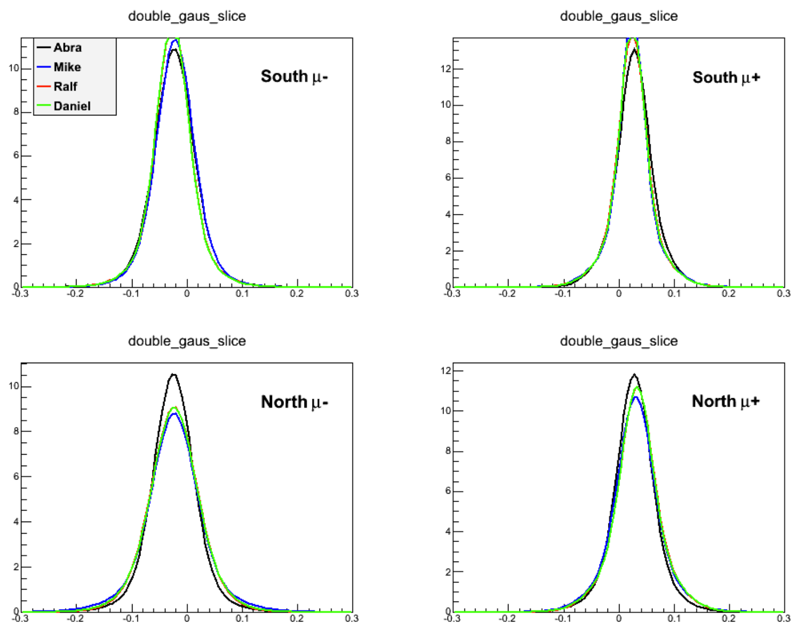

Figure 7.20: Abraham, Mike, Ralf and Daniel all independently parameterized and extrapolated dw_{23} obtaining consistent results. Figure prepared by Dr. Francesca Giordano [29]

7.4.2 Muon Background and W-Signal PDFs

The muon background probability density functions and the W-Signal probability density functions must be carefully summed from simulations so as to match the likely composition of the data set. This is done by using the well known cross-section of each of the processes which are simulated and normalizing with the integrated luminosity delivered to PHENIX during the 2013 run of RHIC. This luminosity was found to be $277pb^{-1}$.

One caveat is that the minimum bias trigger of PHENIX is easily fooled by effects such as pile-up and multiple collisions. Concretely, this occurs when there is more than one collision in a single bunch crossing. This is typically not a problem when PHENIX operates at lower energies and beam luminosities, but for this data set, it was a real factor, that must be corrected for, else all the ingredients in the muon background cocktail will be present in the wrong amounts and we'll get the wrong answer from using them. Pile up refers to the process where some events aren't read out quickly enough, and so one recorded event will contain information for two actual beam crossings. Unaccounted for, pile-up and multiple collisions both have the affect of lowering the measured luminosity.

The $277pb^{-1}$ luminosity figure has been corrected for pile-up and multiple collisions. This is a separate analysis, done by my colleagues working on this analysis, so it will not be described in detail in this thesis, however it is described in detail in our analysis note: [29].

Finally, the PDFs used in the EULMF are shown in Figures 7.21-7.24.

With all PDFs prepared, we can perform the extended unbinned maximum likelihood fit, and extract the yields for the number of signal muons, and the number of fake hadronic background muons (recalling that the number of muon background muons are fixed).

The signal to background ratio extraction is summarized by each analyzer in Table 7.5, for the South Arm $\mu-$ (the canonical cross check).

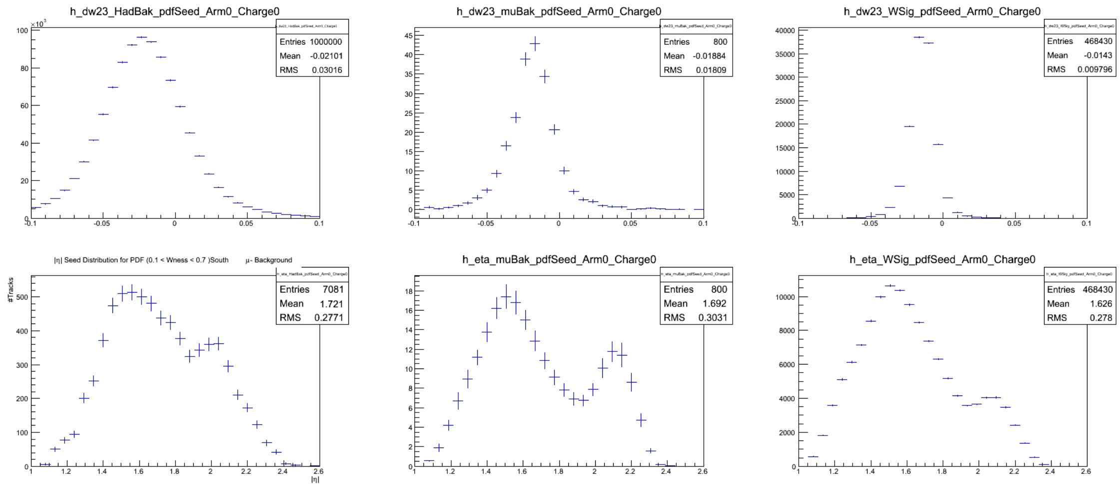

Figure 7.21: Left Column: The hadronic background PDFs, Middle Column: The Summed Muon Background PDFs, Right Column: The W-Signal PDF. For South Arm, $mu+$

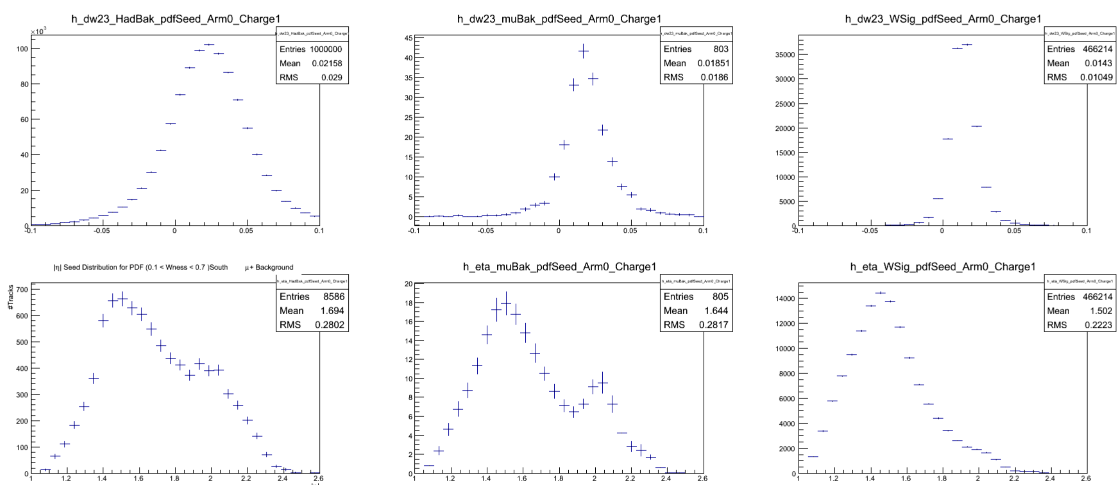

Figure 7.22: Left Column: The hadronic background PDFs, Middle Column: The Summed Muon Background PDFs, Right Column: The W-Signal PDF. For South Arm, $mu-$

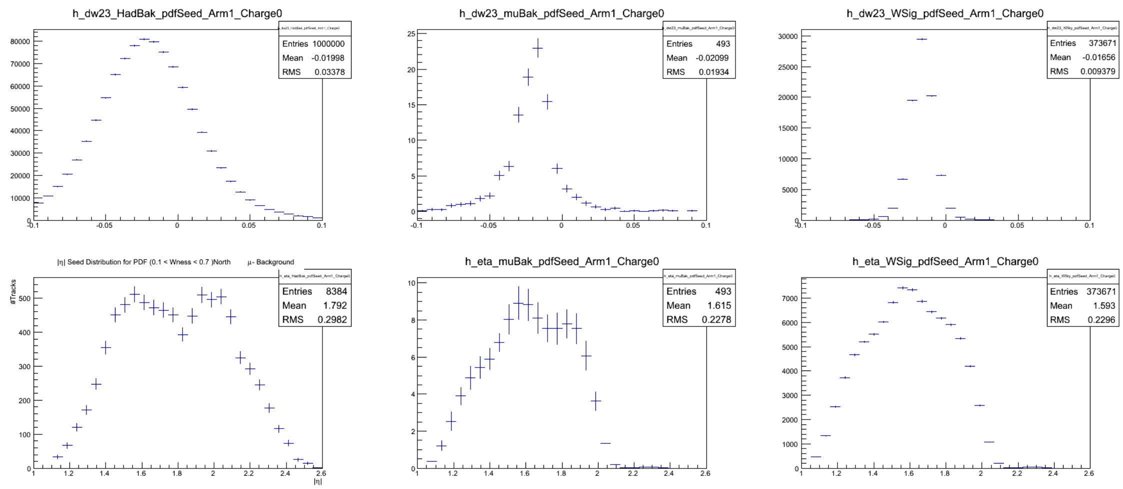

Figure 7.23: Left Column: The hadronic background PDFs, Middle Column: The Summed Muon Background PDFs, Right Column: The W-Signal PDF. For North Arm, $mu-$

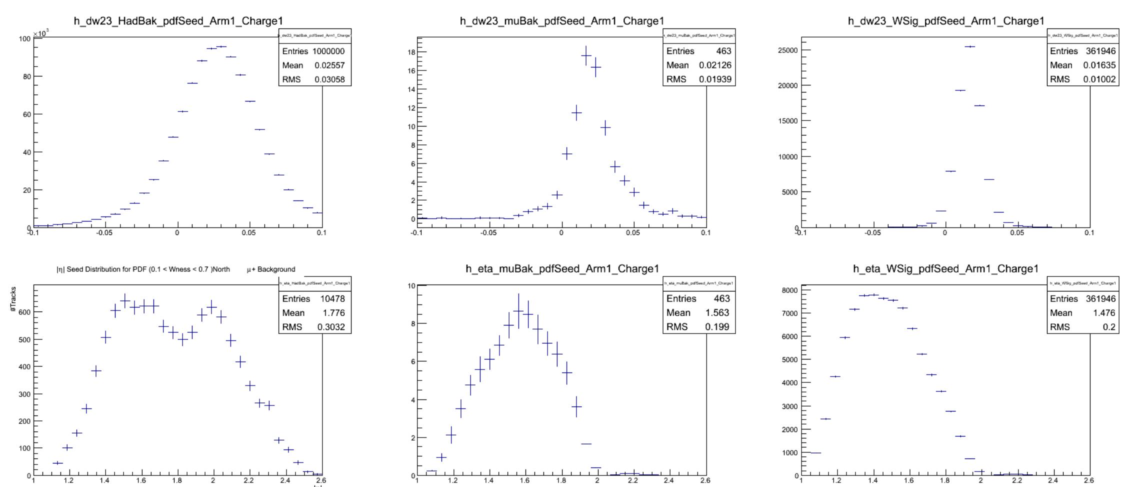

Figure 7.24: Left Column: The hadronic background PDFs, Middle Column: The Summed Muon Background PDFs, Right Column: The W-Signal PDF. For South Arm, $mu+$

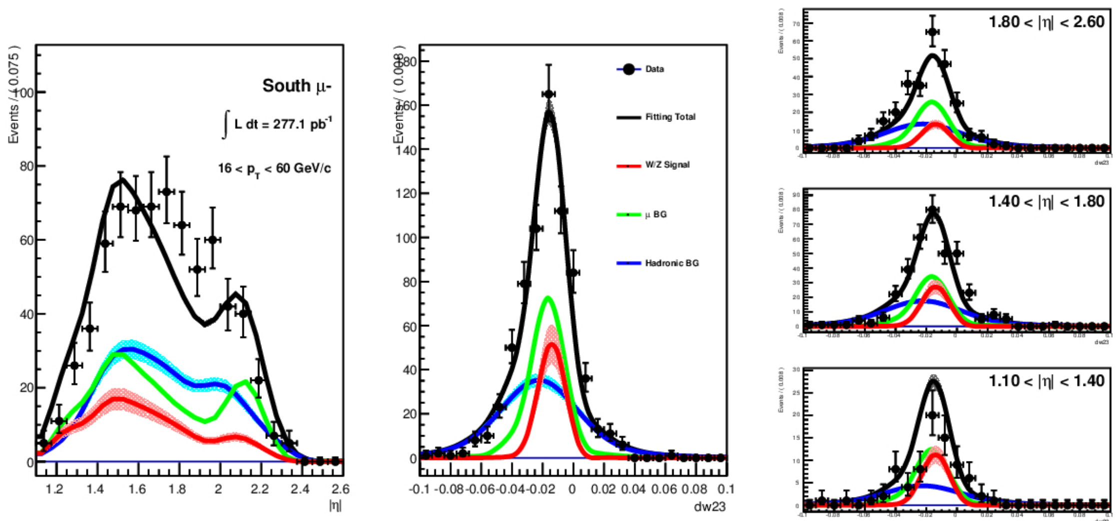

Figure 7.25: Here, we see the preliminary results of the EULMF for the 2013 Run. On the left, η is shown. In the middle, dw_{23}. On the right, dw_{23} is subdivided into the three standard η bins. In all cases, we see the unbinned data in black (with error bars), and the sum of the three fits in black. In Blue, we can see the fake-muon hadronic background. In Green, the muon background. In blue, we see the W-Signal result. The area under the curves represents the yield, relative to the total. Figure prepared by Dr. Ralf Seidl [29]. Shown: South Arm, $\mu-$

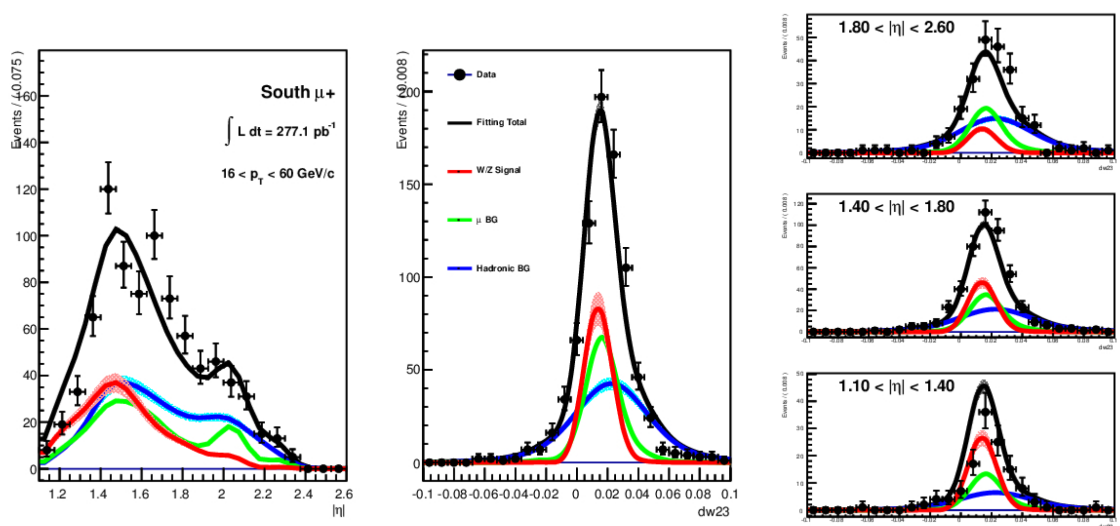

Figure 7.26: Here, we see the preliminary results of the EULMF for the 2013 Run. On the left, η is shown. In the middle, dw_{23}. On the right, dw_{23} is subdivided into the three standard η bins. In all cases, we see the unbinned data in black (with error bars), and the sum of the three fits in black. In Blue, we can see the fake-muon hadronic background. In Green, the muon background. In blue, we see the W-Signal result. The area under the curves represents the yield, relative to the total. Figure prepared by Dr. Ralf Seidl [29]. Shown: South Arm, $\mu+$

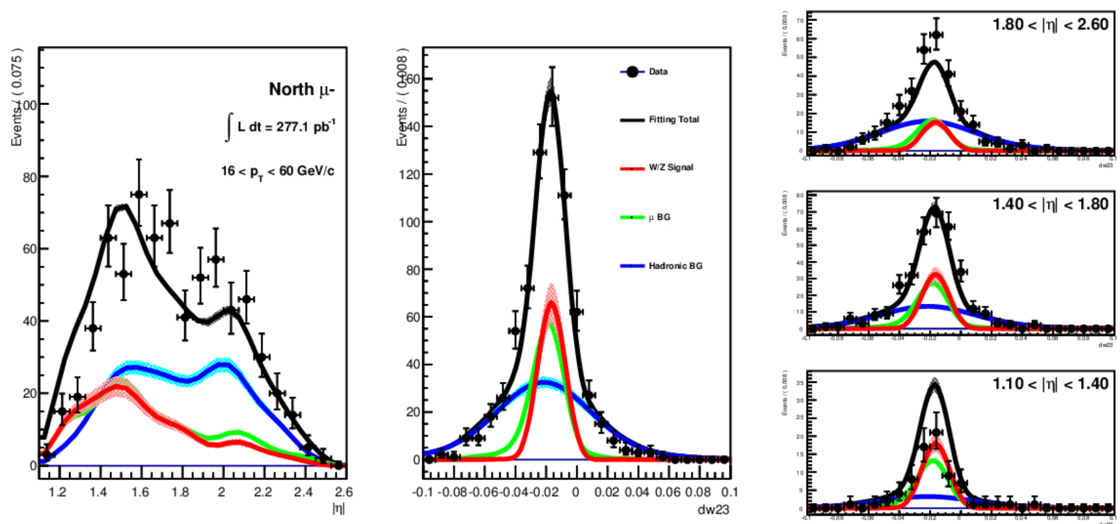

Figure 7.27: Here, we see the preliminary results of the EULMF for the 2013 Run. On the left, η is shown. In the middle, dw_{23}. On the right, dw_{23} is subdivided into the three standard η bins. In all cases, we see the unbinned data in black (with error bars), and the sum of the three fits in black. In Blue, we can see the fake-muon hadronic background. In Green, the muon background. In blue, we see the W-Signal result. The area under the curves represents the yield, relative to the total. Figure prepared by Dr. Ralf Seidl [29]. Shown: North Arm, $\mu-$

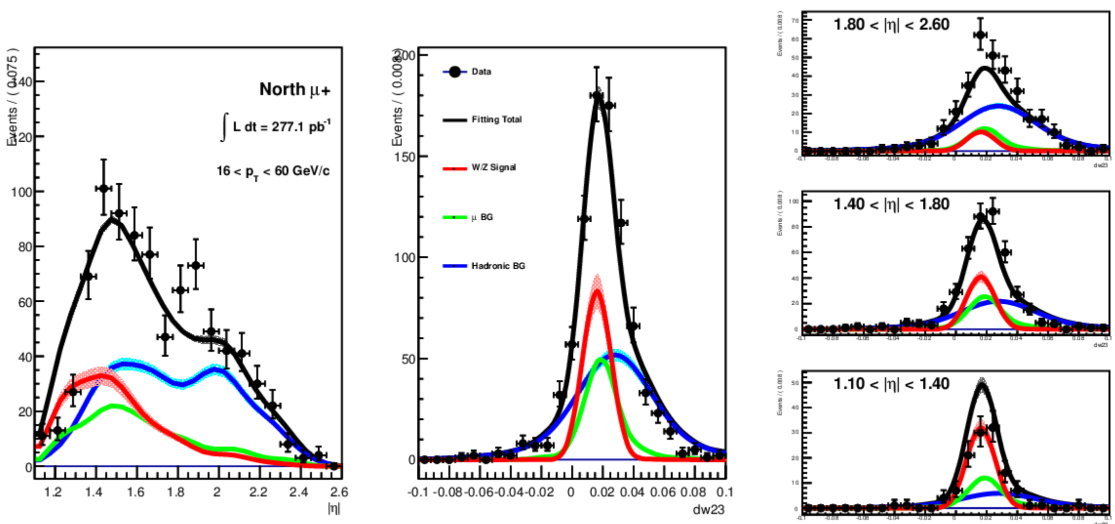

Figure 7.28: Here, we see the preliminary results of the EULMF for the 2013 Run. On the left, η is shown. In the middle, dw_{23}. On the right, dw_{23} is subdivided into the three standard η bins. In all cases, we see the unbinned data in black (with error bars), and the sum of the three fits in black. In Blue, we can see the fake-muon hadronic background. In Green, the muon background. In blue, we see the W-Signal result. The area under the curves represents the yield, relative to the total. Figure prepared by Dr. Ralf Seidl [29]. Shown: North Arm, $\mu+$

South μ^-				
Variable	**Ralf**	**Daniel**	**Mike**	**Abraham**
Total events	2032	2034	2022	2039
Signal events	$340^{+42.14}_{-41.42}$	$303^{+42.31}_{-41.59}$	$332^{+42.28}_{-41.58}$	$294^{+41.38}_{-41.38}$
Hadron events	$1424^{+53.57}_{-52.60}$	$1469^{+54.55}_{-53.59}$	$1433^{+53.97}_{-52.99}$	$1485^{+53.85}_{-53.85}$
Muon events	269	262	257	259
Signal/BG	$0.20^{+0.03}_{-0.03}$	$0.18^{+0.00}_{-0.00}$	$0.20^{+0.03}_{-0.03}$	$0.17^{+0.02}_{-0.00}$

Table 7.5: South arm $W \to \mu^-$ fit results per analyzer [29]

7.5 Systematic Tests

One of the rare advantages of this analysis was that I had the opportunity to undertake it in parallel with others, working as a team to accomplish our goals. That means that we were able perform many systematic tests. These tests are summarized in the Appendix .1, and serve to lend confidence to our extraction of the signal to background ratio.

Arm	Charge	Total Events	Signal Events	Fake Muons	Muon Background	SBR
S	$\mu-$	2023	$354^{+41.9714}_{-41.2598}$	$1448^{53.6777}_{-52.7162}$	$221^{0.212103}_{0.0263482}$	0.0258992
S	$\mu+$	2468	$498^{+44.0941}_{-43.2297}$	$1767^{57.046}_{-56.3006}$	$203^{0.252792}_{0.0238242}$	0.0233755
N	$\mu-$	2029	$370^{+34.4599}_{-33.7046}$	$1555^{48.5042}_{-47.6586}$	$104^{0.223026}_{0.0219055}$	0.0214353
N	$\mu+$	2633	$505^{+37.9628}_{-37.2192}$	$2043^{54.5676}_{-53.7571}$	$85^{0.237312}_{0.0189323}$	0.0185715

Table 7.6: A summary table from the results of the EULMF to the unbinned data set, summed to one η bin per arm and charge.

Chapter 8

Spin Analysis

8.1 Overview

The overall goal of this analysis is to arrive at a calculation of our observable, A_L. As discussed in Chapter 3, A_L is an important probe for the polarized parton distribution functions describing the quarks and anti-quarks of the proton sea-quark population. There is nothing magical about A_L–it just so happens that when we construct the asymmetry, using the cross-sections for a particular process, those cross-sections can be written in two ways:

1. Write it in terms of the machine luminosity and the number of events of a particular type observed
2. Calculate the scattering amplitude for the process, and then the cross-section of the process. Write down the cross-section in terms of experimental observables.

Thus, our strategy is clear–we have several well established theoretical frameworks with a number of degrees of freedom (i.e. item 2), so as experimentalists, we contribute by measuring the cross-section of the $W \rightarrow \mu$ process, and calculating the observable via the strategy in item 1, which is then fed back into the models in order to reduce the degrees of fr and arrive at a more correct model. These models are typically expressed as global QCD fits to world data over a wide kinematic range, and our contribution from PHENIX will help constrain the models, therefore giving a more accurate prediction of how much proton spin we can attribute to coming from the sea-quark polarization.

The Spin Analysis is very much 'turning the crank', we have already done the hard part of the analysis in Chapter 7 and Chapter 6. Lets not neglect too, the monumental task of building a RHIC and a PHENIX. The fact that particle physics can even be done in the first place, is absolutely astounding to me–the amount of infrastructure, technical expertise, collaboration, financial and intellectual capital needed to build such an enormous and precise machine is something that is very difficult to communicate. So, assuming that the other parts of this massive undertaking have been pulled off without a hitch, the actual machinery of the Spin Analysis only relies on three items:

1. What is the total beam polarization?
2. What is the polarization of the blue bunch, and yellow bunch at the time of each beam-beam interaction which generated a W-genic muon?
3. What is the total yield of μ's at forward and backward rapidity, for positive and negative charge?

A_L is then calculated:

$$A_L = \frac{d\sigma^{\Rightarrow} - d\sigma^{\Leftarrow}}{d\sigma^{\Rightarrow} + d\sigma^{\Leftarrow}} \tag{8.1}$$

Where $d\sigma$ is experimentally calculated as:

$$\sigma = \frac{1}{\mathcal{L}}\dot{N} \tag{8.2}$$

With $\Rightarrow$ or $\Leftarrow$ referring to tracks which come from positive($\Rightarrow$) or negative($\Leftarrow$) helicities relative to the initial proton polarization state. $\mathcal{L}$ refers to the beam luminosity, a property of the colliding beams, and $\dot{N}$ refers to the production rate of W-genic muons. Naturally, this calculation is done for forward and backward rapidities for positive and negative charges. Since we can measure $W \to \mu$ for $W+$ or $W-$ at forward or backward rapidities, we treat everything separately, and combine forward and backward rapidity data to get the final answer for A_L^{W+} and A_L^{W-} at forward, and backward rapidity.

In practice, we do not calculate cross-sections for $W \to \mu$ for the purposes of evaluating A_L, as we really only need the yields, since in principal $\mathcal{L}$ will be a common factor in all cross-sections and cancel out. This of course comes with major caveats–$\mathcal{L}$ only cancels out if the relative luminosity of each polarization condition is the same–spin patterns are chosen so that in theory, this happens. This of course is checked. Experimentally, we construct raw asymmetries (simple differences/sums) of the relevant muon yields (ϵ_L), and correct the overall raw asymmetry for less than 100% beam polarization and the dilution from the signal-to-background ratio.

8.2 Measured Beam Polarization

Formally, we obtain the beam polarization from the p-Carbon scattering experiments done every fill, and spin database QA. The polarization of the beams for each fill are measured at the beginning and end of every fill. This was described in Section 4.3. The results of the polarization study and spin database QA are all stored in a PostgreSQL database, indexed by run number (multiple runs are taken in each fill).

The polarization of the blue and yellow beams over the Run 13 run are summarized in Figure 8.1.

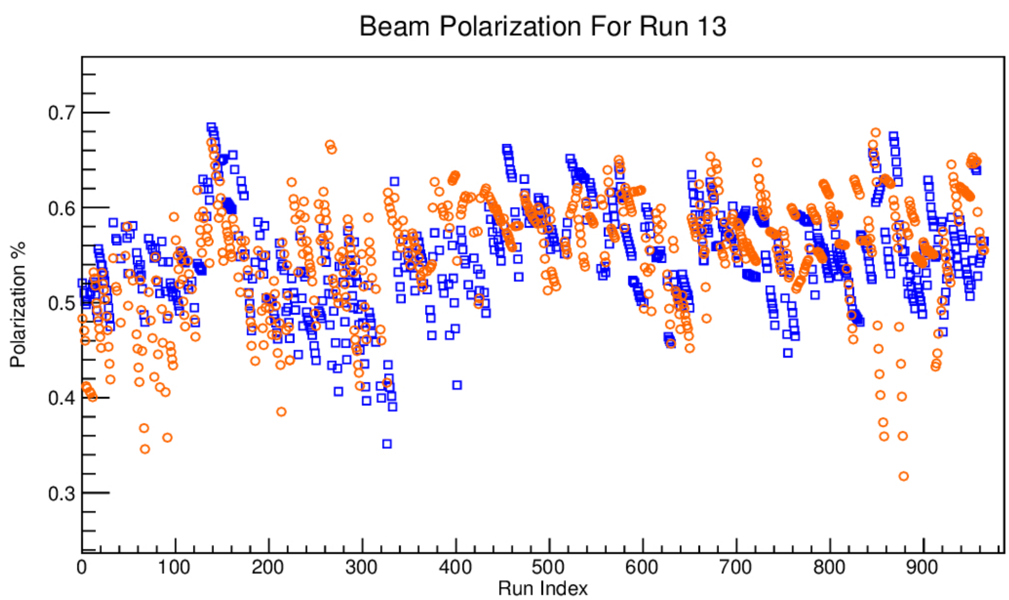

Figure 8.1: Shown: the average beam polarization per run over the course of the 2013 data set. All of the runs in the analysis were indexed from 0 to approximately 1000, and plotted in the order that they were taken. The blue open circles are from the blue beam, the yellow open circles are for the yellow beam.

The polarization over the whole of Run 13 was well over 50% for the majority of the run, with a few poorly polarized runs. This can be accounted for, by calculating an asymmetry for every single run, and weighting that asymmetry with that run's polarization, but it was found that the result was unchanged. This kind of approach would improve things if the polarization was inconsistent, though as evident in Figure 8.1, it was relatively consistent (even improving, generally towards the end of the 2013), distributions of the polarization is summarized in Figure 8.2.

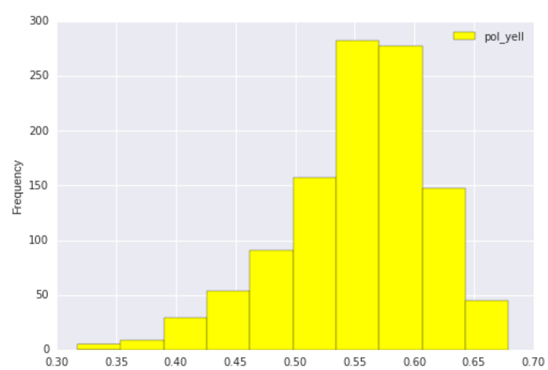

(a) Distribution of Yellow Beam Polarization

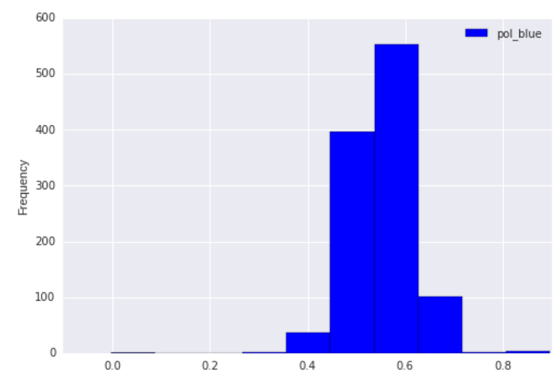

(b) Distribution of Blue Beam Polarization

Figure 8.2: The blue beam had a tighter polarization distribution, peaked at just about 50% polarization, whereas the yellow beam's polarization distribution was broader, still peaking at about 55%.

The other major element to the Spin Analysis is determining with what confidence we can assign to our understanding of the polarization pattern filled into the blue and yellow beams.

8.3 Spin Patterns

In the 2013 Run Period, I was in charge of the PHENIX spin quality assurance while the detector was actively taking data. As part of this work it was my job to maintain the monitoring software as well as confirm that physics fills were 'polarization-ready'. PHENIX uses a numbering system identify which bunch in the blue beam collides with another bunch from the yellow beam. Blue bunch "0" collides with yellow bunch "0" at the PHENIX interaction point, by definition. There are bunches in the blue, and yellow beams which are left purposefully empty, which allows us to later reconstruct and confirm which bunch is colliding with which bunch, since if a filled bunch collides with an empty bunch, we will see no collisions for that event. PHENIX has a slight delay in its triggering electronics related to the time delay between the DAQ receiving the ‘begin run’ event and the first ‘data event’. This delay is exactly five bunch-crossings in length, so when data is reconstructed, recorded bunch crossing numbers in the data stream will be off by 5. We can look at the BBC rate as a function of bunch crossing for a data set to identify, and correct this crossing-shift, which is done in the offline spin data QA.

In the 2013 data taking period, RHIC provided sixteen different bunch patterns - the patterns were varied to help avoid any kind of systematic bias towards one bunch polarization over another. For the first half of the 2013 data period, each beam had two consecutive empty bunches, and a 10-bunch long empty 'abort-gap'. The abort gap is canonically set to occur at bunch number 109-119 (indexing from 0). The consecutive empty bunches occurred at position 68 and 69 in the yellow beam, and 28 and 29 in the blue beam.

Bunch patterns P1-P8 were used in the first half of the data taking period, with P21-P28 being used in the second half of the data taking period in Run 2013. Generally, the spin patterns were defined as a sub-pattern, which is then repeated until the last bunch in a given beam is reached.

The patterns are designed to run through as many permutations of bunch-bunch polarization conditions. The beams are transversely polarized '+' is up and '-' is down during the fill, but the polarizations are rotated towards PHENIX (longitudinally) immediately before collision. Crucially, the various collision conditions need to occur with the same relative frequency–so the patterns are designed to fulfill this requirement.

Two ways of visualizing the consistency of spin patterns include Figure 8.3, which shows, for all muon tracks after the basic cut, consistent fills. Additionally, if we count the various permutations of spin patterns, i.e. ++, -+, +-, –, such that the left character is the blue polarization and the right character is the yellow polarization, we would expect to see very similar yields for each polarization combination (we do), Figure 8.4.

Given that we have seen very consistent distributions of arm/charge, we can move forward confident that there is likely no dilution effects that stem from an excess of one-

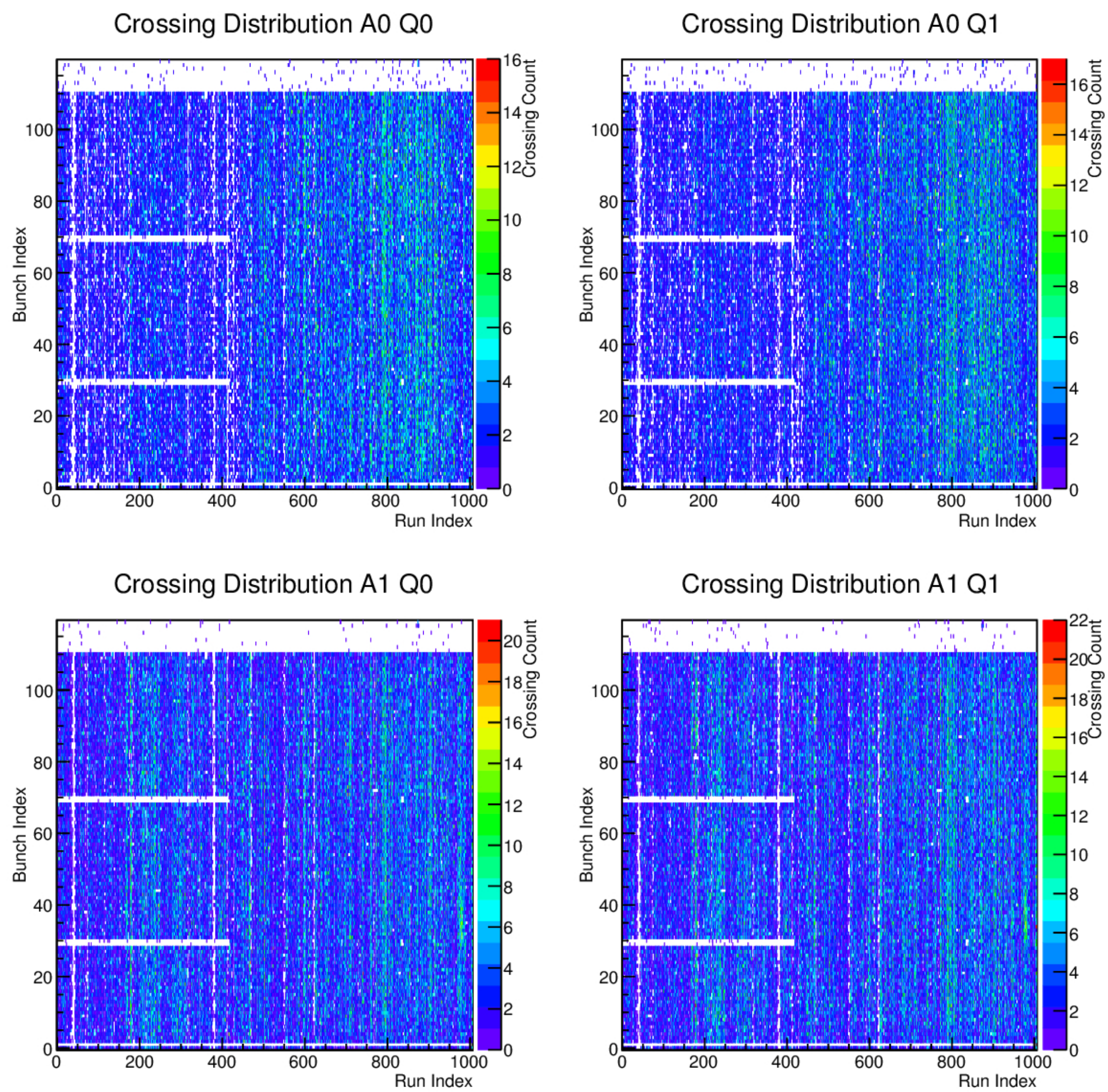

Figure 8.3: Here, we see the crossing distribution for every run taken for the 2013 data set. We use the typical code for arm/charge. The top row is for the South Arm. The bottom row is for the North Arm. The left column is for negative charge, the right column is for positive charge. Note the characteristic empty abort gap, as well as the change from 109×109 colliding bunches to 111×111 colliding bunches about 1/3 of the way through the data taking period.

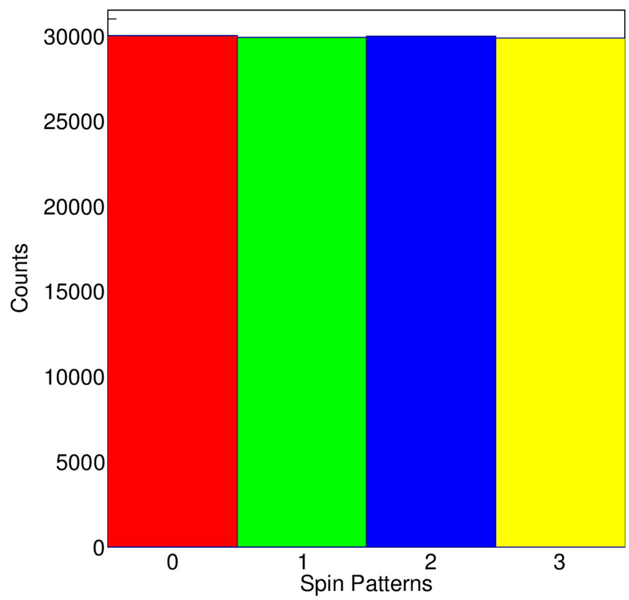

Figure 8.4: Here, we can see the yield for various crossing combinations as taken from the dataset itself, rather than the database. We see a very consistent distribution between the various possible crossing patterns. In this case, the horizontal axis is the crossing pattern code–0:++, 1:−+, 2:+−, 3:−−. Any slight difference between yields for each pattern is well below our experimental precision.

crossing pattern over another. Additionally, this is extensively studied in the yearly spin-database analysis note [73].

Pattern	Blue Pattern	Yellow Pattern
P1	$++--\ ++--\ ++--$	$++++\ ----\ ++++\ --$
P2	$--++\ --++\ --++$	$++++\ ----\ ++++\ --$
P3	$++--\ ++--\ ++--$	$----\ ++++\ ----\ ++$
P4	$--++\ --++\ --++$	$----\ ++++\ ----\ ++$
P5	$++++\ ----\ ++++\ --$	$++--\ ++--\ ++--$
P6	$++++\ ----\ ++++\ --$	$--++\ --++\ --++$
P7	$----\ ++++\ ----\ ++$	$++--\ ++--\ ++--$
P8	$----\ ++++\ ----\ ++$	$--++\ --++\ --++$
P21	$++--\ ++--\ ++--$	$--\ ++++\ ----\ ++++\ ----\ ++++$
P22	$++--\ ++--\ ++--$	$++\ ----\ ++++\ ----\ ++++\ ----$
P23	$--++\ --++\ --++$	$--\ ++++\ ----\ ++++\ ----\ ++++$
P24	$--++\ --++\ --++$	$++\ ----\ ++++\ ----\ ++++\ ----$
P25	$--\ ++++\ ----\ ++++\ ----\ ++++$	$++--\ ++--\ ++--$
P26	$--\ ++++\ ----\ ++++\ ----\ ++++$	$--++\ --++\ --++$
P27	$++\ ----\ ++++\ ----\ ++++\ ----$	$++--\ ++--\ ++--$
P28	$++\ ----\ ++++\ ----\ ++++\ ----$	$--++\ --++\ --++$

Table 8.1: Patters P1-P8 were filled into RHIC for the first portion of the 2013 data taking period, with P21-P28 being filling in the second portion. For each pattern, from left to right, bunch 0 in the blue or yellow beam is filled with the leftmost polarization, with bunch 1 getting the next, and so on. The pattern repeats as soon as the end has been reached, until we get to the last filled bunch, with any empty bunch being 'polarized' as if it were not empty.

8.4 Muon Yields

To calculate A_L, we must obtain yields for positive and negative rapidity muons for all arm and charge conditions. Additionally, if we wish to further separate this data into η bins, this separation must be done as well. The number of 'groups' of muons grow combinatorially as expected with further subcategories. We will discuss how these yields are used to calculate raw-asymmetries, and subsequently full asymmetries in the next section.

We obtain yields for muons in the signal region (since this is the region for which we have calculated the signal-to-background ratio) by applying the standard W_{ness} cut to the physics data set, and then simply sorting the muons. The results of this are summarized in Table 8.2 (standard forward-backward binning), Table 8.5 (south arm, three eta bins), and Table 8.6 (north arm, three eta bins).

At this point, our expectation is that any differences in the raw muon yields is due to the underlying physics–a vanishing A_L would imply the yields should be close to the same, for a fixed arm and charge.

South Arm			
Charge	**Helicity**	**$\lvert\eta\rvert$ Range**	**μ Yield**
-1	$++$	$1.1 < \lvert\eta\rvert < 1.4$	12
-1	$++$	$1.4 < \lvert\eta\rvert < 1.8$	67
-1	$++$	$1.8 < \lvert\eta\rvert < 2.6$	63
-1	$-+$	$1.1 < \lvert\eta\rvert < 1.4$	21
-1	$-+$	$1.4 < \lvert\eta\rvert < 1.8$	99
-1	$-+$	$1.8 < \lvert\eta\rvert < 2.6$	49
-1	$+-$	$1.1 < \lvert\eta\rvert < 1.4$	19
-1	$+-$	$1.4 < \lvert\eta\rvert < 1.8$	76
-1	$+-$	$1.8 < \lvert\eta\rvert < 2.6$	58
-1	$--$	$1.1 < \lvert\eta\rvert < 1.4$	14
-1	$--$	$1.4 < \lvert\eta\rvert < 1.8$	68
-1	$--$	$1.8 < \lvert\eta\rvert < 2.6$	57
-1	$**$	$1.1 < \lvert\eta\rvert < 1.4$	0
-1	$**$	$1.4 < \lvert\eta\rvert < 1.8$	0
-1	$**$	$1.8 < \lvert\eta\rvert < 2.6$	0
$+1$	$++$	$1.1 < \lvert\eta\rvert < 1.4$	28
$+1$	$++$	$1.4 < \lvert\eta\rvert < 1.8$	94
$+1$	$++$	$1.8 < \lvert\eta\rvert < 2.6$	50
$+1$	$-+$	$1.1 < \lvert\eta\rvert < 1.4$	26
$+1$	$-+$	$1.4 < \lvert\eta\rvert < 1.8$	96
$+1$	$-+$	$1.8 < \lvert\eta\rvert < 2.6$	41
$+1$	$+-$	$1.1 < \lvert\eta\rvert < 1.4$	22
$+1$	$+-$	$1.4 < \lvert\eta\rvert < 1.8$	124
$+1$	$+-$	$1.8 < \lvert\eta\rvert < 2.6$	47
$+1$	$--$	$1.1 < \lvert\eta\rvert < 1.4$	26
$+1$	$--$	$1.4 < \lvert\eta\rvert < 1.8$	97
$+1$	$--$	$1.8 < \lvert\eta\rvert < 2.6$	66
$+1$	$**$	$1.1 < \lvert\eta\rvert < 1.4$	0
$+1$	$**$	$1.4 < \lvert\eta\rvert < 1.8$	0
$+1$	$**$	$1.8 < \lvert\eta\rvert < 2.6$	0

Figure 8.5: Due to much higher integrated luminosity of Run 13, we can actually subdivide the muon yields into rapidity bins for the purposes of trying to cover a wider kinematic range (at the expense of uncertainty). Here, we see the South arm's yields for each helicity combination of colliding protons, with the polarization of the blue beam and yellow beams color coded in column 2. Recall that of the yields, about 20% are actual signal events.

North Arm			
Charge	**Helicity**	**$\|\eta\|$ Range**	**μ Yield**
-1	$++$	$1.1 < \|\eta\| < 1.4$	18
-1	$++$	$1.4 < \|\eta\| < 1.8$	76
-1	$++$	$1.8 < \|\eta\| < 2.6$	57
-1	$-+$	$1.1 < \|\eta\| < 1.4$	14
-1	$-+$	$1.4 < \|\eta\| < 1.8$	63
-1	$-+$	$1.8 < \|\eta\| < 2.6$	56
-1	$+-$	$1.1 < \|\eta\| < 1.4$	13
-1	$+-$	$1.4 < \|\eta\| < 1.8$	74
-1	$+-$	$1.8 < \|\eta\| < 2.6$	61
-1	$--$	$1.1 < \|\eta\| < 1.4$	19
-1	$--$	$1.4 < \|\eta\| < 1.8$	63
-1	$--$	$1.8 < \|\eta\| < 2.6$	65
-1	$**$	$1.1 < \|\eta\| < 1.4$	0
-1	$**$	$1.4 < \|\eta\| < 1.8$	0
-1	$**$	$1.8 < \|\eta\| < 2.6$	0
$+1$	$++$	$1.1 < \|\eta\| < 1.4$	24
$+1$	$++$	$1.4 < \|\eta\| < 1.8$	96
$+1$	$++$	$1.8 < \|\eta\| < 2.6$	60
$+1$	$-+$	$1.1 < \|\eta\| < 1.4$	30
$+1$	$-+$	$1.4 < \|\eta\| < 1.8$	95
$+1$	$-+$	$1.8 < \|\eta\| < 2.6$	64
$+1$	$+-$	$1.1 < \|\eta\| < 1.4$	27
$+1$	$+-$	$1.4 < \|\eta\| < 1.8$	68
$+1$	$+-$	$1.8 < \|\eta\| < 2.6$	64
$+1$	$--$	$1.1 < \|\eta\| < 1.4$	33
$+1$	$--$	$1.4 < \|\eta\| < 1.8$	99
$+1$	$--$	$1.8 < \|\eta\| < 2.6$	56
$+1$	$**$	$1.1 < \|\eta\| < 1.4$	0
$+1$	$**$	$1.4 < \|\eta\| < 1.8$	0
$+1$	$**$	$1.8 < \|\eta\| < 2.6$	0

Figure 8.6: Due to much higher integrated luminosity of Run 13, we can actually subdivide the muon yields into rapidity bins for the purposes of trying to cover a wider kinematic range (at the expense of uncertainty). Here, we see the North arm's yields for each helicity combination of colliding protons, with the polarization of the blue beam and yellow beams color coded in column 2. Recall that of the yields, about 20% are actual signal events.

Arm	**Charge**	**Helicity**	μ **Yield**
S	-1	$++$	142
S	-1	$-+$	169
S	-1	$+-$	153
S	-1	$--$	139
S	-1	$**$	0
S	$+1$	$++$	172
S	$+1$	$-+$	163
S	$+1$	$+-$	193
S	$+1$	$--$	189
S	$+1$	$**$	0
N	-1	$++$	151
N	-1	$-+$	133
N	-1	$+-$	148
N	-1	$--$	147
N	-1	$**$	0
N	$+1$	$++$	180
N	$+1$	$-+$	189
N	$+1$	$+-$	159
N	$+1$	$--$	188
N	$+1$	$**$	0

Table 8.2: As a consistency check to previous analysis which only had enough statistics for two η bins, one forward, and one backward for A_L^{W+}, we have binned the data to match. Here, we see a division of the data by arm, charge, and helicity combination, which is color-coded for the polarization of the blue and yellow beams. Note that of the yields, only ~20% of the yield comes from a W-Boson decay.

8.5 Calculation of ϵ_L and A_L for $W \to \mu$

Now that we have ensured that we understand the signal to background ratio, and our various muon yields, we may proceed with the calculation of our observable, A_L.

8.5.1 Defining $A_L^{W\pm}$, $A_{LL}^{W\pm}$

There is a lot of language and terminology that we've inherited from previous work in Deep Inelastic Scattering Experiments, and the models developed to characterize the results of these experiments. One such concept is the idea of a 'probe' particle, and a 'target' particle. In DIS experiments, especially those designed to study proton polarization, there is typically a spin polarized gas, with a high intensity electron beam shining on it. Asymmetries were then defined in terms of scattering cross sections, where the polarization of the beam (or probe) and target were known.

In our case, we have an intersecting ring collider, so the concept of 'probe' and 'target' is more nebulous–however, the typical argument, is that if we can identify the final state, and correlate that to an initial state, then we may adopt this formalism. In this case, we take the polarized proton as our target, and then assume the other proton is our 'probe', and sum over the various probe polarizations so as to only measure the asymmetry effects from unpolarized+polarized quark interactions which produce W-Boson. In our case, we choose the convention of a polarized probe, and unpolarized target.

When we want to describe an Asymmetry, in the context of this analysis, what we are really studying is the difference in W-Boson production for two different initial-state proton polarizations. Mathematically, this is formalized by normalizing this total difference by the total production of W-Bosons from both polarization states. For the calculation of this asymmetry, we expect certain kinematic simplifications in the model for the asymmetry which gives more direct access to sea-quark polarization at very forward rapidities, with more kinematic mixing between the quarks and anti-quarks of the proton sea occurring as rapidities become more central. Therefore, we always evaluate asymmetries at a fixed η bin, which implicitly assumes that we have applied an η range cut on the muons yields participating in the calculation.

One additional comment on our convention for η–helicity in our case is intrinsically dependent on the rapidity of the particles produced, since we primarily kinematically restrict ourselves to forward and backward particles. While we split our muon yields into arm, charge, and η bins (Table 8.5 and Table 8.6) relative to the PHENIX coordinate system, when it comes to calculating the asymmetry, we use a definition for η, relative to the beam axis (z-axis) where the positive z-direction is considered to be co-linear with the probe particle's momentum. This convention is summarized in Table 8.3. Generally, the convention is summarized as "when do we need to apply a factor of -1 to the rapidity measured with respect to the PHENIX coordinate system".

Arm	**Charge**	**Probe Beam**	**Target Beam**	**Sign of η**
N	μ^+	Blue	Yellow	$+\eta$
N	μ^-	Blue	Yellow	$+\eta$
S	μ^+	Blue	Yellow	$-\eta$
S	μ^-	Blue	Yellow	$-\eta$
N	μ^+	Yellow	Blue	$-\eta$
N	μ^-	Yellow	Blue	$-\eta$
S	μ^+	Yellow	Blue	$+\eta$
S	μ^-	Yellow	Blue	$+\eta$

Table 8.3: A summary of the sign convention when we consider rapidity with respect to the probe beam, as opposed to the rapidity of the PHENIX coordinate system.

Keeping this convention straight is very important, as it allows us to combine the results of the raw asymmetries, to obtain a full description for $A_L^{W\pm}$.

Now, since in general we cannot learn anything about the physics of some structure function by just looking at scattering yields, we really want to compare the total cross-sections for each process. However, as we have already seen, we may write a cross-section in terms of a yield and a luminosity, and all else equal, only yields differ, as the luminosities are all the same. Chapter 3 discusses this in great detail, but given everybody skips the theory chapter, I've explained it more succinctly above.

For any fixed rapidity bin, we write down the Single Spin Asymmetry, for a fixed charge:

$$A_L = \frac{d\sigma^{\Rightarrow} - d\sigma^{\Leftarrow}}{d\sigma^{\Rightarrow} + d\sigma^{\Leftarrow}} \tag{8.3}$$

Recall from earlier that $\Leftarrow$ refers to negative helicity of the target proton, while $\Rightarrow$ refers to positive helicity of the target proton. We additionally define the double spin asymmetry, A_{LL} similarly:

$$A_{LL} = \frac{d\sigma^{\Rightarrow\Rightarrow} - d\sigma^{\Leftarrow\Rightarrow}}{d\sigma^{\Rightarrow\Rightarrow} + d\sigma^{\Leftarrow\Rightarrow}} \tag{8.4}$$

A_{LL} is calculated as a positivity constraint [75] in order restrict the allowed domain for spin observables. A_{LL} gives access to the product of quark and anti-quark polarizations, which is an important systematic effect which we must tease out from our result to ensure that we're providing a constraint on the quark polarization.

We now have the required pieces to calculate our asymmetries–the muon yields were summarized in Tables 8.5, 8.6, and 8.2. We have defined our rapidity convention for each bunch crossing, with regards to polarization of probe and target. Therefore, we construct our asymmetries from the set of yields for south:

$$\left\{ n^S_{(++)}, n^S_{(+-)}, n^S_{(-+)}, n^S_{(--)} \right\} \tag{8.5}$$

and north:

$$\left\{ n^N_{(++)}, n^N_{(+-)}, n^N_{(-+)}, n^N_{(--)} \right\} \tag{8.6}$$

With the superscript denoting the Muon Arm which recorded the yield, and the subscript referencing the polarization of the beams (left sign refers to blue polarization, right sign refers to yellow polarization). Implicitly, these yields are taken with respect to an η condition. We use these yields, in our calculation of A_L, along with the signal to background ratio, and the beam polarization.

8.5.2 Calculating $A_L^{W\pm}$, $A_{LL}^{W\pm}$

This thesis will present the method of calculating $A_L^{W\pm}$ and $A_{LL}^{W\pm}$ from a numeric perspective, though another popular method involves fitting a function relating beam polarization and the Asymmetries analytically to the data. Both the numeric results and the analytic results have been shown to give the same results for the asymmetries by Daniel Jumper.

Due to the fact that the relative luminosity of each beam polarization collision configuration has been shown to be relatively flat over the various spin combinations, we do not need to correct yields for any kind of relative luminosity effect.

We can then directly define raw asymmetries in terms of the yields. Note that our calculations for A_L sum over the polarization of one of the two colliding protons.

Single Spin Asymmetries

Polarized Blue Probe, Yellow Target, $\eta > 0$ w.r.t. Probe

$$\epsilon_{L,N}^{\eta>0} = \frac{\sigma^{\Rightarrow} - \sigma^{\Leftarrow}}{\sigma^{\Rightarrow} + \sigma^{\Leftarrow}} \to \frac{\left(n^N_{(++)} + n^N_{(+-)}\right) - \left(n^N_{(-+)} + n^N_{(--)}\right)}{\left(n^N_{(++)} + n^N_{(+-)}\right) + \left(n^N_{(-+)} + n^N_{(--)}\right)} \tag{8.7}$$

Polarized Blue Probe, Yellow Target, $\eta < 0$ w.r.t Probe

$$\epsilon_{L,S}^{\eta<0} = \frac{\sigma^{\Rightarrow} - \sigma^{\Leftarrow}}{\sigma^{\Rightarrow} + \sigma^{\Leftarrow}} \to \frac{\left(n^S_{(++)} + n^S_{(+-)}\right) - \left(n^S_{(-+)} + n^S_{(--)}\right)}{\left(n^S_{(++)} + n^S_{(+-)}\right) + \left(n^S_{(-+)} + n^S_{(--)}\right)} \tag{8.8}$$

Polarized Yellow Probe, Blue Target, $\eta > 0$ w.r.t Probe

$$\epsilon_{L,S}^{\eta>0} = \frac{\sigma^{\Rightarrow} - \sigma^{\Leftarrow}}{\sigma^{\Rightarrow} + \sigma^{\Leftarrow}} \to \frac{\left(n^S_{(++)} + n^S_{(-+)}\right) - \left(n^S_{(+-)} + n^S_{(--)}\right)}{\left(n^S_{(++)} + n^S_{(-+)}\right) + \left(n^S_{(+-)} + n^S_{(--)}\right)} \tag{8.9}$$

Polarized Yellow Probe, Blue Target, $\eta < 0$ w.r.t Probe

$$\epsilon_{L,N}^{\eta<0} = \frac{\sigma^{\Rightarrow} - \sigma^{\Leftarrow}}{\sigma^{\Rightarrow} + \sigma^{\Leftarrow}} \to \frac{\left(n^N_{(++)} + n^N_{(-+)}\right) - \left(n^N_{(+-)} + n^N_{(--)}\right)}{\left(n^N_{(++)} + n^N_{(-+)}\right) + \left(n^N_{(+-)} + n^N_{(--)}\right)} \tag{8.10}$$

Double Spin Asymmetries

A_{LL} North Arm

$$\epsilon_{LL,N} = \frac{\sigma^{\Rightarrow\Rightarrow} - \sigma^{\Leftarrow\Rightarrow}}{\sigma^{\Rightarrow\Rightarrow} + \sigma^{\Leftarrow\Rightarrow}} \to \frac{\left(n^N_{(++)} + n^N_{(--)}\right) - \left(n^N_{(+-)} + n^N_{(-+)}\right)}{\left(n^N_{(++)} + n^N_{(--)}\right) + \left(n^N_{(+-)} + n^N_{(-+)}\right)} \tag{8.11}$$

A_{LL} **South Arm**

$$\epsilon_{LL,S} = \frac{\sigma^{\Rightarrow\Rightarrow} - \sigma^{\Leftarrow\Rightarrow}}{\sigma^{\Rightarrow\Rightarrow} + \sigma^{\Leftarrow\Rightarrow}} \rightarrow \frac{\left(n^S_{(++)} + n^S_{(--)}\right) - \left(n^S_{(+-)} + n^S_{(-+)}\right)}{\left(n^S_{(++)} + n^S_{(--)}\right) + \left(n^S_{(+-)} + n^S_{(-+)}\right)} \tag{8.12}$$

In all cases, ϵ refers to the raw asymmetry, i.e. an asymmetry which has not been corrected for dilution due to background contamination of the yields, or dilution due to less than 100% beam polarization.

The correction for either dilution is straight-forward:

$$A_L^{\eta>0} = \frac{D^N}{P_B}\epsilon_{L,N}^{\eta>0} = \frac{D^S}{P_Y}\epsilon_{L,S}^{\eta>0} \tag{8.13}$$

$$A_L^{\eta<0} = \frac{D^N}{P_B}\epsilon_{L,N}^{\eta<0} = \frac{D^S}{P_Y}\epsilon_{L,S}^{\eta<0} \tag{8.14}$$

$$A_{LL} = \frac{D^N}{P_B P_Y}\epsilon_{LL,N} = \frac{D^S}{P_B P_Y}\epsilon_{LL,S} \tag{8.15}$$

8.5.3 Preliminary Results

I earned PHENIX preliminary status for these results in October of 2015. I recall staying up all night writing the talk after a colleague had to bow out of giving it. It was fortunate that my collaborator, Dr. Ralf Seidl was working from Japan, as he was available all night for me to ask questions to. We successfully submitted our asymmetries for collaboration review, and were subsequently awarded the right to show the following plots at conferences. We can see the calculated asymmetries for multiple η bins in Figure 8.7, and the asymmetries for the standard forward and backward η bins in Figure 8.8.

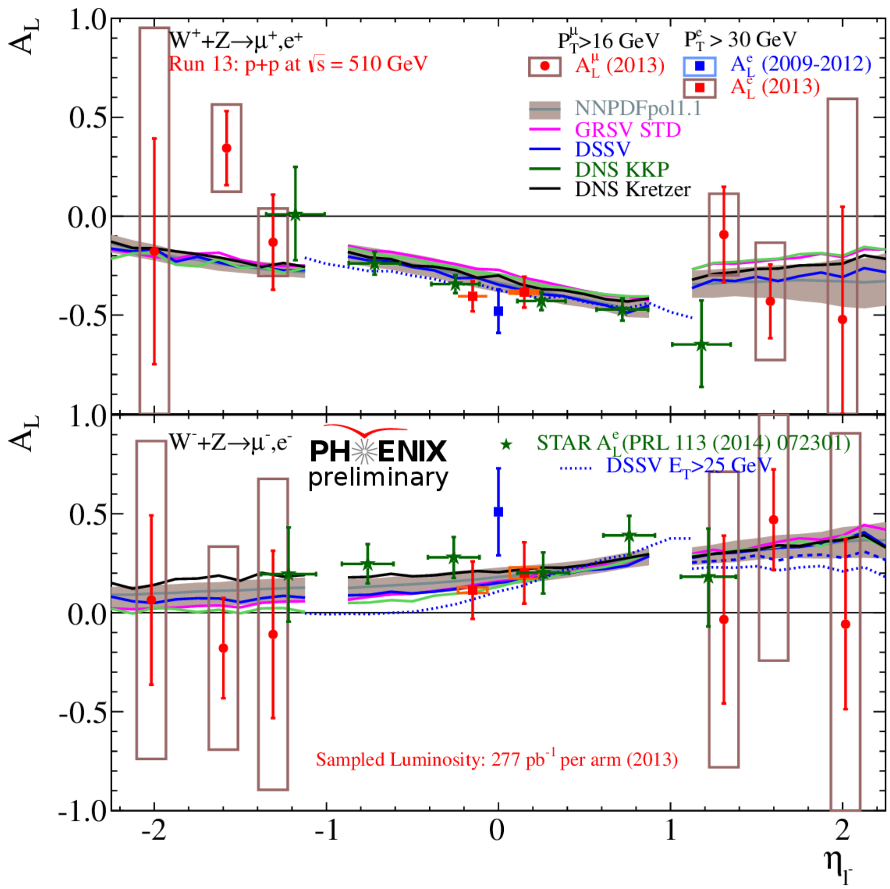

Figure 8.7: 7 years

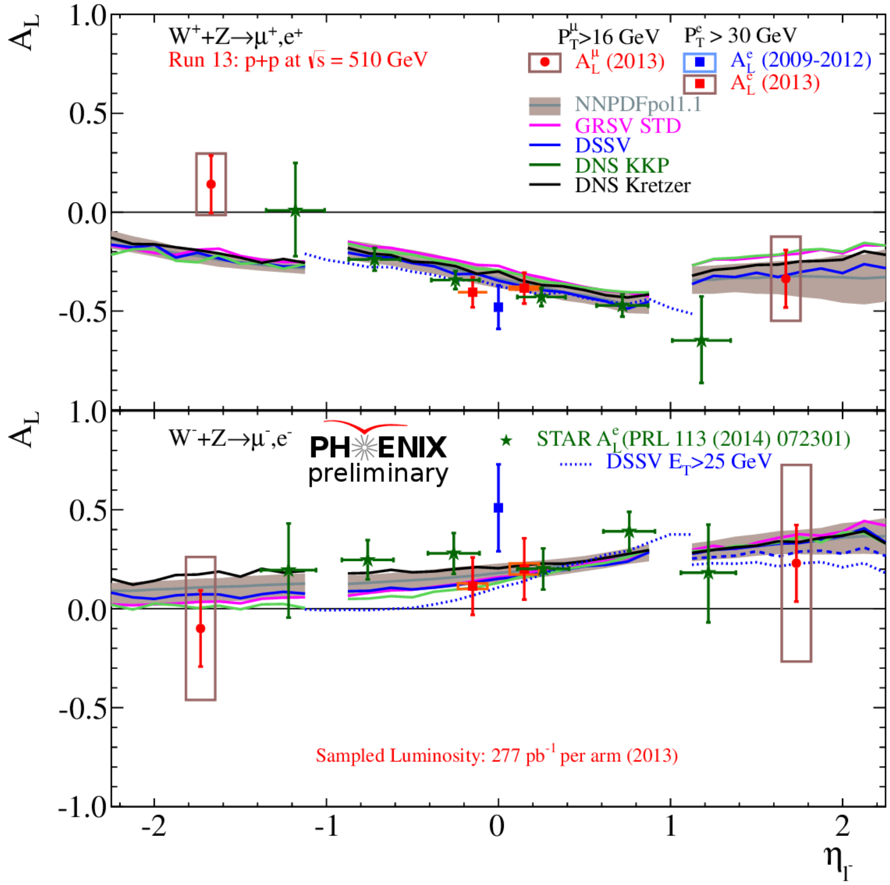

Figure 8.8: 7 years

8.6 Data Validation

Mention Daniel's GPR, Ralf's PEPSI, Abraham's FVTX work, and Francesca's cross-checks.

8.6.1 Simulations and The Signal to Background Ratio

8.6.2 Gaussian Process Regression

8.6.3 Four Way Cross Validation

8.6.4 Asymmetry Consistency Check

8.6.5 Beam Polarization

8.6.6 Beam Luminosity

8.6.7 Code Cross Validation

Chapter 9

The Vernier Analysis

9.1 Overview

9.2 Analysis Note Here

9.3 W Cross Section

Chapter 10

Discussion and Conclusion

The PHENIX results on the Asymmetry put an important constraint on the polarized parton distribution functions, and spin contributions of the sea-quarks to the total proton spin. Due to the vanishing asymmetries found in this analysis, we now know that with:

$$
\begin{aligned}
A_L(x, Q^2) &= \frac{\sigma^+ - \sigma^-}{\sigma^+ + \sigma^-} && (10.1) \\
&\equiv \frac{g_1(x, Q^2)}{F_1(x, Q^2)} && (10.2) \\
&\approx 0 && (10.3)
\end{aligned}
$$

That the sea quarks must contribute very little to the proton's total spin. We additionally know, with good constraints on the contributions from the valence quarks, that the majority of the proton spin must reside in the gluons and the angular momentum of the proton.

Subsequent experiments such as the new Electron Ion Collider, which will be completed in coming years will be able to measure these contributions with certainty, and finality.

Bibliography

[1] J Ashman, Others, B Badelek, G Baum, I G Bird, A W Edwards, and T Walcher. A Measurement Of The Spin Asymmetry And Determination Of The Structure Function \textit{g1} In Deep Inelastic Muon-Proton Scattering. *Phys. Lett. B*, 206(2):364–370, 1988.

[2] a. Accardi, J. L. Albacete, M. Anselmino, N. Armesto, E. C. Aschenauer, A. Bacchetta, D. Boer, W. K. Brooks, T. Burton, N. B. Chang, W. T. Deng, A. Deshpande, M. Diehl, A. Dumitru, R. Dupré, R. Ent, S. Fazio, H. Gao, V. Guzey, H. Hakobyan, Y. Hao, D. Hasch, R. Holt, T. Horn, M. Huang, A. Hutton, C. Hyde, J. Jalilian-Marian, S. Klein, B. Kopeliovich, Y. Kovchegov, K. Kumar, K. Kumerički, M. A. C. Lamont, T. Lappi, J. H. Lee, Y. Lee, E. M. Levin, F. L. Lin, V. Litvinenko, T. W. Ludlam, C. Marquet, Z. E. Meziani, R. McKeown, A. Metz, R. Milner, V. S. Morozov, A. H. Mueller, B. Müller, D. Müller, P. Nadel-Turonski, A. Prokudin, V. Ptitsyn, X. Qian, J. W. Qiu, M. Ramsey-Musolf, T. Roser, F. Sabatié, R. Sassot, G. Schnell, P. Schweitzer, E. Sichtermann, M. Stratmann, M. Strikman, M. Sullivan, S. Taneja, T. Toll, D. Trbojevic, T. Ullrich, R. Venugopalan, S. Vigdor, W. Vogelsang, C. Weiss, B. W. Xiao, F. Yuan, Y. H. Zhang, L. Zheng, H. Paukkunen, A. Prokudin, V. Ptitsyn, X. Qian, J. W. Qiu, M. Ramsey-Musolf, T. Roser, F. Sabatié, R. Sassot, G. Schnell, P. Schweitzer, E. Sichtermann, M. Stratmann, M. Strikman, M. Sullivan, S. Taneja, T. Toll, D. Trbojevic, T. Ullrich, R. Venugopalan, S. Vigdor, W. Vogelsang, C. Weiss, B. W. Xiao, F. Yuan, Y. H. Zhang, and L. Zheng. Electron Ion Collider: The Next QCD Frontier - Understanding the glue that binds us all. *arXiv preprint*, page 164, 2012.

[3] Herbert S. Long. The Unity of Empedocles' Thought. *The American Journal of Philology*, 70(2):142–158, 1949.

[4] Craig Freudenrich. Combined Atomic Orbital, 2001.

[5] Manisearth. scale_of_matter, 2010.

[6] Marco Stratmann. Spin physics at rhic - a theoretical overview. Technical report, 2009.

[7] Arthur Steward Eve. *Rutherford: Being the Life and Letters of the Rt. Hon. Lord Rutherford, O. M.* The University Press, 1939.

[8] Kurzon. Diagram Illustraitng Geiger-Marsden Experiment, 2014.

[9] Bruxelles Benjamin Croupie. Participants of the 5th Solvay Congress. Technical report, 1927.

[10] Wikimedia. Hideki Yukawa. *The Mainichi Graphic*, sep 1952.

[11] FNAL. Fermi National Lab Bubble Chamber, 2005.

[12] ENERGY.GOV. Bubble Chamber Tracks, 1973.

[13] Ddn2. Electron Proton Deep Inelastic Scattering, 2008.

[14] Latham Boyle. standard_model_complete, 2014.

[15] J Beringer, J.-F. Arguin, R M Barnett, K Copic, O Dahl, D E Groom, C.-J. Lin, J Lys, H Murayama, C G Wohl, W.-M. Yao, P A Zyla, C Amsler, M Antonelli, D M Asner, H Baer, H R Band, T Basaglia, C W Bauer, J J Beatty, V I Belousov, E Bergren, G Bernardi, W Bertl, S Bethke, H Bichsel, O Biebel, E Blucher, S Blusk, G Brooijmans, O Buchmueller, R N Cahn, M Carena, A Ceccucci, D Chakraborty, M.-C. Chen, R S Chivukula, G Cowan, G D'Ambrosio, T Damour, D de Florian, A de Gouvêa, T DeGrand, P de Jong, G Dissertori, B Dobrescu, M Doser, M Drees, D A Edwards, S Eidelman, J Erler, V V Ezhela, W Fetscher, B D Fields, B Foster, T K Gaisser, L Garren, H.-J. Gerber, G Gerbier, T Gherghetta, S Golwala, M Goodman, C Grab, A V Gritsan, J.-F. Grivaz, M Grünewald, A Gurtu, T Gutsche, H E Haber, K Hagiwara, C Hagmann, C Hanhart, S Hashimoto, K G Hayes, M Heffner, B Heltsley, J J Hernández-Rey, K Hikasa, A Höcker, J Holder, A Holtkamp, J Huston, J D Jackson, K F Johnson, T Junk, D Karlen, D Kirkby, S R Klein, E Klempt, R V Kowalewski, F Krauss, M Kreps, B Krusche, Y V Kuyanov, Y Kwon, O Lahav, J Laiho, P Langacker, A Liddle, Z Ligeti, T M Liss, L Littenberg, K S Lugovsky, S B Lugovsky, T Mannel, A V Manohar, W J Marciano, A D Martin, A Masoni, J Matthews, D Milstead, R Miquel, K Mönig, F Moortgat, K Nakamura, M Narain, P Nason, S Navas, M Neubert, P Nevski, Y Nir, K A Olive, L Pape, J Parsons, C Patrignani, J A Peacock, S T Petcov, A Piepke, A Pomarol, G Punzi, A Quadt, S Raby, G Raffelt, B N Ratcliff, P Richardson, S Roesler, S Rolli, A Romaniouk, L J Rosenberg, J L Rosner, C T Sachrajda, Y Sakai, G P Salam, S Sarkar, F Sauli, O Schneider, K Scholberg, D Scott, W G Seligman, M H Shaevitz, S R Sharpe, M Silari, T Sjöstrand, P Skands, J G Smith, G F Smoot, S Spanier, H Spieler, A Stahl, T Stanev, S L Stone, T Sumiyoshi, M J Syphers, F Takahashi, M Tanabashi, J Terning, M Titov, N P Tkachenko, N A Törnqvist, D Tovey, G Valencia, K van Bibber, G Venanzoni, M G Vincter, P Vogel, A Vogt, W Walkowiak, C W Walter, D R Ward, T Watari, G Weiglein, E J Weinberg, L R Wiencke, L Wolfenstein, J Womersley, C L Woody, R L Workman, A Yamamoto, G P Zeller, O V Zenin, J Zhang, R.-Y. Zhu, G Harper, V S Lugovsky, and P Schaffner. Review of Particle Physics. {*Textbackslash*}*Prd*, 86(1):1526, jul 2012.

[16] Daniel De Florian, Rodolfo Sassot, Marco Stratmann, and Werner Vogelsang. Extraction of spin-dependent parton densities and their uncertainties. *Physical Review D - Particles, Fields, Gravitation and Cosmology*, 80(3):1–25, 2009.

[17] Christine Aidala and Et Al. Research Plan for Spin Physics at RHIC. *report to DOE*, 2005.

[18] Wolfram Fischer. RHIC Run Overview, 2016.

[19] Karen Walsh and Peter Genzer. BNL Newsroom — Hot Nuclear Matter Featured in Science, 2012.

[20] Brookhaven National Laboratory and Anatoli Zelenski. Towards 100% polarization in the Optically-Pumped Polarized Ion Source at RHIC. Technical report, Brookhaven National Laboratory, 2007.

[21] RHIC, I. Alekseev, C. Allgower, M. Bai, and Et Al. Configuration Manual Polarized Proton Collider at RHIC. *Configuration Manual*, (January), 2006.

[22] PHENIX Collaboration. PHENIX Drawings.

[23] John Haggarty, Martin Purschke, Chris Pinkenburg, and Ed Desmond. PHENIX Shift Duties, 2016.

[24] Tomoaki Nakamura. Introduction to PHENIX Beam Beam Counter (BBC) Purpose of PHENIX BBC. Technical report, 2002.

[25] C. Aidala, L. Anaya, E. Anderssen, A. Bambaugh, A. Barron, J. G. Boissevain, J. Bok, S. Boose, M. L. Brooks, S. Butsyk, M. Cepeda, P. Chacon, S. Chacon, L. Chavez, T. Cote, C. Dagostino, A. Datta, K. Deblasio, L. Delmonte, E. J. Desmond, J. M. Durham, D. Fields, M. Finger, C. Gingu, B. Gonzales, J. S. Haggerty, T. Hawke, H. W. Van Hecke, M. Herron, J. Hoff, J. Huang, X. Jiang, T. Johnson, M. Jonas, J. S. Kapustinsky, A. Key, G. J. Kunde, J. Kurtz, J. Labounty, D. M. Lee, K. B. Lee, M. J. Leitch, M. Lenz, W. Lenz, M. X. Liu, D. Lynch, E. Mannel, P. L. McGaughey, A. Meles, B. Meredith, H. Nguyen, E. Obrien, R. Pak, V. Papavassiliou, S. Pate, H. Pereira, G. D N Perera, M. Phillips, R. Pisani, S. Polizzo, R. J. Poncione, J. Popule, M. Prokop, M. L. Purschke, A. K. Purwar, N. Ronzhina, C. L. Silva, M. Slune??ka, R. Smith, W. E. Sondheim, K. Spendier, M. Stoffer, E. Tennant, D. Thomas, M. Tom????ek, A. Veicht, V. Vrba, X. R. Wang, F. Wei, D. Winter, R. Yarema, Z. You, I. Younus, A. Zimmerman, and T. Zimmerman. The PHENIX forward silicon vertex detector. *Nuclear Instruments and Methods in Physics Research, Section A: Accelerators, Spectrometers, Detectors and Associated Equipment*, 755:44–61, 2014.

[26] Yoshinori Fukao. Forward upgrade for <i>W</i> physics at the RHIC-PHENIX experiment. *Journal of Physics: Conference Series*, 295:012165, 2011.

[27] Mike Beaumier. *Probing the Spin Structure of the Proton Using Polarized Proton+Proton Collisions and the Production of W-Bosons*. PhD thesis, University of California, Riverside, 2016.

[28] Hideyuki Oide. *Measurement of longitudinal spin asymmetry in production of muons from W / Z boson decays in polarized $p + p$ collisions at $s = 500$ GeV with the PHENIX detector at RHIC*. PhD thesis, 2012.

[29] Ralf Seidl, Francesca Giordano, Daniel Jumper, Michael Beaumier, Richard Hollis, and Abraham Meles. Run 13 W Analysis. 2014.

[30] K. Adcox, S. S. Adler, M. Aizama, N. N. Ajitanand, Y. Akiba, H. Akikawa, J. Alexander, A. Al-Jamel, M. Allen, G. Alley, R. Amirikas, L. Aphecetche, Y. Arai, J. B. Archuleta, J. R. Archuleta, R. Armendariz, V. Armijo, S. H. Aronson, D. Autrey, R. Averbeck, T. C. Awes, B. Azmoun, A. Baldisseri, J. Banning, K. N. Barish, A. B. Barker, P. D. Barnes, J. Barrette, F. Barta, B. Bassalleck, S. Bathe, S. Batsouli, V. V. Baublis, A. Bazilevsky, R. Begay, J. Behrendt, S. Belikov, R. Belkin, F. G. Bellaiche, S. T. Belyaev, M. J. Bennett, Y. Berdnikov, S. Bhaganatula, J. C. Biggs, A. W. Bland, C. Blume, M. Bobrek, J. G. Boissevain, S. Boose, H. Borel, D. Borland, E. Bosze, S. Botelho, J. Bowers, C. Britton, L. Britton, M. L. Brooks, A. W. Brown, D. S. Brown, N. Bruner, W. L. Bryan, D. Bucher, H. Buesching, V. Bumazhnov, G. Bunce, J. Burward-Hoy, S. A. Butsyk, M. M. Cafferty, T. A. Carey, J. S. Chai, P. Chand, J. Chang, W. C. Chang, R. B. Chappell, L. L. Chavez, S. Chernichenko, C. Y. Chi, J. Chiba, M. Chiu, S. Chollet, R. K. Choudhury, T. Christ, T. Chujo, M. S. Chung, P. Chung, V. Cianciolo, D. J. Clark, Y. Cobigo, B. A. Cole, P. Constantin, R. Conway, K. C. Cook, D. W. Crook, H. Cunitz, R. Cunningham, M. Cutshaw, D. G. D'Enterria, C. M. Dabrowski, G. Danby, S. Daniels, A. Danmura, G. David, A. Debraine, H. Delagrange, J. DeMoss, A. Denisov, A. Deshpande, E. J. Desmond, O. Dietzsch, B. V. Dinesh, J. L. Drachenberg, O. Drapier, A. Drees, R. du Rietz, A. Durum, D. Dutta, K. Ebisu, M. A. Echave, Y. V. Efremenko, K. El Chenawi, M. S. Emery, D. Engo, A. Enokizono, K. Enosawa, H. En'yo, N. Ericson, S. Esumi, V. A. Evseev, L. Ewell, O. Fackler, J. Fellenstein, T. Ferdousi, J. Ferrierra, D. E. Fields, F. Fleuret, S. L. Fokin, B. Fox, Z. Fraenkel, S. Frank, A. Franz, J. E. Frantz, A. D. Frawley, J. Fried, J. P. Freidberg, E. Fujisawa, H. Funahashi, S. Y. Fung, S. Gadrat, J. Gannon, S. Garpman, F. Gastaldi, T. F. Gee, R. Gentry, T. K. Ghosh, P. Giannotti, A. Glenn, A. L. Godoi, M. Gonin, G. Gogiberidze, J. Gosset, Y. Goto, R. Granier de Cassagnac, S. V. Greene, V. Griffin, M. Grosse Perdekamp, S. K. Gupta, W. Guryn, H. A. Gustafsson, T. Hachiya, J. S. Haggerty, S. Hahn, J. Halliwell, H. Hamagaki, R. H. Hance, A. G. Hansen, H. Hara, J. Harder, G. W. Hart, E. P. Hartouni, A. Harvey, L. Hawkins, R. S. Hayano, H. Hayashi, N. Hayashi, X. He, N. Heine, F. Heistermann, S. Held, T. K. Hemmick, J. M. Heuser, M. Hibino, J. S. Hicks, R. Higuchi, J. C. Hill, T. Hirano, D. S. Ho, R. Hoade, W. Holzmann, K. Homma, B. Hong, A. Hoover, T. Honaguchi, C. T. Hunter, D. E. Hurst, R. Hutter, T. Ichihara, V. V. Ikonnikov, K. Imai, M. Inaba, M. S. Ippolitov, L. Davis Isenhower, L. Donald Isenhower, M. Ishihara, M. Issah, V. I. Ivanov, B. V. Jacak, G. Jackson, J. Jackson, D. Jaffe, U. Jagadish, W. Y. Jang, R. Jayakumar, J. Jia, B. M. Johnson, J. Johnson, S. C. Johnson, J. P. Jones, K. Jones, K. S. Joo, D. Jouan, S. Kahn, F. Kajihara, S. Kametani, N. Kamihara, Y. Kamyshkov, A. Kandasamy, J. H. Kang, M. R. Kann, S. S. Kapoor, J. Kapustinsky, K. V. Karadjev, V. Kashikhin, S. Kato, K. Katou, H. J. Kehayias, M. A. Kelley, S. Kelly, M. Kennedy, B. Khachaturov, A. V. Khanzadeev, A. Khomutnikov, J. Kikuchi, D. J. Kim, D. W. Kim, G. B. Kim, H. J. Kim, S. Y. Kim, Y. G. Kim, W. W. Kinnison, E. Kistenev, A. Kiyomichi, C. Klein-Boesing, S. Klinksiek, L. Kluberg, H. Kobayashi, V. Kochetkov, D. Koehler, T. Kohama, B. G. Komkov, M. L. Kopytine, K. Koseki, L. Kotchenda,

D. Kotchetkov, Iou A. Koutcheryaev, A. Kozlov, V. S. Kozlov, P. A. Kravtsov, P. J. Kroon, C. H. Kuberg, L. G. Kudin, M. Kurata-Nishimura, V. V. Kuriatkov, K. Kurita, Y. Kuroki, M. J. Kweon, Y. Kwon, G. S. Kyle, J. J. LaBounty, R. Lacey, J. G. Lajoie, J. Lauret, A. Lebedev, V. A. Lebedev, V. D. Lebedev, D. M. Lee, S. Lee, M. J. Leitch, M. Lenz, W. Lenz, X. H. Li, Z. Li, B. Libby, M. Libkind, W. Liccardi, D. J. Lim, S. Lin, M. X. Liu, X. Liu, Y. Liu, Z. Liu, E. Lockner, N. Longbotham, J. D. Lopez, R. Machnowski, C. F. Maguire, J. Mahon, Y. I. Makdisi, V. I. Manko, Y. Mao, S. Marino, S. K. Mark, S. Markacs, D. G. Markushin, G. Martinez, X. B. Martinez, M. D. Marx, A. Masaike, F. Matathias, T. Matsumoto, P. L. McGaughey, M. C. McCain, J. Mead, E. Melnikov, Y. Melnikov, W. Z. Meng, M. Merschmeyer, F. Messer, M. Messer, Y. Miake, N. M. Miftakhov, S. Migluolio, J. Milan, T. E. Miller, A. Milov, K. Minuzzo, S. Mioduszewski, R. E. Mischke, G. C. Mishra, J. T. Mitchell, Y. Miyamoto, A. K. Mohanty, B. C. Montoya, A. Moore, T. Moore, D. P. Morrison, G. G. Moscone, J. M. Moss, F. Mühlbacher, M. Muniruzzaman, J. Murata, M. M. Murray, M. Musrock, S. Nagamiya, Y. Nagasaka, J. L. Nagle, Y. Nakada, T. Nakamura, B. K. Nandi, J. Negrin, J. Newby, L. Nikkinen, S. A. Nikolaev, P. Nilsson, S. Nishimura, A. S. Nyanin, J. Nystrand, E. O'Brien, P. O'Conner, F. Obenshain, C. A. Ogilvie, H. Ohnishi, I. D. Ojha, M. Ono, V. Onuchin, A. Oskarsson, L. Österman, I. Otterlund, K. Oyama, L. Paffrath, A. P T Palounek, C. E. Pancake, V. S. Pantuev, V. Papavassiliou, S. F. Pate, T. Peitzmann, R. Petersen, A. N. Petridis, C. H. Pinkenburg, R. P. Pisani, P. Pitukhin, T. Plagge, F. Plasil, M. Pollack, K. Pope, R. Prigl, M. L. Purschke, A. K. Purwar, J. M. Qualls, S. Rankowitz, G. Rao, R. Rao, M. Rau, I. Ravinovich, R. Raynis, K. F. Read, K. Reygers, G. Riabov, V. G. Riabov, Y. G. Riabov, S. H. Robinson, G. Roche, A. Romana, M. Rosati, E. V. Roschin, A. A. Rose, P. Rosnet, R. Roth, R. Ruggiero, S. S. Ryu, N. Saito, A. Sakaguchi, T. Sakaguchi, S. Sakai, H. Sako, T. Sakuma, S. Salomone, V. M. Samsonov, W. F. Sandhoff, L. Sanfratello, T. C. Sangster, R. Santo, H. D. Sato, S. Sato, R. Savino, S. Sawada, B. R. Schlei, R. Schleuter, Y. Schutz, M. Sekimoto, V. Semenov, R. Seto, Y. Severgin, A. Shajii, V. Shangin, M. R. Shaw, T. K. Shea, I. Shein, V. Shelikhov, T. A. Shibata, K. Shigaki, T. Shiina, T. Shimada, Y. H. Shin, I. G. Sibiriak, D. Silvermyr, K. S. Sim, J. Simon-Gillo, M. Simpson, C. P. Singh, V. Singh, W. Sippach, M. Sivertz, H. D. Skank, S. Skutnik, G. A. Sleege, D. C. Smith, G. D. Smith, M. Smith, A. Soldatov, G. P. Solodov, R. A. Soltz, W. E. Sondheim, S. Sorensen, I. Sourikova, F. Staley, P. W. Stankus, N. Starinsky, S. Steffens, E. M. Stein, P. Steinberg, E. Stenlund, M. Stepanov, A. Ster, J. Stewering, W. Stokes, S. P. Stoll, M. Sugioka, T. Sugitate, J. P. Sullivan, Y. Sumi, Z. Sun, M. Suzuki-Nara, E. M. Takagui, A. Taketani, M. Tamai, K. H. Tanaka, Y. Tanaka, E. Taniguchi, M. J. Tannenbaum, V. I. Tarakanov, O. P. Tarasenkova, J. D. Tepe, R. Thern, J. H. Thomas, J. L. Thomas, T. L. Thomas, W. D. Thomas, G. W. Thornton, W. Tian, R. Todd, J. Tojo, F. Toldo, H. Torii, R. S. Towell, J. Tradeski, V. A. Trofimov, I. Tserruya, H. Tsuruoka, A. A. Tsvetkov, S. K. Tuli, G. Turner, H. Tydesjö, N. Tyurin, S. Urasawa, A. Usachev, T. Ushiroda, H. W. van Hecke, M. van Lith, A. A. Vasiliev, V. Vasiliev, M. Vassent, C. Velissaris, J. Velkovska, M. Velkovsky, W. Verhoeven, L. Villatte, A. A. Vinogradov, V. I. Vishnevskii, M. A. Volkov, W. von Achen, A. A. Vorobyov, E. A. Vznuzdaev, M. Vznuzdaev, J. W. Walker, Y. Wan, H. Q.

Wang, S. Wang, Y. Watanabe, L. C. Watkins, T. Weimer, S. N. White, B. R. Whitus, C. Williams, P. S. Willis, A. L. Wintenberg, C. Witzig, F. K. Wohn, K. Wolniewicz, B. G. Wong-Swanson, L. Wood, C. L. Woody, L. W. Wright, J. Wu, W. Xie, N. Xu, K. Yagi, R. Yamamoto, Y. Yang, S. Yokkaichi, Y. Yokota, S. Yoneyama, G. R. Young, I. E. Yushmanov, W. A. Zajc, C. Zhang, L. Zhang, Z. Zhang, and S. Zhou. PHENIX detector overview. *Nuclear Instruments and Methods in Physics Research, Section A: Accelerators, Spectrometers, Detectors and Associated Equipment*, 499(2-3):469–479, 2003.

[31] Abraham Meles. *Measurement of longitudinal spin asymmetry in production of muons from W / Z boson decays in polarized p + p collisions at s = 500 GeV with the PHENIX detector at RHIC*. PhD thesis, 2012.

[32] M. Breidenbach, J. I. Friedman, H. W. Kendall, E. D. Bloom, D. H. Coward, H. Destaebler, J. Drees, L. W. Mo, and R. E. Taylor. Observed behavior of highly inelastic electron-proton scattering. *Physical Review Letters*, 23(16):935–939, 1969.

[33] J. D. Bjorken and E. A. Paschos. Inelastic electron-proton and ??-proton scattering and the structure of the nucleon. *Physical Review*, 185(5):1975–1982, 1969.

[34] Bogdan Povh and Thomas Walcher. The end of the nucleon-spin crisis. 2016.

[35] Stanley J. Brodsky, John Ellis, and Marek Karliner. Chiral symmetry and the spin of the proton. *Physics Letters B*, 206(2):309–315, 1988.

[36] Thomas Stanley. The History of Philosophy, 1655.

[37] Hendrick ter Brugghen. Democritus, 1628.

[38] Richard W. Baldes. 'Divisibility' and 'Division' in Democritus. *Apeiron: A Journal for Ancient Philosophy and Science*, 12(1):1–12, 1978.

[39] Konstantinos Alexakos and Wladina Antoine. The Golden Age of Islam and Science Teaching: Teachers and students develop a deeper understanding of the foundations of modern science by learning about the contributions of Arab-Islamic scientists and scholars. *The Science Teacher*, 72(3):36–39, 2005.

[40] Fraser Cowley. *A Critique of British Empiricism*. MacMillan, 1968.

[41] Ottavio Leoni. Galileo Galilei, Portrait in Crayon by Leoni, 1624.

[42] A. Rupert Hall. Galileo and the Science of Motion. *The British Journal for the History of Science*, 2(3):185–199, 1965.

[43] Roger H. Stuewer. A Critical Analysis of Newton's Work on Diffraction. *Isis*, 61(2):188–205, 1970.

[44] Gary Patterson. Jean Perrin and the triumph of the atomic doctrine. *Endeavour*, 31(2):50–53, jun 2007.

[45] George Thomson. J. J. Thomson, 1956.

[46] Kurzon. Diagram of JJ Thomson's Experiment With Cathod Rays, 2010.

[47] Nobel Media. J.J. Thomson - Biographical, 2014.

[48] M Planck. On the law of the energy distribution in the normal spectrum. *Ann. Phys*, 4:1–11, 1901.

[49] J. Clerk Maxwell. A Dynamical Theory of the Electromagnetic Field [J]. *Philosophical Transactions of the Royal Society of London*, 155(January):459–512, 1865.

[50] P. A. M. Dirac. The Quantum Theory of the Electron. *Proceedings of the Royal Society A: Mathematical, Physical and Engineering Sciences*, 117(778):610, 1928.

[51] Nobel Foundation. Paul Dirac, 1933.

[52] Frank Krauss. History of Particle Physics. Technical report, Institute for Particle physics Phenomenology, University of Durham, Durham, 2015.

[53] W Heisenberg. Production of Mesons as a Shock Wave Problem Visual description of a shock wave. pages 1–17, 1952.

[54] H. Yukawa, S. Sakata, and M. Taketani. On the interaction of elementary particles. III. *Progress of Theoretical Physics Supplement*, 1(Received):24–45, 1955.

[55] Pj Bryant. A brief history and review of accelerators. *Cern European Organization for ...*, 1994.

[56] M. Gell-Mann. Isotopic spin and new unstable particles. *Physical Review*, 92(3):833–834, 1953.

[57] M. Gell-Mann. The interpretation of the new particles as displaced charge multiplets. *Il Nuovo Cimento Series 10*, 4(1 Supplement):848–866, 1956.

[58] Michael Riordan. The Discovery of Quarks. 1992.

[59] GW Bennett, B Bousquet, HN Brown, G Bunce, RM Carey, P Cushman, GT Danby, PT Debevec, M Deile, H Deng, SK Dhawan, VP Druzhinin, L Duong, FJM Farley, GV Fedotovich, Fe Gray, D Grigoriev, M Grosse-Perdekamp, A Grossmann, MF Hare, DW Hertzog, X Huang, VW Hughes, M Iwasaki, K Jungmann, D Kawall, Bi Khazin, F Krienen, I Kronkvist, A Lam, R Larsen, YY Lee, I Logashenko, R McNabb, W Meng, JP Miller, WM Morse, D Nikas, CJG Onderwater, Y Orlov, CS Ozben, JM Paley, Q Peng, CC Polly, J Pretz, R Prigl, G zu Putlitz, T Qian, Si Redin, O Rind, BL Roberts, N Ryskulov, YK Semertzidis, P Shagin, YuM Shatunov, Ep Sichtermann, E Solodov, M Sossong, LR Sulak, A Trofimov, P von Walter, and A Yamamoto. Measurement of the Negative Muon Anomalous Magnetic Moment to 0.7 ppm. 2004.

[60] J.J. Aubert, G. Bassompierre, K.H. Becks, C. Best, E. Böhm, X. de Bouard, F.W. Brasse, C. Broll, S. Brown, J. Carr, R.W. Clifft, J.H. Cobb, G. Coignet, F. Combley, G.R. Court, G. D'Agostini, W.D. Dau, J.K. Davies, Y. Déclais, R.W. Dobinson, U. Dosselli, J. Drees, A.W. Edwards, M. Edwards, J. Favier, M.I. Ferrero, W. Flauger, E. Gabathuler, R. Gamet, J. Gayler, V. Gerhardt, C. Gössling, J. Haas, K. Hamacher, P. Hayman, M. Henckes, V. Korbel, U. Landgraf, M. Leenen, M. Maire, H. Minssieux, W. Mohr, H.E. Montgomery, K. Moser, R.P. Mount, P.R. Norton, J. McNicholas, A.M. Osborne, P. Payre, C. Peroni, H. Pessard, U. Pietrzyk, K. Rith, M. Schneegans, T. Sloan, H.E. Stier, W. Stockhausen, J.M. Thénard, J.C. Thompson, L. Urban, M. Villers, H. Wahlen, M. Whalley, D. Williams, W.S.C. Williams, J. Williamson, and S.J. Wimpenny. The ratio of the nucleon structure functions F2N for iron and deuterium. *Physics Letters B*, 123(3):275–278, 1983.

[61] Ciprian Gal. *Measuring the anti-quark contribution to the proton spin using parity violating W production in polarized proton proton collisions.* PhD thesis, Stony Brook University, 2014.

[62] Guido Altarelli. QCD Evolution Equations For Parton Densities - Scholarpedia, 2009.

[63] John Ellis and Robert Jaffe. Sum rule for deep-inelastic electroproduction from polarized protons. *Physical Review D*, 9(5):1444–1446, 1974.

[64] Brookhaven National Laboratory. RHIC Complex, 2011.

[65] RHIC. RHIC — Accelerator Complex, 2016.

[66] I. Alekseev, C. Allgower, M. Bai, Y. Batygin, L. Bozano, K. Brown, G. Bunce, P. Cameron, E. Courant, S. Erin, J. Escallier, W. Fischer, R. Gupta, K. Hatanaka, H. Huang, K. Imai, M. Ishihara, A. Jain, A. Lehrach, V. Kanavets, T. Katayama, T. Kawaguchi, E. Kelly, K. Kurita, S. Y. Lee, A. Luccio, W. W. MacKay, G. Mahler, Y. Makdisi, F. Mariam, W. McGahern, G. Morgan, J. Muratore, M. Okamura, S. Peggs, F. Pilat, V. Ptitsin, L. Ratner, T. Roser, N. Saito, H. Satoh, Y. Shatunov, H. Spinka, M. Syphers, S. Tepikian, T. Tominaka, N. Tsoupas, D. Underwood, A. Vasiliev, P. Wanderer, E. Willen, H. Wu, A. Yokosawa, and A. N. Zelenski. Polarized proton collider at RHIC. *Nuclear Instruments and Methods in Physics Research, Section A: Accelerators, Spectrometers, Detectors and Associated Equipment*, 499(2-3):392–414, 2003.

[67] Shoji Nagamiya. PHENIX Experiment at RHIC. *Nuclear Physics A*, 566:287c–298 c, 1994.

[68] PHENIX Collaboration and N. Saito. Spin Physics with the PHENIX Detector System. *Nuclear Physics A*, 638:575–578, 1998.

[69] PHENIX Collaboration. Measurement of parity-violating spin asymmetries in W production at midrapidity in longitudinally polarized p+p collisions. page 8, 2015.

[70] M. Allen, M. J. Bennett, M. Bobrek, J. B. Boissevain, S. Boose, E. Bosze, C. Britton, J. Chang, C. Y. Chi, M. Chiu, R. Conway, R. Cunningham, A. Denisov, A. Deshpande,

M. S. Emery, A. Enokizono, N. Ericson, B. Fox, S. Y. Fung, P. Giannotti, T. Hachiya, A. G. Hansen, K. Homma, B. V. Jacak, D. Jaffe, J. H. Kang, J. Kapustinsky, S. Y. Kim, Y. G. Kim, T. Kohama, P. J. Kroon, W. Lenz, N. Longbotham, M. Musrock, T. Nakamura, H. Ohnishi, S. S. Ryu, A. Sakaguchi, R. Seto, T. Shiina, M. Simpson, J. Simon-Gillo, W. E. Sondheim, T. Sugitate, J. P. Sullivan, H. W. Van Hecke, J. W. Walker, S. N. White, P. Willis, and N. Xu. PHENIX inner detectors. *Nuclear Instruments and Methods in Physics Research, Section A: Accelerators, Spectrometers, Detectors and Associated Equipment*, 499(2-3):549–559, 2003.

[71] A. Adare, S. Afanasiev, C. Aidala, N. N. Ajitanand, Y. Akiba, R. Akiimoto, J. Alexander, H. Al-Taani, K. R. Andrews, A. Angerami, K. Aoki, N. Apadula, E. Appelt, Y. Aramak, R. Armendariz, E. C. Aschenauer, T. C. Awes, B. Azmoun, V. Babintsev, M. Bai, B. Bannier, K. N. Barish, B. Bassalleck, A. T. Basye, S. Bathe, V. Baublis, C. Baumann, A. Bazilevsky, R. Belmont, R. Bennett, A. Berdnikov, Y. Berdnikov, D. S. Blau, J. S. Bok, K. Boyle, M. L. Brooks, H. Buesching, V. Bumazhnov, G. Bunce, S. Butsyk, S. Campbell, A. Caringi, C. H. Chen, C. Y. Chi, M. Chiu, I. J. Choi, J. B. Choi, R. K. Choudhury, P. Christiansen, T. Chujo, O. Chvala, V. Cianciolo, Z. Citron, B. A. Cole, Z. Conesa del Valle, M. Connors, M. Csanád, T. Csörg, S. Dairaku, A. Datta, G. David, M. K. Dayananda, A. Denisov, A. Deshpande, E. J. Desmond, K. V. Dharmawardane, O. Dietzsch, A. Dion, M. Donadelli, L. D Orazio, O. Drapier, A. Drees, K. A. Drees, J. M. Durham, A. Durum, Y. V. Efremenko, T. Engelmore, A. Enokizono, H. En'yo, S. Esumi, B. Fadem, D. E. Fields, M. Finger, Jr., F. Fleuret, S. L. Fokin, J. E. Frantz, A. Franz, A. D. Frawley, Y. Fukao, T. Fusayasu, I. Garishvili, A. Glenn, M. Gonin, Y. Goto, R. Granier de Cassagnac, N. Grau, S. V. Greene, M. Grosse Perdekamp, T. Gunji, L. Guo, H. Å. Gustafsson, J. S. Haggerty, K. I. Hahn, H. Hamagaki, J. Hamblen, J. Hanks, R. Han, E. Haslum, R. Hayano, T. K. Hemmick, T. Hester, X. He, J. C. Hill, R. S. Hollis, W. Holzmann, K. Homma, B. Hong, T. Horaguchi, Y. Hori, D. Hornback, S. Huang, T. Ichihara, R. Ichimiya, H. Iinuma, Y. Ikeda, K. Imai, M. Inaba, A. Iordanova, D. Isenhower, M. Ishihara, M. Issah, A. Isupov, D. Ivanischev, Y. Iwanaga, B. V. Jacak, PHENIX: J. Jia, X. Jiang, B. M. Johnson, T. Jones, K. S. Joo, D. Jouan, J. Kamin, S. Kaneti, B. H. Kang, J. H. Kang, J. Kapustinsky, K. Karatsu, M. Kasai, D. Kawall, A. V. Kazantsev, T. Kempel, A. Khanzadeev, K. M. Kijima, B. I. Kim, D. J. Kim, E. J. Kim, J. S. Kim, Y. J. Kim, Y. K. Kim, E. Kinney, Á. Kiss, E. Kistenev, D. Kleinjan, P. Kline, L. Kochenda, B. Komkov, M. Konno, J. Koster, D. Kotov, A. Král, G. J. Kunde, K. Kurita, M. Kurosawa, Y. Kwon, G. S. Kyle, R. Lacey, Y. S. Lai, J. G. Lajoie, A. Lebedev, D. M. Lee, J. Lee, K. B. Lee, K. S. Lee, S. R. Lee, M. J. Leitch, M. A. L. Leite, P. Lichtenwalner, S. H. Lim, L. A. Linden Levy, A. Litvinenko, H. Liu, M. X. Liu, X. Li, B. Love, D. Lynch, C. F. Maguire, Y. I. Makdisi, A. Malakhov, V. I. Manko, E. Mannel, Y. Mao, H. Masui, M. McCumber, P. L. McGaughey, D. McGlinchey, C. McKinney, N. Means, M. Mendoza, B. Meredith, Y. Miake, T. Mibe, A. C. Mignerey, K. Miki, A. Milov, J. T. Mitchell, Y. Miyachi, A. K. Mohanty, H. J. Moon, Y. Morino, A. Morreale, D. P. Morrison, T. V. Moukhanova, T. Murakami, J. Murata, S. Nagamiya, J. L. Nagle, M. Naglis, M. I. Nagy, I. Nakagawa, Y. Nakamiya, K. R. Nakamura, T. Nakamura, K. Nakano, J. Newby, M. Nguyen, M. Nihashi, R. Nouicer, A. S. Nyanin, C. Oakley,

E. O'Brien, C. A. Ogilvie, K. Okada, M. Oka, A. Oskarsson, M. Ouchida, K. Ozawa, R. Pak, V. Pantuev, V. Papavassiliou, B. H. Park, I. H. Park, S. K. Park, S. F. Pate, H. Pei, J. C. Peng, H. Pereira, V. Peresedov, D. Yu. Peressounko, R. Petti, C. Pinkenburg, R. P. Pisani, M. Proissl, M. L. Purschke, H. Qu, J. Rak, I. Ravinovich, K. F. Read, K. Reygers, V. Riabov, Y. Riabov, E. Richardson, D. Roach, G. Roche, S. D. Rolnick, M. Rosati, S. S. E. Rosendahl, P. Rukoyatkin, B. Sahlmueller, N. Saito, T. Sakaguchi, V. Samsonov, S. Sano, M. Sarsour, T. Sato, M. Savastio, S. Sawada, K. Sedgwick, R. Seidl, R. Seto, D. Sharma, I. Shein, T. A. Shibata, K. Shigaki, H. H. Shim, M. Shimomura, K. Shoji, P. Shukla, A. Sickles, C. L. Silva, D. Silvermyr, C. Silvestre, K. S. Sim, B. K. Singh, C. P. Singh, V. Singh, M. Slunečka, R. A. Soltz, W. E. Sondheim, S. P. Sorensen, I. V. Sourikova, P. W. Stankus, E. Stenlund, S. P. Stoll, T. Sugitate, A. Sukhanov, J. Sun, J. Sziklai, E. M. Takagui, A. Takahara, A. Taketani, R. Tanabe, Y. Tanaka, S. Taneja, K. Tanida, M. J. Tannenbaum, S. Tarafdar, A. Taranenko, E. Tennant, H. Themann, D. Thomas, M. Togawa, L. Tomášek, M. Tomášek, H. Torii, R. S. Towell, I. Tserruya, Y. Tsuchimoto, K. Utsunomiya, C. Vale, H. W. van Hecke, E. Vazquez-Zambrano, A. Veicht, J. Velkovska, R. Vértesi, M. Virius, A. Vossen, V. Vrba, E. Vznuzdaev, X. R. Wang, D. Watanabe, K. Watanabe, Y. Watanabe, F. Wei, J. Wessels, S. N. White, D. Winter, C. L. Woody, R. M. Wright, M. Wysocki, Y. L. Yamaguchi, R. Yang, A. Yanovich, J. Ying, S. Yokkaichi, J. S. Yoo, G. R. Young, I. Younus, Z. You, I. E. Yushmanov, W. A. Zajc, A. Zelenski, S. Zhou, and L. Zolin. Cross Section and Parity Violating Spin Asymmetries of Wˆ+/- Boson Production in Polarized p+p Collisions at sqrt(s)=500 GeV. page 6, 2010.

[72] Kensuke Okada. Observation of W decay in 500 GeV p+p collisions at RHIC. page 4, 2010.

[73] Mike Beaumier, Ciprian Gal, Minjung Kim, Sanghwa Park, R Seidl, and Inseok Yoon. Run 13 Spin Database Quality Assurance. Technical report, 2014.

[74] Michael Collins. The Naive Bayes Model, Maximum-Likelihood Estimation, and the EM Algorithm. pages 1–21, 2013.

[75] Zhong Bo Kang and Jacques Soffer. General positivity bounds for spin observables in single particle inclusive production. *Physical Review D - Particles, Fields, Gravitation and Cosmology*, 83(11):1–8, 2011.

.1 Systematic Studies–A_L

This Appendix has been directly copied without modification from the Run 13 analyzers' analysis note. This is not my work. It was carried out by Daniel Jumper and Ralf Seidl in our common analysis note [29]

.2 Combined systematic studies

As could be seen in the previous section, it seems, that using the data-based signal to background extraction in the way introduced in [?] the resulting background corrected asymmetries are significantly inconsistent with any of the parameterizations. The up and down quark polarizations are generally well enough known, as are the W kinematics, that there is little doubt in the asymmetries mostly related to them, namely the forward $W^- \to \mu^-$ asymmetries and the backward $W^+ \to \mu^+$ asymmetries. It seems therefore much more likely, that either a statistical fluctuation or analysis error creates the resulting discrepancies. When taking the signal to background values at face value a statistical fluctuation is essentially excluded, however, if there is a significant overestimation of these ratios it could still be possible.

In order to understand the origins of the data parameterization discrepancy better we are studying the asymmetries and the signal to background ratios as a function of various relevant variables. In most cases the background corrected asymmetries as well as the signal to background ratios are displayed together to give a better idea of the impact on the background. Either the data-based or W-MC based signal to background ratios are displayed and used to see the difference it makes.

.2.1 Asymmetries as function of W selection and deflection angular bands

As the asymmetry calculation only uses the dw_{23} region with supposedly W support the whole region and the inverse selection are also of interest. As the inverse region is expected to be dominated by more background its asymmetries should be closer to zero as only the W/Z production gives parity violating asymmetries. However, it seems, that while statistical uncertainties are generally larger the asymmetries have a tendency to be nonzero in particular also the double spin asymmetries. This could either be an indication of remaining signal in the sidebands or some remaining background asymmetries. The Asymmetries in the dw_{23} sidebands can be seen in Figs. .1

.2.2 Asymmetries and Signal to BG ratio as a function of rate, time and transverse momentum range

Another important test is whether the asymmetries show any kind of rate or run dependence effect. For this purpose the data was split up into three rapidity ranges with about equal luminosity: The multi-collision parameters were chosen as 0, 0.69, 0.83, 2. Naively a rate dependent effect would result in a certain ordering of the asymmetries with either increasing or decreasing asymmetries as the rates increase. All the asymmetries as a function of minimum W_{ness} cut are displayed in Fig. .2. Out of the 12 different asymmetries (arm x charge x singe,double spin asymmetry) a few display such a behavior while the majority appears to be randomly distributed between the different rates.

A t-test between low and high to intermediate rates was performed and the distribution is given in Fig. .3. The amount of larger differences is on the order expected for statistical fluctuations around an average value and therefore one can conclude, that no obvious rate dependent effect is visible.

Similarly, the run dependence was studied in three range bins from 0, 392276, 395770, 399000. While some correlation with the rates is likely, it should be mostly washed out as the collision rates decrease within fills. With the run dependence it would be possible to see, if time dependent detector or accelerator related effects bias the results in some way. The resulting asymmetries can be seen in Fig. .4 and the corresponding t-test between low, high and mid run ranges is given in Fig. .5. Again, while some asymmetries show a range dependence the overall distribution of differences as consistent with fluctuations only.

Another test is the dependence on the minimum transverse momentum cut or the transverse momentum range selected. As mentioned earlier in this analysis note the W and Z decay muons dominate at larger transverse momenta while at lower transverse momenta even more dilution from other muon processes and fake hadrons contribute. As a consequence any asymmetry should be largely diluted and start to appear as the minimum transverse momentum cut is increased. Such a behavior can be seen in Fig. .6 where essentially all asymmetries are consistent with zero at low transverse momenta and then increase in some of the cases. What appears different than expectation is the signal to background ratio obtained from the fits. The signal to background ratios from the fits seem to be not increasing while the MC based signal to background ratios show the expected behavior.

The asymmetries in ranges of transverse momenta are shown in Fig. .7. After small initial asymmetries they are mostly consistent at intermediate transverse momentum ranges and only seem to change again at transverse momenta of around 18. The signal-to-background distribution is again unexpected as obtained from the fits while it is more consistent with expectations in the MC based extraction.

.2.3 Addition of artificial MC-based signal and asymmetries

Another type of test uses the generated signal MC and includes a fraction of it into the data set before calculating asymmetries and signal to background ratios. In order to do so, crossings are assigned randomly to the MC such, that a certain set of asymmetries can be generated. As an initial test only constant asymmetries were generated. Not any asymmetries can be physically created as the yields in the 4 helicity combinations need to non-negative. The double spin asymmetries need to be within a certain range of the other two. The initial asymmetries created were 40% and 10% for the negative generated muons and -20% and -30% for the positive generated muons while no double spin asymmetries were generated.

The resulting asymmetries and signal-to-background ratios are displayed in Fig. .8 for an MC admixture of 20 fb^{-1} as a function of the minimum W_{ness} cut. One can see, that with increasing minimum W_{ness} the resulting asymmetries begin to increase as expected while the generally fall short of the generated asymmetries. In Fig. .9 the asymmetries and signal-to-background ratios are displayed as a function of the MC admixture. Also the background corrected asymmetries are displayed which should return the generated asymmetries with the exception of the actual signal based asymmetries in the actual data. As one can see, the asymmetries are not properly recovered especially at low admixtures. While part of it could be coming from the Physics asymmetries its contribution should be small. Again, using the MC based signal to background ratios seem to better recover the generated asymmetries.

.2.4 Checking the relative luminosities between patterns

In the previous evaluation of the asymmetries we were implicitly assuming that we took the same luminosity for every spin pattern. To make sure this is the case, we explicitly counted the scalers from the spin Data Base from the entry ScalerBbcNoCut for each spin pattern and we found the following:

Spin Pattern (Blue, Yellow)	
+1, +1	5.29+11
-1, +1	5.28e+11
+1, -1	5.29e+11
-1, -1	5.29e+11.

As can be seen in the previous table, there is only a 0.2% difference between the luminosity of the spin patterns, so the previous assumption that there are no differences in luminosities between spin patterns is safe. As a double check, we rescaled the yield for each spin pattern according to the scalers just reported, and as expected no significant differences were observed in the combined asymmetries, as shown in figure .10.

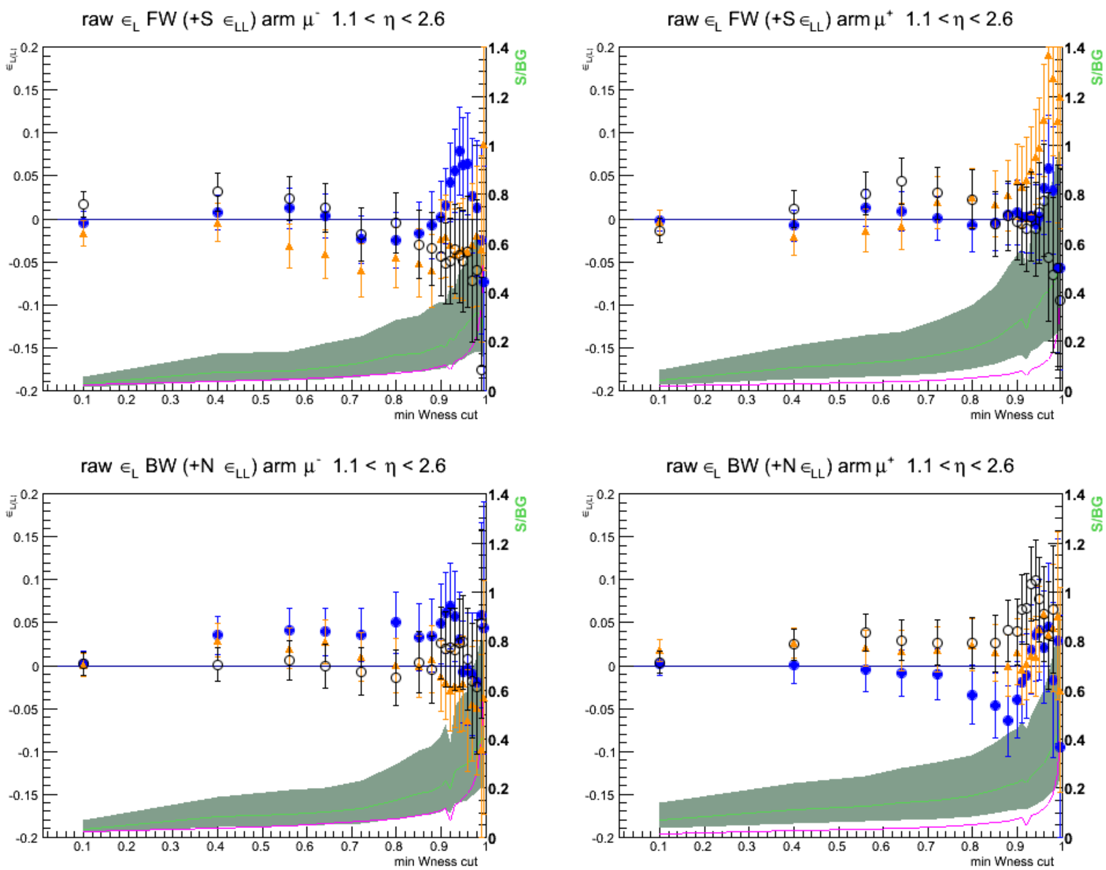

Figure .1: Raw asymmetries ϵ_L for the Blue (blue symbols) and Yellow (orange symbols) beams and ϵ_{LL} (black symbols) for both arms and charges as a function of the pre-selection range. The combination of all rapidities in one bin after selecting the **sideband** dw_{23} region is displayed. In addition the extracted signal to background ratios are displayed using the right-hand axis values. The green line displays the data-based extraction method while the magenta line represents the MC signal based extraction.

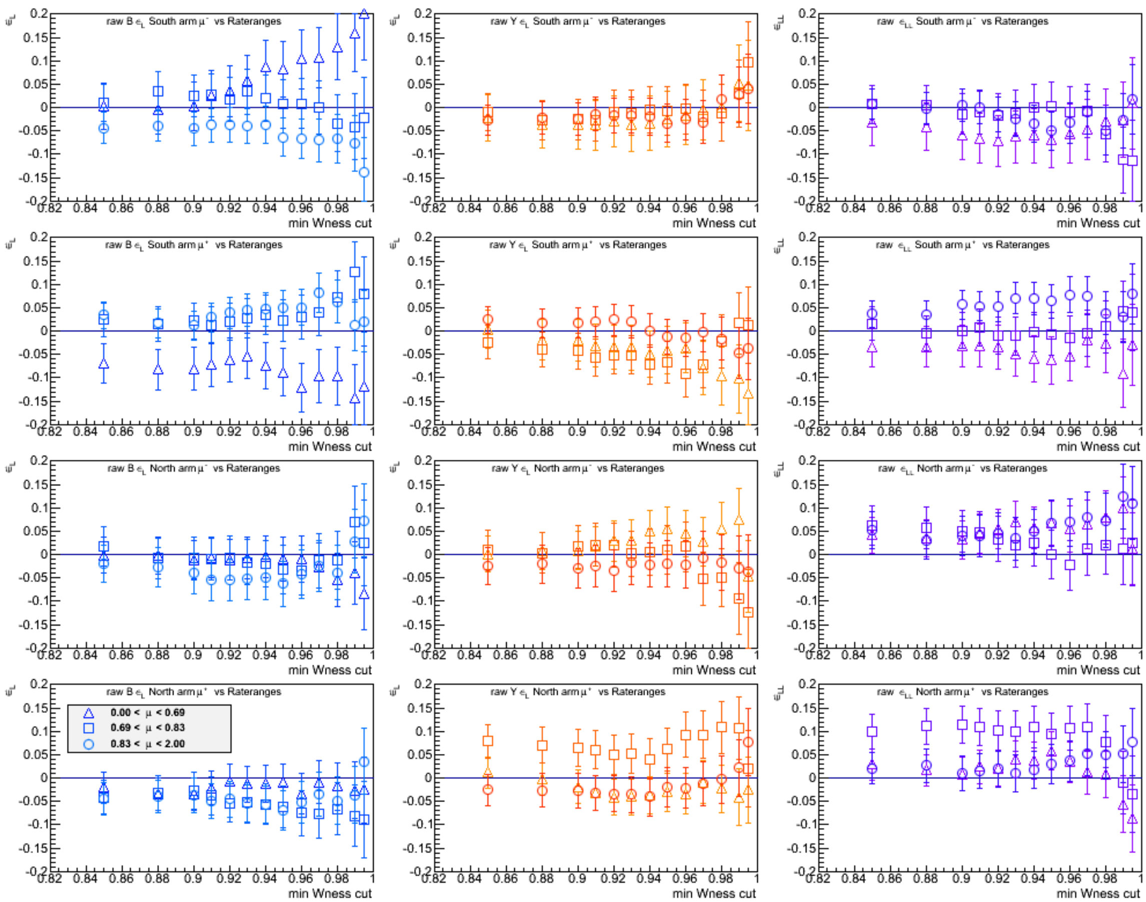

Figure .2: Raw asymmetries as a function of minimal W_{ness} cut when splitting the data sample into three nearly equal luminosity bins of increasing BBC rate in the order of open triangles, open squares and open circles. Each plot displays one asymmetry for each arm and charge. The central dw_{23} region has been selected. In addition the extracted signal to background ratios are displayed using the right-hand axis values. The green line displays the data-based extraction method while the magenta line represents the MC signal based extraction.

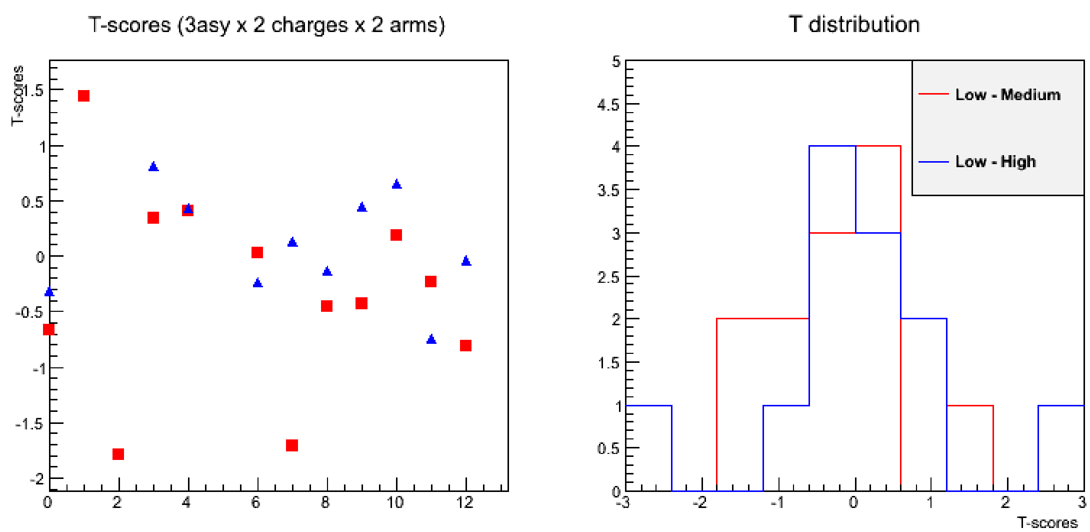

Figure .3: Student T scores and distribution when comparing the lot to medium and the low to high rate subset.

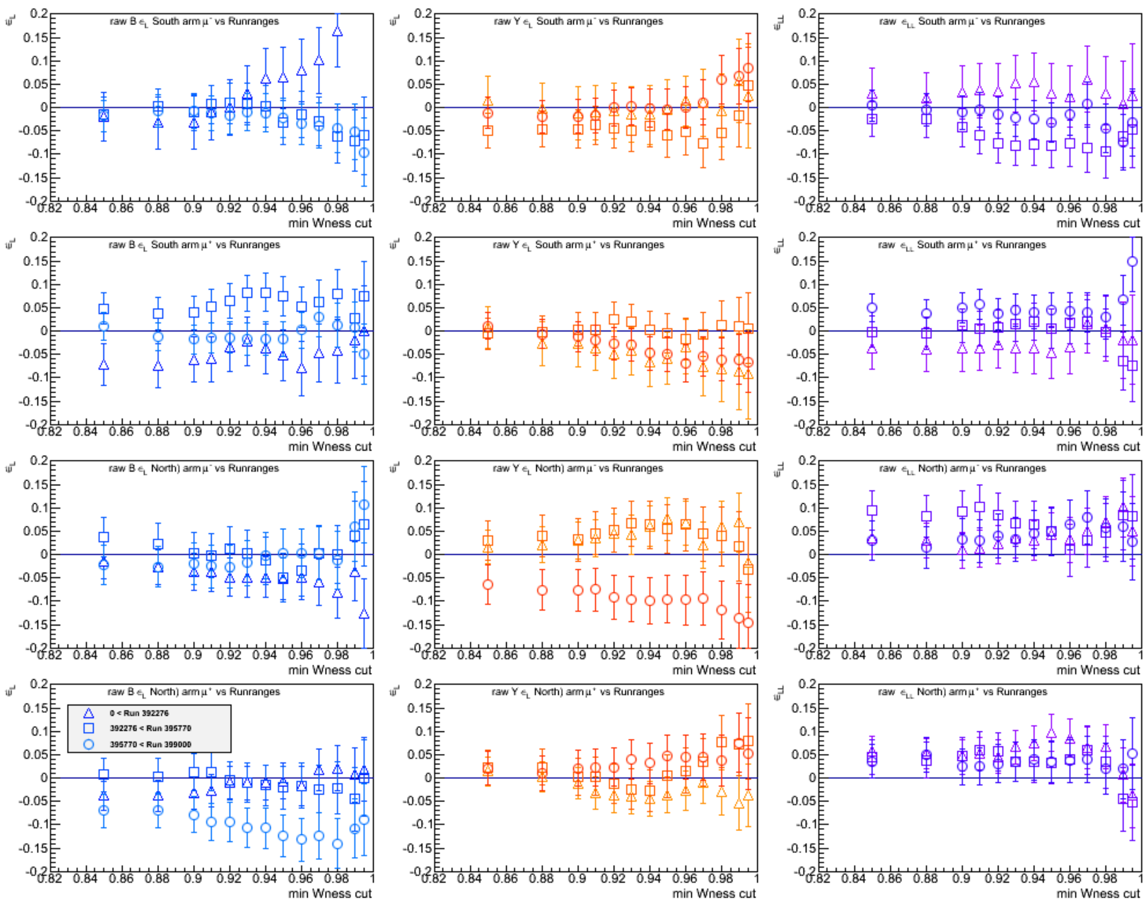

Figure .4: Raw asymmetries as a function of minimal W_{ness} cut when splitting the data sample into three nearly equal luminosity bins of increasing run number in the order of open triangles, open squares and open circles. Each plot displays one asymmetry for each arm and charge. The central dw_{23} region has been selected. In addition the extracted signal to background ratios are displayed using the right-hand axis values. The green line displays the data-based extraction method while the magenta line represents the MC signal based extraction.

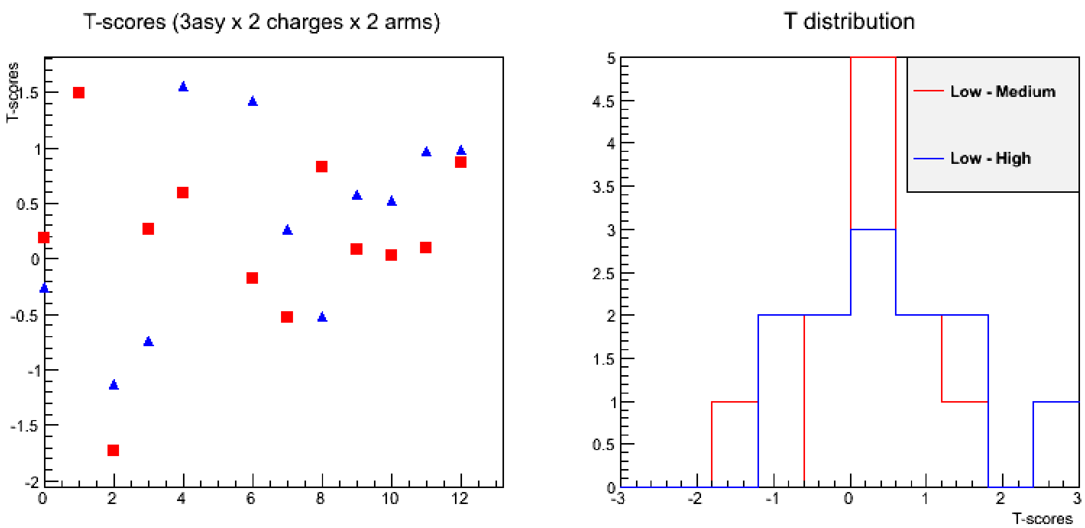

Figure .5: Student T scores and distribution when comparing the lot to medium and the low to high run number subset

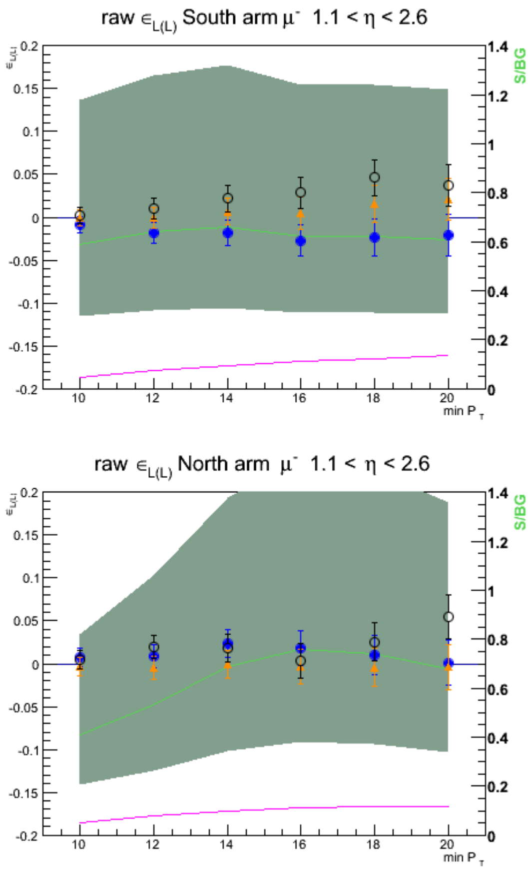

Figure .6: Raw asymmetries ϵ_L for the Blue (blue symbols) and Yellow (orange symbols) beams and ϵ_{LL} (black symbols) for both arms and charges as a function of the minimal transverse momentum cut are displayed. In addition the extracted signal to background ratios are displayed using the right-hand axis values. The green line displays the data-based extraction method while the magenta line represents the MC signal based extraction.

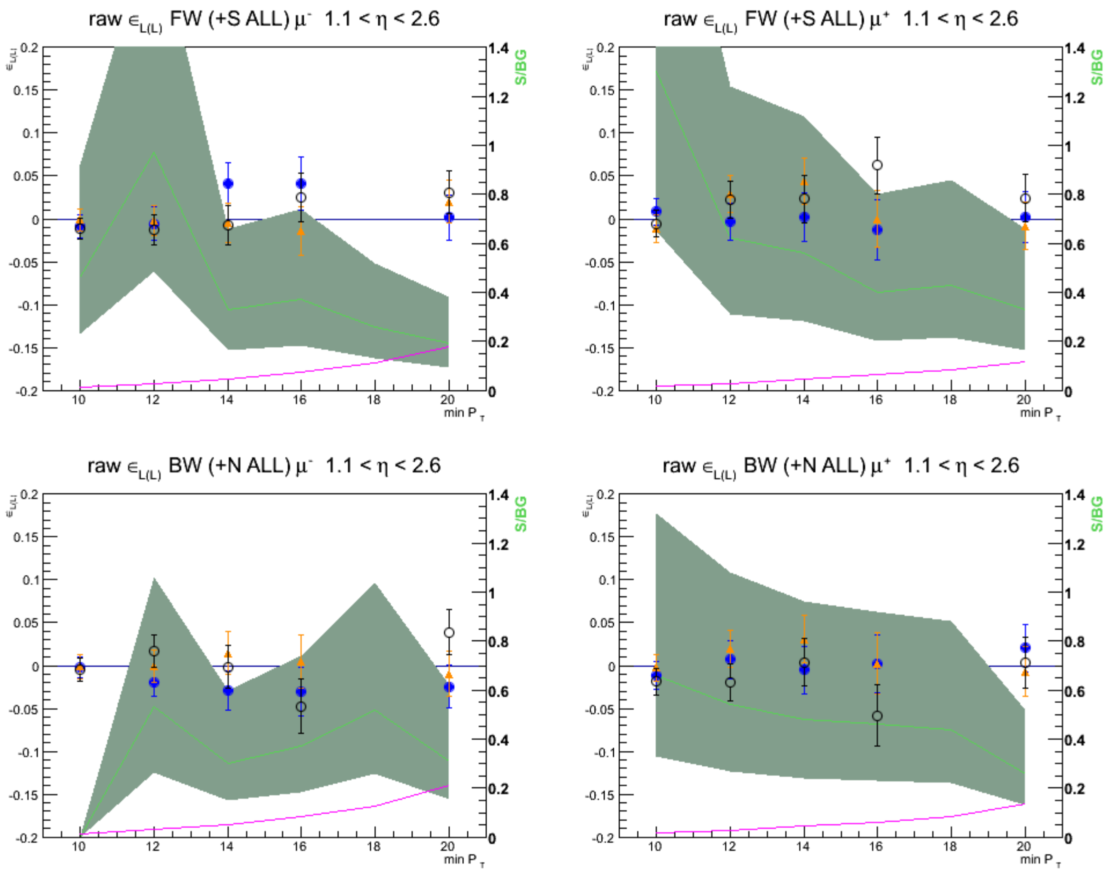

Figure .7: Raw asymmetries ϵ_L for the Blue (blue symbols) and Yellow (orange symbols) beams and ϵ_{LL} (black symbols) for both arms and charges as a function of transverse momentum are displayed. The combination of all rapidities in one bin after selecting the central dw_{23} region is displayed. In addition the extracted signal to background ratios are displayed using the right-hand axis values. The green line displays the data-based extraction method while the magenta line represents the MC signal based extraction.

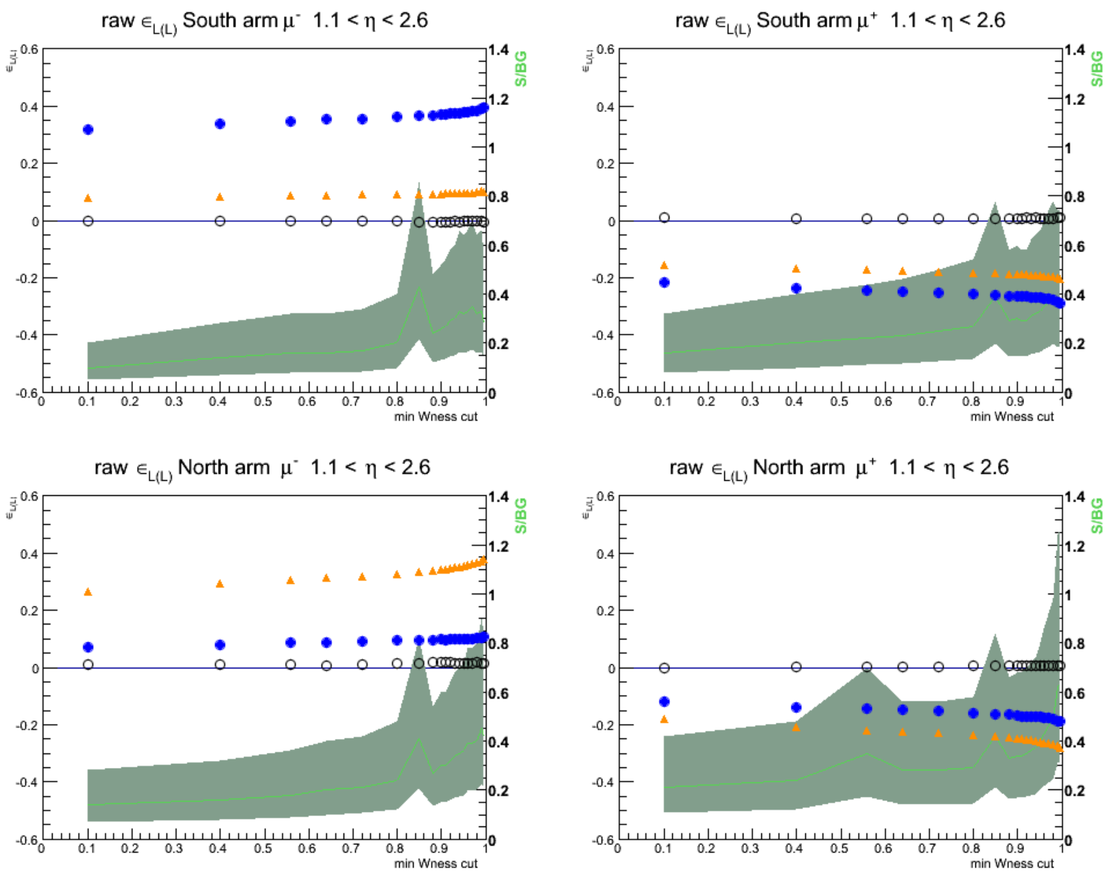

Figure .8: Raw asymmetries ϵ_L for the Blue (blue symbols) and Yellow (orange symbols) beams and ϵ_{LL} (black symbols) for both arms and charges as a function of the minimum W_{ness} cut are displayed with a fixed signal MC addition of 20 fb^{-1}. The combination of all rapidities in one bin after selecting the central dw_{23} region is displayed. In addition the extracted signal to background ratios are displayed using the right-hand axis values. The green line displays the data-based extraction method while the magenta line represents the MC signal based extraction.

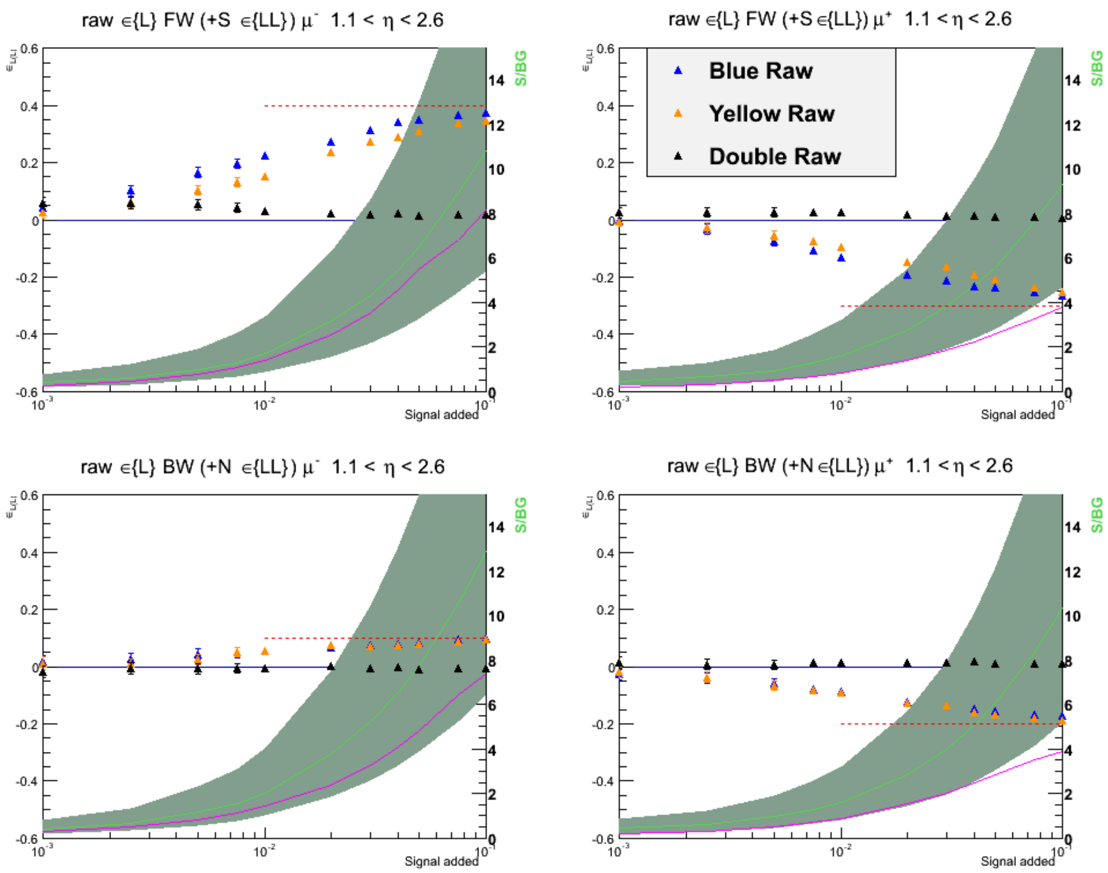

Figure .9: Raw asymmetries ϵ_L for the Blue (blue symbols) and Yellow (orange symbols) beams and ϵ_{LL} (black symbols) for both arms and charges as a function of the total Signal MC added are displayed. The combination of all rapidities in one bin after selecting the central dw_{23} region is displayed. In addition the extracted signal to background ratios are displayed using the right-hand axis values. The green line displays the data-based extraction method while the magenta line represents the MC signal based extraction. The background corrected asymmetries using either the fit based S/BG values (downward open triangles) or old extraction (upward open triangles) are also displayed.

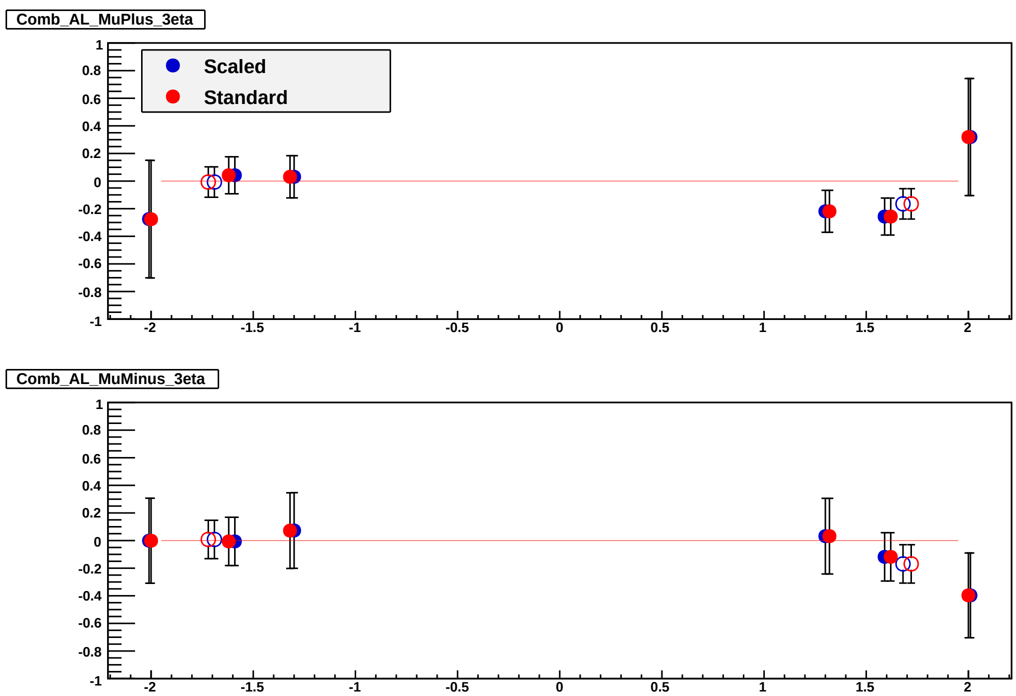

Figure .10: Comparison between the combined asymmetries with (in blue) and without (in red) the yield rescaling by the relative luminosity of each spin pattern.